DESIGN STRATEGIES FOR METAL-ORGANIC FRAMEWORKS AS ACID GAS ADSORBENTS

A Dissertation
Presented to
The Academic Faculty

by

Jayraj Nayan Joshi

In Partial Fulfillment
of the Requirements for the Degree
Doctor of Philosophy in the
School of Chemical and Biomolecular Engineering

Georgia Institute of Technology
August 2019

DESIGN STRATEGIES FOR METAL-ORGANIC FRAMEWORKS AS ACID GAS ADSORBENTS

Approved by:

Dr. Krista S. Walton, Advisor
School of Chemical and Biomolecular Engineering
Georgia Institute of Technology

Dr. David S. Sholl
School of Chemical and Biomolecular Engineering
Georgia Institute of Technology

Dr. Faisal Alamgir
School of Materials Science and Engineering
Georgia Institute of Technology

Dr. Ryan P. Lively
School of Chemical and Biomolecular Engineering
Georgia Institute of Technology

Dr. J. Carson Meredith
School of Chemical and Biomolecular Engineering
Georgia Institute of Technology

Date Approved: [May 16th, 2019]

To The People That Supported Me

ACKNOWLEDGEMENTS

I would like to first thank my academic advisor, Dr. Krista Walton, who allowed me to join her research group when I was struggling to stay in the PhD program. Dr. Walton cultivated an environment of academic creativity, self-ambition, and facile collaboration, which imbued a lasting effect on my personal and professional development. I would also like to acknowledge my doctoral committee members: Dr. Alamgir, Dr. Meredith, Dr. Sholl, and Dr. Lively. I appreciate their time and expert insight into my graduate work.

I am grateful for interacting with all of Dr. Krista Walton's research group members from 2014 to 2019. The group culture is friendly, collaborative, and diverse, which made my tenure very enjoyable. Even when they wouldn't stay out of my office. The scientific curiosity and dedication of undergraduate researchers James Dow and Patrick Feininger generated significant contributions to my portfolio of work. I specifically acknowledge Dr. Colton Moran here, whom I worked with and learned from over multiple collaborative and fruitful research projects that encompass a large portion of my dissertation. I am additionally grateful for the many others I worked and interacted with during my time in graduate school—I am fortunate to have many of them as friends going forward.

I would finally like to acknowledge the staff of Georgia Tech's IEN and NMR centers for frequent assistance with data collection and analysis. Finally, thanks to the EH&S department and building manager Rod Sefton for help in setting up and troubleshooting hazardous gas handling systems necessary for my PhD studies.

TABLE OF CONTENTS

LIST OF TABLES

LIST OF FIGURES

LIST OF SYMBOLS AND ABBREVIATIONS

^{1}H	Proton Nuclei
^{13}C	Isotope-13 Carbon Nuclei
^{27}Al	Aluminum Nuclei
%RH	Percent Relative Humidity
°C	Degree Centigrade
α-Al_2O_3	Alumina/Alpha-Aluminum Oxide
α-Fe_2O_3	Hematite
μ(E)	Absorption Coefficient
μm	Micron
Å	Angstrom
Al(s)	Metallic Aluminum
Al-MOF	Aluminum-based Metal-Organic Framework
$Al(OH)_3$	Aluminum Hydroxide
Al_2O_3	Aluminum Oxide
Al_4C_3	Aluminum Carbide
$AlCl_3$	Aluminum Chloride
as-	As-synthesized
atm	Atmosphere of Pressure
bar	Bar of Pressure
BDC	Terephthalic Acid
BDC-COOH	Trimellitic Acid
BDC-(COOH)2	1,2,4,5-Benzenetetracarboxylic Acid

$BDC\text{-}NH_2$	2-Aminoterephthalic Acid
$BDC\text{-}NO_2$	2-Nitroterephthalic acid
BET	Brunauer, Emmett, and Teller
BTC	Trimesic Acid
CDC	Carbide-Derived Carbon
cc	Cubic Centimeter
cc g^{-1}	Normalized Volume (Cubic Centimeter) per Gram Material
CO	Carbon Monoxide
CO_2	Carbon Dioxide
-COOH	Uncoordinated Carboxylic Acid
D_2O	Deuterium Oxide
DFT	Density Functional Theory
DMF	N,N'-Dimethylformamide
EDS	Energy Dispersive Spectroscopy
eV	Electron Volt
EXAFS	Extended X-ray Absorption Fine Structures
Fe_2O_3	Iron Oxide
GCMC	Grand Canonical Monte Carlo
g	Gram
h	Hour
H_2O	Water
$H_2O(v)$	Water Vapor
H_2S	Hydrogen Sulfide
H_2SO_4	Sulfuric Acid
HKUST	Hong Kong University of Science and Technology

IAST	Ideal Adsorbed Solution Theory
ICDD	International Centre for Diffraction Data
K	Kelvin
keV	Kiloelectron Volt
kg	Kilogram
kJ	Kilojoule
lbs	Pound(s)
lp-	Large Pore
$m^2 g^{-1}$	Square Meter per Gram
MFC	Mass Flow Controller
mg	Milligram
MHz	Megahertz
MIL	Material Institute Lavoisier
min	Minute
mL	Milliliter
mmol	Millimole
mmol g^{-1}	Adsorption Capacity in Millimole per Gram
MOF	Metal-Organic Framework
mol	Mole
N_2	Nitrogen
NaOH	Sodium Hydroxide
NG	Natural Gas
NLDFT	Non-local Density Functional Theory
nm	Nanometer
NMR	Nuclear Magnetic Resonance

NO_2	Nitrogen Dioxide
np-	Narrow Pore
NP	Nanoparticle
MAS	Magic-Angle Spinning
MQMAS	Multi-Quantum Magic-Angle Spinning
P/P_0	Relative Pressure
PSD	Pore Size Distribution
psi	Pounds per Square Inch
PSM	Post-Synthetic Modification
PXRD	Powder X-Ray Diffraction
QSDFT	Quenched Solid Density Functional Theory
s	Second
SBU	Standard Building Unit
SEM	Scanning Electron Microscopy
SO_2	Sulfur Dioxide
SS	Solid-state
STP	Standard Temperature and Pressure
TEM	Transmission Electron Microscopy
TGA	Thermogravimetric Analysis
UiO	University of Oslo
wt%	Weight Percent
XAS	X-ray Absorption Spectroscopy
XAFS	X-ray Absorption Fine Structure
XANES	X-ray Absorption Near-Edge Structure
XPS	X-ray Photoelectron Spectroscopy

SUMMARY

This dissertation investigates modification and production pathways for metal-organic frameworks (MOFs) to facilitate their use as acid gas adsorption media. Prior art substantiating the potential and motivation for creating MOF-based acid gas adsorbents are detailed in Chapter 1. Current issues and technology concerning acid gas removal are also reviewed. The impact of framework structure and functionalization on resulting MOF stability and adsorption potential for acid gases (H_2S, SO_2, NO_2, etc.) requires further understanding due to the experimental complications involved with handling these hazardous compounds. Additionally, strategies for integrating MOFs onto pragmatic end-use media (thin films, filters/membranes, monoliths, etc.) are nascent, complex, and expensive. Accordingly, work herein aims to develop new MOF-based acid gas adsorption technology through experimental methods and techniques described in Chapter 2.

Chapter 3 discusses the relationship between MOF material properties and acid gas stability. Point defects were installed into traditionally-stable MIL-125-NH_2(Ti) for the first time. Defect incorporation controllably manipulates internal porosity, but fosters framework instability in humid environments. In another study, irreversible H_2S chemisorption sites were installed onto zirconium-based frameworks through ligand functionalization. Unlike MOFs containing reactive metal centers, the accessible porosity and structure of functionalized MOFs were not sacrificed from resulting chemisorption reactions. This study outlines a method for avoiding degradation from MOF metal-adsorbate interactions while allowing high irreversible acid gas uptake. Finally, the impact of adsorbent pelletization on acid gas stability was probed for various candidate MOF

systems. Highly connected zirconium- and titanium-based frameworks do not degrade following hydrogen sulfide (H_2S) exposure as non-processed and pelletized powders. MIL-101(Cr) frameworks similarly remain stable as pristine powders, but inherit crystalline microstrain and accessible surface area losses after pelletization. Structural features in MIL-101(Cr) materials were lost after subsequent acid gas exposure. Results inform how framework mechanical stability impacts the tolerance of candidate porous materials in acid gas environments when standard material processing procedures are carried out.

MOF ligand functionalization is a commonly employed method for introducing chemical specificity into frameworks. As such, this technique is applied to enhance H_2S and SO_2 adsorption in Chapter 4. UiO-66(Zr) was modified with linker-based carboxylic acid (-COOH) groups to encourage electronic adsorption interactions with polar SO_2 and H_2S. Structure refinement confirmed produced materials remain isostructural to UiO-66(Zr). Despite crystallographic measurements, various material defects in synthesized products were identified through multiple experimental characterization techniques. Fixed-bed adsorption experiments revealed enhanced reversible uptake potential for MOFs containing -COOH groups. Following up from Chapter 3, post-synthetic modification of accessible –COOH sites created reactive copper carboxylate (-COOCu) moieties. Newly-formed UiO-66-COOCu and UiO-66-$(COOCu)_2$ adsorbents reactively removed H_2S at strongly enhanced capacities, allowing both reversible and irreversible acid gas removal design strategies. In another investigation, multicomponent $CH_4/CO_2/H_2S$ adsorption experiments were performed on a series of frameworks, both with and without pendant primary amine (-NH_2) binding sites. Amine functional groups enhanced H_2S selectivity and uptake capacity at low concentrations (1% H_2S) from non-modified structures. *In situ*

FTIR measurements affirmed reversible physisorption interactions between pendant amines and H_2S, revealing cycling potential supported by multicomponent breakthrough data. Results from Chapter 4 exhibit the applicability of MOF ligand functionalization on enabling and tuning acid gas interactions.

Unconventional MOF production pathways yield unique composite materials through green and inexpensive approaches in Chapter 5. Supported aluminum frameworks were created in one-step from insoluble aluminum-based support structures. MOF products display inherent preferred crystal growth orientation and distinct textural properties from conventionally-synthesized frameworks. Adding strong acid reagents produced non-supported frameworks through the same method. Resultant morphology, porosity, and crystalline orientation of non-supported products are adjustable—this control is importantly not possible with conventional metal precursors. Chapter 6 utilizes the structured materials produced in Chapter 5 to create MOF-derived aluminum oxide microtubes. Pillared alumina materials obtain macro/meso/microporous openings. This material is utilized as an iron oxide/aluminum oxide composite for H_2S removal applications. Sulfur loadings and distributions are determined through inductively coupled plasma (ICP) measurements and microscopy techniques. Aluminum terephthalate MIL-53(Al) was also regrown on and from derived oxide nanotubes two successive times, regaining full porosity and crystallinity each cycle. Spatial distribution and architectural attributes are directly translated onto MOF-derived media from supported MIL-53(Al) precursors, demonstrating a high level of inherent nanoscale porous material growth control.

CHAPTER 1. INTRODUCTION

1.1 Acid Gases

1.1.1 Emission Sources

Separations are the most pervasive engineering operations across the chemical industry.[1] Energy harvesting, commodity chemical production, air quality control, hazardous gas sequestration, and a variety of niche markets mandate gas separation techniques encompassing a vast library of chemical species and reagents.[2–5] Among these, separations involving acid gases carry unique challenges. The inherent corrosive and toxic nature of acidic compounds such as hydrogen sulfide (H_2S), sulfur dioxide (SO_2), and nitrogen dioxide (NO_2) create operational problems with separation equipment and necessitate controlled handling procedures.[6,7] Acid gases furthermore exact phenomena such as acid rain and other detrimental effects on human health, infrastructure, and the environment.[8,9] Restrictive tolerances exist for even trace amounts of these compounds within industrial processes for these reasons. Consequently, acid gas separations must exhibit high removal performance to have practical consideration.

Acidic emissions arise from various sources. Post-combustion streams account for most NO_2 and SO_2 discharge.[10] Example producers include transportation, power generation, and fossil fuel combustion.[11,12] As a result, NO_2 and SO_2 emissions occur consistently across the globe. Aside from their inherent toxicity, these gases interact with other atmospheric constituents to create aerosols and other pollutants which strongly affect air quality and climate.[9] Most hydrogen sulfide emissions root from another ubiquitous

human activity—oil and natural gas extraction. This is important, as natural gas exhibits the strongest worldwide growth out of all fossil fuel sources. Global demand has increased at a rate of 3% per year over the past thirty years, and is predicted to account for nearly 23% of the global energy supply by 2030.[13] Consequently, efficient and cost-effective natural gas purification is becoming increasingly important for the petroleum industry. However, about 40% of extraction fields possess sufficient levels of hydrogen sulfide (H_2S) to necessitate removal, in order to satisfy environmental guidelines and preserve the economic viability of the fuel.[13,14] Mixtures of naturally present hydrogen sulfide with methane and other hydrocarbons are referred to as "sour gas", which often also contain acid gases such as carbon dioxide (CO_2), mercaptans, and a variety of other contaminants that vary by region.[13,15]

1.1.2 Current Removal Techniques

1.1.2.1 Flue Gas Remediation

Although regenerable SO_2 removal techniques such as selective catalytic reduction offer benefits in cost and process waste minimization, non-regenerable wet flue gas desulfurization (FGD) is more well-established and widely utilized.[16] Wet FGD processes generally introduce SO_2 into slurries containing alkaline absorption media—most commonly lime and limestone.[17] As such, acid gases are neutralized through acid-base reactions. A schematic of wet FGD is presented in Figure 1-1, where acid gases are introduced into the bottom of the absorber and contacted by downward-flowing scrubbing solution. Srivastava and Jozewicz detailed a large expanse of utilized FGD technologies constituting the most common industry approaches to satisfy emission regulations.[17]

Although efficient, FGD and other conventional acid gas absorption processes foster high capital and operations costs.

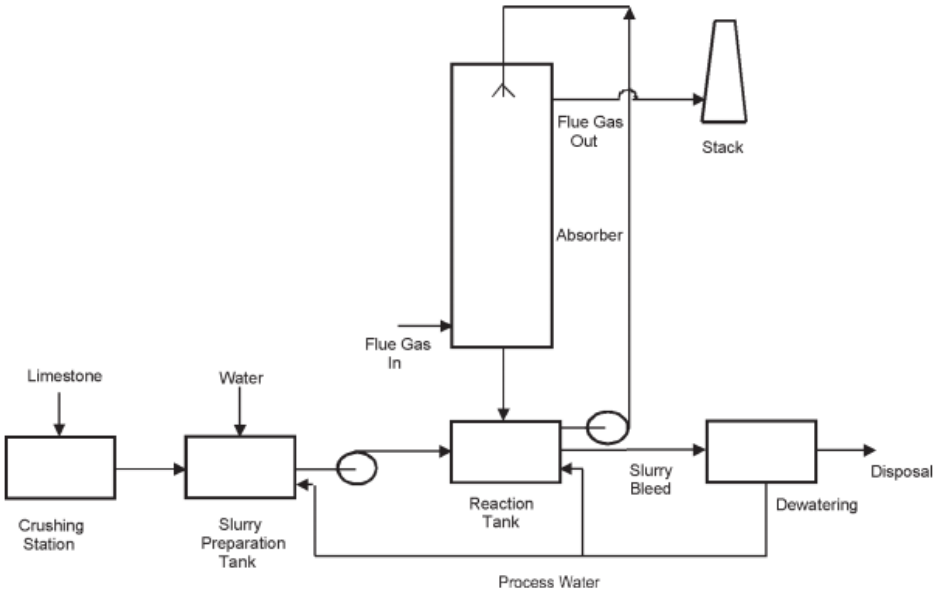

Figure 1-1: Simplified schematic of wet flue gas desulfurization (FGD) process. Image reproduced from Srivastava and Jozewicz[17]

1.1.2.2 Hydrogen Sulfide Removal from Natural Gas Sources

Sour gas streams are either flared or sent to sulfur recovery units. Figure 1-2 illustrates the latter via the Claus process, which entails the hydrogen sulfide oxidation to SO_2 and subsequent reaction of both acid gases to precipitate sulfur. Sulfur products may be used as feedstock for commodity chemical production to offset remediation costs. This conversion is achieved through multiple stages of combustion and selective catalysis.[18] The strongly exothermic oxidation reactions and evolution of corrosive sulfur dioxide (SO_2) unfortunately generate high operational costs.[19,20] Furthermore, SO_2 is evolved as another acidic by-product that must be sequestered, neutralized, or converted. Separation of acid

gases from hydrocarbons is also required prior to Claus conversion. Chemical absorption using aqueous alkanolamine solutions, most popularly N-methyldiethanolamine (MDEA), and metal chelating agents are typically employed to enact these separations.[21] These processes exhibit high acid gas selectivities, but mandate expensive absorbent solution regeneration schemes and equipment costs.[21,22]

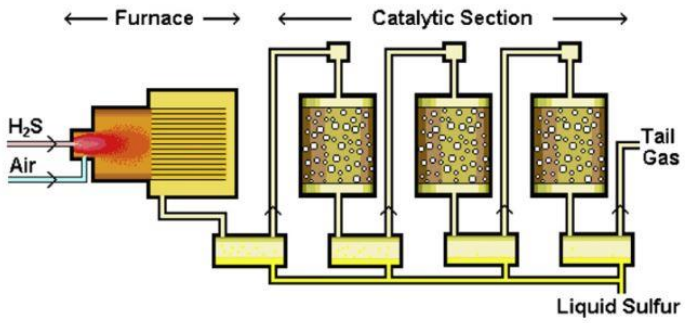

Figure 1-2: Simplified Claus process scheme. Image reproduced from de Angelis.[19]

1.2 Adsorption as an Alternative Acid Gas Removal Technique

The common disadvantage amongst traditional acid gas removal processes is economic. Because acid gases need to be removed to extremely low (commonly ppm-level) concentrations, sometimes large unit volumes and multistage operations are required to achieve desired purities. Regenerating spent absorbent liquids in discussed technologies also incurs large energy utilities to overcome the high heat capacities of aqueous solutions.[23] FGD schemes experience significant cost increases when using proprietary neutralizers and suffer energy penalties imparted by steam generation via exothermic aqueous scrubbing.[24] Capital costs stem from necessary equipment to withstand corrosive alkaline scrubbing media, large pumping units to cycle dense absorbent slurries, and energy utilities emerging from Claus Tail Gas Treating (TGT) units.[25] Perhaps the most

economical treatment is performed routinely in upstream petrochemical operations: wellhead gas mixtures containing hydrogen sulfide are often flared. Although undoubtedly inexpensive, flaring releases SO_2, CO_2 and harmful particulate matter into the atmosphere, while simultaneously wasting ~3.5% of the non-renewable resource worldwide.[26,27]

Adsorptive removal processes can avoid these issues. Generally, gas mixtures are flowed over a selective adsorbent in a unit operation. In the idealized situation imagined in Figure 1-3, if adsorption sites and/or pore structure on solid media generate high affinity (or exclusion) for specific mixture constituents, target adsorbates are selectively removed from even complex mixtures without external energy input. Adsorptive separations proceed through differences in sterics (exclusion and acceptance of molecules based on adsorbate accessibility), thermodynamic equilibrium, or kinetics (e.g. diffusion-limited separations).[28] In any case, complex processes and excessive energy penalties are circumvented in adsorption *if* adsorbent-adsorbate interactions are highly selective and thermodynamically favorable. Regeneration costs are similarly mitigated in comparison to aqueous sequestration methods. Additionally, adsorbent surfaces may foster catalytic gas conversion/removal. Many circumstances of course add complexities depending on the mixture(s) being separated, mass transfer limitations, adsorbent cost, and determining the relative strength of adsorbate removal desired (e.g. irreversible vs. reversible). Regardless, adsorptive separations are lucrative alternatives to presently expensive acid gas abatement schemes.[29,30]

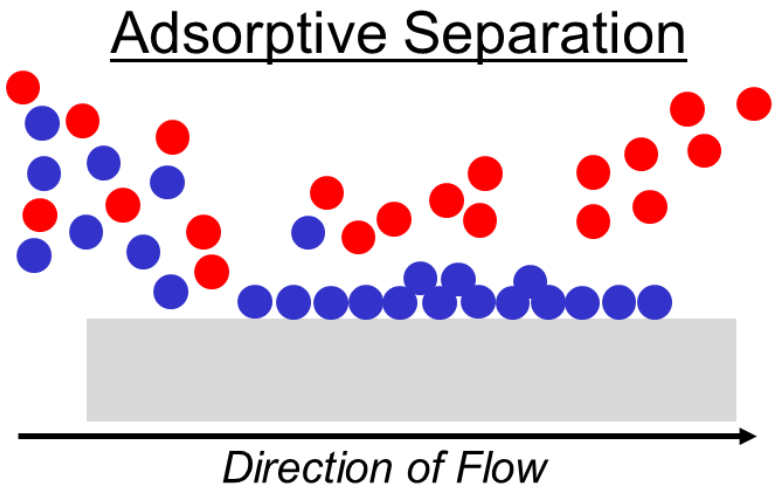

Figure 1-3: Cartoon describing an idealized equilibrium-based adsorption process. Grey rectangle represents adsorbent surface. Red and blue balls represent a mixture of different species flowing left to right.

1.2.1 Prior Work in Adsorptive Acid Gas Removal

Designing adsorbent materials for direct vapor-phase capture of acid gases inherently mitigates the pitfalls of aforementioned separation schemes in their waste generation, high energy requirements, and other operating costs. Activated carbon[31], metal oxide[32,33], and zeolite[34,35] adsorbents are already evaluated for desulfurization applications in both scientific literature and industrial reports. Surface and pore chemistry modification[31,36], along with functional group and catalyst incorporation[32,33,37] markedly improves capture of low pressure sour gas contaminants such as CO_2 and H_2S. Similarly, selective catalytic reduction (SCR) processes utilize porous solids, notably zeolite ZSM-5, to scavenge and destroy dilute NO_x and SO_x pollutants.[38] Designing tunable adsorbents with these attributes can produce materials with strong acid gas removal capabilities.

1.2.2 Tuning Desirable Adsorption Properties

Regardless of the adsorbent utilized, it is important materials can be tailored towards their intended use. As previously discussed with the ideal adsorption example in Figure 1-3, great separation performance can arise from material properties, as long as adsorbates have a stronger uptake capacity and binding selectivity than other competitive components in a mixture. This means adsorbents which can be adjusted and tailored towards specific gas removal scenarios (concerning variables such as gas concentration, mixture constituents, temperature, pressure, etc.), will portray stronger gas separation performance.

Two general types of adsorption can be imagined: (1) reversible and (2) irreversible.[39] Reversible (physical) adsorption describes binding interactions where captured adsorbate molecules can be released. These phenomena are governed by weak intermolecular forces between adsorbent surfaces and adsorbing molecules. Adsorbent regneration is typically achieved by exacting external stimuli on the spent adsorbent, such as raising the temperature and/or lowering the system pressure/adsorbate partial pressure. Economic and operational motivations in recycling adsorptive media in large-scale processes can mandate reversible adsorption characteristics. Relatively gentle regeneration conditions for reversible adsorption processes lower (create less expensive) separation utilities. Reversible separation schemes also complement adsorbate conversion/upgrading operations, as performed for H_2S via Claus units, to offset remediation costs. Adsorbents allowing reversible acid gas binding facilitate long-term removal solutions for industrial post-combustion and natural gas purification duties.

Conversely, irreversible adsorption entails permanent adsorbate capture. Such interactions proceed via strong chemical reaction, and are thusly referred to as chemisorption in contrast to reversible physisorption. For acid gases such as SO_2 and H_2S, chemisorptive removal typically involves the reactive deposition of sulfur. Subsequently, surfaces available for adsorption gradually saturate, and cannot be regenerated as in physisorption processes. At first glance, chemisorption may appear less desirable than reversible binding. But, irreversible adsorption mechanisms offer unique benefits. The impossibility of gas desorption through irreversible binding makes chemisorbent use advisable for personal protection equipment, where users cannot be subjected to eluting toxic compounds from filtration media.[37,40] Strong adsorbent-adsorbate reactions via chemical reactions foster large uptake capacities and selectivities in even complex mixtures where target adsorbate partial pressures are small. This is especially relevant for acid gas removal, as SO_x and NO_x concentrations in flue gas and H_2S concentrations in North American sour gas are typically << 1 vol% (although CO_2 amounts often approach 20%).[21,41,42] Additionally, the complete destruction of acid gases is sometimes required. Desorbing these vapors produces an acid gas-rich stream that must be dealt with, either by successive neutralization or chemical upgrading. It is sometimes advantageous to dispose of spent chemisorbent as acidic compounds are no longer acutely hazardous, and can be handled safely through simpler means.

Trade-offs between hosting reversible or irreversible adsorption processes are situation-dependent. Regardless, it is important to design adsorbent materials to address both acid gas removal mechanisms. Post-synthetic tailoring of traditional adsorbent media such as metal oxides, carbons, and silicas are performed, but methods are inherently

limited. For example, impregnation is the most common means of adsorbent modification.[33,35,43–46] The simple treatment introduces materials which preferentially bind adsorbing species into porous substrate hosts. The pore network of the adsorbent facilitates adsorbate interactions with the impregnate while reducing agglomeration and accessibility issues to enhance binding efficiency. Because impregnates reside in the pore space of the adsorbent, impregnation inherently sacrifices available adsorption surface area for adsorbate affinity. So enhancements in gas capture must offset adsorption surface area loss, which may or may not be significant. An obvious limitation is that the impregnate must penetrate the pore space. This is difficult if the impregnates in question are large, as with amine-containing polymers commonly scaffolded onto porous silicas and carbons that cannot easily diffuse into microporous substrates. Finally, traditional impregnation offers little-to-no control over impregnate distribution. Heterogeneous impregnation creates inconsistent adsorbent performance between batches, and imbues non-uniform mass transfer throughout adsorbent particles during separation. This in-turn can lead to localized thermal and pressure drop effects. Other means of adsorbent surface modification certainly exist. But methods of post-synthetic modification always add acquisition costs.

1.3 Metal-Organic Framework (MOF) Adsorbents

1.3.1 Adsorption in MOFs

Designer chemistry solutions in framework material construction conversely impart favorable adsorption qualities into porous structures as they are produced. On the vanguard of these materials, metal-organic frameworks (MOFs) constitute a class of crystalline, nanoporous materials that offer a unique breadth of tailorability through large accessible

surface areas[47–49], tunable pore functionalities[50–55], and reactive open metal sites.[56–60] MOF construction is visualized in Figure 1-4. As apparent from their name, MOFs are structured from metal-based centers bridged by coordinating organic ligands. These porous frameworks possess markedly greater modularity than other porous materials.[61,62] Eighty-four metals are listed on the periodic table, barring metalloids, while thousands of distinct organic bridging ligands are all available for MOF construction. Consequently, scientists can pick-and-choose the chemical constituents of MOF adsorbents. Constructing MOFs from metals and/or ligands which possess favorable binding chemistries with desired adsorbates generates tailor-made adsorbents for specific gas separations. Inherent chemical selectivity and porosity of MOFs through functionalities such as ligand pendant groups (-OH, -NH_2, -COOH, etc.) makes them potentially advantageous over materials that may require post-synthesis treatment to acquire chemical specificity, such as activated carbons, silicas, and zeolites, or those that may suffer from relatively low internal porosities, such as metal oxides. Still, MOF post-synthetic modification (PSM) strategies can adjust the characteristics of MOFs even further to enhance adsorption affinities.[63,64]

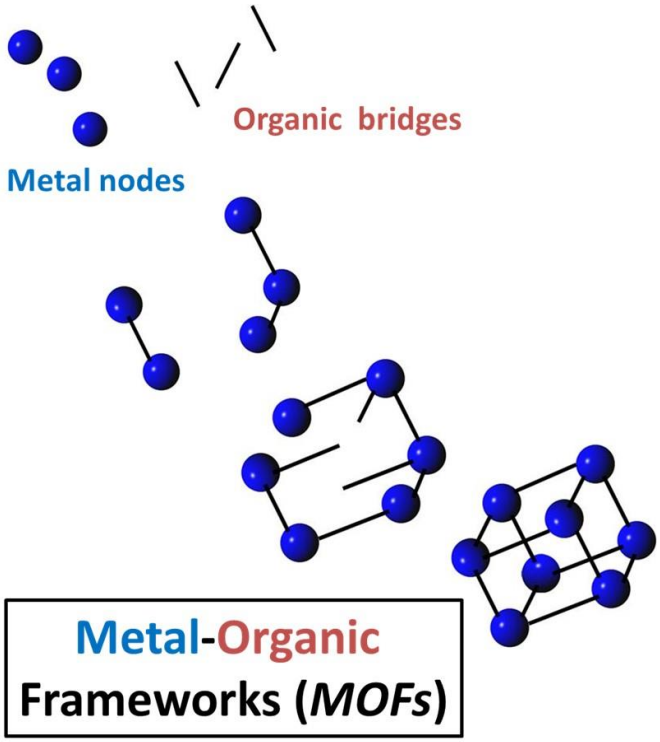

Figure 1-4: Illustration of MOF construction (top to bottom) by self-assembly of metal (blue) and organic ligand (black) precursors

Scientific investigations on MOFs span over two decades. The literature is rich with demonstrations of both reversible and irreversible gas uptake using framework adsorbents. One example for instilling impressive reversible CO_2 sequestration performance was achieved by researchers in Berkley and Georgia Tech through post-synthetic appending of flexible diamines to accessible metal centers.[65–68] Reversible adsorption is also attained through ligand functionalization, afforded by choosing coordinating ligands containing pendant chemical functionalities. For certain framework ligands such as terephthalates, pre-functionalized ligands are commercially available. Cmarik et al. showed how different ligand functionalities strongly impact isosteric heats of adsorption for several small molecules in zirconium MOF UiO-66.[69] These impacts are furthermore predictable, as primary amine ($-NH_2$) and nitro ($-NO_2$) chemical groups enhanced CO_2 and H_2O uptake

through introduced electrostatic binding and Van der Waals interactions from appended functionalities. So, choosing ligand-based functionalities that enact favorable binding events with select adsorbates will generally improve adsorption performance. Irreversible adsorption in MOFs is typically achieved by frameworks containing reactive metal sites. Depending on coordination geometry, MOFs that contain periodically distributed unsaturated metal centers can enact acid-base or other covalent bonding interactions.[70,71] Adsorption strengths with accessible binding sites depend on the specific interaction between metal cations and adsorbing gas species.[72]

1.3.2 MOF Stability in Acid Gases

Candidate adsorbents must remain structurally stable in acidic environments to maintain longevity in use and consistent separation performance. Thermodynamic MOF stability is governed by how inert the MOF metal center is towards a target acid gas.[73] Ding and Yazaydin provide one example of this, where acidic flue gas constituents were particularly destructive towards MOFs containing reactive open metal centers.[74] Understanding that MOFs are held together by metal-ligand bonds, it can be imagined any chemical attack on these sites may damage the structure. Defects add an interesting layer of complexity to MOF stability. Crystals are often wrought with defect sites. These imperfections have been observed to make otherwise stable frameworks susceptible to degradation during gas exposure.[55,75,76]

The above being said, a common misconception with MOFs is that they are generally unstable. This is not true. The expansive library of existing MOFs hosts many example crystals that remain stable in even highly corrosive acid gas environments. A

short-list of thirty acid gas-stable frameworks in Table 1-1 constitute a few of the many example acid gas-stable MOFs (within specified conditions) already uncovered by published reports.

Table 1-1: List of Reportedly Acid Gas-Stable MOFs. Materials are organized alphabetically

MOF	Acid Gas ([a]Condition)	Reference
Ce-BTC	H_2S (1000Pa)	77
Cu-BTC	SO_2 (3bar)	78
Cu-HF	SO_2 (15ppm, humid, 5day), NO_2 (10ppm, humid, 5day)	79
DMOF-TM	SO_2 (dry, ~3bar)	80
MFM-300(In)	SO_2 (dry and humid, 1ppm)	81
Mg-MOF-74	H_2S (1000Pa)	77
MIL-47(V)		
MIL-53(Cr)	H_2S (2MPa)	82
MIL-53(Al)		
MIL-101(Cr)	H_2S (1000Pa, 10,000ppm)	77,83
MIL-101-NH_2(Cr)	H_2S (10,000ppm)	83
MIL-125(Ti)	SO_2 (dry), H_2S (10,000ppm, 10bar)	83–85

MIL-125-NH_2(Ti)	SO_2 (dry, aqueous, humid, up to 1bar), H_2S (10,000ppm, 10bar)	83–86
MIL-160(Al)	SO_2 (dry, humid, up to 1bar)	86
Ni(bdc)(ted)$_{0.5}$	SO_2 (dry, ~1.7bar)	87
Ni-NIC	SO_2 (15ppm, humid, 5day), NO_2 (10ppm, humid, 5day)	79
Re-fcu-MOFs	H_2S (5%)	88,89
SIFSIX-3-Ni	H_2S(10%)	90
soc-MOF(Ga^{3+}, Al^{3+})	H_2S (5vol%)	91
UiO-66(Zr)	NO_2 (2138ppm), SO_2 (1000ppm), H_2S (1000Pa, 10,000ppm)	77,83,92
UiO-66-NH_2(Zr)	H_2S (1000Pa, 10,000ppm), NO_2 (50-700ppm dry, humid)	77,83,93
UiO-66-ox(Zr)	SO_2 (1000ppm)	92
UiO-67(bipy)	H_2S (1000ppm, humid)	94
ZIF-7	SO_2 (dry, 2.5bar)	95
ZIF-8	SO_2 (dry) H_2S (1000Pa)	77,95
ZIF-11		
ZIF-14	SO_2 (dry, 2.5bar)	95
ZIF-65		

ZIF-71	
ZIF-90	

[a]Test conditions summarized from descriptions in original reports

1.3.3 Creating Macroscopic MOF-based Media

MOFs are nano-to-microscale crystals. As such, the small particle sizes of MOFs limit their direct implementation into gas separation processes. Forming adsorbent powders into macroscopic shapes improves heat and mass transport management during separations, although resulting structures must possess sufficient tolerance for chemical and mechanical stresses and sources of attrition in a given operation.[96] Perhaps the simplest and most utilized method of structuring adsorbents is to press them into uniform granules, enabling use as packed bed media. However, the integration of adsorbents onto more intricate structured contactors such as monoliths, membranes, thin films, non-wovens, etc., adds flexibility in operational design and employment of adsorption media.[97] Rezaei and Webley provided an expansive detail of structured media development and subsequent impacts in gas separations literature.[98] An illustration of such composites, their various production routes, and subsequent applications is reproduced in Figure 1-5. Note the image includes metal-organic frameworks in described porous powders.

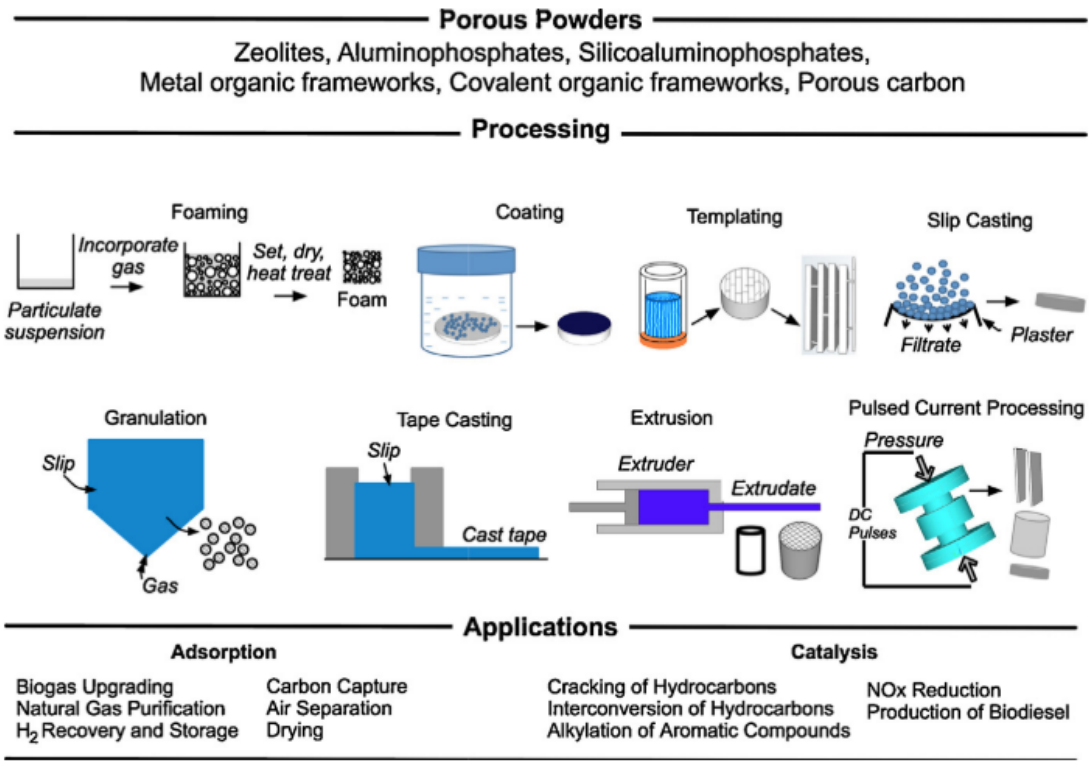

Figure 1-5: Graphical overview of porous materials, various processing routes, and potential applications. Image reproduced from Bergström and coworkers[96]

Researchers routinely attempt to effectively structure MOF adsorbents. On the topic of acid gases, the dilute CO_2 concentrations faced by direct air capture (DAC) technologies mandate the development of structured adsorbents. As such, Darunte et al. appended mmen-Mg_2(dobpdc) onto a monolithic gas-solid contactor to accommodate the large volumetric air throughputs required by DAC while providing cyclic, high capacity CO_2 removal from installed MOF adsorbents.[99] This study demonstrates how synergetic effects between novel adsorbents and appropriate supporting structures enhance the applicability of adsorption media. Similarly, techniques for adhering MOFs membrane materials have been proposed.[89,97,100–105] MOF/nanofiber composites from Zhang et al. portray SO_2 removal at 100ppm, while allowing fabrication onto facemasks, gloves, and

other personal protection equipment (PPE).[106] The prior report utilized electrospinning to create fibers however, which is difficult to scale up, restricts solvent choice, and is relatively slow. In response to these limitations, Deneff and Walton recently detailed how faster and more actionable solution blown MOF-fiber composites are rapidly produced, and outlined heuristics to their optimization.[107] Controllable supported MOF growth is frequently demonstrated through enacting layer-by-layer crystal growth on surfaces through self-assembled monolayers (SAMs).[108] Though these techniques allow for monolayer control, the rigorous and involved synthesis procedures rely on cyclic exposures to metal salts and linkers with intermittent rinsing steps.[109,110]

Multiple processing steps are commonly required across all described supported MOF growth methods. Either MOFs are first premade and then prepared (degassing, solvent exchange, surface modification, etc.) for substrate integration, or cyclic MOF growth must be pursued as with SAM-based production. Adding more production steps, especially ones entailing long time frames, stringent operational control, or potentially high expenses, adds production costs. Resulting composites may yield technologically superior adsorption and catalysis performance, but can become economically inferior options to other separation methods. Accordingly, methods of reducing MOF-based composite synthesis costs and enhancing manufacturing simplicity should be pursued to bridge the already-evident high separation performance of framework adsorbents with their potential cost competitiveness against traditional separation media.

1.4 Dissertation Overview

This dissertation aims to address the challenge of acid gas removal through pursuit of two general aims: discover methods of designing MOFs for acid gas capture that (1) create adsorbents with acid gas selectivity and improve uptake capacity, and (2) produce practically-usable MOF-based adsorbents through inexpensive and accessible techniques. Work detailed throughout this dissertation are motivated by the above research aims. Chapters 3 & 4 primarily focus on aim 1, where Chapters 5 & 6 communicate work relevant to aim 2, although both motivations are prevalent throughout the document.

In the first aim, both the stability and adsorption performance of researched materials are evaluated. Studies on MOF stability are reported in Chapter 3, whereas acid gas removal performances for the same materials are collectively presented in Chapter 4. Design guidelines for MOF-based acid gas adsorbents are mainly explored in both. Specifically, the impacts of defect engineering, reversible/irreversible binding site installation, and powder processing are considered in both Chapters 3 and 4. Framework assembly is controlled through combinatorial chemistry, where manufacturers select metal and organic bridging ligand pairs that directly influence chemical interactions with species in resulting adsorbent materials. Subsequently, this part of the dissertation focuses on the impact of bridging ligand chemistry on the acid gas adsorption efficacy of framework adsorbents. Investigated ligand-based functional groups are either inherent of selected MOF linkers (e.g. $-NH_2$, -COOH), or installed after MOF formation (e.g. Lewis acidic metal sites). Importantly, examined groups are manipulated to foster reversible and irreversible adsorption. Generating MOF design heuristics to achieve both binding

properties enhances the actionability of MOF adsorbents in addressing a broad span of acid gas separation and removal goals.

Through the second aim, a new methodology of creating MOFs both on and from support media is presented. In Chapter 5, aluminum frameworks of different topologies and chemical functionalities are created from insoluble aluminum-based media. Commercially available aluminum-based supports (membranes, tubes, filters) successfully yield MOFs. Al-MOFs are effectively scaffolded on prefabricated aluminum support media relevant for gas separation applications. Supported MOF growth parameters are optimized. Additionally, insoluble media affords non-supported MOF production if desired, communicating the manufacturing flexibility offered by techniques developed in Chapter 5. Non-supported media produced from insoluble aluminum sources obtain growth control (porosity, morphology, crystal structure, etc.), production ease (time, reaction temperature), and potential cost benefits unavailable from traditional production schemes utilizing metal salts. Chapter 6 expands on the work detailed throughout Chapter 5, where MOF-derived porous carbon/oxide materials are produced from structured frameworks grown from insoluble aluminum carbide and aluminum metal. MOF-derived porous media has been previously developed. However, the unique morphological attributes of insoluble precursor-derived MIL-53(Al) frameworks are imparted onto subsequent MOF-derived media created in Chapter 6. As a result, self-structured alumina nanotubes with broad pore size distributions and architectures are acquired. The new composite allows location-controlled cyclic MOF regrowth. Separately, aluminum oxide/iron oxide H_2S chemisorptive media is also made from the new material. These two uses serve as example applications which can be pursued with MOF-derived media detailed in Chapter 6. Results

from this aim present a new approach to integrating MOFs and MOF-derived media onto hierarchical media of diverse geometries and intended uses.

Altogether, the body of work is intended to evaluate and progress the capability of MOFs as pragmatic acid gas adsorbent/separation materials. The text attempts to communicate framework design heuristics as they pertain to acid gas capture. Design strategies are provided for nanoscale framework construction parameters (Chapters 3 and 4) and macroscopic separation media synthesis (Chapters 5 and 6). Detriments in the stability and uptake performance of evaluated MOFs are simultaneously reported to evidence potential weaknesses of MOFs as acid gas adsorbents. Conclusions and recommendations are summarized in Chapter 8. Work described herein intends to provide clarity and insight into how MOF-based materials may be utilized in processes containing acid gases, and what strategies may be used to enhance their applicability and performance.

1.5 Chapter 1 References

1. *Materials for Separation Technologies: Energy and Emission Reduction Opportunities Industrial Technologies Program.* Oak Ridge National Laboraotry, (2005).
2. Aaron, D. & Tsouris, C. Separation of CO_2 from Flue Gas: A Review. *Sep. Sci. Technol.* **40**, 321–348 (2005).
3. Eldridge, R. B. *Olefin/Paraffin Separation Technology: A Review*. *Ind. Eng. Chem. Res.* **32**, 2208-2212, (1993).
4. Baker, R. W. Future Directions of Membrane Gas Separation Technology. *Ind. Eng. Chem. Res.* **41**, 1393–1411 (2002).
5. Sholl, D. S. & Lively, R. P. Seven chemical separations to change the world. *Nature* **532**, 435–437 (2016).
6. Huo, D. The Global Sour Gas Problem. *Stanford Energy Club* (2012). Available at: https://energyclub.stanford.edu/the-global-sour-gas-problem/. (Accessed: 18th April 2019)
7. Franey, J. P. & Graedel, T. E. Corrosive Effects of Mixtures of Pollutants. *J. Air*

Pollut. Control Assoc. **35**, 644–648 (1985).

8. Acid deposition. *Air Pollution Information System* (2016). Available at: http://www.apis.ac.uk/overview/pollutants/acid-deposition. (Accessed: 10th April 2019)

9. Patrick, D. L., Murray, T. P., Sullivan Jr, R. K. & Kimmell, K. L. *Health & Environmental Effects of Air Pollution*. Commonwealth of Massachusetts Executive Office of Energy & Environmental Affairs: Boston, MA. Available at: http://www.epa.gov/globalwarming/

10. *Annual Energy Outlook 2019*. U.S. Energy Information Administration: Washington D.C., 2019

11. Sulfur dioxide (SO_2) - Air quality fact sheet. *Australian Department of the Environment and Heritage* (2005). Available at: https://www.environment.gov.au/protection/publications/factsheet-sulfur-dioxide-so2. (Accessed: 18th April 2019)

12. Sudalma, S., Purwanto, P. & Santoso, L. W. The Effect of SO_2 and NO_2 from Transportation and Stationary Emissions Sources to SO_4^{2-} and NO_3^- in Rain Water in Semarang. *Procedia Environ. Sci.* **23**, 247–252 (2015).

13. *SOUR GAS: A History of Expertise*. Total S.A.: Paris (2007).

14. Burgers, W. F. J., Northrop, P. S., Kheshgi, H. S. & Valencia, J. A. Worldwide development potential for sour gas. *Energy Procedia* **4**, 2178–2184 (2011).

15. Processing Natural Gas. *American Petroleum Institute* (2013). Available at: http://naturalgas.org/naturalgas/processing-ng/. (Accessed: 22nd August 2016)

16. Rezaei, F., Rownaghi, A. A., Monjezi, S., Lively, R. P. & Jones, C. W. SO_x /NO_x Removal from Flue Gas Streams by Solid Adsorbents: A Review of Current Challenges and Future Directions. *Energy & Fuels* **29**, 5467–5486 (2015).

17. Srivastava, R. K., Jozewicz, W. & Srivastava, J. Flue Gas Desulfurization: The State of the Art. *J. Air Waste Manage. Assoc.* **51**, 1676–1688 (2001).

18. Abedini, R., Koolivand Salooki, M. & Ghasemian, S. Modeling and simulation of condensed sulfur in catalytic beds of Claus process: Rapid estimation. *Chem. Eng. Res. Bull.* **14**, 110–114 (2010).

19. de Angelis, A. Natural gas removal of hydrogen sulphide and mercaptans. *Appl. Catal. B Environ.* **113**–**114**, 37–42 (2012).

20. Shi, L., Yang, K., Zhao, Q., Wang, H. & Cui, Q. Characterization and Mechanisms of H_2S and SO_2 Adsorption by Activated Carbon. *Energy & Fuels* **29**, 6678–6685 (2015).

21. Manning, F. S. & Thompson, R. E. *Oilfield Processing of Petroleum: Natural Gas*, 1st ed.; (PennWell Books: Tulsa, OK 1991).

22. Wang, X., Ma, X., Xu, X., Sun, L. & Song, C. Mesoporous-molecular-sieve-supported polymer sorbents for removing H_2S from hydrogen gas streams. *Top. Catal.* **49**, 108–117 (2008).

23. Weiland, R. H., Dingman, J. C. & Cronin, D. B. Heat Capacity of Aqueous Monoethanolamine, Diethanolamine, N-Methyldiethanolamine, and N-Methyldiethanolamine-Based Blends with Carbon Dioxide. *J. Chem. Eng. Data* **42**, 1004–1006 (1997).

24. *Air Pollution Control Technology EPA-CICA Fact Sheet Flue Gas Desulfurization EPA-452/F-03-034*. U.S. Environmental Protection Agency.

25. Lagas, J. A., Borsboom, J. & Berben, P. H. THE SUPERCLAUS PROCESS in *38th Annual Laurance Reid Gas Conditioning Conference* (1988).

26. Tollefson, J. 'Flaring' wastes 3.5% of world's natural gas. *Nature* (2016).

27. Fawole, O. G., Cai, X.-M. & MacKenzie, A. R. Gas flaring and resultant air pollution: A review focusing on black carbon. *Environ. Pollut.* **216**, 182–197 (2016).

28. Do, D. D. *Adsorption Analysis: Equilibria and Kinetics,* Vol. 2; (Imperial College Press: London, 1998).

29. Sircar, S. Pressure Swing Adsorption. *Ind. Eng. Chem. Res.* **41**, 1389–1392 (2002).

30. Yang, R. T. *Gas Separation by Adsorption Processes*; (Butterworth Publishers: Stoneham MA, 1987).

31. Wu, X. X., Schwartz, V., Overbury, S. H. & Armstrong, T. R. Desulfurization of gaseous fuels using activated carbons as catalysts for the selective oxidation of hydrogen sulfide. *Energy & Fuels* **19**, 1774–1782 (2005).

32. Zhang, X. *et al.* Selective catalytic oxidation of H_2S over iron oxide supported on alumina-intercalated Laponite clay catalysts. *J. Hazard. Mater.* **260**, 104–111 (2013).

33. Yang, H. & Tartarchuk, B. Novel-Doped Zinc Oxide Sorbents for Low Temperature Regenerable Deslfurization Applications. *IFAC Proc. Vol.* **56**, 2898–2904 (2010).

34. Shah, M. S., Tsapatsis, M. & Siepmann, J. I. Monte Carlo simulations probing the adsorptive separation of hydrogen sulfide/methane mixtures using all-silica zeolites. *Langmuir* **31**, 12268–12278 (2015).

35. Ozekmekci, M., Salkic, G. & Fellah, M. F. Use of zeolites for the removal of H_2S: A mini-review. *Fuel Process. Technol.* **139**, 49–60 (2015).

36. Adib, F., Bagreev, A. A. & Bandosz, T. J. Effect of pH and Surface Chemistry on the Mechanism of H_2S Removal by Activated Carbons. *J. Colloid Interface Sci.* **216**, 360–369 (1999).

37. Jacoby, M. Air Filters for the Face. *C&EN Chicago* 34–38 (2014).

38. Shelef, M. *Selective Catalytic Reduction of NO* with N-Free Reductants*. *Chem. Rev* **95**, 209-225 (1995).

39. Thommes, M. *et al.* Physisorption of gases, with special reference to the evaluation of surface area and pore size distribution (IUPAC Technical Report). *Pure Appl. Chem* **87**, 1051–1069 (2015).

40. DeCoste, J. B. & Peterson, G. W. Metal- Organic Frameworks for Air Purification

of Toxic Chemicals. *Chem. Rev.* **114**, 5695−5727 (2014).

41. Aouini, I., Ledoux, A., Estel, L. & Mary, S. Pilot Plant Studies for CO_2 Capture from Waste Incinerator Flue Gas Using MEA Based Solvent. *Oil Gas Sci. Technol.* **69**, 1091–1104 (2014).

42. Abatzoglou, N. & Boivin, S. A review of biogas purification processes. *Biofuels, Bioprod. Biorefin.* **3**, 42–71 (2009).

43. Sarazen, M. L., Sakwa-Novak, M. A., Ping, E. W. & Jones, C. W. Effect of Different Acid Initiators on Branched Poly(propyleneimine) Synthesis and CO_2 Sorption Performance. *ACS Sustain. Chem. Eng.* **7**, 7, 7338-7345 (2019)

44. Tailor, R., Abboud, M. & Sayari, A. Supported Polytertiary Amines: Highly Efficient and Selective SO_2 Adsorbents. *Environ. Sci. Technol.* **48**, 2025–2034 (2014).

45. Leyva Ramos, R., Ovalle-Turrubiartes, J. & Sanchez-Castillo, M. . Adsorption of fluoride from aqueous solution on aluminum-impregnated carbon. *Carbon N. Y.* **37**, 609–617 (1999).

46. Meilikhov, M. *et al.* Metals@MOFs - Loading MOFs with metal nanoparticles for hybrid functions. *Eur. J. Inorg. Chem.* 3701–3714 (2010)

47. Yaghi, O. M., O'Keeffe, M. & Ockwig, N. Reticular synthesis and the design of new materials. *Nature* **423**, 705–714 (2003).

48. Farha, O. K. *et al.* Metal–Organic Framework Materials with Ultrahigh Surface Areas: Is the Sky the Limit? *J. Am. Chem. Soc.* **134**, 15016–15021 (2012).

49. Furukawa, H. *et al.* Ultrahigh porosity in metal-organic frameworks. *Science* **329**, 424–8 (2010).

50. Britt, D. K., Tranchemontagne, D. & Yaghi, O. M. Metal-organic frameworks with high capacity and selectivity for harmful gases. *Proc. Natl. Acad. Sci. U. S. A.* **105**, 11623–11627 (2008).

51. Chen, B., Xiang, S. & Qian, G. Metal-Organic Frameworks with funtional pores for recognition of small molecules. *Acc. Chem. Res.* **43**, 1115–1124 (2010).

52. Jasuja, H. & Walton, K. S. Experimental Study of CO_2, CH_4, and Water Vapor Adsorption on a Dimethyl-Functionalized UiO-66 Framework. *J. Phys. Chem. C* **117**, 7062–7068 (2013).

53. Jasuja, H., Peterson, G. W., Decoste, J. B., Browe, M. a. & Walton, K. S. Evaluation of MOFs for air purification and air quality control applications: Ammonia removal from air. *Chem. Eng. Sci.* **124**, 118–124 (2015).

54. Hendon, C. H. *et al.* Engineering the Optical Response of the Titanium-MIL-125 Metal-Organic Framework through Ligand Functionalisation. *J. Am. Chem. Soc.* 10942–10945 (2013).

55. Joshi, J. N., Garcia-Gutierrez, E. Y., Moran, C. M., Deneff, J. I. & Walton, K. S. Engineering Copper Carboxylate Functionalities on Water Stable Metal-Organic Frameworks for Enhancement of Ammonia Removal Capacities. *J. Phys. Chem. C*

121, 3310–3319 (2017).

56. Kajiwara, T. *et al.* A systematic study on the stability of porous coordination polymers against ammonia. *Chem. Eur. J.* **20**, 15611–15617 (2014).

57. Watanabe, T. & Sholl, D. S. Molecular chemisorption on open metal sites in Cu_3 (benzenetricarboxylate)$_2$: A spatially periodic density functional theory study. *J. Chem. Phys.* **133**, 094509 (2010).

58. Duan, X. *et al.* Highly selective separation of small hydrocarbons and carbon dioxide in a metal–organic framework with open copper(ii) coordination sites. *RSC Adv.* **4**, 23058–23063 (2014).

59. Bloch, E. D. *et al.* Hydrocarbon Separations in a Metal-Organic Framework with Open Iron(II) Coordination Sites. *Science.* **335**, 1606–1610 (2012).

60. Heinen, J., Burtch, N. C., Walton, K. S., Fonseca Guerra, C. & Dubbeldam, D. Predicting Multicomponent Adsorption Isotherms in Open-Metal Site Materials Using Force Field Calculations Based on Energy Decomposed Density Functional Theory. *Chem. - A Eur. J.* **22**, 18045–18050 (2016).

61. Eddaoudi, M. *et al.* Modular Chemistry: Secondary Building Units as a Basis for the Design of Highly Porous and Robust Metal−Organic Carboxylate Frameworks. *Acc. Chem. Res.* **34**, 319–330 (2001).

62. Li, J.-R., Kuppler, R. J. & Zhou, H.-C. Selective gas adsorption and separation in metal-organic frameworks. *Chem. Soc. Rev.* **38**, 1477–1504 (2009).

63. Costa, J. S. *et al.* Chemical modification of a bridging ligand inside a metal-organic framework while maintaining the 3D structure. *Eur. J. Inorg. Chem.* 1551–1554 (2008)

64. Gadzikwa, T., Farha, O. K., Mulfort, K. L., Hupp, J. T. & Nguyen, S. T. A Zn-based, pillared paddlewheel MOF containing free carboxylic acids via covalent post-synthesis elaboration. *Chem. Commun.* 3720–3722 (2009)

65. McDonald, T. M. *et al.* Capture of Carbon Dioxide from Air and Flue Gas in the Alkylamine-Appended Metal–Organic Framework mmen-Mg_2(dobpdc). *J. Am. Chem. Soc.* **134**, 7056–7065 (2012).

66. Demessence, A., D'Alessandro, D. M., Foo, M. L. & Long, J. R. Strong CO_2 binding in a water-stable, triazolate-bridged metal-organic framework functionalized with ethylenediamine. *J. Am. Chem. Soc.* **131**, 8784–8786 (2009).

67. Darunte, L. A., Oetomo, A. D., Walton, K. S., Sholl, D. S. & Jones, C. W. Direct Air Capture of CO_2 Using Amine Functionalized MIL-101(Cr). *ACS Sustain. Chem. Eng.* **4**, 5761–5768 (2016).

68. Choi, S., Watanabe, T., Bae, T.-H., Sholl, D. S. & Jones, C. W. Modification of the Mg/DOBDC MOF with Amines to Enhance CO_2 Adsorption from Ultradilute Gases. *J. Phys. Chem. Lett.* **3**, 1136–1141 (2012).

69. Cmarik, G. E., Kim, M., Cohen, S. M. & Walton, K. S. Tuning the Adsorption Properties of UiO-66 via Ligand Functionalization. *Langmuir* **28**, 15606–15613

(2012).

70. Chui, S. S.-Y., Lo, S. M.-F., Charmant, J. P. H., Orpen, A. G. & Williams, I. D. A chemically functionalizable nanoporous material. *Science* **283**, 1148–50 (1999).

71. Lee, J. *et al.* Metal–organic framework materials as catalysts. *Chem. Soc. Rev.* **38**, 1450-1459 (2009).

72. Queen, W. L. *et al.* Comprehensive study of carbon dioxide adsorption in the metal–organic frameworks M_2(dobdc) (M = Mg, Mn, Fe, Co, Ni, Cu, Zn). *Chem. Sci.* **5**, 4569–4581 (2014).

73. Burtch, N. C., Jasuja, H. & Walton, K. S. Water Stability and Adsorption in Metal-Organic Frameworks. *Chem. Rev.* **114**, 10575–10612 (2014).

74. Ding, L. & Yazaydin, A. Ö. How Well Do Metal–Organic Frameworks Tolerate Flue Gas Impurities? *J. Phys. Chem. C* **116**, 22987–22991 (2012).

75. Fang, Z., Bueken, B., De Vos, D. E. & Fischer, R. A. Defect-Engineered Metal-Organic Frameworks. *Angew. Chemie Int. Ed.* **54**, 7234–7254 (2015).

76. Sholl, D. S. & Lively, R. P. Defects in Metal-Organic Frameworks: Challenge or Opportunity? *J. Phys. Chem. Lett.* **6**, 3437–3444 (2015).

77. Liu, J., Wei, Y., Li, P., Zhao, Y. & Zou, R. Selective H_2S/CO_2 Separation by Metal−Organic Frameworks Based on Chemical-Physical Adsorption. *J. Phys. Chem. C* **121**, 13249–13255 (2017).

78. Hungerford, J. T. Synthesis and Stability: Metal-Organic Frameworks Exposure to Water, Sulfur Dioxide, Hydrogen Sulfide. PhD Dissertation. (Georgia Institute of Technology, 2019).

79. Han, S. *et al.* MOF stability and gas adsorption as a function of exposure to water, humid air, SO_2, and NO_2. *Microporous Mesoporous Mater.* **173**, 86–91 (2013).

80. Hungerford, J. *et al.* DMOF-1 as a Representative MOF for SO_2 Adsorption in Both Humid and Dry Conditions. *J. Phys. Chem. C* **122**, 23493–23500 (2018).

81. Eddaoudi, S. M. & Salama, K. N. Highly sensitive and selective SO_2 MOF sensor: the integration of MFM-300 MOF as a sensitive layer on a capacitive interdigitated electrode. *J. Mater. Chem. A* **6**, 5550 (2018).

82. Hamon, L. *et al.* Comparative Study of Hydrogen Sulfide Adsorption in the MIL-53 (Al, Cr, Fe), MIL-47 (V), MIL-100 (Cr), and MIL-101 (Cr) Metal- Organic Frameworks at Room Temperature. *J. Am. Chem. Soc.* **131**, 8775–8777 (2009).

83. Joshi, J. N. *et al.* Probing Metal–Organic Framework Design for Adsorptive Natural Gas Purification. *Langmuir* **34**, 8443–8450 (2018).

84. Mounfield III, W. P. *et al.* Synergistic Effects of Water and SO_2 on Degradation of MIL-125 in the Presence of Acid Gases. *J. Phys. Chem. C* **120**, 27230–27240 (2016).

85. Vaesen, S. *et al.* A robust amino-functionalized titanium(IV) based MOF for improved separation of acid gases. *Chem. Commun.* **49**, 10082–10084 (2013).

86. Brandt, P. *et al.* MOFs with Potential Application for SO_2-Separation and Flue Gas Desulfurization. *ACS Appl. Mater. Interfaces* (2019).

87. Tan, K. *et al.* Mechanism of Preferential Adsorption of SO_2 into Two Microporous Paddle Wheel Frameworks M(bdc)(ted)$_{0.5}$. *Chem. Mater.* **25**, 4653–4662 (2013).

88. Bhatt, P. M. *et al.* Isoreticular rare earth fcu-MOFs for the selective removal of H_2S from CO_2 containing gases. *Chem. Eng. J.* **324**, 392–396 (2017).

89. Liu, G. *et al.* Mixed matrix formulations with MOF molecular sieving for key energy-intensive separations. *Nat. Mater.* **17**, 283–289 (2018).

90. Shekhah, O. *et al.* A facile solvent-free synthesis route for the assembly of a highly CO_2 selective and H_2S tolerant NiSIFSIX metal-organic framework. *Chem. Commun.* **51**, 13595 (2015).

91. Belmabkhout, Y. *et al.* Metal-Organic Frameworks to Satisfy Gas Upgrading Demands: Fine-tuning the soc-MOF platform for the Operative Removal of H_2S. *J. Mater. Chem. A* **5**, 3293–3303 (2017).

92. DeCoste, J. B., Demasky, T. J., Katz, M. J., Farha, O. K. & Hupp, J. T. A UiO-66 analogue with uncoordinated carboxylic acids for the broad-spectrum removal of toxic chemicals. *New J. Chem.* **39**, 2396–2399 (2015).

93. Peterson, G. W., Mahle, J. J., Decoste, J. B., Gordon, W. O. & Rossin, J. A. Extraordinary NO_2 Removal by the Metal-Organic Framework UiO-66-NH_2. *Angew. Chemie Int. Ed.* **55**, 6235–6238 (2016).

94. Nickerl, G. *et al.* Integration of accessible secondary metal sites into MOFs for H_2S removal. *Inorg. Chem. Front.* **1**, 325 (2014).

95. Bhattacharyya, S. *et al.* Acid Gas Stability of Zeolitic Imidazolate Frameworks: Generalized Kinetic and Thermodynamic Characteristics. *Chem. Mater.* **30**, 4089–4101 (2018).

96. Akhtar, F., Andersson, L., Ogunwumi, S., Hedin, N. & Bergström, L. Structuring adsorbents and catalysts by processing of porous powders. *J. Eur. Ceram. Soc.* **34**, 1643–1666 (2014).

97. DeWitt, S. J. A. *et al.* Critical Comparison of Structured Contactors for Adsorption-Based Gas Separations. *Annu. Rev. Chem. Biomol. Eng.* **9**, 129–152 (2018).

98. Rezaei, F. & Webley, P. Structured adsorbents in gas separation processes. *Sep. Purif. Technol.* **70**, 243–256 (2010).

99. Darunte, L. A. *et al.* Monolith-Supported Amine-Functionalized Mg_2(dobpdc) Adsorbents for CO_2 Capture. *ACS Appl. Mater. Interfaces* **9**, 17042–17050 (2017).

100. Liu, X., Demir, N. K., Wu, Z. & Li, K. Highly Water-Stable Zirconium Metal–Organic Framework UiO-66 Membranes Supported on Alumina Hollow Fibers for Desalination. *J. Am. Chem. Soc.* **137**, 6999–7002 (2015).

101. Pimentel, B. R., Fultz, A. W., Presnell, K. V. & Lively, R. P. Synthesis of Water-Sensitive Metal-Organic Frameworks within Fiber Sorbent Modules. *Ind. Eng. Chem. Res.* **56**, 5070–5077 (2017).

102. Pimentel, B. R. & Lively, R. P. Propylene Enrichment via Kinetic Vacuum Pressure Swing Adsorption Using ZIF-8 Fiber Sorbents. *ACS Appl. Mater. Interfaces* **10**, 36323–36331 (2018).

103. Hossain, M. I. *et al.* Membrane Coated UiO-66 MOF Adsorbents. *Ind. Eng. Chem. Res.* **58**, 1352–1362 (2019).

104. Guo, X. *et al.* Mixed matrix membranes incorporated with amine-functionalized titanium-based metal-organic framework for CO_2/CH_4 separation. *J. Memb. Sci.* **478**, 130–139 (2015).

105. Zhang, Y. *et al.* Constructing Free Standing Metal Organic Framework MIL-53 Membrane Based on Anodized Aluminum Oxide Precursor. *Sci. Rep.* **4**, 4947 (2014).

106. Zhang, Y. *et al.* Preparation of Nanofibrous Metal–Organic Framework Filters for Efficient Air Pollution Control. *J. Am. Chem. Soc.* **138**, 5785–5788 (2016).

107. Deneff, J. I. & Walton, K. S. Production of metal-organic framework-bearing polystyrene fibers by solution blow spinning. *Chem. Eng. Sci.* **203**, 220–227 (2019).

108. Osama Shekhah *et al.* Step-by-Step Route for the Synthesis of Metal−Organic Frameworks. *J. Am. Chem. Soc.* **129**, 15118–15119 (2007).

109. Shekhah, O., Liu, J., Fischer, R. A. & Woll, C. MOF thin films: existing and future applications. *Chem. Soc. Rev.* **40**, 1081–1106 (2011).

110. Summerfield, A., Cebula, I., Schröder, M. & Beton, P. H. Nucleation and Early Stages of Layer-by-Layer Growth of Metal Organic Frameworks on Surfaces. *J. Phys. Chem. C* **119**, 23544–23551 (2015).

CHAPTER 2. EXPERIMENTAL MATERIALS AND METHODS

2.1 Reagents

2.1.1 Metal Sources Used for MOF Production

Both soluble and insoluble metal precursors were utilized to generate metal-organic frameworks investigated in this study. Ionic metal salts were used for soluble metal precursors in MOF synthesis. Many different metal precursors were utilized as insoluble metal precursors, and were typically derived from prefabricated commercial products. No surface or chemical pretreatment was performed on any metal precursors prior to use.

2.1.1.1 Soluble Metal Precursor Reagents

Metal salts were purchased commercially from Sigma Aldrich and Fisher Scientific. All metal salts utilized in this study were purchased in their hydrated form, and stored in a cool, dry location.

2.1.1.2 Insoluble Metal Precursor Reagents

Insoluble metal precursors used are described in Chapters 5 and 6. They were utilized as-purchased. Non-powdered precursors were cut or broken to fit pieces into reaction vessels. Aluminum carbide was stored separately from other reagents described here in a sealed box purged with dry N_2 to mitigate oxidation.

2.1.2 Organic Bridging Ligand Reagents Used for MOF Production

All organic bridging ligands were acquired from Sigma Aldrich or Fisher Scientific, and used without further purification. MOF linkers were retrieved as solid powders at room temperature. No subsequent organic synthesis was used to tune or modify bridging ligands in any way prior to MOF formation. Ligands were stored in a cool, dry location.

2.2 Metal-Organic Frameworks (MOFs)

2.2.1 MIL-96(Al)

MIL-96(Al) is an aluminum-based trimesate framework with the formula $Al_{12}O(OH)_{18}(H_2O)_3(Al_2(OH)_4)[BTC]_6,24H_2O$, first developed by Latroche and coworkers.[1] Trinuclear aluminum cores are interconnected by coordinated trimesic acid, forming large (18-member) hexagonal rings, as depicted in Figure 2-1. The framework displays mixed micro- and mesoporosity.[2] Elongated dodecahedron shapes of MIL-96(Al) are truncated by hindering the crystal growth rate during reaction.[3] Isolating MIL-96(Al) products can be difficult, as MIL-100(Al) and MIL-110(Al) are also produced through reaction of trimesic acid and aluminium ions—previous studies obtain the MOF through kinetic control and synthesis modulation.[4–6] Although relatively less-studied than isomer MIL-100(Al)[7], MIL-96(Al) is amenable to membrane integration, and shows favourable CO_2 uptake, even in humidity, through accessible Lewis acid Al^{3+} sites and interior μ_3 hydroxyl groups.[8,9]

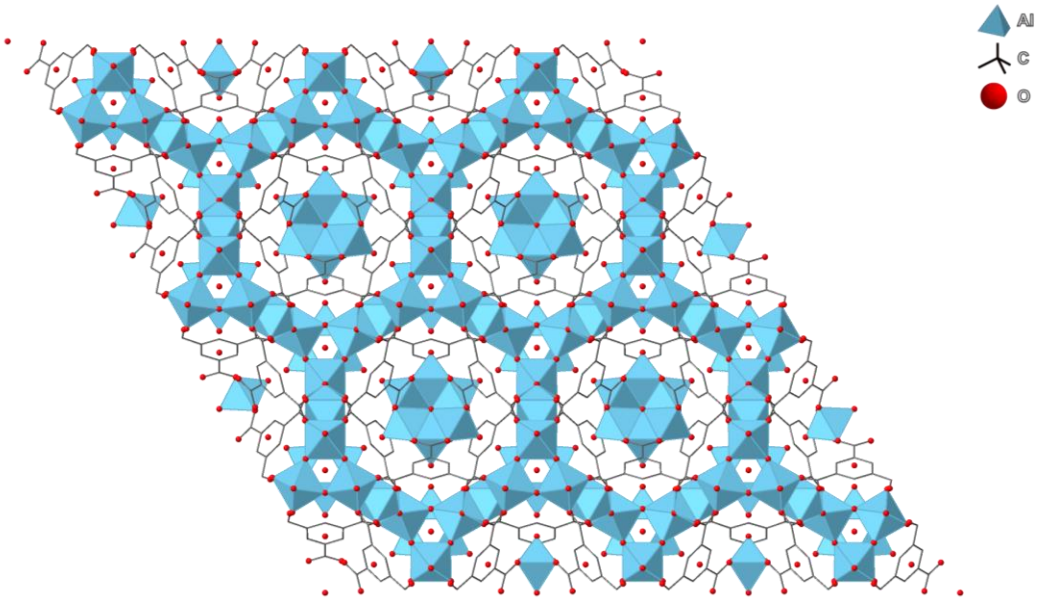

Figure 2-1: Assembly of aluminum trimesate framework rings within MIL-96(Al) through the *c* axis. Legend denotes elements in top-right corner. Image produced using CrystalMaker and diffraction data from Latroche and coworkers.[1]

2.2.2 MIL-101(Cr)

MIL-101(Cr) is a mesoporous chromium-based framework with the chemical formula $Cr_3OH(H_2O)_2O[(O_2C)\text{-}C_6H_4\text{-}(CO_2)]_3.nH_2O$ (non-fluorinated synthesis). The structure (spacegroup *F d-3m*) is constructed from chromium oxide clusters arranged in a trimer, and connected by three terephthalate ligands and a μ_3O per trimer building block. Two large cages with internal diameters of about 2.9nm and 3.4nm and mesoporous aperture openings of about 1.45nm and 1.60nm exist within the framework.[10] A smaller cage with openings of 1.2nm is also present. Chromium centers are typically capped with either fluorine or water, depending on the synthesis route, but can become unsaturated when degassed.[11] MIL-101(Cr) boasts impressive BET surface areas in excess of 2000 m^2g^{-1}.[12] A cage of MIL-101(Cr) is reproduced below in Figure 2-2 which is geometrically similar to trimers within MIL-96, described above. The large void volume and accessible

surface has fostered many investigations into the gas storage capabilities of MIL-101(Cr).[13–15] Additionally, the framework purports stability in aqueous and humid environments, as well as under acid gas exposure.[16–20]

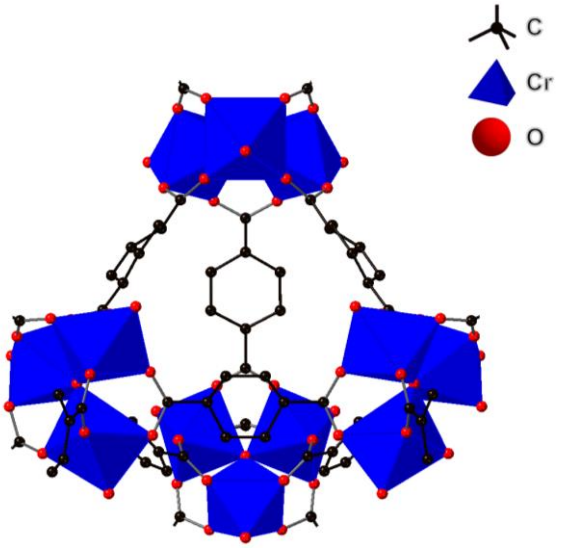

Figure 2-2: Depiction of MIL-101(Cr) trimer building block in the (1 0 1) direction. Legend in top-right corner describes elemental distribution. Structure originally reported by Férey and coworkers.[10] Image created using CrystalMaker

2.2.3 MIL-125(Ti)

MIL-125(Ti) is a three-dimensional titanium-based MOF comprised of titanium oxide clusters, $Ti_8O_8(OH)_4$, connected 12-fold by terephthalic acid ($C_8H_6O_4$, BDC) coordinating ligands.[21] A quasi-cubic, tetragonal structure results. The framework features tetrahedral and octahedral cages of 6.13Å and 12.55Å, respectively. Triangular windows from 5-7Å decorate the cages of the framework, creating a strictly microporous material. Figure 2-3 illustrates the topology of MIL-125(Ti). The framework is frequently investigated for photocatalytic conversion processes of various organic compounds, but also hold potential for gas storage and separation applications.[21–25] Modified terephthalate

ligands can construct MIL-125(Ti), where in this text 2-aminoterephthalic acid ligands are used to create MIL-125-NH_2(Ti). Accessible primary amine groups reside on the windows of MIL-125-NH_2(Ti), creating pores of 4.7Å and 10.7Å.[26] Although MIL-125(Ti) has been cited as stable up to 373K in humid environments, the addition of pendant -NH_2 groups was observed to instil stability in humid acid gas environments.[27] These functionalities have also promote acid gas adsorption selectivity through electronic interactions, as well as catalytic activity.[26,28–30]

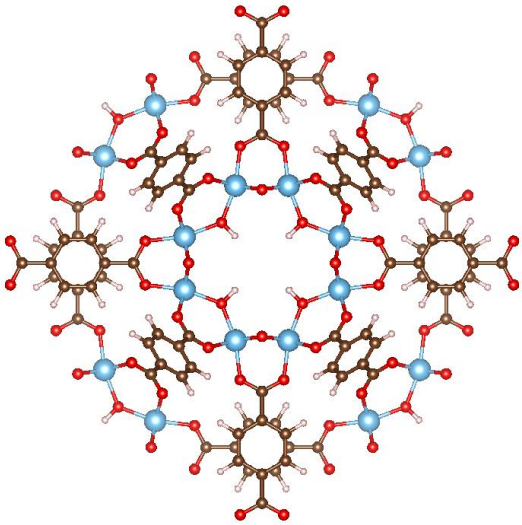

Figure 2-3: MIL-125(Ti) crystal structure. Light blue-titanium, brown-carbon, red-oxygen, white-hydrogen. Images created using VESTA

2.2.4 MIL-53(Al)

MIL-53(Al) is an aluminium terephthalate comprised of one-dimensional aluminium oxide chains connected by bridging μ_2-OH groups. A three-dimensional porous structure results from interconnecting terephthalic acid ligands. MIL-53 exhibits a large degree of framework flexibility under various stimuli (temperature, pressure, guest molecules, etc.).[31] It should be noted the MIL-53 framework may be acquired for iron,

gallium, chromium, scandium, or indium metal centers as well, but these analogues possess slight differences breathing behaviour and pore sizes.[32] The various framework forms of MIL-53(Al) are presented below in Figure 2-4. Breathing forms of MIL-53(Al) are denoted in the literature as follows: *as*-as synthesized, *lp*-large pore, and *np*-narrow pore (e.g. narrow pore form is written *np*-MIL-53).[33]

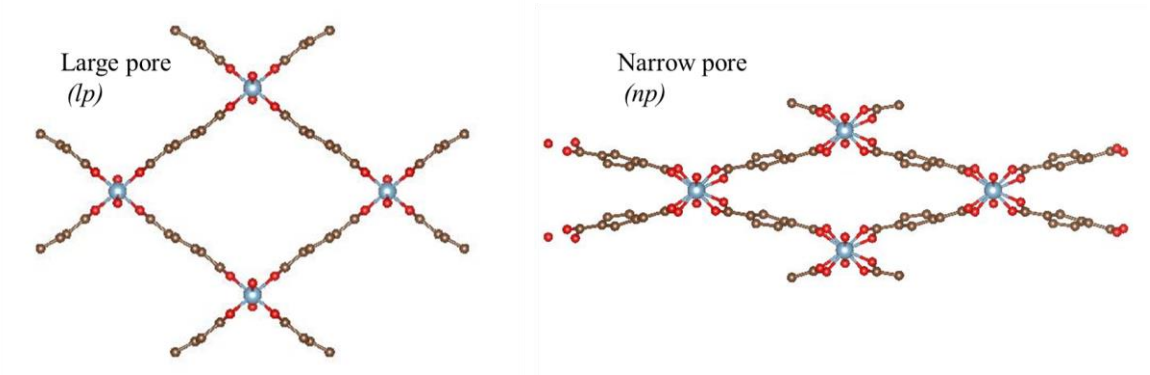

Figure 2-4: Range of large (left) and narrow (right) flexible pore forms demonstrated by MIL-53(Al). Color code is as follows: light blue-aluminum, brown-carbon, and red-oxygen. Crystal structures from Loiseau et al.[31] Images created using VESTA

2.2.5 UiO-66(Zr)

UiO-66(Zr) is a zirconium-based terephthalate, renowned in the literature for its high chemical stability. The robust chemical and structural characteristics of UiO-66(Zr) are owed largely to its 12-fold connectivity of $Zr_6O_4(OH)_4$ clusters, capped by μ_3-O and μ_3-OH species. Window sizes are approximately 6Å. Figure 2-5 illustrates a Maltese cross geometry formed by metal cluster coordination, which interconnect via terephthalate bridging molecules to form an FCC crystal structure. UiO-66 dehydroxylates upon heating between 250°C-300°C and evolves a molar equivalent of $2H_2O$, changing the MOF

formula unit to $Zr_6O_6(BDC)_{12}$. This transition enacts a rearrangement of atomic distances within the unit cell.[34]

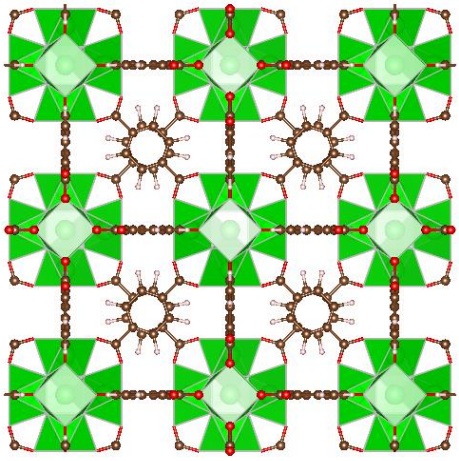

Figure 2-5: Structure of UiO-66(Zr) from Cavka et al.[34] Green polyhedral represent zirconium metal clusters, brown molecules represent coordinating terephthalate ligands. Picture generated using VESTA software

2.3 Experimental Methods

2.3.1 Synthesis Methods

2.3.1.1 MOF Synthesis and Post-synthetic Modification

Solvothermal methods were utilized to synthesize all MOFs studied in the text. The technique consists of mixing the metal precursor and organic bridging ligand in a solvent. Through time and heat, MOFs are formed and collected from the solvent mixture. Cartoon representation of solvothermal MOF synthesis is provided in Figure 2-6. Lab-scale non-supported MOF products are typically separated from reaction mixtures via gravity filtration or centrifugation, and washed with various solvents. Wash solvents are primarily selected based on MOF stability parameters (e.g. only water-stable frameworks may be

washed with water). Rinsing is typically performed in order of increasing vapor pressure. This is done to gradually evacuate guests that are more difficult to degas. For example, a standard sequence of solvent washes may be N,N-dimethylformamide ($P_{vap} \approx 3.5$hPa at 20°C), then methanol ($P_{vap} \approx 128$hPa at 20°C), and then acetone ($P_{vap} \approx 240$hPa at 20°C).[35]

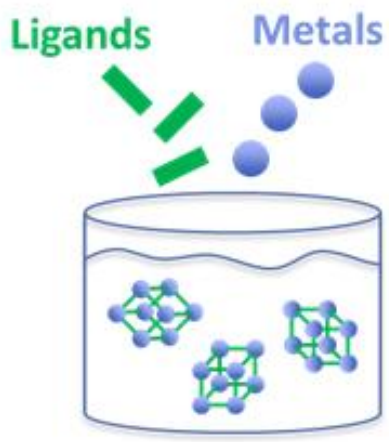

Figure 2-6: Cartoon representation of solvothermal MOF synthesis strategy

Reagent solvent molecules and wash chemicals remain entrapped in MOF pores after material separation. Additionally, molecular guests from the environment (e.g. atmospheric CO_2 and H_2O) adhere to internal surfaces of the frameworks. Materials were subsequently degassed under elevated temperature and/or decreased system pressure prior to experiments. Heating was carried out well below the thermal degradation temperatures of respective frameworks. Typical MOF degas conditions include elevated temperature and vacuum/purging with non-adsorbing gas.

Post-synthetic modification of prefabricated MOF materials was also performed solvothermally. Reactive components were stirred in solution with frameworks being

modified, at sometimes elevated temperature. After completion of reaction time, solvent extraction steps described above were performed on MOF materials.

2.3.2 Material Characterization Methods

2.3.2.1 Fixed-Bed Gas Adsorption/Exposure

In contrast to equilibrium measurements, fixed-bed gas adsorption experiments allow collection of dynamic (variance with time) adsorption data. During experiments, gas passes through the adsorbent being evaluated, which is often housed in cylindrical vessel (packed bed). A simple layout of this is provided in Figure 2-7. The outlet concentrations of target adsorbate(s) are measured during experiments. The time it takes for gas to elute from the packed bed is typically referred to as breakthrough time—*how long it takes for adsorbates to "break through" the bed*. Consequently, dynamic adsorption experiments are commonly called breakthrough experiments.

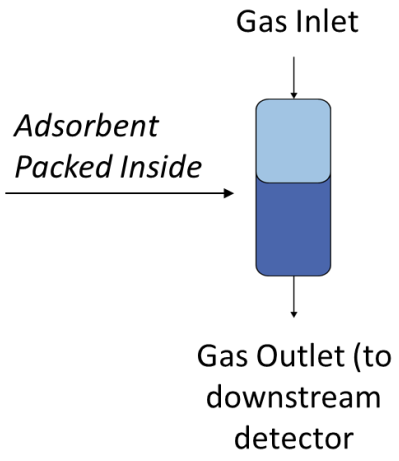

Figure 2-7: Depiction of test bed during breakthrough adsorption experiment

The cross-sectional area of the bed through which adsorption occurs at a specified point in time is referred to as the mass transfer zone. Many different process parameters in addition to mass transfer and thermodynamic properties of adsorbent-adsorbate interactions determine the progression of gas through the mass transfer zone. This process is briefly described with the aid of Figure 2-8 and stages mentioned below:

- At t=0: Gas/a gas mixture enters the packed bed. The outlet concentration of the component being measured (c) is zero
- At $t=t_i$: The measured gas component has progressed through the bed, and begins to elute. The gas is detected downstream of the bed, and $c_{out} > 0$. This is referred to as **breakthrough**. Gas is still being adsorbed in the bed. However the driving force for adsorption is insufficient to completely remove the adsorbate for the given amount of adsorbent.
- At $t=t_b$: The outlet gas concentration reaches a pre-determined concentration, defined as the breakthrough concentration (c_b). The time it takes to reach c_b is t_b.
- At $t=t_e$: The adsorbent is saturated and can no longer remove adsorbate at the inlet concentration, pressure, and temperature. Consequently, the outlet gas concentration equals the inlet gas concentration. This is sometimes referred to as dynamic equilibrium, or saturation.

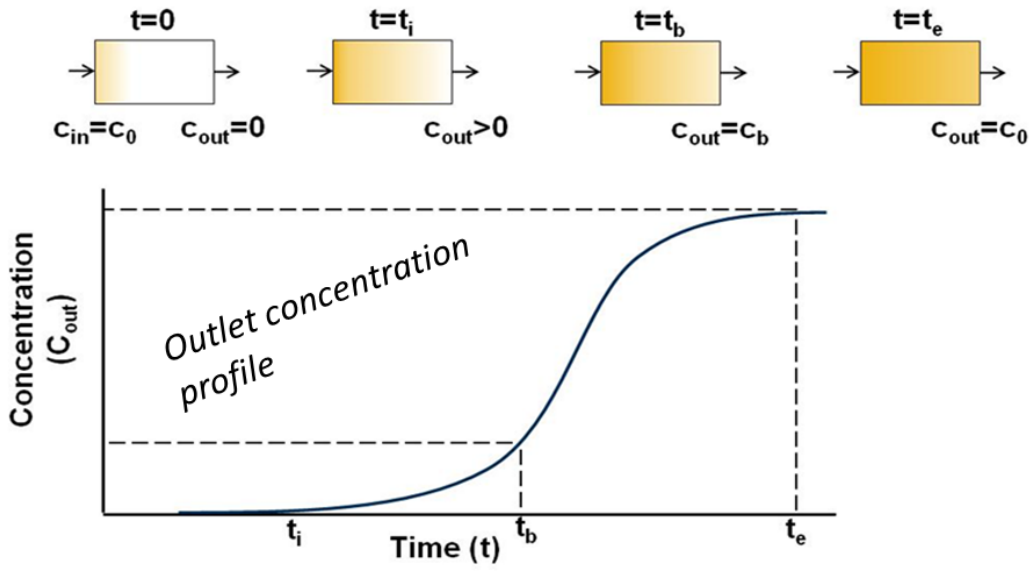

Figure 2-8: Hypothetical progression of adsorption front during a typical breakthrough experiment.

Adsorption capacities for materials are deduced with breakthrough data illustrated in Figure 2-8 through integration of the area behind the adsorption curve. Capacities are commonly determined through numerical integration methods, and are then normalized by either adsorbent mass or volume. Capacity estimations here assumed local equilibrium in fixed-bed studies, which encompass (1) negligible external and internal mass transfer resistances, (2) ideal plug flow, (3) adsorbents do not contain target adsorbates at beginning of experiments, and (4) isothermal & isobaric conditions.[36]

A homemade fixed-bed apparatus was utilized to acquire dynamic adsorption measurements. Because of the hazardous nature of gases evaluated in this dissertation, the entire setup was housed inside a well-ventilated chemical hood in an acid gas laboratory, housed with ambient and process gas monitoring, emergency shutoff equipment, and self-ventilated gas cylinder cabinets which route directly to test equipment. A schematic of the apparatus is provided in Figure 2-9. A total volumetric flowrate of 300mL min^{-1} is

achievable. The setup allows evaluation of multiple gases simultaneously, but notably SO_2, and H_2S in this dissertation under either dry or humid (up to ~85%RH) conditions. Bed sizes are interchangeable. Gases were detected using a Pfeiffer GSD 320 O2C, OmniStar Gas analysis system 1-200amu, 100-230V, 50/60Hz corrosive gas version mass spectrometer. Although room temperature experiments were typically performed, variable temperature experiments were facilitated using heat tape and a temperature controller. All outlet lines were directed to a 1N NaOH solution to neutralize eluting acid gases. Packing aspect ratios were estimated using the Ergun Equation[37], and pressure drop (rather the absence of) was monitored during experiments using an in-line pressure gauge. Cyclic adsorption studies were carried out by purging samples with an inert gas and simultaneously applying heat to material-specific degas temperatures after termination of the adsorption step. Desorption continued until adsorbates could no longer be detected from the bed outlet to concentrations < 1ppm.

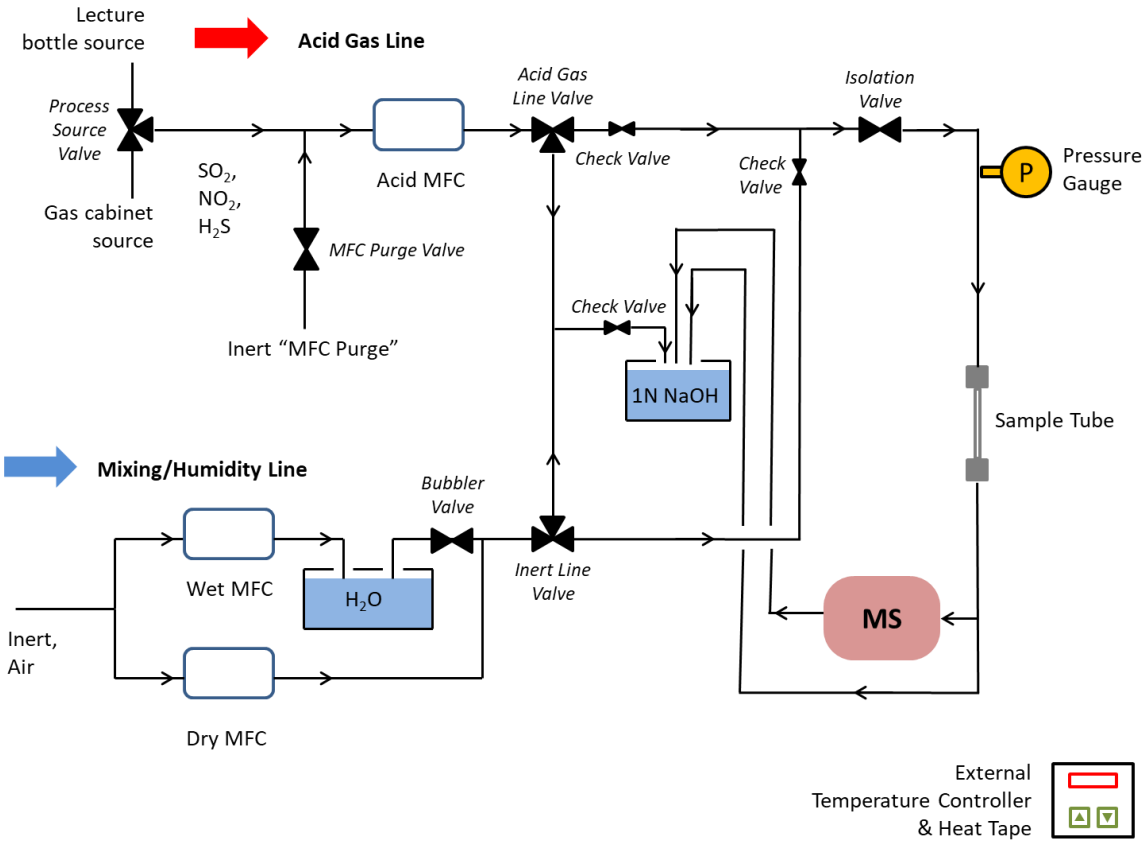

Figure 2-9: Schematic of hazardous gas adsorption and exposure system

2.3.2.2 Microscopy

Morphological and compositional analyses were pursued using microscopy techniques. Electron microscopy was specifically utilized to study micro- and nanoscale materials developed here.

Scanning electron microscopy (SEM) uses scattered electrons from samples subjected to an electron beam. Imaging is influenced by the specific detection method used in SEM experiments. Inelastic electron scattering between the incident beam and electrons in a studied sample produces *secondary electrons*. Detected secondary electrons primarily emanate from sample surfaces, providing high resolution imaging of morphological

features and topography. Conversely, higher energy elastically scattered electrons from deeper regions within the sample are called *backscatter electrons*. Backscatter electrons lack the same degree of surface sensitivity possessed by secondary electrons, and instead are more descriptive of elemental composition. For instance, elements with greater mean atomic numbers produce proportionally brighter contrast (higher) backscatter electron production, allowing different elements within a material to be differentiated. Subsequently, both topological and elemental analyses are allowed through SEM.

A Zeiss Ultra 60 Field Emission (FE) SEM was used to acquire electron images. Samples were placed onto carbon tape secured on stands prior to imaging. An accelerating voltage range of 1-20keV was used, depending on the sample and scan parameters. Elemental analysis was performed on the same instrument through energy dispersive spectroscopy (EDS), processed using AZtec software. An accelerating voltage of at least 10kV and a working distance of approximately 8.7mm was utilized for EDS measurements, which were pre-calibrated with titanium and silicon standards. Accelerating voltages used during EDS measurements were dependent on the Kα. emission energies of target absorbing atoms.

Transmission electron microscopy (TEM) relies on the detection of electrons transmitted through a material. Samples studied under TEM are essentially cross-sectioned by the incident electron beam, and visual information about the interior of specimens are provided. The distribution of nanoparticles in composites, for instance, can be ascertained through TEM. Properly dispersing specimen particles onto lacy carbon grids prior to examination allows crystallite size determination.

A JEOL 100 CX-II TEM was used for transmission-based imaging. The instrument utilizes a tungsten filament at accelerating voltages up to 100keV, and can tilt samples using a side-entry goniometer. Powdered TEM samples were first prepped by dispersing small amounts (~5mg) in either acetone, methanol, or isopropanol, and then adding up to 3 droplets onto a lacy carbon grid. Images were visualized through a fluorescent screen generated by electromagnetic lenses within the microscope column, and an external digital camera.

2.3.2.3 N_2 Physisorption Measurements

Nitrogen adsorption measurements primarily provide porosity information. Surface area, pore volume, pore size(s), and other metrics are discerned non-destructively from this experiment, relevant for characterizing highly porous materials such as MOFs. Measurements are specifically performed at the liquid temperature of nitrogen, 77K.

The Brunauer–Emmett–Teller (BET) method was utilized to extrapolate specific surface area information. This method assesses multilayer adsorption to estimate a monolayer loading, which is then used to calculate accessible adsorption area information.[38,39] BET estimations through N_2 and other candidate probe molecules are importantly more descriptive of adsorption surfaces than surface areas derived from adsorbent geometry or Connelly areas.[40] Although BET theory was initially applied for flat surfaces, its applicability for MOF materials has been demonstrated over the typically-used pressure range of $0.05 > P/P_0 > 0.3$.[41,42]

Pore size distributions (PSD) are also extrapolated from N_2 adsorption data. Density functional theory (DFT) models are applied to analyze a variety of porous systems. DFT

models approximate fluid phase behavior of specified adsorbates as a function of pore size, geometry, pressure, temperature, and sometimes mixtures of these and other variables. The specific function is often referred to as a kernel. A generic form of a pore size distribution in the so-called *integral adsorption equation* is reproduced from Ravikovitch et al.[43] in Equation 2.1. The variable H describes the pore size, N_{exp} is the isotherm, N_s is the kernel, and x(H) is the pore size distribution function. Most models utilize non-local (NLDFT) kernels based on independent slit pores and ideal wall interactions. However, more heterogeneous surfaces are better modelled with quenched solid (QSDFT) kernels, which essentially use a variable spatial distribution of site densities to account for diverse surface chemistry within an adsorbent.[39,44] Unfortunately, a uniform PSD model has not been developed for MOFs. MOF pore sizes are instead obtained from crystallographic data. Accordingly, MOF PSDs reported in this dissertation are intended to aid qualitative comparisons. PSD kernel choice for non-MOF materials presented in this study were selected primarily based on pore geometry, and utilize NLDFT and QSDFT.

$$N_{exp} = \sum_{H_{min}}^{H_{max}} N_s(P,H)x(H)dH \tag{2.1}$$

A Quantachrome Quadrasorb Evo was used to collect N_2 physisorption data. Liquid nitrogen-filled dewars were utilized to hold samples isothermally at 77K during analyses. Approximately 50-100 mg of sample were utilized for porosity measurements. Powders were placed into glass tubes of known void volumes to facilitate volumetric adsorption calculations. Activation at reported MOF degas temperatures under vacuum were performed prior to measurements using a Quantachrome Instruments FloVac Degasser.

Pore size distributions, BET surface areas, and total pore volumes were approximated using QuadraWin software for analyzed materials.

2.3.2.4 Thermogravimetric Analysis (TGA)

Thermogravimetry entails the heating of materials to gauge material mass changes with respect to temperature. TG data is used here to estimate desolvation conditions, material composition, defect quantities, and thermal degradation temperatures.

One major application of thermogravimetry in this dissertation was to approximate and quantify point defects in synthesized materials. For frameworks, the mass loss of both metal clusters and bridging linkers are coupled. So, this technique provides a metric on the total defects caused by vacancies, as well as the final metal-to-linker mass ratio. To force combustion products through heating, which is sometimes helpful for normalizing stoichiometric calculations, air is used as a carrier. Practice of this evaluation has been eloquently outlined by Lillerud and coworkers[45] for UiO-66(Zr), where an in-depth approach to understanding defect modulation in UiO-66(Zr) is outlined in their Supporting Information. This approach with respect to UiO-66(Zr) materials, as investigated in Chapter 4, is briefly summarized here in the below example for the parent framework:

The first assumption is that the final product of the thermal degradation of the Zr MOF will be the corresponding metal oxide: ZrO_2. To normalize the molar amount expected, the dehydroxylated unit of UiO-66 is considered[46], where $Zr_6O_6(BDC)_6$ would be expected to decompose to 6 ZrO_2, based on stoichiometry. Accordingly, TGA data of the sample following solvent loss should be considered—for UiO-66(Zr) this form is attained at temperatures approximately > 300°C.[45] So now, the starting ($Zr_6O_6(BDC)_6$) and

end (6 ZrO_2) molar bases have been defined. Figure 2-10 shows example TGA curves for UiO-66(Zr) from the literature using this normalization approach (albeit two different normalizations) to calculate linker/metal cluster deficiency. Percent loss calculations come from the relative molecular weights of the two assumed materials at the beginning and end of the measurement. The molecular weights of $Zr_6O_6(BDC)_6$ and 6 ZrO_2 are **1628 g mol^{-1}** and **739 g mol^{-1}**, respectively. If the end weight is normalized to 100%, the theoretical plateau of the UiO-66(Zr) SBU from stoichiometry is expected to occur at about 220%. Taking the difference and accounting for 6 BDC linkers per UiO-66(Zr) formula unit gives a 20% expected mass loss per framework ligand. So based on the percentage mass loss of the activated MOF, framework deficiencies on samples are estimated.

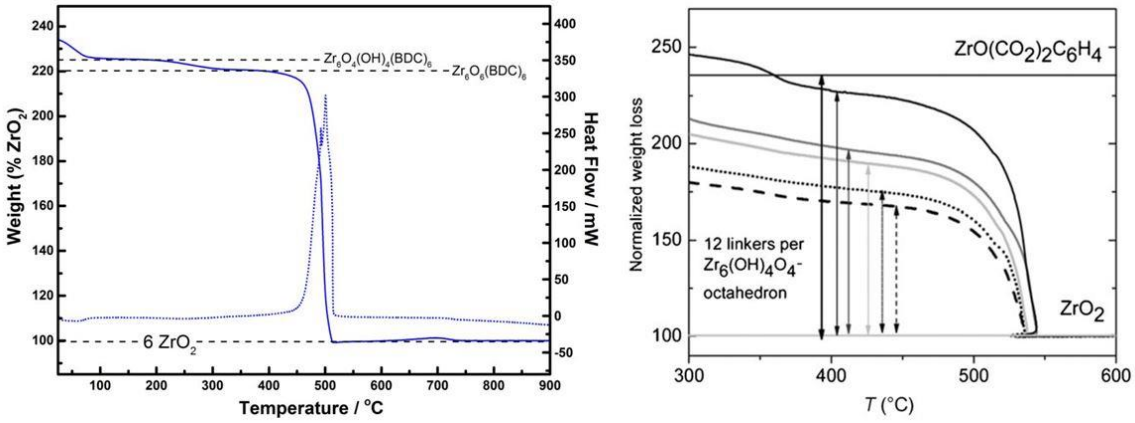

Figure 2-10: Two examples of normalized TGA curves on UiO-66(Zr). From Lillerud and coworkers[45] (left) and Lamberti and coworkers[47] (right).

TG experiments were programmed and carried out using a Netzsch STA 449 Jupiter Simultaneous TG-DSC. Samples quantities of 10-40mg were loaded into a ceramic crucible and placed on a scale with 25ng resolution.[48] Either ultrapure helium or air carrier gas was passed through the system at a total flow rate of 40mL min^{-1}, depending on whether

material pyrolysis or combustion was desired, respectively. Temperature ramps ranging from 2-10°C min^{-1} and isothermal holds were both utilized while collecting TG data.

2.3.2.5 Powder X-ray Diffraction

Crystalline materials diffract incident X-ray radiation. Spacing between the unique planes of a structure is directly related to the angle of scattered X-rays through Bragg's Law in Equation 2.2

$$n\lambda = 2dsin\left(\frac{2\theta}{2}\right) \quad (2.2)$$

Where λ is the wavelength of incident X-ray radiation, d (d-spacing) describes the interplanar spacing, and θ is the scattering angle of X-rays. Unit cells may be determined by satisfaction of the Bragg condition, described in Equation 2.3, also known as the 'order of diffraction'.[49] *h, k,* and *l* represent the three dimensions of Miller indices, and are found through the reciprocal of planar intercepts within a crystal structure (represented as the smallest integer number). Consequently, the structure of an ordered material directly dictates the X-ray scatter from incident radiation.

$$n = \sqrt{h^2 + k^2 + l^2} \quad (2.3)$$

The scattering angle θ directly relates to the spacing between crystal planes through Bragg's Law. Diffraction only results from the long-range order of crystalline solids. So, X-ray diffraction (XRD) experiments can discriminate between crystalline and amorphous materials.

Materials whose crystals are difficult to isolate for traditional single crystal XRD measurements, mainly due to size, may be evaluated through powder X-ray diffraction (PXRD). Powders are typically placed on a plate or well which emits relatively low background scatter when irradiated, The working assumption for powder samples entails crystal orientations being randomly arranged and distributed isotropically. Peak position in resultant 2-D data describe unit cell dimensions and structure properties. Parameters such as crystal size and microstrain may be ascertained by peak width, while the intensity of individual reflections correlates to the number of atoms encompassed by a crystallographic plane. Accordingly, PXRD data refinement approximates one or more of these structural qualities for an examined specimen, which is dependent on input refinement information (e.g. presence of appropriate structural model) and complexity of the fitting model.

2.3.2.6 X-ray Absorption and Photoelectron Spectroscopy

X-ray absorption spectroscopy (XAS) is a non-destructive material characterization technique that provides chemical composition and structure information. It is also often referred to as X-ray absorption fine structure (XAFS). X-ray photoelectron spectroscopy (XPS) operates on the same working principle and provides similar information, but relies on the measurement of photoelectrons instead.

X-rays encompass energies ranging from ~500eV to 500keV (wavelengths ~25Å to 0.25Å).[50] Experiments operate on bombarding test samples with X-rays of varying incident intensity. If incident X-ray energies are less than the binding energy of electrons within a sample ($E_{X\text{-}ray} < E_{binding}$), then electrons within a sample are unperturbed. Through the photoelectric effect, when the incident energy of X-rays exceeds the binding energy of

electrons in a given orbital level ($E_{X\text{-}ray} \geq E_{binding}$), X-ray energy is absorbed, and a photoelectron is ejected. This process within an atom's nominal energy levels is illustrated below in Figure 2-11. Ejected photoelectrons are measured through XPS, and relay element-specific chemical state information. Photoelectrons emerging from deeper regions of a packed sample are likely to scatter and/or possibly reabsorb. Consequently, XPS measurements are generally surface-specific, and may not accurately communicate bulk properties. Ultra-high vacuum is utilized to obtain high photoelectron intensities. In this dissertation, a Thermo K-alpha, monochromatic Al Kα source instrument with a double-focusing hemispherical analyzer was used to collect XPS data. High resolution spectra were taken using a 50ms dwell time, 50eV pass energy, and a 400µm spot size. Samples were activated prior to data collection.

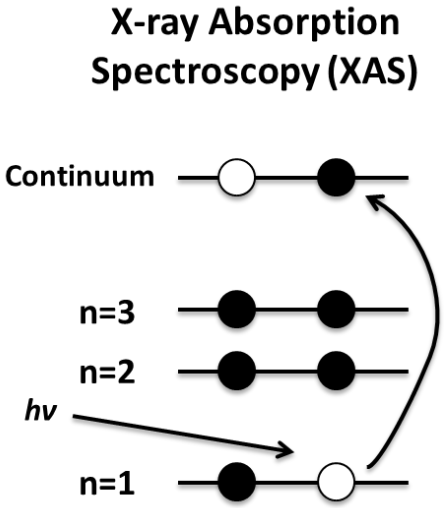

Figure 2-11: Cartoon illustration of core shell electron ejection upon energetic excitation

Conversely, the difference in X-ray intensity via transmission is most commonly measured in XAS, although fluorescence-based measurements (also referred to as X-ray

emission spectroscopy, XES—see Figure 2-12) are also utilized. Beer-Lambert's Law is related to sample characteristics and the absorption coefficient μ(E) in Figure 2-13. The exponential relationship of μ(E) to intensity changes differs by magnitudes across elements, making XAS and XPS *element specific*.[51]

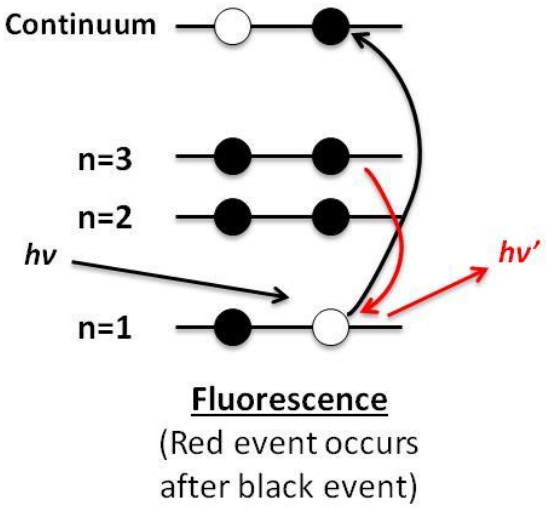

Figure 2-12: Cartoon illustration of fluorescence emission (hv') upon incident energy (hv) excitation

$$\frac{I}{I_0} = e^{-\mu t}$$

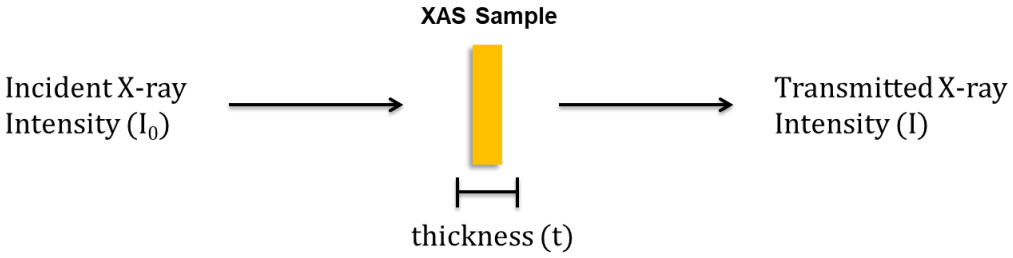

Figure 2-13: Relation of Beer's Law to XAS sample characteristics. Yellow rectangle is representative of a XAS sample. μ is the absorption coefficient, and is a function of energy (E).

Ejected photoelectrons may scatter from neighboring atoms and "return" to the original absorbing species. Figure 2-14 tracks the hypothetical path of photoelectron scattering and its impact on atomic energy absorption. Information about "nearest neighbor" atoms within a compound, such as covalently bonded atoms, is transferred onto μ(E) measurements during XAS measurements through this phenomenon. Consequently, changes in μ(E) become dependent on material aspects such as coordination geometry and composition—structural information may be deduced from XAS data in addition to oxidation state and elemental detection. Importantly, structure determination through XAFS experiments do not require assumptions of periodicity or symmetry.[52]

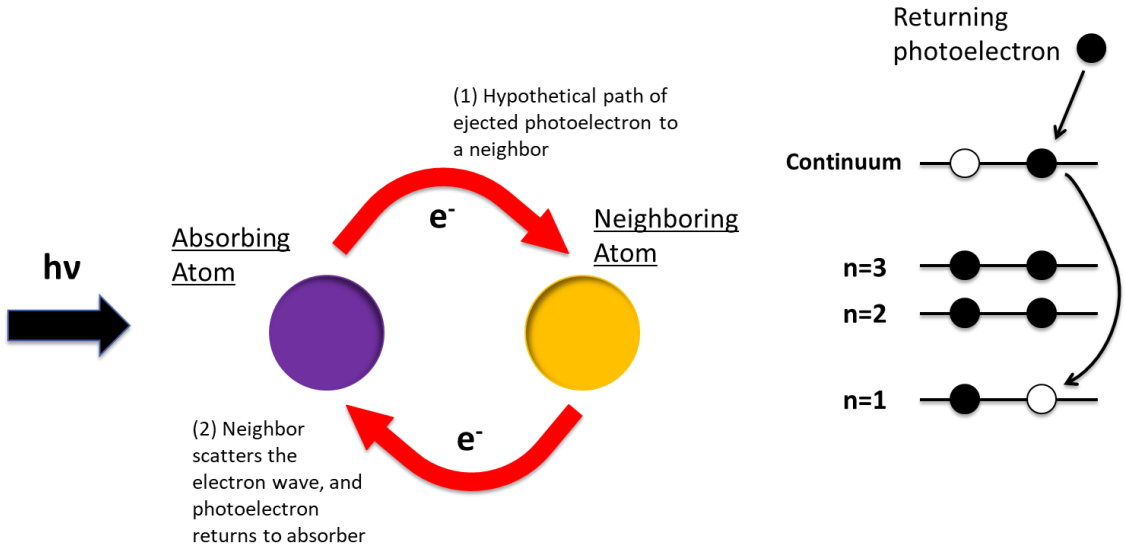

Figure 2-14: Cartoon depicting the impact of photoelectron scatter on atomic absorption at high energies (hv)

An example plot of output XAS data is provided in Figure 2-15. Separate regions of the measurement are highlighted within Figure 2-15–X-ray Absorption Near Edge Spectra (XANES) and Extended X-ray Absorption Fine Structure (EXAFS). Although the regions are certainly not limited to this, XANES features are often utilized to discern

chemical information, such as oxidation state, and qualitative structure information. Because of the stronger amount of photoelectron scatter depicted in Figure 2-14 at high energies, the EXAFS data region communicates structural features of tested compounds, such as nearest neighbor identities, number of nearest neighbors, and bonding geometries.

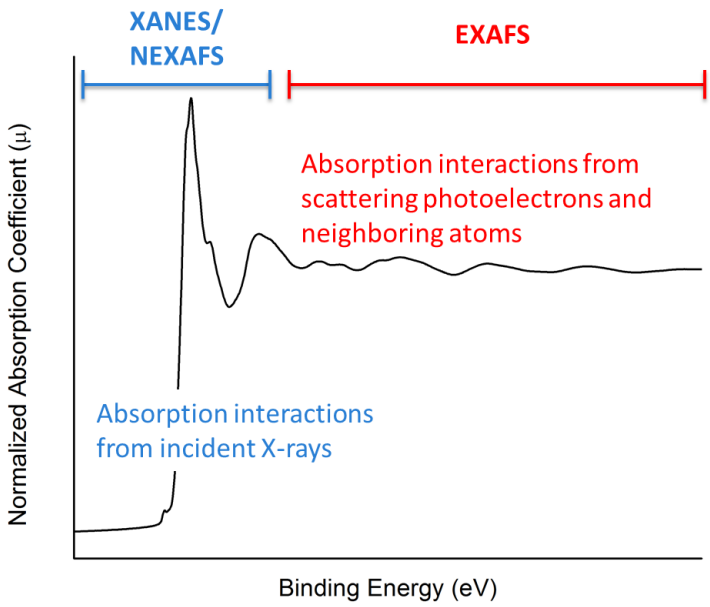

Figure 2-15: Example XAS measurement plot, highlighting nominal XANES and EXAFS regions

XAS measurements reported in this dissertation were obtained at the Advanced Photon Source (APS) at Argonne National Laboratory beamline 12-BM.[53] Transmission-based measurements were used, where samples were either pelletized with boron nitride binder, or applied as a thin powder film (~1cm in diameter) to adhesive tape. Data processing was performed with the Demeter software suite.[54]

2.4 Chapter 2 References

1. Loiseau, T. *et al.* MIL-96, a Porous Aluminum Trimesate 3D Structure Constructed from a Hexagonal Network of 18-Membered Rings and μ_3-Oxo-Centered Trinuclear Units. *J. Am. Chem. Soc.* **128**, 10223–10230 (2006).

2. Abid, H. R., Rada, Z. H., Shang, J. & Wang, S. Synthesis, characterization, and CO_2 adsorption of three metal-organic frameworks (MOFs): MIL-53, MIL-96, and amino-MIL-53. *Polyhedron* **120**, 103–111 (2016).

3. Liu, D. *et al.* Size- and morphology-controllable synthesis of MIL-96 (Al) by hydrolysis and coordination modulation of dual aluminium source and ligand systems. *Dalt. Trans.* **44**, 16421–16429 (2015).

4. Haouas, M., Volkringer, C., Loiseau, T., Ferey, G. & Taulelle, F. In Situ NMR, Ex Situ XRD and SEM Study of the Hydrothermal Crystallization of Nanoporous Aluminum Trimesates MIL-96, MIL- 100, and MIL-110. *Chem. Mater.* **24**, 2462–2471 (2012).

5. Seoane, B. *et al.* Metal organic framework synthesis in the presence of surfactants: towards hierarchical MOFs? *CrystEngComm* **17**, 1693–1700 (2015).

6. Qiu, M., Guan, Q. & Li, W. Controllable Assembly of Al-MIL-100 via an Inducing Occupied Effect and Its Selective Adsorption Activity. *Cryst. Growth Des.* **16**, 3639–3646 (2016).

7. Volkringer, C. *et al.* Synthesis, Single-Crystal X-ray Microdiffraction, and NMR Characterizations of the Giant Pore Metal-Organic Framework Aluminum Trimesate MIL-100. *Chem. Mater.* **21**, 5695–5697 (2009).

8. Benzaqui, M. *et al.* Revisiting the Aluminum Trimesate-Based MOF (MIL-96): From Structure Determination to the Processing of Mixed Matrix Membranes for CO_2 Capture. *Chem. Mater* **29**, 10326–10338 (2017).

9. Benoit, V. *et al.* A promising metal–organic framework (MOF), MIL-96(Al), for CO_2 separation under humid conditions. *J. Mater. Chem. A* **6**, 2081–2090 (2018).

10. Férey, G. *et al.* A chromium terephthalate-based solid with unusually large pore volumes and surface area. *Science* **309**, 2040–2042 (2005).

11. Wittmann, T. *et al.* Probing Interactions of N-Donor Molecules with Open Metal Sites within Paramagnetic Cr-MIL-101: A Solid-State NMR Spectroscopic and Density Functional Theory Study. *J. Am. Chem. Soc.* **140**, 2135–2144 (2018).

12. Leng, K., Sun, Y., Li, X., Sun, S. & Xu, W. Rapid Synthesis of Metal–Organic Frameworks MIL-101(Cr) Without the Addition of Solvent and Hydrofluoric Acid. *Cryst. Growth Des.* **16**, 1168–1171 (2016).

13. Latroche, M. *et al.* Hydrogen Storage in the Giant-Pore Metal–Organic Frameworks MIL-100 and MIL-101. *Angew. Chemie Int. Ed.* **45**, 8227–8231 (2006).

14. Yang, J., Zhao, Q., Li, J. & Dong, J. Synthesis of metal–organic framework MIL-101 in TMAOH-$Cr(NO_3)_3$-H_2BDC-H_2O and its hydrogen-storage behavior. *Microporous Mesoporous Mater.* **130**, 174–179 (2010).

15. Llewellyn, P. L. *et al.* High Uptakes of CO_2 and CH_4 in Mesoporous Metal Organic Frameworks MIL-100 and MIL-101. *Langmuir* **24**, 7245–7250 (2008).

16. Burtch, N. C., Jasuja, H. & Walton, K. S. Water Stability and Adsorption in Metal-Organic Frameworks. *Chem. Rev.* **114**, 10575–10612 (2014).

17. Henschel, A., Gedrich, K., Kraehnert, R. & Kaskel, S. Catalytic properties of MIL-101. *Chem. Commun.* 4192–4194 (2008).

18. Liu, J., Wei, Y., Li, P., Zhao, Y. & Zou, R. Selective H_2S/CO_2 Separation by Metal−Organic Frameworks Based on Chemical-Physical Adsorption. *J. Phys. Chem. C* **121**, 13249–13255 (2017).

19. Hamon, L. *et al.* Comparative Study of Hydrogen Sulfide Adsorption in the MIL-53 (Al, Cr, Fe), MIL-47 (V), MIL-100 (Cr), and MIL-101 (Cr) Metal-Organic Frameworks at Room Temperature. *J. Am. Chem. Soc.* **131**, 8775–8777 (2009).

20. Liu, Q. *et al.* Adsorption of Carbon Dioxide by MIL-101(Cr): Regeneration Conditions and Influence of Flue Gas Contaminants. *Sci. Rep.* **3**, 2916 (2013).

21. Dan-Hardi, M. *et al.* A New Photoactive Crystalline Highly Porous Titanium (IV) Dicarboxylate. *J. Am. Chem. Soc.* **131**, 10857–10859 (2009).

22. Hou, C., Xu, Q., Wang, Y. & Hu, X. Synthesis of Pt@NH_2-MIL-125(Ti) as a photocathode material for photoelectrochemical hydrogen production. *RSC Adv.* **3**, 19820–19823 (2013).

23. Khaletskaya, K. *et al.* Fabrication of Gold/Titania Photocatalyst for CO_2 Reduction Based on Pyrolytic Conversion of the Metal-Organic Framework NH_2-MIL-125(Ti) Loaded with Gold Nanoparticles. *Chem. Mater.* **27**, 7248–7257 (2015).

24. Nasalevich, M. A., Goesten, M. G., Savenije, T. J., Kapteijn, F. & Gascon, J. Enhancing optical absorption of metal-organic frameworks for improved visible light photocatalysis. *Chem. Commun.* **49**, 10575–10577 (2013).

25. Nasalevich, M. A. *et al.* Co@NH_2-MIL-125(Ti): cobaloxime-derived metal–organic framework-based composite for light-driven H2 production. *Energy Environ. Sci.* **8**, 364–375 (2015).

26. Vaesen, S. *et al.* A robust amino-functionalized titanium(IV) based MOF for improved separation of acid gases. *Chem. Commun.* **49**, 10082–10084 (2013).

27. Mounfield III, W. P. *et al.* Synergistic Effects of Water and SO_2 on Degradation of MIL-125 in the Presence of Acid Gases. *J. Phys. Chem. C* **120**, 27230–27240 (2016).

28. Hendon, C. H. *et al.* Engineering the Optical Response of the Titanium-MIL-125 Metal-Organic Framework through Ligand Functionalisation. *J. Am. Chem. Soc.* 10942–10945 (2013).

29. Puthiaraj, P. & Ahn, W.-S. Highly active palladium nanoparticles immobilized on NH_2-MIL-125 as efficient and recyclable catalysts for Suzuki-Miyaura cross coupling reaction. *Catal. Commun.* **65**, 91–95 (2015).

30. Guo, X. *et al.* Mixed matrix membranes incorporated with amine-functionalized titanium-based metal-organic framework for CO_2/CH_4 separation. *J. Memb. Sci.* **478**, 130–139 (2015).

31. Loiseau, T. *et al.* A Rationale for the Large Breathing of the Porous Aluminum Terephthalate (MIL-53) Upon Hydration. *Chem. – A Eur. J.* **10**, 1373–1382 (2004).

32. Giovine, R. *et al.* NMR crystallography to probe the breathing effect of the MIL-53(Al) metal–organic framework using solid-state NMR measurements of $^{13}C - ^{27}Al$ distances. *Acta Cryst.* **C73**, 176–183 (2017).

33. Ferey, G. & Serre, C. Large breathing effects in three-dimensional porous hybrid matter: facts, analyses, rules and consequences. *Chem. Soc. Rev* **38**, 1380–1399 (2009).

34. Cavka, J. H. *et al.* A new zirconium inorganic building brick forming metal organic frameworks with exceptional stability. *J. Am. Chem. Soc.* **130**, 13850–13851 (2008).

35. Properties of Solvents Used in Organic Chemistry. Available at: http://murov.info/orgsolvents.htm. (Accessed: 3rd December 2018)

36. Seader, J. D., Henley, E. J. & Roper, D. K. *Separation Process Principles Chemical and Biochemical Operations*. (John Wiley & Sons Ltd: Hoboken, NJ 2011).

37. Ergun, S. Fluid flow through packed columns. *Chem. Eng. Prog.* **48**, 89 (1952).

38. Brunauer, S., Emmett, P. H. & Teller, E. Adsorption of gases in multimolecular layers. *J. Am. Chem. Soc.* **60**, 309–319 (1938).

39. Thommes, M. *et al.* Physisorption of gases, with special reference to the evaluation of surface area and pore size distribution (IUPAC Technical Report). *Pure Appl. Chem* **87**, 1051–1069 (2015).

40. Du, T., Millange, F., Férey, G., Walton, K. S. & Snurr, R. Q. Calculating Geometric Surface Areas as a Characterization Tool for Metal-Organic Frameworks. *J. Phys. Chem. C* **111**, 15350–15356 (2007).

41. Sing, K. S. W. *et al.* Reporting Physisorption Data for Gas/Solid Systems with Special Reference to the Determination of Surface Area and Porosity. *Pure Appl. Chem.* **54**, 2201–2218 (1982).

42. Walton, K. S. & Snurr, R. Q. Applicability of the BET method for determining surface areas of microporous metal-organic frameworks. *J. Am. Chem. Soc.* **129**, 8552–8556 (2007).

43. Ravikovitch, P. I., Vishnyakov, A., Russo, R. & Neimark, A. V. Unified Approach to Pore Size Characterization of Microporous Carbonaceous Materials from N_2 , Ar, and CO_2 Adsorption Isotherms. *Langmuir* **16**, 2311–2320 (2000).

44. Quantachrome Instruments. Quenched Solid State Functional Theory (QSDFT) for Pore Size Analysis of Disordered Carbon. *AZO Materials* (2010). Available at: https://www.azom.com/article.aspx?ArticleID=5191. (Accessed: 1st February 2019)

45. Shearer, G. C. *et al.* Tuned to perfection: Ironing out the defects in metal-organic framework UiO-66. *Chem. Mater.* **26**, 4068–4071 (2014).

46. Vandichel, M. *et al.* Active site engineering in UiO-66 type metal–organic frameworks by intentional creation of defects: a theoretical rationalization. *CrystEngComm* **17**, 395–406 (2014).

47. Valenzano, L. *et al.* Disclosing the complex structure of UiO-66 metal organic framework: A synergic combination of experiment and theory. *Chem. Mater.* **23**, 1700–1718 (2011).

48. STA 449 F1 Jupiter®. *Netzsch* Available at: https://www.netzsch-thermal-analysis.com/us/products-solutions/simultaneous-thermogravimetry-differential-scanning-calorimetry/sta-449-f1-jupiter/. (Accessed: 3rd December 2019)

49. Vickerman, J. C. & Gilmore, I. S. *Surface Analysis-The Principal Techniques*. (John Wiley & Sons Ltd: Teddington 2009).

50. Newville, M. Fundamentals of XAFS. *ReVision* 43 (2004).

51. Kuzmin, A. & Chaboy, J. EXAFS and XANES analysis of oxides at the nanoscale. *IUCrJ* **1**, 571–589 (2014).

52. Ravel, B. & Kelly, S. D. The Difficult Chore of Measuring Coordination by EXAFS. *X-Ray Absorpt. Fine Struct. 13* 1–3 (2007)

53. 12-BM Home Page Advanced Photon Source. Available at: https://www.aps.anl.gov/Sector-12/12-BM. (Accessed: 24th March 2019)

54. Ravel, B. About Demeter. (2006). Available at: https://bruceravel.github.io/demeter/. (Accessed: 24th March 2019)

CHAPTER 3. SYNTHESIS AND PROCESSING IMPACTS ON FRAMEWORK STABILITY

3.1 Introduction

Chemical and physical properties of *ideal* MOF structures often differ from synthesized structures. Crystalline defects are prevalent in MOFs, and often manipulate their intrinsic properties.[1] In a 2015 review on the subject, Fischer and coworkers detailed how various methods of intentionally engineering defects can enhance the applicability of porous crystalline solids for gas sieving, adsorption, catalysis, and sensing applications.[2] Sometimes these imperfections do not strongly impact separations. This was the case for stacking defaults in ZIF materials probed by Han and Sholl, where surface areas and channel sizes were not significantly impacted.[3] But tradeoffs exist. Coudert and coworkers noted one example of this, where although simulated CO_2 uptake observably increased with point defect density in a series of UiO-66(Zr) structures, mechanical stability was sacrificed from the loss of framework connectivity.[4] Hydrophilicity also increases with defect density in the zirconium framework, as seen through water vapor uptake measurements.[5,6] This strongly affects separation performance in humid environments. Hydrophilic defect sites benefit systems with favorable adsorbate-adsorbate binding affinities in the presence of water vapor[7,8], but hinder selectivity if H_2O(v) acts as a competitive adsorbing species.[9] It is subsequently important to learn how crystalline defects may improve MOF separation performance, but remain cognizant of their possible detriments on structural stability and adsorption efficacy in relevant environments.

A different scenario exemplifying the 'give-and-take' between MOF stability and adsorption performance is encompassed by frameworks possessing open (coordinatively unsaturated) metal sites. Coordinating metals foster remarkable uptake capacity and selectivity when reactive and accessible to incoming adsorbates. For example, the well-known chemical affinity of Fe(III) for H_2S at even low concentrations[10–15] generates impressive sulfur scavenging capabilities in iron-based MOFs.[16,17] Unsaturated copper sites within HKUST-1, a particularly well-studied MOF, was shown by Watanabe and Sholl to generate strong binding interactions with acid gases NO and H_2S, as well as other molecules.[18] A large number of MOFs enumerated in Ki Chul Kim's summary of hazardous gas-selective adsorbents notably possess reactive open metal sites.[19] As with defect engineering however, structural integrity is often compromised through the strong adsorption interactions afforded by unsaturated metal sites.[5,20] Given the application advantages of MOFs with metal binding locations, techniques for manifesting these reaction sites while simultaneously maintaining structural stability in the presence of reactive acid gas adsorbates are desired.

Aside from engineering the internal properties of adsorbents, their external implementation into end-use media requires attention. Literature in the area of new-age adsorbent design often report measurements on nanoscale powders. Unfortunately, products cannot be practically employed in this form. Ideally, structured adsorbent contactors with controllable distributions and loadings of next-generation acid gas removal media are more actionable for optimizing operational parameters such as pressure drop, heat management, and mass transfer.[21] Hierarchical porous structures for housing nanomaterials such as the MOFs can be formed through extrusions, coatings, colloidal

media, and casting.[22] Regardless of the exact process, adsorbents have to withstand some amount of mechanical fatigue and/or stress. Binders are frequently employed to ameliorate these issues in inorganic porous material processing, as with clays and silicas, and are feasible options for MOFs as well.[23] In the relatively younger field of MOF research though, meaningful efforts investigating how framework mechanical stability affects subsequent uses, especially in applications concerning highly corrosive and reactive acid gases, has not been rigorously pursued.

In this chapter, the interplay between both MOF (1) stability and (2) adsorption performance is investigated. Experiments are pursued to further the understanding of how changes in MOF structures either provoke or negate degradation—if they are affected at all. Specifically, MOF design concerning both intentionally engineered point defects and installed reactive metal sites are probed. Consequences on resulting adsorbent stability and adsorption performance are studied for select frameworks. Also, the impact of MOF powder processing on acid gas capture and post-exposure stability is studied for sour gas remediation-relevant environments.

3.2 Materials and Methods

3.2.1 Synthesis and Materials Preparation

Synthesis instructions for various frameworks described here are provided below. With the exception of materials described in 3.2.1.3 and 3.2.1.4, all porous materials were degassed at 150°C for at least 24h under vacuum or inert purge prior to experiments. Materials in sections 3.2.1.3 and 3.2.1.4 were degassed at 65°C for at least 24h.

3.2.1.1 UiO-66

UiO-66(Zr) was synthesized through a scaled-up procedure based on Cavka et al.[24] Zirconium chloride (0.43mmol, 100mg) and terephthalic acid (0.43mmol, 71.3mg) were dispersed in 26.5 mL of N,N-dimethylformamide (DMF), and the mixture was heated at 120°C for 24h in a 60mL glass vial. The product was filtered and washed with DMF and then methanol three times each. Afterwards, the material was dried in a chemical hood overnight.

3.2.1.2 UiO-66-NH_2

UiO-66-NH_2(Zr) was made by adjusting previously reported procedures.[24,25] Equimolar amounts of $ZrCl_4$ (160 mg) and 2-aminoterephthalic acid (124 mg) were added to a 60mL glass vial. DMF was then introduced (26.5 mL), as well as 100 µL of DI water to improve product crystallinity. The vial was securely closed and placed in an isothermal oven at 120°C for 18h. Afterwards, the product was filtered and washed three times each with DMF, and then methanol.

3.2.1.3 UiO-66-COOH and UiO-66-$(COOH)_2$

Production of MOFs with uncoordinated -COOH moieties was achieved by using terephthalate based ligands with additional carboxylic acid groups; trimellitic acid and 1,2,4,5-benzenetetracarboxylic acid were used in the synthesis of UiO-66-COOH and UiO-66-$(COOH)_2$, respectively. The graphic in Figure 3-1 describes an idealized representation of how -COOH functionalities are integrated into the parent UiO-66(Zr) structure. Note actual structural aspects are significantly more complicated than what is represented in

Figure 3-1—the illustration is intended for descriptive purposes. A degas temperature of 65°C was utilized for UiO-66-COOH and UiO-66-$(COOH)_2$. Degas times were at minimum 24h, or until evacuating molecular guests could no longer be detected via mass spectroscopy of eluting species.

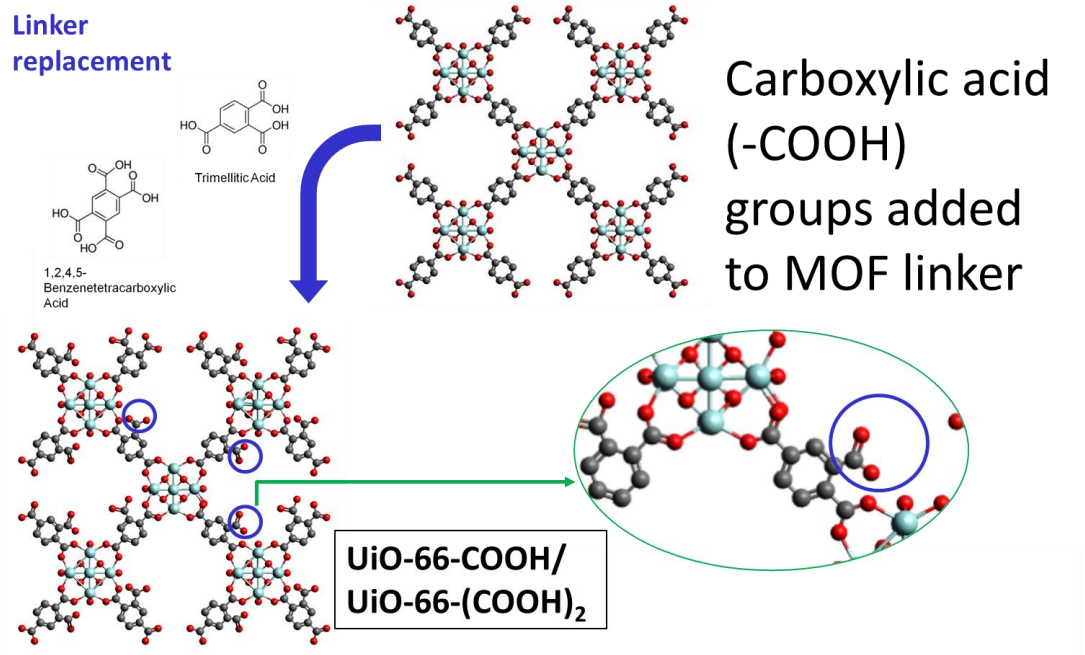

Figure 3-1: Graphical representation of installed, uncoordinated carboxylic acid groups on UiO-66(Zr) structure (parent UiO-66 structure reported by Cavka et al.).[24] Trimellitic and 1,2,4,5-benzenetetracarboxylic acid molecule images produced using ChemDraw software.

UiO-66-COOH was synthesized using a scaled-up procedure based on Biswas et al.[26] Zirconium oxynitrate hydrate (1.29 mmol, 300 mg), 1,2,4-Benzenetricarboxylic acid (2.58, 546 mg), and benzoic acid (38.82 mmol, 4.74 g), were added to N,N-dimethylformamide (116 mmol, 9 mL). The addition of 0.38% (v/v) of deionized water improves crystallinity of the resulting MOF, and has been noted elsewhere[27] to assist in producing highly ordered functionalized UiO-66 crystals. The reagent mixture was transferred without agitation to a stainless-steel lined PTFE reactor, and heated to 150°C

with a ramp rate of 2.2°C min^{-1}, and held isothermally for 24 h. The resulting solid was filtered and washed three times with DMF and methanol, and subsequently dried overnight in ambient conditions.

The synthesis for UiO-66-$(COOH)_2$ was scaled up from an original reported by Biswas et al.[28] N-N dimethylacetamide (DMA) was added (96.8 mmol, 9mL) to formic acid (95.4 mmol, 3.6mL). As with UiO-66-COOH, the addition of 0.38% (v/v) of deionized water was observed to improve the crystallinity of the final product. Equimolar amounts of zirconyl chloride octahydrate (0.93 mmol, 300 mg) and 1,2,4,5-benzenetetracarboxylic acid (0.93 mmol, 236.4 mg) were then added, and the reagents were transferred to Teflon-lined stainless-steel reactors, without stirring. The mixture was heated to 150°C with a ramp rate of 2.2°C min^{-1}, and afterwards, held isothermally for 24 h. The resulting solid was then washed three times with DMF, acetone, and methanol, and then left to dry overnight under ambient conditions.

3.2.1.4 Copper Insertion to Produce UiO-66-COOCu and UiO-66-$(COOCu)_2$

Copper containing UiO-66 analogues were created using parent UiO-66 samples created in this study. The naming convention is outlined for materials following metal incorporation and their corresponding parent materials in Table 3-1. The general approach for metal insertion has been pursued for metal incorporation into MOFs in previous work[29–31], which involves mixing the parent MOF and a metal salt solvothermally to enable transport of the target metal into the MOF pore system.

The presence of solvent has been suggested to impact metal incorporation into MOFs[32], so precursor MOFs were activated before metal insertion. A 0.1 M solution of

copper nitrate trihydrate (99% purity) in 25 mL N,N-dimethylformamide was prepared in a 60 mL glass scintillation vial. Respective parent MOFs summarized in Table 3-1 were added to the reagent mixture in a ratio of 7.6 mg MOF mL^{-1} solution (190 mg MOF for 25 mL of solution). The mixture was then transferred to an oil bath at 65°C, and gently stirred with a magnetic stir bar for 24 h to promote homogenous mixing of reactants.[33] The resulting MOFs were then filtered, washed, and activated according to the aforementioned procedures of the corresponding parent MOFs.

Table 3-1: Nomenclature for parent materials and corresponding MOFs post-metal insertion

Parent MOF	MOF After Copper Insertion
UiO-66-COOH	UiO-66-COOCu
UiO-66-$(COOH)_2$	UiO-66-$(COOCu)_2$

3.2.1.5 MIL-125(Ti)

MIL-125(Ti) was produced using a scaled-up technique by Tulig.[34] Terephthalic acid (500 mg) was placed in a 60 mL glass vial. Anhydrous DMF (8.6 mL) was then pipetted into the container. The mixture was briefly sonicated to disperse the ligand. Using a micropipette, 300 µL of dry titanium isopropoxide was added into the vial. 8.7 mL of methanol was introduced into the mixture last, immediately after the addition of the titanium precursor. The capped vial was then heated in an oil bath at 110°C for 24 h under vigorous stirring using a magnetic stir bar. This reaction was carried out in a chemical hood, as methanol slowly evaporates from the reaction vessel during the heating. The sample was then filtered and washed with DMF and then methanol three times each.

3.2.1.6 MIL-125-NH_2

Reagent amounts/ratios for the production of MIL-125-NH_2(Ti) were adapted from Dong and coworkers.[35] First, DMF and methanol were added in equal volumetric amounts (4.15 mL) into a 20 mL PTFE-lined autoclave, with a stainless steel casing. 2-aminoterephthalic acid was then placed in the solution (180 mg), and the mixture was sonicated for at least 5 minutes to disperse the linker. Immediately before sealing the reactor, 150 µL of dry titanium isopropoxide was micropipetted into the vessel. The final reactant solution was placed in an isothermal oven at 120°C for 24 h. The product was gravity filtered and washed with DMF and methanol three times each.

Defect installation experiments studied in Section 3.2.3 require acid modulators in MIL-125-NH_2 syntheses. A hypothetical illustration of possible structural changes in MIL-125-NH_2(Ti) through defect engineering is presented in Figure 3-2. The five acid modulators considered were (1) benzoic acid, (2) acetic acid, (3) trifluoroacetic acid, (4) hydrochloric acid, and (5) formic acid. Weights/volumes of modulators used in the 30:1 modulator to metal precursor molar ratio experiments are provided in Table A-1 as an example. Volumetric additions to synthesis baths were done using a micropipette. The only solid acid modulator, benzoic acid, was sonicated in the reaction solution until dissolution prior to the addition of linker and metal precursors to mitigate solvation issues. All other reaction procedures, reagent amounts, and post-synthesis treatments were kept the same as mentioned in the above paragraph. Experiments varying the concentration of benzoic acid and acetic acid were done by maintaining a constant concentration of titanium (IV) isopropoxide. Table A-2 shows the quantities used in these tests for each acid modulator. High benzoic acid masses required sonication of the reagent in the DMF/methanol mixture,

which was done prior to the addition of titanium isopropoxide and 2-aminoterephthalic acid, to avoid any resulting effects on MOF formation through this treatment.

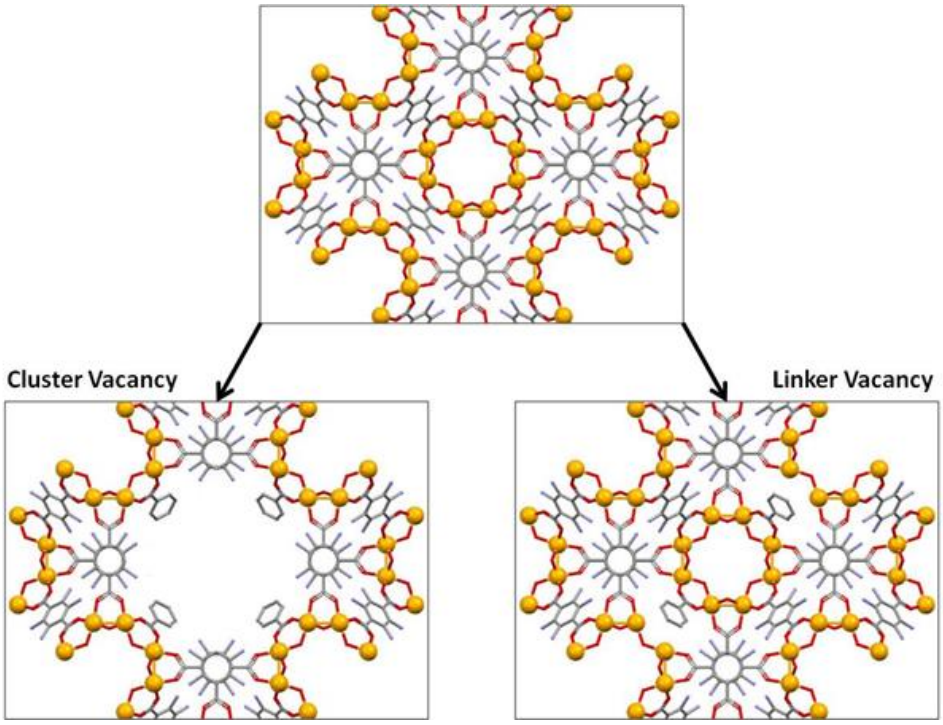

Figure 3-2: Illustration of point defects in MIL-125-NH_2(Ti). Top image shows MOF unit cell subsection. Bottom images delineate cluster and linker vacancies around central metal cluster. Color coding is as follows: gold-titanium, red-oxygen, grey-carbon, blue-nitrogen. Benzoic acid was chosen as the charge compensating modulator in this example

3.2.1.7 MIL-101(Cr)

MIL-101(Cr) was synthesized by scaling up the procedure found in Darunte et al.[36] by a factor of five. In a typical synthesis, chromium nitrate nonahydrate (4 g, 16.8 mmol) and terephthalic acid (1.64 g, 9.8 mmol) were mixed in 50 mL of deionized water and 7.5 mL of 36% acetic acid for 2h. Between 3-6 mg of previously synthesized MIL-101(Cr) were added as seed crystals prior to the mixing. The mixture was placed in a 100 mL Teflon lined reactor and heated at 200°C for 12h, followed by a programmed cooling to room

temperature at a rate of 1°C/min. The product was filtered and washed at ambient conditions with methanol six times, DMF three times, and finally methanol again three times. Following the washing step, the product dried in a chemical hood.

3.2.1.8 MIL-101-NH_2

MIL-101-NH_2(Cr) was produced similarly to a method detailed by Edler and coworkers.[37] 2-aminoterephthalic acid (1.14g) and $Cr(NO_3)_3x9H_2O$ (2.5g) were added to 35 mL of deionized water in a 45 mL PTFE-lined autoclave. Reagents were mixed vigorously using a magnetic stir bar for three hours. The reaction vessel was then sealed in a stainless-steel container, and held isothermally at 130°C for 24h. The assembly cooled to ambient temperature afterwards. Contents were first centrifuged and intermittently dispersed in DMF five times, then ethanol three times, and finally acetone three times. The product was then removed from the centrifuge tubes and dried in a well-ventilated chemical hood prior to activation.

3.2.1.9 Pelletization

In Section 3.2.5, UiO-66(Zr), UiO-66-NH_2(Zr), MIL-125(Ti), MIL-125-NH_2(Ti), MIL-101(Cr), and MIL-101-NH_2(Cr) were pressed into pellets to examine the impact of mechanical strain on H_2S stability. Materials were pelletized at a pressure of ~8000psig using a Carver brand powder press, and held for 10s to aggregate powder particles. MOF pellets were then gently sieved through 20 x 40 mesh (425μm-850μm) to attain uniform particle sizes. Note pellets were not crushed with a mortar before sieving, to prevent crystal damage. Instead, a laboratory spatula was used to gently abrade pellets against mesh wires.

3.2.2 Sample Characterization Methods

3.2.2.1 Attenuated Total Reflectance Fourier Transform Infrared Spectroscopy (ATR-FTIR)

Attenuated total reflectance (ATR-FTIR) spectra were acquired using a Thermo Scientific Nicolet iS50 spectrometer coupled with an iS50 ATR module. Dry KBr powder samples were utilized for background subtraction. Small amounts of unactivated MOF powders were placed under the ATR probe crystal after cleaning with isopropanol. Measurements were acquired through 128 scans, with a data resolution of $0.48 cm^{-1}$.

3.2.2.2 Nitrogen Physisorption at 77K

A Quantachrome Quadrasorb SI volumetric system with 5.11 QuadraWin™ software package was used to collect nitrogen adsorption data at 77K. Sample quantities between 5A-100mg (after degassing) were utilized in measurements. BET surface area measurements were approximated using a pressure range of $P/P_0 = 0.005–0.03$.[38]

Although MOF pore sizes are most accurately attained from crystal structure data, pore size distributions were determined for frameworks as well to lend qualitative comparisons. Distribution data are not intended to communicate quantitative changes in textural properties. Models utilized non-local density functional theory (NLDFT), assuming carbon surface with cylindrical pores.[39]

3.2.2.3 Powder X-ray Diffraction (PXRD)

Powder X-ray diffraction (PXRD) measurements were acquired using an X-Pert Pro PANanalytical X-ray diffractometer. The X-ray source was Cu Kα radiation: $\lambda = 1.542$ Å. Measurements were taken using a step size of 0.02° from $2\theta = 4°$- 40° for UiO-66(Zr) and MIL-125(Ti) materials and a step size of 0.01° from $2\theta = 2°$- 40° for MIL-101(Cr) materials.

3.2.2.4 Solution-State ^{1}H NMR

Proton NMR measurements were collected on MOF samples using a 400.13MHz Brucker Avance III 400 magnet. MOFs were activated according to their specified degassing conditions prior to measurement. Powders were first dissolved in approximately 7mL of 1M NaOH/D_2O overnight. Afterwards, 5mL of the mixture were introduced into a glass NMR tube. 64 ^{1}H scans were collected per sample. NMR data were processed using version 11.0 of MestreNova.

3.2.2.5 Water Vapor Adsorption

Water vapor adsorption measurements were conducted at 298 K and 1 bar. Temperature control was maintained using a water-cooled jacketed heat exchanger surrounding the stainless-steel bomb sample chamber. An intelligent gravimetric analyzer (IGA-3) was used for data collection. Samples were activated *in situ* at their respective activation conditions until sample weight loss was no longer observed. Tested materials were exposed to water vapor up to 90% RH, to avoid condensation. A total gas flow rate of 200 mL min^{-1} was used with a balance of dry nitrogen to generate humid gas mixtures.

3.2.3 Defect Engineering in MIL-125-NH_2(Ti)

Perfect crystals do not exist. For MOFs, intentional point defects may be installed during synthesis to modify material properties.[40] MOF defect engineering is predominantly reported for the zirconium-based framework UiO-66. UiO-66 ($Zr_6O_4(OH)_4(CO)_{12}$) possesses a cubic close-packed crystal arrangement, where octahedral zirconium metal clusters are 12-coordinated to oxygen atoms on surrounding terephthalic acid ligands.[24,41–43] This high degree of coordination partially explains structure and porosity retention despite "pristine" materials containing multiple point defect sites per unit cell.[40,44] These point defects, commonly missing framework ligands and/or metal clusters, are quantitatively and qualitatively observable through PXRD, N_2 physisorption, gravimetry, and NMR experiments.[45,46] Crystalline imperfections are fostered in UiO-66 through acid modulation. This method entails adding acidic reagents into synthesis batches to hinder ligand deprotonation and/or cap nucleating metal sites—both effects prevent metal-ligand coordination bonds to form.[47] Highly coordinated UiO-66(Zr) allows some control over the relative amount integrated point defects, which is dictated by the type and amount of acid modulator utilized.[48] Adsorption and stability behavior changes through defect tuning. For example, Ghosh et al. noted increased hydrophilia through markedly stronger water vapor adsorption heats in defective UiO-66(Zr) unit cells relative to their ideal counterparts.[6] Jiao et al. similarly uncovered a 20% SO_2 uptake increase in defective UiO-66(Zr) samples over parent materials, which retained structural stability.[39] However, adsorbents were no longer acid gas-stable when capping modulator molecules over missing-linker defect sites were removed—showing the potential sacrifice of chemical stability that can be manifested through defect incorporation.

Aside from a few investigations into ZIFs and HKUST-1, there is no direct extension of intentional defect creation from UiO-66 applied to other MOF systems.[49] MOFs with similar coordination environments, crystal structures, linkers, etc. are predicted to obtain crystalline defects similarly. MIL-125(Ti) accordingly lends itself as a great candidate for such a study. Titanium and zirconium as metal centers portray similar organometallic chemistry relevant to carbonyl reactivity involved in MOF formation.[50] Furthermore, MOFs formed from high-valency Group 4 transition metals are notorious for their chemical stability.[51] MIL-125 and UiO-66 both possess cubic structures, similar chemical and thermal stabilities, form nanoscale terephthalate crystals, and display permanent microporosity. More importantly for defect incorporation, MIL-125 possesses Ti^{4+} octahedral metal center clusters, that are 12-coordinated to terephthalate ligands, as with UiO-66(Zr).[24,52] Stability reports on MIL-125(Ti) materials are also intriguing—the material is reported stable under water vapor at 100°C and up to 10bar of acid gases CO_2 and H_2S.[53] Seperate work by Mounfield III et al. revealed MIL-125(Ti) degradation in humid and aqueous SO_2 environments, driven by the creation of defect sites within the MOF and MIL-125(Ti)-derived materials.[54,55] Interestingly an analogue of the MOF containing primary amine groups created using 2-aminoterepthalic acid ligands, MIL-125-NH_2(Ti), displays strong acid gas resistance.[53,55]

Possible control over engineering linker/cluster point defects in MIL-125-NH_2(Ti) could produce enhanced affinities and selectivities for acid gases by indirectly manipulating the ratio of $–NH_2$ /-OH groups within the structure. Additinoally, enhancements in pore volume seen in UiO-66(Zr) defect modulation studies would increase overall acid gas loadings in MIL-125-NH_2(Ti). However, stability trends for MIL-

125-NH_2(Ti) as a function of point defect sites must be studied to understand titanium framework tolerances towards harsh chemical environments. Furthermore, it is unknown if defects may even be incorporated into MIL-125(Ti) materials through acid modulation. Therefore, this section presents the first defect modulation study for MIL-125(Ti)-type materials, and explores the subsequent impact of incorporated defects on chemical stability.

3.2.3.1 Acid Modulation of MIL-125-NH_2(Ti)

Common acid modulators in UiO-66(Zr) synthesis literature were adapted for defective MIL-125-NH_2(Ti) production. Five frequently used modulators in UiO-66(Zr) modulation literature are benzoic acid[27,56,57,28], acetic acid[27,58,59], trifluoroacetic acid (TFA)[2,28,60], hydrochloric acid (HCl)[44,60-61], and formic acid[40,46]. These five compounds were used to synthesize MIL-125-NH_2(Ti) at various modulator (acid reagent) to metal precursor (titanium isopropoxide) molar ratios: 1:1, 15:1, 30:1, 60:1, 120:1, and 240:1. Synthesis information is provided in Section 3.2.1.6. Reactions yielding MOFs are highlighted in Table 3-2. Entries marked with framework retrieval denote extracted powder samples that contain internal porosity (detailed later). It appears the relative pK_a of acid modulators dictates MOF formation. A ranking of acidity is provided in Table A-3, where weaker benzoic and acetic acids allow MIL-125-NH_2(Ti) formation up to 30:1 molar ratios, but stronger acids do not. This was observed previously for UiO-66(Zr) production.[40] Powder production failure at high modulator concentration reactions is probably due to greater difficulty of terephthalic acid ligand deprotonation in lower pH solutions. This generates point defects at moderate levels but prevents framework construction altogether at high concentrations. TFA is an outlier with respect to MOF formation using HCl at a 1:1 concentration ratio. However, size exclusion effects around nucleating metal clusters may

have hindered MOF production with relatively large TFA molecules capping ligand-coordination sites versus ionic HCl modulators.

Table 3-2: Retrievable framework precipitates in MIL-125-NH_2(Ti) modulation reactions

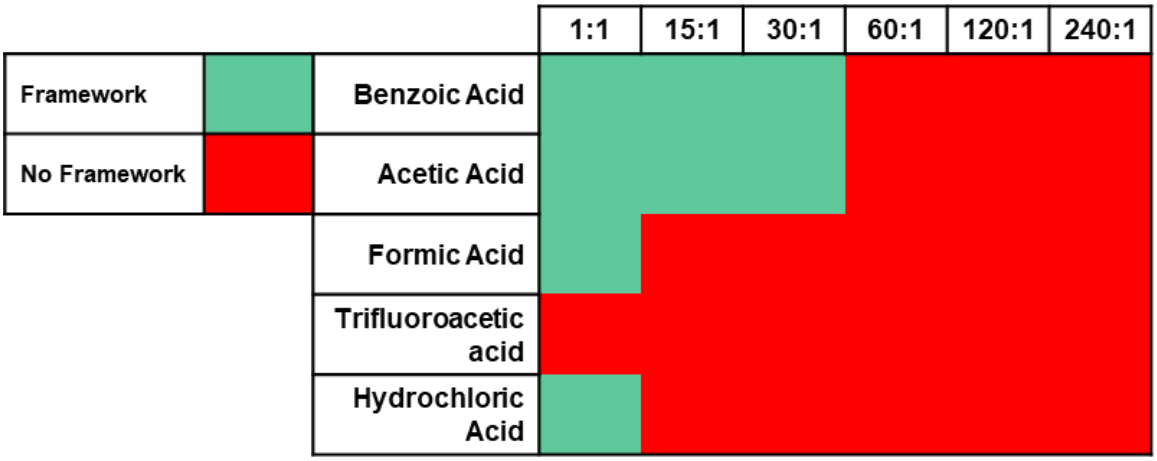

Although formic and hydrochloric acid-modulated samples yielded powders at 1:1 molar ratios, resulting materials possess lower accessible porosity than parent MIL-125-NH_2, as seen through N_2 uptake experiments at 77K (Figure 3-3a). TFA-produced samples were nonporous. Conversely, benzoic and acetic acid modulated samples showcase enhanced microporosities. Integrated point defects decrease framework density, in turn increasing mass-normalized N_2 uptake in the micropore regime (up to $P/P_0 \approx 0.05$).[38] Although porous materials were created using formic and hydrochloric acids, the stronger acid modulators disrupt formation of the pore network. Figure 3-3b affirms powders collected from reactions utilizing HCl and formic acid are largely amorphous, explaining their relatively low porosities in N_2 data.

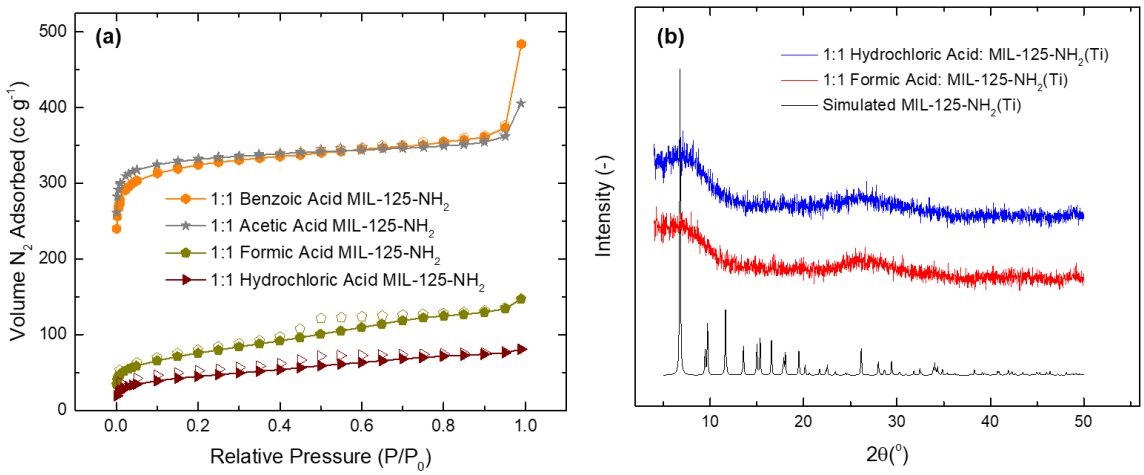

Figure 3-3: Textural properties of obtained powders from modulator concentration syntheses of MIL-125-NH_2(Ti). (a) N_2 adsorption curves at 77K for parent and 1:1 modulated MIL-125-NH_2 powders, (b) PXRD patterns for amorphous materials obtained from formic and hydrochloric acid modulation studies at 1:1 molar ratios, contrasted with simulated data[62]

Textural property changes in 30:1 modulator-to-metal precursor molar ratio samples were also investigated. Products that do not produce frameworks are visually distinct from yellow powdered MIL-125-NH_2(Ti) samples in Figure 3-4a. Interestingly, formic acid-modulated samples appear in-between the transition of yellow frameworks to red powders. This is consistent with the moderate pK_a of formic acid among tested reagents. It is notable that formate acidity ($pK_a \approx 3.75$) is comparable to that of 2-aminoterephthalic acid linkers ($pK_a \approx 3.95$)—benzoic and acetic acids have magnitude lower K_a values, and TFA and HCl are far more acidic. Framework formation hinderance appears largely predictable based on modulator acidity relative to coordinating ligand molecules. PXRD patterns for as-synthesized samples are contrasted with parent MIL-125-NH_2(Ti) in Figure 3-4b. Materials modulated with benzoic and acetic acid portray structural agreement with simulated and parent MOF diffraction patterns. A low intensity peak corresponding to the $2\theta = 6.7°$ in formic acid modulated MIL-125-NH_2(Ti) holds

semblance to (1 0 1) plane in MIL-125-NH_2(Ti).[62] However syntheses using formic acid, TFA, and HCl yield amorphous materials, in agreement with distinct orange and red powder colors from yellow MIL-125-NH_2(Ti). A new, broad reflection is present at 2θ = 22°-27° for formic acid and HCl modulated materials and also seen in Figure 3-3b. The feature is ascribed to amorphous carbon.[63] Results show synthesis modulation protocols utilized previously for UiO-66(Zr) are transferrable to the MIL-125(Ti) crystal system.

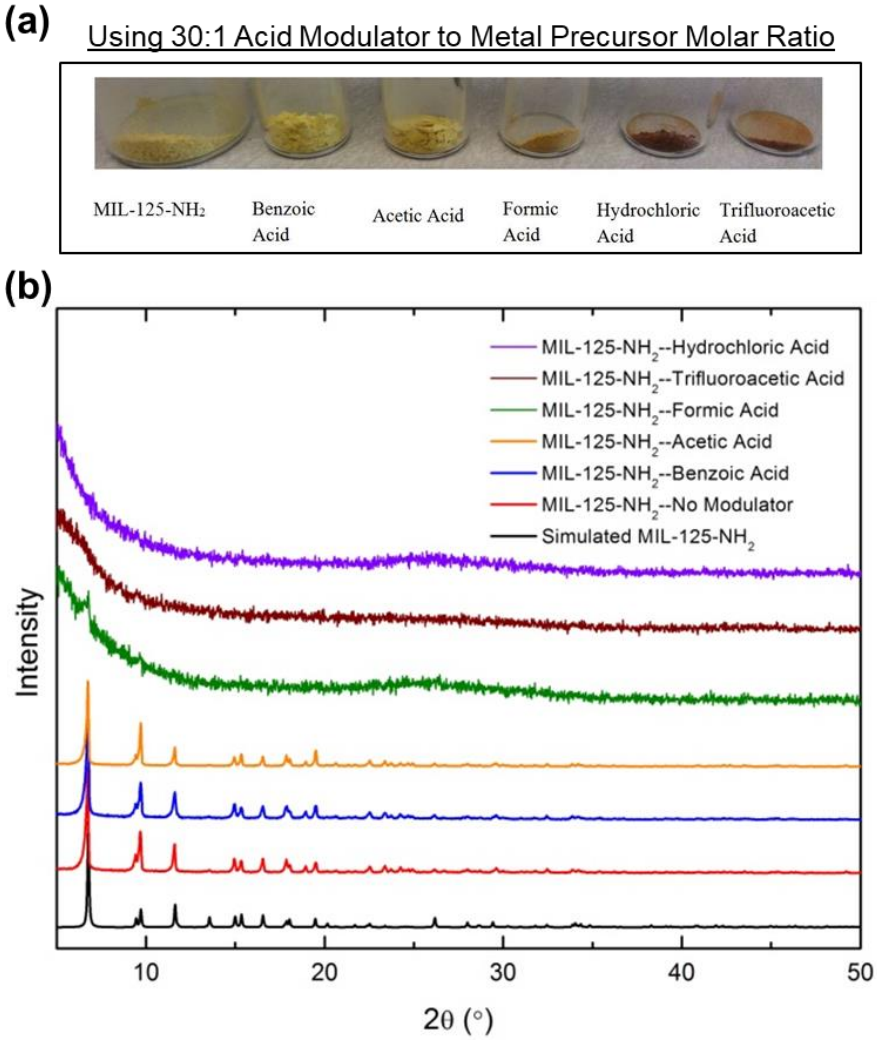

Figure 3-4: Modulation studies on MIL-125-NH_2 using a 30:1 modulator-to-metal precursor ratio. (a) Image of extracted precipitates, and (b) PXRD patterns of retrieved products along with simulated MIL-125-NH_2 scan from Smalley et al.[62]

3.2.3.2 Defect Tuning MIL-125-NH_2

Presented data in Figure 3-3 and Figure 3-4 suggest defect tuning in MIL-125-NH_2(Ti) is more promising when using acetic and benzoic acid as modulators, since porous crystalline products are retrievable at several different concentrations. As such, samples created with varying amounts of both modulators are further probed. Figure 3-5 shows accessible microporosity increases with acid modulator concentration. Pore volumes similarly increase. Lillerud and coworkers demonstrated the same behavior with UiO-66(Zr) modulation.[40] BET surface area measurements are within 5% of one another for materials modulated with acetic acid and benzoic acid at each test concentration. So, the effects of either modulator regarding pore accessibility are comparable. ^{1}H NMR data presented in Figure A-1, Figure A-3, and Figure 3-6 elucidate differences in modulator coordination. Characteristic resonances for BDC-NH_2 linkers in Figure 3-6a expectedly remain within parent MIL-125-NH_2(Ti). Doublets at 7.09ppm and 7.58ppm arise from neighboring protons on the phenyl ring of BDC-NH_2, 8.35ppm indicates carboxylic acids (reprotonated through ^{1}H exchange in solution), and the singlet at 7.15ppm is consequent of the adjacent proton to the primary amine group. Figure 3-6b indicates acetic acid is not present in MIL-125-NH_2(Ti) samples modulated with the reagent. Solvent or water-based capping species possibly displace acetic acid on unsaturated titanium sites. Figure 3-6c clearly distinguishes new features corresponding to benzoic acid from 7.50-7.33ppm when benzoic acid is employed as a modulator.[64] Peak integration (Figure A-3), shows the molar ratio of benzoic acid modulators to BDC-NH_2 linkers is approximately 1:12; a feasible ratio of defects for the 12-fold connected framework. NMR data importantly show benzoic acid remains in defective MIL-125-NH_2(Ti) structures, likely for charge compensation,

while acetic acid does not. Subsequently, slightly greater porosities in 30:1 benzoic acid-modulated samples over acetic acid can result from steric hinderance of coordinating BDC-NH_2 ligands from coordinated benzoates around titanium metal centers. Altogether, measurements show manipulating benzoic and acetic acid concentrations successfully tune relative amounts of point defects within MIL-125-NH_2(Ti).

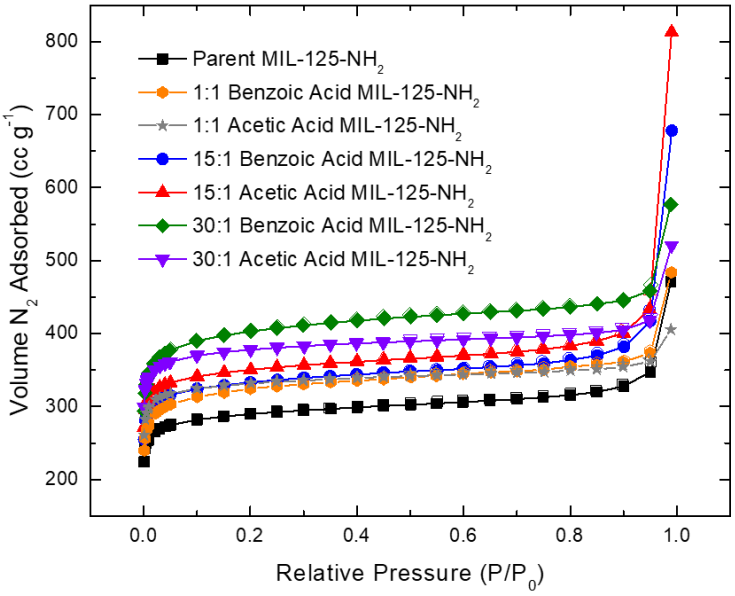

Modulator	Modulator : Metal Precursor Molar Ratio	BET Surface Area (m^2 g^{-1})	Total Pore Volume (cc g^{-1})
No modulator	N/A	1150	0.54
Acetic Acid	1:1	1331	0.54
	15 : 1	1393	0.67
	30 : 1	1513	0.65
Benzoic Acid	1:1	1269	0.55
	15 : 1	1324	0.65
	30 : 1	1579	0.71

Figure 3-5: Changes in porosity with acid modulation, depicted through N_2 adsorption curves taken at 77K (top) and corresponding BET surface area and pore volume calculations (bottom). Pore volumes estimated at P/P_0 = 0.8

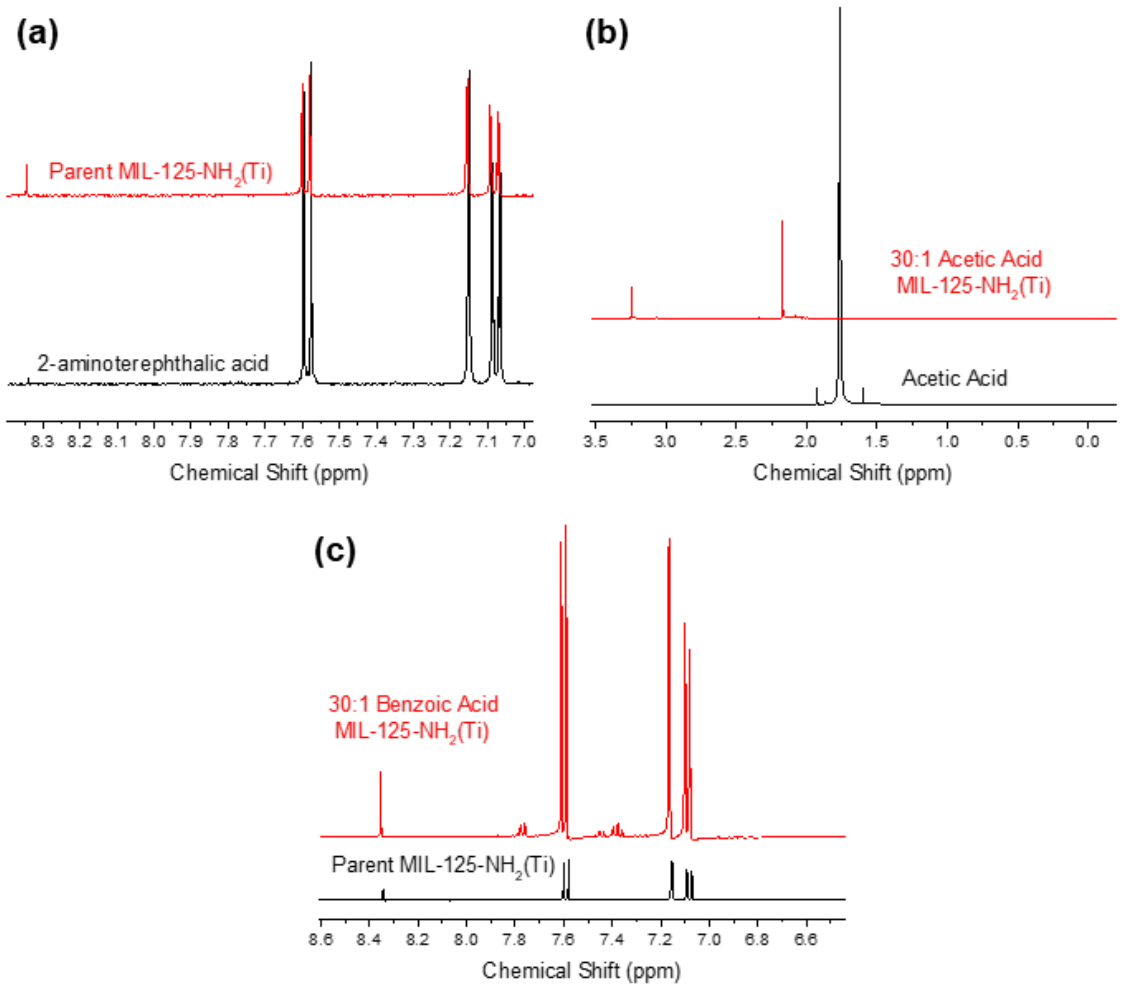

Figure 3-6: Solution ^{1}H NMR spectra of solvated MOF and reagent samples. a) comparison of BDC-NH_2 linker and solvated MIL-125-NH_2(Ti), b) comparison of 33% glacial acetic acid/D_2O with 30:1 acetic acid-modulated MIL-125-NH_2(Ti), comparison of 30:1 benzoic acid-modulated MIL-125-NH_2(Ti) to parent (non-modulated) MIL-125-NH_2(Ti).

3.2.3.3 Impact of MIL-125-NH_2(Ti) Defects on Water Vapor Stability

Benzoic acid-modulated samples were exposed to water vapor (up to 90% relative humidity) at 25°C to gauge changes in MIL-125-NH_2(Ti) adsorption performance with the integration of framework defects. In prior studies investigating defective UiO-66(Zr), water vapor affinity increased with defect concentration. This was caused by the reduction

of hydrophobic terephthalate ligands and greater available volume for water clustering within pores.[6] Isothermal adsorption measurements for defective MIL-125-NH_2(Ti) in Figure 3-7 unexpectedly go against previous observations. Water vapor loadings for defective MOFs at low partial pressures (20% RH) are over 80% lower than measured uptake for parent MIL-125-NH_2(Ti). Accordingly, defects enhance hydrophobicity in MIL-125-NH_2(Ti). The density of hydrophilic linker-based primary amine (-NH_2) and metal cluster-based hydroxyl (-OH) binding sites is lowered through defect modulation (e.g. missing linker defects, missing cluster defects). So, the removal of hydrophilic binding sites decreases water vapor affinity. Consequently, defect installation into MIL-125-NH_2(Ti) may be a synthesis strategy to enhance hydrophobicity from parent materials. This is useful for adsorbate selectivity over water vapor in humid environments. At higher water vapor pressures (> 30% RH), the relatively larger pore volumes of defective MIL-125-NH_2(Ti) samples foster larger uptake capacities. Water vapor loadings trend with relative defect quantity—the loading at 90% RH for the 30:1 benzoic acid modulated sample is ~7 mmol g^{-1} and ~10 mmol g^{-1} higher than observed for 1:1 modulated and parent MOF adsorbents, respectively. Absence of hysteresis upon desorption in Figure A-4 confirms reversible binding interactions remain, despite the enhanced accessibility of H_2O(v) into the framework.

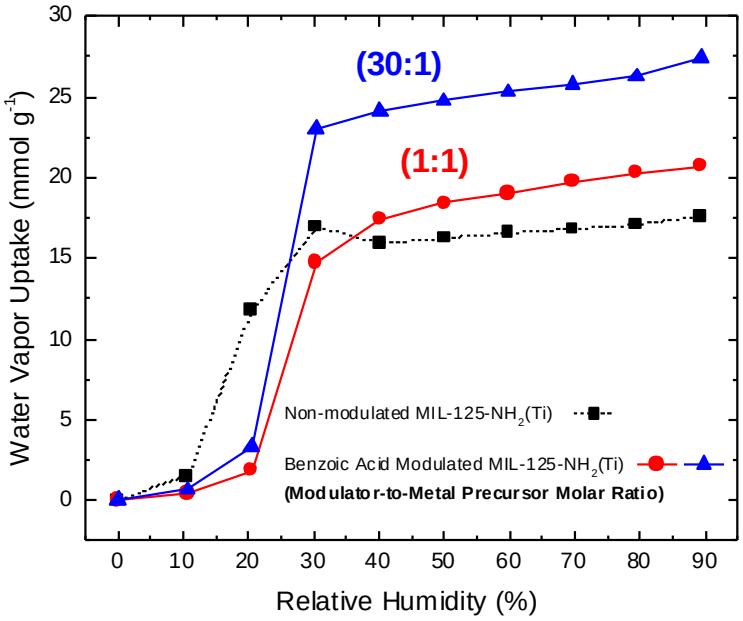

Figure 3-7: Water vapor adsorption measurements on MIL-125-NH_2(Ti) samples. Taken at 25°C. Dashed line represents non-modulated MOF sample. Lines are only intended to guide the eye

MIL-125-NH_2(Ti) remains structurally stable in both humid and corrosive aqueous environments.[55] However, this chemical stability is altered in the presence of defects. Post-water vapor exposed 1:1 benzoic acid modulated MIL-125-NH_2(Ti) shows significant changes in crystallinity in Figure 3-8. Although characteristic diffraction peaks are still discernable for the modulated MOF, their stark decrease in intensity and broadening indicates diminished long-range order and introduced microstrain. Apparent decreases in microporosity and pore volume are also observed from N_2 adsorption curves in Figure 3-8 following water vapor uptake experiments. Pre-exposure BET surface area of 1269 m^2 g^{-1} falls to 700 m^2 g^{-1} after humid exposure. These data sets indicate the inherent chemical stability of MIL-125-NH_2(Ti) is lost when point defects are introduced. Previous DFT investigations on non-functionalized MIL-125(Ti) suggest H_2O molecules displace Ti-O framework bonds, effectively creating dangling linkers.[50] A similar mechanism is plausible

in isostructural MIL-125-NH_2(Ti) studied here. Higher defect quantities enhance the accessibility of water vapor molecules, which garner closer proximity to titanium metal clusters.

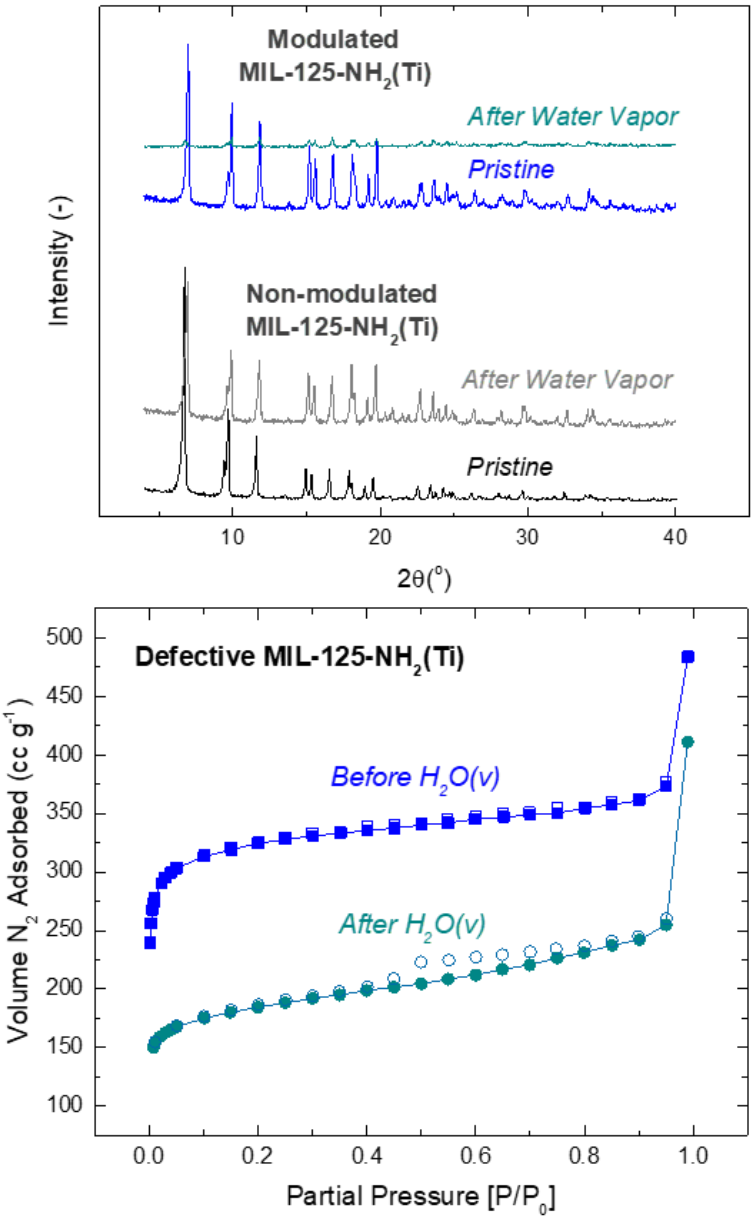

Figure 3-8: MIL-125-NH_2(Ti) samples before and after water vapor exposure (up to 90% RH) at 25°C. PXRD patterns for parent and 1:1 benzoic acid modulated MOF (top) and N_2 physisorption curves acquired at 77K for defective MIL-125-NH_2(Ti) (bottom)

3.2.3.4 Summary: Defect Engineering in MIL-125-NH_2(Ti)

For the first time, defects were intentionally engineered into MIL-125-NH_2(Ti). Traditional acid modulation strategies from previous UiO-66(Zr) literature were successfully applied to MIL-125-NH_2(Ti) production. This demonstrates the extendibility of modulation techniques across different crystal structures and metal-ligand coordination chemistries. For tested modulator concentrations, lower acidity reagents such as benzoic and acetic acid provide greater tolerance over allowing MOF formation and tuning relative defect amounts. Accessible surface area and pore volume are enhanced by increasing modulator amounts. But modulator concentrations exceeding 30:1 failed to yield MIL-125-NH_2(Ti) for tested acid reagents. Data provided here lend synthesis heuristics for manipulating the textural properties of MIL-125(Ti)-type materials. The removal of hydrophilic binding sites through defect incorporation likely decreases water vapor affinity for modulated samples. This was coupled with a loss of characteristic water stability after defect incorporation—indicating chemical susceptibility of MIL-125-NH_2(Ti) is affected by framework connectivity. As point defects are added, it is probable Ti-O framework linkages become more accessible. Hydrophilic binding sites on pendant linkers (e.g. -NH_2) are also lost upon modulation, which likely increases the local density of unbound water molecules available to attack framework bonds. Overall structural engineering impacts on adsorption and stability for titanium-based frameworks are summarized by collected data.

3.2.4 Stable Acid Gas Chemisorption Sites Through Ligand-based Carboxylic Acid Metalation

Although not always true, a standard assumption for MOFs containing coordinatively unsaturated metal sites is they are chemically unstable in most process situations. Unfortunately, practical scenarios often include water vapor and/or acid gases, which are pervasive in gas separation processes. Instability typically stems from localized chemisorption on the same metal centers responsible for bridging framework ligands. Connections between MOF ligands become displaced during the adsorption process from attacking adsorbate molecules. Tuning the chemistry around reactive metal sites can therefore manipulate adsorbent stability. By replacing relative amounts of Mg^{2+} metal centers with relatively inert Ni^{2+} and Co^{2+} in mixed-metal MOF-74 analogues, Walton and coworkers demonstrated how simply decreasing the density of "unstable" metal centers bolsters overall kinetic stability.[65] In general, methods of exchanging labile metal centers with higher valency ions improves structural resiliency.[66] Morris and coworkers alternatively installed sacrificial bonds in typically unstable HKUST-1, where non-structural bonds are attacked by reactive adsorbates instead of accessible metal sites—preserving framework linkage through hemilability.[67] Discovering methods to mitigate degradation while encouraging irreversible binding interactions would greatly justify the employment of MOFs into the corrosive and harsh environments often encountered in acid gas remediation processes.

An alternative methodology explored here is delineated in Figure 3-9. Reactive metal sites are scaffolded on ligand functionalities, so MOF metal centers no longer serve as primary adsorption sites. Through this method, strong gas adsorption is directed onto

pendant ligand-based sites without compromising adsorbent stability. This ligand metalation technique has been pursued on stable zirconium[68,69] and aluminum[70] framework platforms. For the MOFs investigated here, post-synthetic modification of uncoordinated carboxylic acid sites was performed to create copper carboxylate (-COOCu) functionalities.[71–73] Resulting frameworks (naming convention in Table 3-1) portrayed significant enhancements in ammonia sequestration; up to 125% increase going from non-functionalized UiO-66-$(COOH)_2$ to UiO-66-$(COOCu)_2$. Accessible Cu^{2+} sites allowed chemical bonding of ammonia guest species, even at low (~1000ppm) concentrations. Because functionalities reside in the sub-nanometer windows of UiO-66(Zr), interactions between chemical groups and small molecules are encouraged. To probe the extendibility of reactive copper carboxylate moieties as chemisorption sites for small molecules, the same modification procedure is employed here to create UiO-66-COOCu and UiO-66-$(COOCu)_2$ to instill irreversible acid gas uptake.

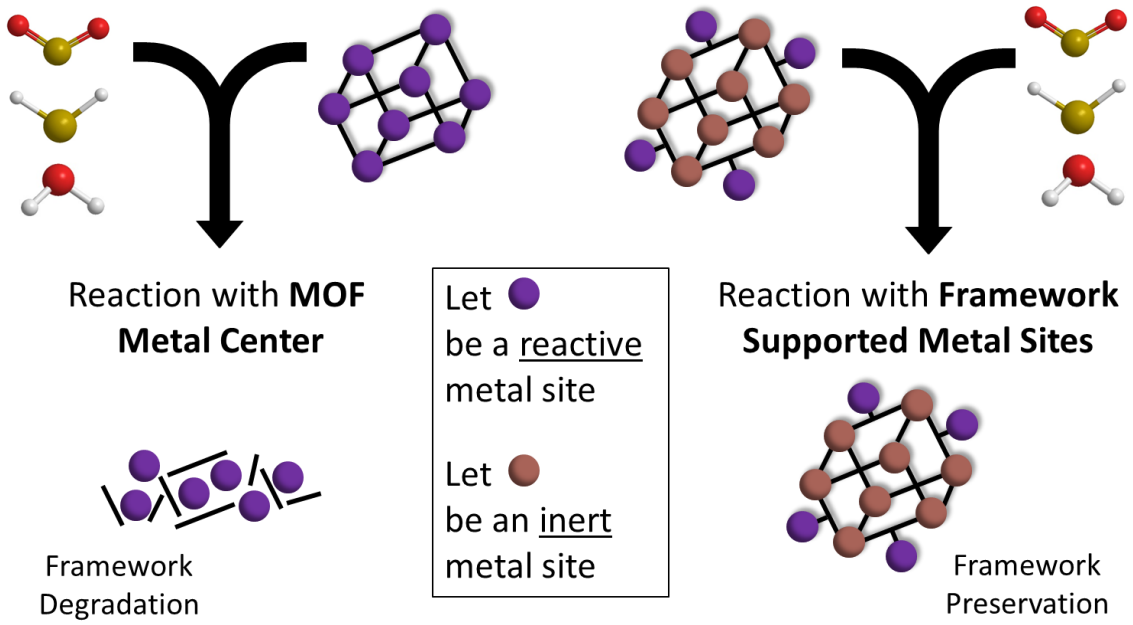

Figure 3-9: Cartoon motivating installation of reactive metal sites on ligand functionalities. Molecules on upper right- and left-hand side of graphic were created using ChemDraw, and represent sulfur dioxide, hydrogen sulfide, and water Molecules are intended to represent adsorbates that would bind chemically with reactive metal sites

PXRD patterns for metalated MOFs in Figure A-5 (crystallography detailed further in Chapter 4) show modified materials remain stable and isostructural to parent frameworks. ATR-FTIR spectra of UiO-66-$(COOH)_2$ and UiO-66-$(COOCu)_2$ in Figure 3-10 reveal an interesting inversion of the in-plane -OH bending mode of uncoordinated carboxylic acid (1426cm^{-1}) and symmetric -COO^- stretches (1383cm^{-1}).[64] Other framework features (vibrational modes assigned in Table A-4) remain consistent with one another—unperturbed by metalation. The -OH bend assignment is further supported by exceedingly low peak intensity in the ATR spectrum for UiO-66(Zr) in Figure A-6, due to the absence of uncoordinated -COOH groups in the parent framework (some result from point defects). The ratio between the -OH bending mode and -COO^- stretch decreases after metalation. This suggests proton displacement by coordinating copper atoms on "free" carboxylic acid

groups within the framework, and agrees well with previous examinations of UiO-66-COOCu and UiO-66-$(COOCu)_2$ via XAS and XPS.[71] A similar overlay of ATR spectra for UiO-66-COOH and UiO-66-COOCu are shown in Figure A-7.

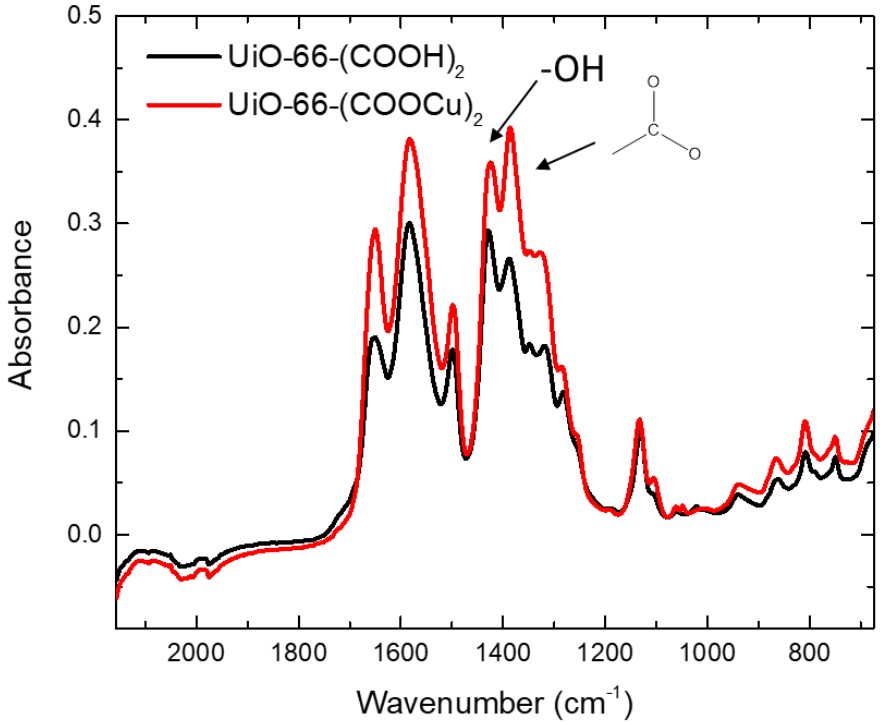

Figure 3-10: Inset of ATR-FTIR spectra for UiO-66-$(COOH)_2$ before (black) and after (red) copper coordination. "-OH" label assigns in-plane hydroxyl bending mode of carboxylic acid. Carboxylic acid structure is intended to assign symmetric -COO^- stretching mode

3.2.4.1 Acid Gas Stability of Metalated MOFs after Acid Gas Exposure

UiO-66-COOCu and UiO-66-$(COOCu)_2$ were exposed to dilute (< 1%) streams of SO_2 and H_2S. Adsorption/exposure experiments are detailed in Chapter 4. Copper carboxylate-containing MOFs did not react with SO_2 at tested pressures. Unsurprisingly, no observable framework damage occurred. Lack of strong SO_2 uptake was also noted for unsaturated copper carboxylate-containing HKUST-1 at even higher pressures (up to 3

bar), supporting an absence of strong reactivity for the chemical pair.[74] Negligible changes through post-exposure N_2 uptake in Figure 3-11 support this. Apparent H_2S chemisorption did occur however for both frameworks. H_2S reactivity is supported in Figure 4-9 (Chapter 4) where originally blue MOF adsorbents become black upon H_2S exposure, due to copper sulfide formation. Cu^{2+} is Lewis acidic. In this instance, the acid gas H_2S likely behaves as a Lewis base—two lone-pair electrons of the sulfur atom are donated to accessible Cu^{2+} acceptor sites throughout UiO-66-COOCu and UiO-66-$(COOCu)_2$. Previous literature on the copper carboxylate MOF HKUST-1 shows the same color change, which was attributed to CuS production through spectroscopic methods, and coupled with framework collapse from displaced metal-ligand coordination bonds.[75,76] In this case however, post-exposure N_2 measurements in Figure 3-11 evidence only slight decreases in microporosity. Diffraction patterns of MOFs after H_2S exposure in Figure A-8 do not evidence crystal structure damage. So, minute decreases in N_2 uptake at 77K after H_2S adsorption are likely due to the small increase in framework density from sulfur deposition onto UiO-66-COOCu and UiO-66-$(COOCu)_2$, and not structure collapse.

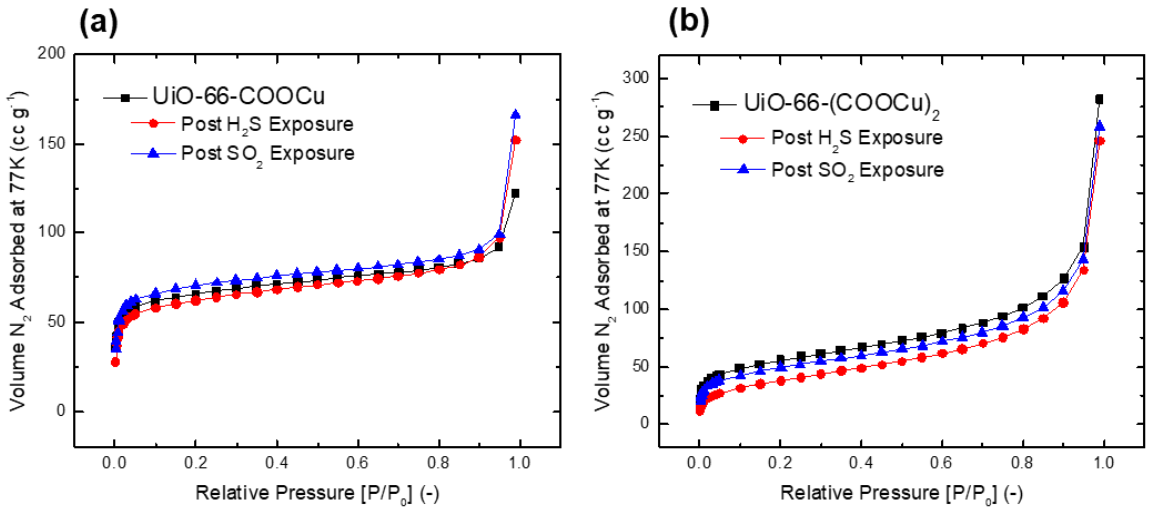

Figure 3-11: N_2 adsorption curves for (a) UiO-66-COOCu and (b) UiO-66-$(COOCu)_2$ before (black) and after H_2S (red) & SO_2 (blue) fixed-bed experiments. Acquired at 77K

3.2.4.2 Summary: Stable Acid Gas Chemisorption Sites Through Ligand-based Carboxylic Acid Metalation

A methodology for scaffolding ligand-based metal chemisorption sites was extended to address challenges in fostering irreversible acid gas removal.[68,71] Uncoordinated carboxylic acid sites in parent frameworks UiO-66-COOH and UiO-66-$(COOH)_2$ were functionalized with Cu^{2+} to create copper carboxylate functionalities (-COOCu). The incorporation of metal cation-based reaction sites, studied through various characterization techniques here and in previous literature[69,71] exemplifies how ligand-based carboxyl groups are easily tailored into useful binding sites. Reactivity parameters of added sites are consistent with previous studies concerning open metal site MOFs; H_2S reactivity >> SO_2 reactivity on -COOCu sites concurs with literature on MOFs containing -COOCu groups within their inherent framework structure (i.e. HKUST-1). Accordingly, literature on open-metal site MOFs and their reactivity with candidate adsorbent-metal site

pairs guide how reactive select adsorbents may be with ligand-based metal carboxylates. This was demonstrated here through prior observations on HKUST-1 and pendant -COOCu functionalities with SO_2 and H_2S. Finally, the strong chemisorption of H_2S with both UiO-66-COOCu and UiO-66-$(COOCu)_2$ did not provoke adsorbent degradation. As hypothesized, Zr-metal centers in UiO-66(Zr)-type frameworks were not primary acid gas adsorption sites. So, framework stability was not sacrificed to leverage strong acid-base adsorption interaction afforded by unsaturated metal cations. The adsorption performance of the studied frameworks is detailed later in Chapter 4, Section 4.3.1.

3.2.5 Relationships Between MOF Mechanical and Chemical Stability Towards Hydrogen Sulfide

As mentioned in Section 3.1, MOFs are often probed as pristine systems. Impacts of various post-synthesis modifications (e.g. powder processing, integration onto hierarchical media, recycling) are not aggressively explored. Typically, nanoscale adsorbents are only application-relevant as macroscopic products, which need to possess resistance towards both external mechanical and chemical stresses.[22] The latter is especially true for acid gas-containing environments. Evidence exists to affirm interplay between mechanical and chemical stability for adsorbent systems. Jones and coworkers noted a pressure dependence on the porosity and CO_2 removal performance of amino-coated alumina and aminosilane powders post-pressing.[77] In one of the few reports concerning this matter on MOFs, Walton and coworkers examined the impact of pelletizing HKUST-1 and UiO-66(Zr) on subsequent adsorption properties.[78] Only the accessible surface area of HKUST-1 decreased through tested pelletization pressures (up to 10,000psi), where UiO-66(Zr) did not exhibit changes. Therefore, different frameworks

portray disparate mechanical stability properties. Physical adsorption performance of UiO-66(Zr) still decreased in samples following pelletization, even though structural degradation was not evident. Accordingly, changes not clearly discerned in long-range order or porosity can still manifest in frameworks which experience mechanical stress. Pressing binders with MOFs can mitigate detrimental effects, but sacrifices mass-normalized surface area and adsorption properties of adsorbents within composites.[23]

Prior work shows a considerable collection of MOFs showcase acid gas stability as pristine, non-pelletized powders.[16,17,53,79,80] But there are no studies concerning MOF stability in acid gases following pelletization. Including powder processing steps provides a more realistic evaluation of adsorbent acid gas stability. Accordingly, a series of frameworks that were previously shown to be stable under H_2S exposure were investigated: UiO-66(Zr), MIL-101(Cr), and MIL-125(Ti). Their respective primary amine ($-NH_2$) analogues were also investigated[55–57], and constructed using 2-aminoterephthalic acid as a framework ligand. Pelletization procedures are described above in Section 3.2.1.9.

3.2.5.1 Pelletization Effects on Crystal Structure and Acid Gas Stability

Acid gas stability of the candidate frameworks was probed to ascertain the efficacy of these materials as reusable adsorption media. Diffraction patterns for pristine materials before and after H_2S exposure are presented to elucidate possible structural degradation in Figure 3-12a. It should be stated that samples were exposed to the ambient air following H_2S exposure, which could have affected their subsequent characterization (e.g., atmospheric water vapor exposure). There is no observable change in crystallinity for any powder samples after exposure. Figure A-9, Figure A-10, and Table A-5 show pelletization

and subsequent H_2S exposure does not affect the diffraction patterns or accessible surface areas of UiO-66(Zr), UiO-66-NH_2(Zr), MIL-125(Ti), or MIL-125-NH_2(Ti). However, sample pelletization did change the diffraction pattern for MIL-101(Cr). Figure 3-12b evidences microstrained crystalline features between $2\theta = 2\text{-}5°$ for MIL-101(Cr) and MIL-101-NH_2(Cr) after pelletization. These low-angle peaks are furthermore absent in the pattern for MIL-101(Cr) after H_2S exposure. Decreased N_2 uptake at 77K after pelletization in Figure A-11 and Figure A-12 support structural damage observations. Table A-5 additionally indicates BET surface areas for MIL-101(Cr) materials significantly decrease after pelletization. Qualitative changes after pelletization are also apparent in the pore size distributions for MIL-101(Cr)-type MOFs in Figure A-15 to Figure A-17. A relatively larger porosity loss is experienced for these pelletized samples after acid gas exposure in Figure A-12, in comparison to their pristine counterparts. Pelletized MIL-101(Cr) exhibits a 10% loss in BET surface area, greater than that seen with MIL-101-NH_2(Cr). These results show the pelletization process partially destroys the MIL-101(Cr) framework, and in-turn compromises the characteristic acid gas stability of the material. Post-exposure N_2 uptake curves for pelletized UiO-66(Zr)- and MIL-125(Ti)-type frameworks are unaffected (Figure A-13 and Figure A-14). Changes in structure-property relationships in other porous structured adsorbents through similar processing have been examined as well.[22,77] Walton and Sholl[84] recently remarked on the importance of investigating industrially relevant processing procedures on materials discussed in academic work, and pelletization is often required for powder adsorbents in packed-bed columns.[85] Subsequently, this observation recognizes how the H_2S adsorption potential and stability of MIL-101(Cr) is susceptible to change through pre-exposure processing steps. Decreased adsorption potential is most

obvious from the measured sharp decrease in accessible pore space, as compared to the pristine framework. Observed structural changes may lead to further chemically-induced degradation in the presence of other possible natural gas species, such as water vapor.

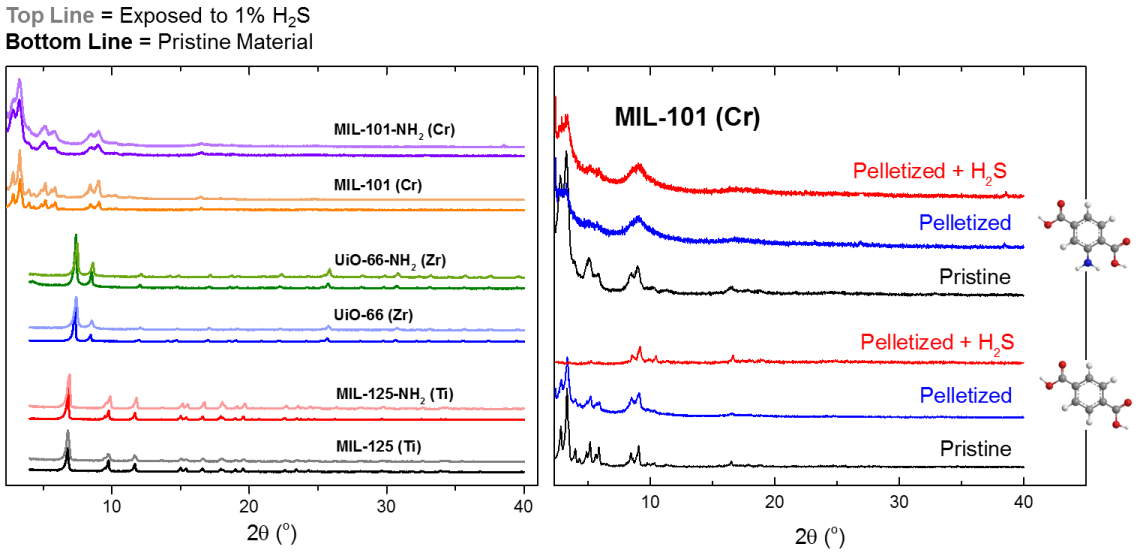

Figure 3-12: Powder diffraction patterns of pristine and 1% H_2S exposed samples (right), and powder diffraction patterns of MIL-101 (Cr) and MIL-101-NH_2 (Cr) before and after pelletization and subsequent 1% H_2S exposure (left). Exposures conducted at ambient conditions. BDC and BDC-NH_2 linkers on left-hand side graphic denote patterns corresponding to parent and amine functionalized MOFs, respectively

3.2.5.2 Summary: Relationships Between MOF Mechanical and Chemical Stability Towards Hydrogen Sulfide

Despite exhibiting acid-gas stability as a pristine material, degradation of pelletized MIL-101(Cr) and MIL-101-NH_2(Cr) after acid gas exposure suggests these adsorbents may not be pragmatic choices in large scale adsorption operations requiring similar material processing. Relationships between mechanical and chemical stabilities are understudied in current MOF literature. So, these observations demonstrate how the interplay between

these two properties exact important consequences on materials used for adsorption-based separations.

This short study precedes the investigation of sour gas-relevant adsorption properties for candidate H_2S adsorbents discussed later in Chapter 4. Frameworks display different mechanical stabilities from one another based on their intrinsic structural properties. The high interconnectivity of UiO-66(Zr) and MIL-125(Ti) and relatively stronger metal-carboxylate bonding from 4+ valency cations probably contributed to their resilience under pelletization at pressures tested here. Contrasting chemical stability behaviors between pristine and pelletized MIL-101(Cr)-type materials exemplifies the strong influence of powder processing on acid gas stability. Readers should note conducting this evaluation on pristine MIL-101(Cr) powders alone would falsely identify these frameworks as stable under otherwise relevant H_2S removal test conditions. As a result, the intent for studying processed MOF adsorbents here is to promote the dissemination of pragmatic and realistic MOF stability information. This select example serves as a critical demonstration of inspecting adsorbents in their practical, end-use form, rather than as idealized nanoscale powders.

3.3 Chapter 3 References

1. Sholl, D. S. & Lively, R. P. Defects in Metal-Organic Frameworks: Challenge or Opportunity? *J. Phys. Chem. Lett.* **6**, 3437–3444 (2015).
2. Fang, Z., Bueken, B., De Vos, D. E. & Fischer, R. A. Defect-Engineered Metal-Organic Frameworks. *Angew. Chemie Int. Ed.* **54**, 7234–7254 (2015).
3. Han, R. & Sholl, D. S. Computational Model and Characterization of Stacking Faults in ZIF-8 Polymorphs. *J. Phys. Chem. C* **120**, 27380–27388 (2016).
4. Thornton, A. W., Babarao, R., Jain, A., Trousselet, F. & Coudert, F. X. Defects in metal-organic frameworks: A compromise between adsorption and stability? *Dalt. Trans.* **45**, 4352–4359 (2016).

5. Burtch, N. C., Jasuja, H. & Walton, K. S. Water Stability and Adsorption in Metal-Organic Frameworks. *Chem. Rev.* **114**, 10575–10612 (2014).

6. Ghosh, P., Colón, Y. J. & Snurr, R. Q. Water Adsorption in UiO-66: The Importance of Defects. *Chem. Commun.* **50**, 11329–11331 (2014).

7. Nijem, N., Fursich, K., Bluhm, H., Leone, S. R. & Gilles, M. K. Ammonia Adsorption and Co-adsorption with Water in HKUST-1: Spectroscopic Evidence for Cooperative Interactions. *J. Phys. Chem. C* **119**, 24781–24788 (2015).

8. Soubeyrand-Lenoir, E. *et al.* How Water Fosters a Remarkable 5-Fold Increase in Low-Pressure CO_2 Uptake within Mesoporous MIL-100(Fe). *J. Am. Chem. Soc.* **134**, 10174–10181 (2012).

9. Jasuja, H., Peterson, G. W., Decoste, J. B., Browe, M. a. & Walton, K. S. Evaluation of MOFs for air purification and air quality control applications: Ammonia removal from air. *Chem. Eng. Sci.* **124**, 118–124 (2015).

10. Abatzoglou, N. & Boivin, S. A review of biogas purification processes. *Biofuels, Bioprod. Biorefin.* **3**, 42–71 (2009).

11. Siefers, A. M. A Novel and Cost-Effective Hydrogen Sulfide Removal Technology Using Tire Derived Rubber Particles. *Iowa State University Digital Repository*. MS Thesis. (Iowa State University, 2010)

12. Fauteux-Lefebvre, C., Abatzoglou, N., Braidy, N. & Hu, Y. Carbon Nanofilaments Functionalized with Iron Oxide Nanoparticles for in-Depth Hydrogen Sulfide Adsorption. *Ind. Eng. Chem. Res.* **54**, 9230–9237 (2015).

13. Parkinson, G. S. Iron Oxide Surfaces. *Surf. Sci. Rep.* **71**, 272–365 (2016).

14. Reshetenko, T. V., Khairulin, S. R., Ismagilov, Z. R. & Kuznetsov, V. V. Study of the reaction of high-temperature H_2S decomposition on metal oxides (γ-Al_2O_3, α-Fe_2O_3, V_2O_5). *Int. J. Hydrogen Energy* **27**, 387–394 (2002).

15. Huang, G. *et al.* Synthesis and Characterization of γ-Fe_2O_3 for H_2S Removal at Low Temperature. *Ind. Eng. Chem. Res.* **54**, 8469–8478 (2015).

16. Hamon, L. *et al.* Comparative Study of Hydrogen Sulfide Adsorption in the MIL-53 (Al, Cr, Fe), MIL-47 (V), MIL-100 (Cr), and MIL-101 (Cr) Metal- Organic Frameworks at Room Temperature. *J. Am. Chem. Soc.* **131**, 8775–8777 (2009).

17. Liu, J., Wei, Y., Li, P., Zhao, Y. & Zou, R. Selective H_2S/CO_2 Separation by Metal−Organic Frameworks Based on Chemical-Physical Adsorption. *J. Phys. Chem. C* **121**, 13249–13255 (2017).

18. Watanabe, T. & Sholl, D. S. Molecular chemisorption on open metal sites in Cu_3 (benzenetricarboxylate)$_2$: A spatially periodic density functional theory study. *J. Chem. Phys.* **133**, 094509 (2010).

19. Kim, K. C. Design strategies for metal-organic frameworks selectively capturing harmful gases. *J. Organomet. Chem.* **854**, 94–105 (2018).

20. Sumida, K. *et al.* Carbon Dioxide Capture in Metal–Organic Frameworks. *Chem. Rev.* **112**, 724–781 (2012).

21. Shekhah, O., Liu, J., Fischer, R. A. & Woll, C. MOF thin films: existing and future applications. *Chem. Soc. Rev.* **40**, 1081–1106 (2011).

22. Akhtar, F., Andersson, L., Ogunwumi, S., Hedin, N. & Bergström, L. Structuring adsorbents and catalysts by processing of porous powders. *J. Eur. Ceram. Soc.* **34**, 1643–1666 (2014).

23. Valekar, A. H. *et al.* Shaping of porous metal–organic framework granules using mesoporous ρ-alumina as a binder. *RSC Adv.* **7**, 55767–55777 (2017).

24. Cavka, J. H. *et al.* A new zirconium inorganic building brick forming metal organic frameworks with exceptional stability. *J. Am. Chem. Soc.* **130**, 13850–13851 (2008).

25. Schoenecker, P. M., Belancik, G. A., Grabicka, B. E. & Walton, K. S. Kinetics study and crystallization process design for scale-up of UiO-66-NH_2 synthesis. *AIChE J.* **59**, 1255–1262 (2013).

26. Biswas, S. *et al.* Enhanced selectivity of CO_2 over CH_4 in sulphonate-, carboxylate- and iodo-functionalized UiO-66 frameworks. *Dalt. Trans.* **42**, 4730–4737 (2013).

27. Schaate, A. *et al.* Modulated synthesis of Zr-based metal-organic frameworks: from nano to single crystals. *Chem. Eur. J.* **17**, 6643–51 (2011).

28. Biswas, S. & Van Der Voort, P. A general strategy for the synthesis of functionalised UiO-66 frameworks: Characterisation, stability and CO_2 adsorption properties. *Eur. J. Inorg. Chem.* 2154–2160 (2013). doi:10.1002/ejic.201201228

29. Guo, Z. *et al.* Pt Nanoclusters Confined within Metal–Organic Framework Cavities for Chemoselective Cinnamaldehyde Hydrogenation. *ACS Catal.* **4**, 1340–1348 (2014).

30. Tulig, K. & Walton, K. S. An alternative UiO-66 synthesis for HCl-sensitive nanoparticle encapsulation. *RSC Adv.* **4**, 51080–51083 (2014).

31. Sabo, M., Henschel, A., Fröde, H., Klemm, E. & Kaskel, S. Solution infiltration of palladium into MOF-5: synthesis, physisorption and catalytic properties. *J. Mater. Chem.* **17**, 3827 (2007).

32. Bellarosa, L., Brozek, C. K., García-Melchor, M., Dincă, M. & López, N. When the Solvent Locks the Cage: Theoretical Insight into the Transmetalation of MOF-5 Lattices and Its Kinetic Limitations. *Chem. Mater.* **27**, 3422–3429 (2015).

33. Garcia-Gutierrez, E. Copper Insertion in a Series of Metal-Organic Frameworks with Uncoordinated Carboxylic Acid Groups for Ammonia Removal. (2015).

34. Tulig, K. Encapsulation of Nanoparticles in Metal-Organic Frameworks for Air Purification. PhD Dissertation. (Georgia Institute of Technology, 2016).

35. Su, Z., Chen, J. H., Sun, X., Huang, Y. & Dong, X. Amine-functionalized metal organic framework (NH2 -MIL-125(Ti)) incorporated sodium alginate mixed matrix membranes for dehydration of acetic acid by pervaporation. *RSC Adv.* **5**, 99008 (2015).

36. Darunte, L. A., Oetomo, A. D., Walton, K. S., Sholl, D. S. & Jones, C. W. Direct Air Capture of CO_2 Using Amine Functionalized MIL-101(Cr). *ACS Sustain. Chem.*

Eng. **4**, 5761–5768 (2016).

37. Jiang, D., Keenan, L. L., Burrows, A. D. & Edler, K. J. Synthesis and post-synthetic modification of MIL-101(Cr)-NH_2 via a tandem diazotisation process. *Chem. Commun.* **48**, 12053–12055 (2012).

38. Walton, K. S. & Snurr, R. Q. Applicability of the BET method for determining surface areas of microporous metal-organic frameworks. *J. Am. Chem. Soc.* **129**, 8552–8556 (2007).

39. Jiao, Y. *et al.* Heat-Treatment of Defective UiO-66 from Modulated Synthesis: Adsorption and Stability Studies. *J. Phys. Chem. C* **121**, 23471–23479 (2017).

40. Shearer, G. C. *et al.* Defect Engineering: Tuning the Porosity and Composition of the Metal-Organic Framework UiO-66. *Chem. Mater.* **28**, 3749–3761 (2016).

41. Piscopo, C. G., Polyzoidis, A., Schwarzer, M. & Loebbecke, S. Stability of UiO-66 under acidic treatment: Opportunities and limitations for post-synthetic modifications. *Microporous Mesoporous Mater.* **208**, 30–35 (2015).

42. Wu, H., Yildirim, T. & Zhou, W. Exceptional Mechanical Stability of Highly Porous Zirconium Metal–Organic Framework UiO-66 and Its Important Implications. *J. Phys. Chem. Lett.* **4**, 925–930 (2013).

43. Kandiah, M. *et al.* Synthesis and Stability of Tagged UiO-66 Zr-MOFs. *Chem. Mater.* **22**, 6632–6640 (2010).

44. Katz, M. J. *et al.* A facile synthesis of UiO-66, UiO-67 and their derivatives. *Chem. Commun. (Camb).* **49**, 9449–9451 (2013).

45. Valenzano, L. *et al.* Disclosing the complex structure of UiO-66 metal organic framework: A synergic combination of experiment and theory. *Chem. Mater.* **23**, 1700–1718 (2011).

46. Cliffe, M. J. *et al.* Correlated defect nanoregions in a metal-organic framework. *Nat. Commun.* **5**, (2014).

47. Zahn, G. *et al.* Insight into the mechanism of modulated syntheses: *in situ* synchrotron diffraction studies on the formation of Zr-fumarate MOF. *CrystEngComm* **16**, 9198–9207 (2014).

48. Shearer, G. C. *et al.* Tuned to perfection: Ironing out the defects in metal-organic framework UiO-66. *Chem. Mater.* **26**, 4068–4071 (2014).

49. McGuire, C. V. & Forgan, R. S. The surface chemistry of metal-organic frameworks. *Chem. Commun.* **51**, 5199–5217 (2015).

50. Weidmann, B. & Seebach, D. Organometallic Compounds of Titanium and Zirconium as Selective Nucleophilic Reagents in Organic Synthesis. *Angew. Chemie Int. Ed.* **22**, 31–45 (1983).

51. Yuan, S., Qin, J. S., Lollar, C. T. & Zhou, H. C. Stable Metal-Organic Frameworks with Group 4 Metals: Current Status and Trends. *ACS Cent. Sci.* **4**, 440–450 (2018).

52. Dan-Hardi, M. *et al.* A New Photoactive Crystalline Highly Porous Titanium (IV) Dicarboxylate. *J. Am. Chem. Soc.* **131**, 10857–10859 (2009).

53. Vaesen, S. *et al.* A robust amino-functionalized titanium(IV) based MOF for improved separation of acid gases. *Chem. Commun.* **49**, 10082–10084 (2013).

54. Mounfield III, W. P. *et al.* Role of defects and metal coordination on adsorption of acid gases in MOFs and metal oxides: An in situ IR spectroscopic study. *Microporous Mesoporous Mater.* **227**, 65–75 (2016).

55. Mounfield III, W. P. *et al.* Synergistic Effects of Water and SO_2 on Degradation of MIL-125 in the Presence of Acid Gases. *J. Phys. Chem. C* **120**, 27230–27240 (2016).

56. Liu, Y., Klet, R. C., Hupp, J. T. & Farha, O. K. Probing the correlations between the defects in metal-organic frameworks and their catalytic activity by an epoxide ring-opening reaction. *Chem. Commun.* **52**, 7806–7809 (2016).

57. Stock, N. & Biswas, S. Synthesis of Metal-Organic Frameworks (MOFs): Routes to Various MOF Topologies, Morphologies, and Composites. *Chem. Rev.* **112**, 933–969 (2012).

58. Wu, H. *et al.* Unusual and highly tunable missing-linker defects in zirconium metal-organic framework UiO-66 and their important effects on gas adsorption. *J. Am. Chem. Soc.* **135**, 10525–10532 (2013).

59. Yang, D. *et al.* Tuning Zr6 Metal-Organic Framework (MOF) Nodes as Catalyst Supports: Site Densities and Electron-Donor Properties Influence Molecular Iridium Complexes as Ethylene Conversion Catalysts. *ACS Catal.* **6**, 235–247 (2016).

60. Vandichel, M. *et al.* Active site engineering in UiO-66 type metal–organic frameworks by intentional creation of defects: a theoretical rationalization. *CrystEngComm* **17**, 395–406 (2014).

61. DeCoste, J. B., Demasky, T. J., Katz, M. J., Farha, O. K. & Hupp, J. T. A UiO-66 analogue with uncoordinated carboxylic acids for the broad-spectrum removal of toxic chemicals. *New J. Chem.* **39**, 2396–2399 (2015).

62. Smalley, A. P., Reid, D. G., Tan, J. C. & Lloyd, G. O. Alternative synthetic methodology for amide formation in the post-synthetic modification of Ti-MIL125-NH_2. *CrystEngComm* **15**, 9368–9371 (2013).

63. Moran, C. M., Marti, R. M., Hayes, S. E. & Walton, K. S. Synthesis and characterization of aluminum carbide-derived carbon with residual aluminum-based nanoparticles. *Carbon N. Y.* **114**, 482–495 (2017).

64. Lambert, J. B. *Organic Structural Spectroscopy*. (Prentice-Hall, Inc: Upper Saddle River, NJ 1998).

65. Jiao, Y. *et al.* Tuning the Kinetic Water Stability and Adsorption Interactions of Mg-MOF-74 by Partial Substitution with Co or Ni. *Ind. Eng. Chem. Res.* **54**, 12408–12414 (2015).

66. Bosch, M., Zhang, M. & Zhou, H.-C. Increasing the Stability of Metal-Organic Frameworks. *Adv. Chem.* **2014**, 1–8 (2014).

67. McHugh, L. N. *et al.* Hydrolytic stability in hemilabile metal–organic frameworks.

Nat. Chem. **10**, 1096–1102 (2018).

68. Barkhordarian, A. A. & Kepert, C. J. Two new porous UiO-66-type zirconium frameworks; open aromatic N-donor sites and their post-synthetic methylation and metallation. *J. Mater. Chem. A* **5**, 5612–5618 (2017).

69. Hu, Z., Faucher, S., Zhuo, Y., Sun, Y. & Wang, S. Combination of Optimization and Metalated-Ligand Exchange : An Effective Approach to Functionalize UiO-66 (Zr) MOFs for CO_2 Separation. *ChemPubSoc* **66**, 17246–17255 (2015).

70. Valvekens, P., Bloch, E. D., Long, J. R., Ameloot, R. & De Vos, D. E. Counteranion effects on the catalytic activity of copper salts immobilized on the 2,2′-bipyridine-functionalized metal–organic framework MOF-253. *Catal. Today* **246**, 55–59 (2015).

71. Joshi, J. N., Garcia-Gutierrez, E. Y., Moran, C. M., Deneff, J. I. & Walton, K. S. Engineering Copper Carboxylate Functionalities on Water Stable Metal-Organic Frameworks for Enhancement of Ammonia Removal Capacities. *J. Phys. Chem. C* **121**, 3310–3319 (2017).

72. Joshi, J. N. Copper Insertion in UiO-66 Analogues for Ammonia Removal Applications. MS Thesis. (Georgia Institute of Technology, 2016).

73. Kim, K. C., Moghadam, P. Z., Fairen-Jimenez, D. & Snurr, R. Q. Computational Screening of Functional Groups for Ammonia Capture in Metal–Organic Frameworks. *Langmuir* **54**, 3257–3267 (2015).

74. Hungerford, J. T. Synthesis and Stability: Metal-Organic Frameworks Exposure to Water, Sulfur Dioxide, Hydrogen Sulfide. PhD Dissertation. (Georgia Institute of Technology, 2019).

75. Ethiraj, J., Bonino, F., Lamberti, C. & Bordiga, S. H_2S interaction with HKUST-1 and ZIF-8 MOFs: A multitechnique study. *Microporous Mesoporous Mater.* **207**, 90–94 (2015).

76. Petit, C., Mendoza, B. & Bandosz, T. J. Hydrogen sulfide adsorption on MOFs and MOF/Graphite oxide composites. *ChemPhysChem* **11**, 3678–3684 (2010).

77. Rezaei, F., Sakwa-Novak, M. A., Bali, S., Duncanson, D. M. & Jones, C. W. Shaping amine-based solid CO_2 adsorbents: Effects of pelletization pressure on the physical and chemical properties. *Microporous Mesoporous Mater.* **204**, 34–42 (2015).

78. Peterson, G. W. *et al.* Effects of pelletization pressure on the physical and chemical properties of the metal–organic frameworks $Cu_3(BTC)_2$ and UiO-66. *Microporous Mesoporous Mater.* **179**, 48–53 (2013).

79. Song, J. *et al.* A Multiunit Catalyst with Synergistic Stability and Reactivity: A Polyoxometalate-Metal Organic Framework for Aerobic Decontamination. *J. Am. Chem. Soc.* **133**, 16839–16846 (2011).

80. Hamon, L. *et al.* Molecular Insight into the Adsorption of H_2S in the Flexible MIL-53 (Cr) and Rigid MIL-47 (V) MOFs : Infrared Spectroscopy Combined to Molecular Simulations. *J. Phys. Chem. C* **115**, 2047–2056 (2011).

81. Peterson, G. W., DeCoste, J. B., Fatollahi-Fard, F. & Britt, D. K. Engineering UiO-66-NH_2 for Toxic Gas Removal. *Ind. Eng. Chem. Res.* **53**, 701–707 (2014).

82. Schoenecker, P. M., Carson, C. G., Jasuja, H., Flemming, C. J. J. & Walton, K. S. Effect of Water Adsorption on Retention of Structure and Surface Area of Metal–Organic Frameworks. *Ind. Eng. Chem. Res.* **51**, 6513–6519 (2012).

83. Zlotea, C. *et al.* Effect of NH_2 and CF_3 functionalization on the hydrogen sorption properties of MOFs. *Dalt. Trans.* **40**, 4879–4881 (2011).

84. Walton, K. S. & Sholl, D. S. Research Challenges in Avoiding " Showstoppers " in Developing Materials for Large-Scale Energy Applications. *Joule* **1**, 208–211 (2017).

85. Jiří Čejka, Naděžda Žilková, P. N. *Molecular Sieves: From Basic Research to Industrial Applications : Proceedings of the 3rd International Zeolite Symposium (3rd FEZA)*. (Elsevier, 2005).

CHAPTER 4. TARGETED ACID GAS REMOVAL THROUGH FRAMEWORK FUNCTIONALIZATION

4.1 Introduction

Metal-organic frameworks (MOFs) exhibit a high degree of exploitable tunability for complex acid gas removal processes. This is particularly important for SO_2, NO_2, and H_2S capture, which are commonly found in dilute concentrations. For example, standard post-combustion streams contain 10-15% CO_2, 3-7% O_2, 8-10% water vapor, up to 50ppm hydrochloric acid, and concentrations on the order of 0.1% for SO_x and NO_x, respectively.[1] Similarly, sour natural gas mixtures in North America generally possess H_2S levels below 1 vol%, along with high CO_2 concentrations and balance C_2-C_6 hydrocarbon mixtures.[2] Challenging acid gas-containing stream compositions requires adsorbents possessing favorable and selective binding efficiencies at both low partial pressures and complex mixture environments. Experimental testing on these systems is difficult to control due to their complexity and safety concerns. As a result, relevant gas separation studies which investigate MOFs primarily employ computational methods and/or single-component isothermal uptake experiments with spectroscopic studies.[3–9] These investigations are extremely informative for identifying (1) MOFs that remain stable following acid gas exposure, and (2) understanding H_2S and SO_2 adsorption interactions with tested frameworks. However, equilibrium measurements can incorrectly predict multicomponent selectivities, particularly for the aforementioned adsorbates which exhibit non-ideal physical binding interactions and sometimes chemisorption.[10] Heterogeneous charge distributions (e.g. polarity) and strong reaction potentials of acid gas adsorbates can alter

the adsorption behavior of other mixture constituents through promoting surface tension in the adsorbed phase, as shown previously with several chemisorbing molecules in the presence of water vapor in HKUST-1.[11,12] Lack of adsorption data at low H_2S and SO_2 partial pressures additionally complicates the comparison of MOF adsorption performance in typical concentrations sour and flue gas mixtures, hindering the accurate employment of multicomponent prediction models such as IAST.[13,14] Multicomponent adsorption experiments utilizing realistic concentrations and environmental conditions are instead necessary to provide pragmatic separation information.

Fixed-bed experiments commonly facilitate such studies. Investigations on rare-earth metal center[15] and soc-MOFs[16] evaluated in very sour (5% H_2S) mixtures with CO_2 and CH_4 demonstrate how frameworks can be designed to facilitate natural gas separations while maintaining stability through acid gas exposure. The same materials showcase desirable permeation and selectivity performance after incorporation into membranes as well.[17] Zou and coworkers[18] reported informative breakthrough experiments using H_2S and CO_2 containing mixtures to uncover low pressure H_2S capture potential for more commonly studied and produced MOFs. They found materials containing open-metal sites exhibit the highest uptake capacities and H_2S/CO_2 selectivities. Vacant electron orbitals of unsaturated metal centers preferentially interact with electronegative species, such as sulfur sites on H_2S, over non-polar molecules.[19] However, tests by Zou were conducted in an inert carrier gas, producing slight selectivity differences in comparison to predominantly hydrocarbon environments. Despite a few key exceptions such as CPO-27(Ni)[20], MOFs with open metal sites irreversibly bind sulfur and/or degrade through strong chemisorption reactions, preventing their reuse.[21,22]

One simple strategy to enhance MOF adsorption potential while preserving structural integrity and regenerability is ligand functionalization. Modification of these nanoporous materials with a myriad of chemical groups (-NH_2, -COOH, -F, -OH, etc.) through either reacting pre-functionalized ligands or post-synthetic modification strategies generates framework stability and adsorbate selectivity in a variety of adsorption applications.[23–30] Cmarik et al. pointed out the strong impact of this functionalization strategy on carbon dioxide adsorption—a more well-studied acid gas in MOF literature.[27] Jasuja et al. similarly observed ammonia affinity differences in UiO-66 materials containing various ligand-based functionalities.[26] The relative knowledge gap for SO_2 and H_2S-MOF adsorption systems would be addressed by probing ligand functionalities in post-combustion and sour gas-relevant environments. Specifically, integrated acid gas-selective functionalities in MOFs can design targeted capture in the extremely complex multicomponent environments being investigated.

In this chapter, MOFs are constructed with appended ligand functionalities to enhance SO_2 and H_2S adsorption in different environments. First, carboxylic acid (-COOH) groups are integrated onto the terephthalate linkers of highly stable UiO-66(Zr) analogues. Pendant -COOH sites are integrated using pre-functionalized MOF linkers to create UiO-66-COOH and UiO-66-$(COOH)_2$, respectively. The strong polarity and electron-rich binding sites within accessible -COOH demonstrate reversible adsorption interactions with the adsorbates at concentrations >>1%. Reversible gas capture behavior is converted to permeant binding through post-synthetic modification of carboxylic acid sites with copper, to form reactive copper carboxylates (-COOCu) on tested materials. Metalated materials reactively bind H_2S, fostering significant enhancements in adsorption capacity relative to

parent UiO-66-COOH and UiO-66-$(COOH)_2$. Then, low partial pressure H_2S removal from natural gas-related mixtures using MOFs is explored. Favorable interactions between primary amines and acid gas adsorbates are leveraged by evaluating effects of linker-based amine ($-NH_2$) MOF functionalization on adsorptive sour gas purification. Three well-studied, stable MOFs previously demonstrated to allow functionalization via linker-based amines[31–34] are examined as candidate frameworks: UiO-66(Zr), MIL-101(Cr), MIL-125(Ti). Their respective amine analogues are all constructed using 2-aminoterephalic acid as a framework ligand. These materials are chosen due to their previously reported H_2S stability and facile ability for amine functionalization, making them promising candidate adsorbents for cyclable H_2S capture.

4.2 Materials and Methods

4.2.1 Synthesis and Materials Preparation

Material synthesis procedures for MOFs discussed in this chapter are already described in Chapter 3. Please refer to the degas conditions of respective materials, also mentioned in Chapter 3, used prior to adsorption and materials characterization measurements described below.

4.2.2 Sample Characterization Methods

4.2.2.1 Fourier Transform Infrared Spectroscopy (FTIR)

FTIR spectra of powder MOF samples were collected using a Thermo Nicolet iS50 spectrometer, equipped with a liquid-nitrogen cooled MCT/A detector. A Pfeiffer GSD 320 O2C, OmniStar Gas analysis system (1-200amu, 100-230V, 50/60Hz corrosive gas

version) mass spectrometer monitored outlet gases from the spectrometer during *in situ* measurements.

In situ FTIR measurements were acquired via diffuse reflectance infrared Fourier transform spectroscopy (DRIFTS). DRIFTS experiments were performed with a diffuse reflectance accessory (Praying Mantis, Harrick), and a high temperature reaction chamber (HVC, Harrick). The chamber used in H_2S adsorption experiments was coated with SilcoNert. MOF samples were pretreated at 150°C for 1 h with 20 cc min^{-1} He in the DRIFTS cell. The temperature was then reduced to 25°C. After temperature steadied, 10 % CO_2/He or 5000 ppm H_2S/N_2 was supplied to the cell at 20 cm^3/min for 45 min. Residual gas was purged with He flow at 20 cc min^{-1} for 10 min. IR spectra were collected every 1 minute during the adsorption step over 30 scans. The outlet gases from the DRIFTS reactor were analyzed using a quadrupole mass spectrometer (Omnistar GSD-320C corrosive gas version, Pfeiffer Vacuum).

Attenuated total reflectance (ATR-FTIR) spectra were acquired using a Thermo Scientific Nicolet iS50 spectrometer coupled with an iS50 ATR module. Dry KBr powder samples were utilized for background subtraction. Small amounts of unactivated MOF powders were placed under the ATR probe crystal after cleaning with isopropanol. Measurements were acquired through 128 scans, with a data resolution of 0.48cm^{-1}.

4.2.2.2 Nitrogen Physisorption at 77K

A Quantachrome Quadrasorb SI volumetric system with 5.11 QuadraWin™ software package was used to collect nitrogen adsorption data at 77K. Sample quantities

between 50-100mg (after degassing) were utilized in measurements. BET surface area measurements were approximated using a pressure range of $P/P_0 = 0.005–0.03$.[35]

Although MOF pore sizes are most accurately attained from crystal structure data, pore size distributions were determined for frameworks as well to lend qualitative comparisons. Distribution data are not intended to communicate quantitative changes in textural properties. Models utilized non-local density functional theory (NLDFT), assuming carbon surface with cylindrical pores.[36]

4.2.2.3 Powder X-ray Diffraction

Powder X-ray diffraction (PXRD) measurements were acquired using an X-Pert Pro PANanalytical X-ray diffractometer. The X-ray source was Cu Kα radiation: $\lambda = 1.542$ Å. Measurements were taken using a step size of 0.02° from $2\theta = 4°- 40°$ for UiO-66(Zr) and MIL-125(Ti) materials and a step size of 0.01° from $2\theta = 2°- 40°$ for MIL-101(Cr) materials.

Version 3.0.5 of PANalytical HighScore Plus software suite enabled powder data refinement. A profile fit of peak heights on raw PXRD data was first carried out for UiO-66-COOH and UiO-66-$(COOH)_2$ samples, where experimental peak intensities were affixed to measured values. Least-squared minimization fitting of the measurements were then carried out using standard constraints prescribed by Pawley, along with referenced cell volumes and space groups deduced earlier.[24,37]

4.2.2.4 Scanning Electron Microscopy (SEM)/Energy Dispersive Spectroscopy (EDS)

A Zeiss Ultra 60 Field Emission (FE) SEM was used to acquire electron images. Samples were placed onto carbon tape secured on image stands prior to imaging. An accelerating voltage range from 3-5keV was utilized for imaging MOFs in this study.

EDS measurements were attained using the same apparatus. A working distance of approximately 8.7mm was targeted for data collection. An accelerating voltage of 15-20keV was utilized while collecting copper, sulfur, carbon, oxygen, and zirconium EDS data. AZtec software was used to process EDS data and collect point-based elemental composition data. An average of three scans per point were utilized to quantify elemental distributions, where final composition averages presented are products of multiple scans across examined sample stages.

4.2.2.5 Solid-State Nuclear Magnetic Resonance (NMR)

To collect ^{1}H and ^{13}C NMR data on powder samples, an AV3-HD 500 solid-state NMR spectrometer with a narrow-bore HX-magic angle spinning (MAS) probe was used. The instrument operates at a ^{1}H frequency of 500MHz. The diameter of the MAS rotors was 3.2 mm, allowing MAS speeds of up to 23kHz—a rotational frequency of 20kHz was used here. ^{13}C measurements were taken through cross polarization magic angle spinning (CPMAS), using a ^{1}H 90° 5μs pulse length, 5s repetition delay, TPPM decoupling, cross polarization for 2ms using a linear ramp with an amplitude increasing from 50% to 100%. 4000 up to 10000 averages were recorded for each spectrum.

4.2.2.6 Thermogravimetric Analysis

TGA data were acquired by a Nietzsche STA 449 F1 Jupiter. Samples were held in a ceramic crucible during measurement. Material combustion was desired for weight loss normalizations presented in the text, So, dry air (Ultra Zero Airgas) was used as a carrier gas to flow over samples at 40mL min^{-1} during data collection. Details on defect quantity estimation methods using TG data are provided in Section 2.3.2.4

4.2.3 Acid Gas Adsorption Experiments

4.2.3.1 Fixed-Bed Adsorption

Dynamic adsorption micro-breakthrough experiments were carried out on MOF samples. The apparatus is described in the experimental Section 2.3.2.1. Activated samples (100−200 mg) were tested. Sample degassing was achieved *in situ* under 50mL min^{-1} He flow at sample activation temperatures for durations at least overnight, and until no more eluting species could be detected. For single-component measurements, adsorbate concentrations of 963ppm SO_2 and 4988ppm H_2S in balance nitrogen were fed from stock gas cylinder mixes, purchased from Airgas. In multicomponent studies, 1% H_2S/99% CH_4 and 1% H_2S/10% CO_2/89% CH_4 gas mixtures were utilized from disposable bottle sources, also acquired from Airgas. In either case, gases were introduced into the sample bed at 50mL min^{-1}. Following experiments, desorption was performed by simultaneously heating samples to their degas temperatures while terminating acid gas adsorbate flow and introducing helium at 50mL min^{-1} into the sample bed. Desorption stopped when the concentration of eluting species could be no longer detected (< 0.1ppm). Samples cooled to room temperature before being removed from the apparatus, and were then weighed.

Using tracer N_2 and acid gas adsorbate (SO_2 or H_2S) concentration vs. time data, adsorption breakthrough capacities were determined. Capacities are reported for materials "at saturation"—meaning times were chosen when the outlet adsorbate concentrations became roughly equal to their inlet concentration ($C_{out} \approx C_{in}$), prior to desorption. Source code in MATLAB for calculating breakthrough capacities is reproduced in APPENDIX C. script for determining breakthrough capacities.

4.3 Results and Discussion

4.3.1 Carboxylic Acid Groups Targeting Polar Acid Gas (SO_2, H_2S) Capture

4.3.1.1 Installation of Carboxylic Acid Sites on UiO-66(Zr) Ligand Moieties

UiO-66(Zr) is a desirable framework support for acid gas-selective chemical functionalities due to its high accessibility and robust chemical stability. Carboxylic acid (-COOH) groups have been installed on UiO-66(Zr) in previous studies[38,39], and are particularly interesting for SO_2 and H_2S capture. This is argued graphically in Figure 4-1, where the mixed charge distribution across a carboxylic acid group can facilitate different electronic binding interactions (e.g. hydrogen bonding, dipole-dipole interactions) with polar SO_2 and H_2S adsorbates. One can imagine multiple binding geometries and interactions between the acid gases and pendant -COOH functionalities. Furthermore, electrostatic adsorbate-adsorbent interactions allow reversible binding, beneficial for adsorbent regeneration. Accordingly, UiO-66-COOH and UiO-66-$(COOH)_2$ frameworks were synthesized using procedures described in Section 3.2.1.3, ideally incorporating one and two uncoordinated carboxylic acid groups per framework ligand, respectively.

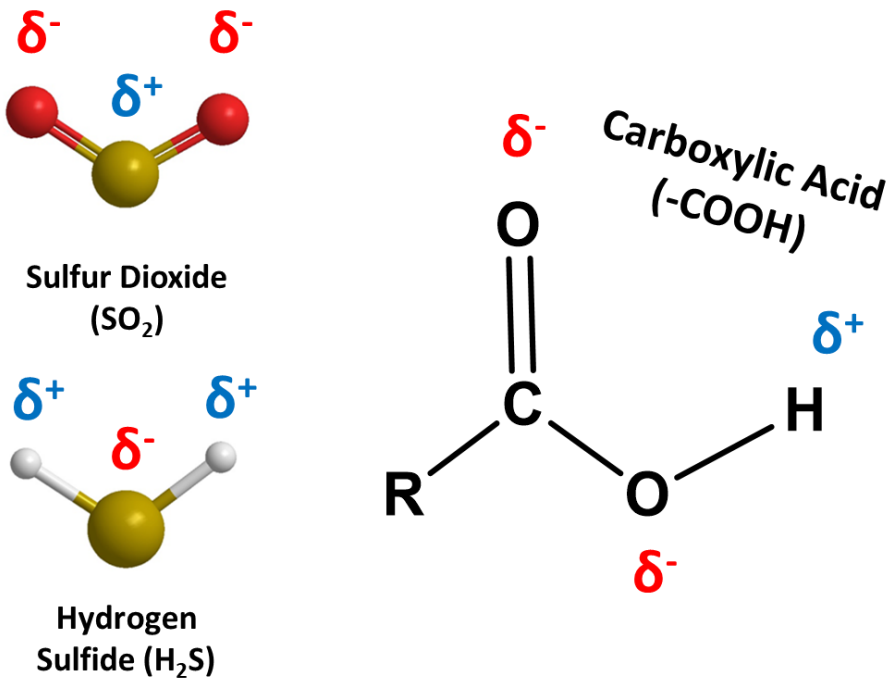

Figure 4-1: Illustration of general charge distribution for adsorbates (SO_2, H_2S) and hypothetical carboxylic acid adsorption sites. Partial charges on molecules symbolized by δ (blue = partial positive, red = partial negative). Molecules created using ChemDraw software.

Synthesized products obtain expected UiO-66(Zr) topology.[40] Pawley crystal structure refinement of UiO-66-COOH and UiO-66-$(COOH)_2$ powder diffraction measurements was carried out using space group and lattice parameter information from DFT and NMR structure optimization work on the same materials by Ragon et al.[24] Experimental and fit patterns in Figure 4-2a and b evidence close agreement of powder data with UiO-66(Zr) topology for UiO-66-COOH and UiO-66-$(COOH)_2$, respectively. Amorphous broadening is apparent around $2\theta \approx 8°$ for UiO-66-$(COOH)_2$, indicating lattice strain over large d-spacings. The long-range order of UiO-66-$(COOH)_2$ is therefore defective—likely caused by various modes of possible BDC-$(COOH)_2$ ligand coordination during synthesis. Difference plots in Figure 4-2c and d reveal the greatest disagreement

arises from peak height in both samples at low 2θ values. Peak height is not refined through the Pawley method due to the absence of a reference structure.[37] This is important, since relative peak intensities in XRD relate to the occupancy of atoms within a given diffraction plane. More atoms are involved in diffraction at low 2θ scan values from Bragg's Law, as these reflections correspond to larger d-spacings across the crystal lattice. So, this disagreement is expected since the model does not contain atomic density information as a function of crystal geometry. Regardless, agreement indices listed in Figure 4-2e support that synthesized materials are isostructural to UiO-66(Zr), where cubic lattice parameters remain close to expected cell volumes, and χ^2 values approach 1. Note this information does not indicate the absence of framework defects or mixed phases. But, the data evidences the dominant crystalline phase is consistent with that of UiO-66, and by extension confirms successful integration of -COOH functionalities into the crystalline networks.

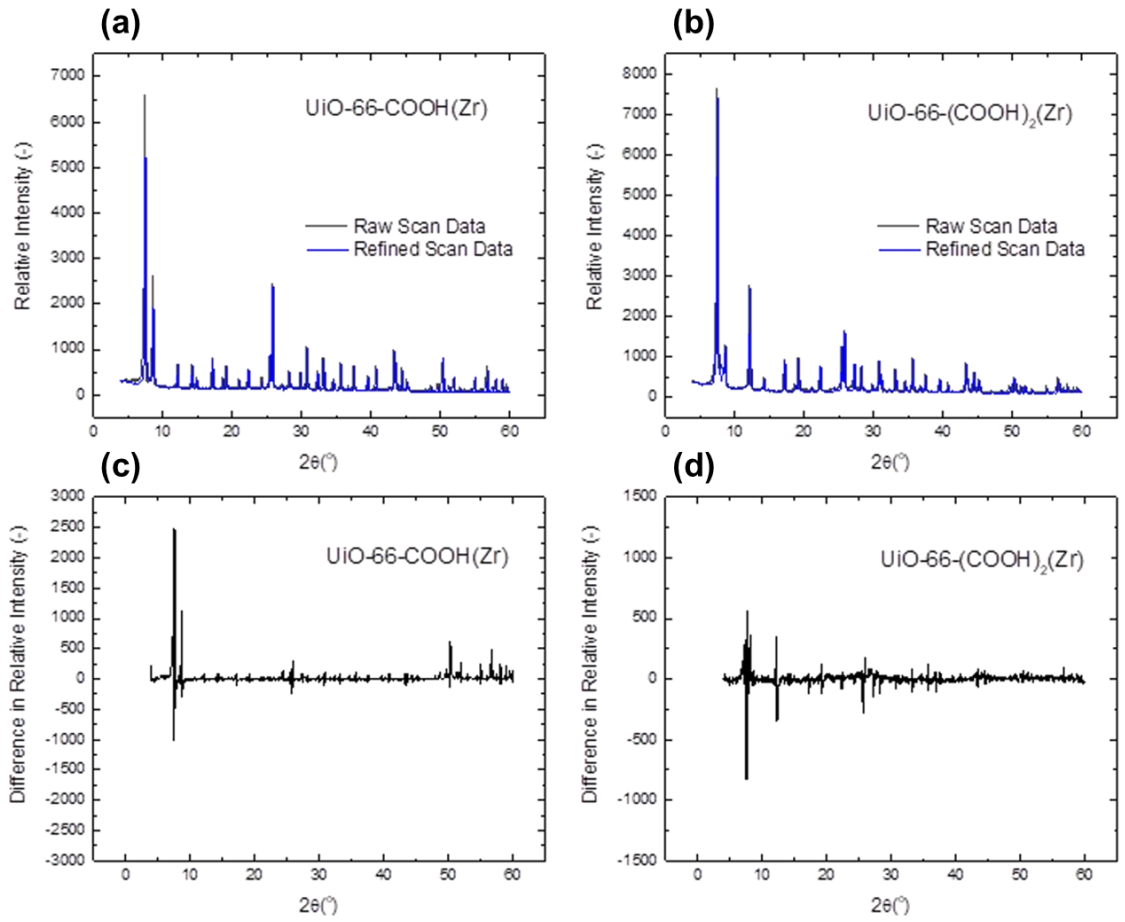

(e)

Materials	Space Group	Lattice Parameters (Å)		Weighted R (R_{wp})	Goodness of Fit (χ^2)
		Reference	*Refined*		
UiO-66-COOH	*F23*	20.758(1)	20.799(3)	11.23	1.45
UiO-66-$(COOH)_2$	*F23*	20.731(5)	20.688(6)	5.22	1.31

Figure 4-2: Crystal structure refinement data for UiO-66-COOH(Zr) and UiO-66-$(COOH)_2$(Zr). Measurements acquired at room temperature. Overlay of Pawley refinement fits (blue) and raw data (black) are presented in (a) and (b), along with difference plots as a function of 2θ in (c) and (d). Refined parameters and fit statistics summarized in (e). Refinement was performed using HighScorePlus software

4.3.1.2 Inspection of Framework Defects

Missing linker/cluster defects are frequently reported throughout UiO-66(Zr) literature.[41–43] Therefore, some degree of framework vacancies are expected in UiO-66-COOH and UiO-66-$(COOH)_2$. TGA curves are presented in Figure 4-3 to gauge differences between expected and measured weight losses of the two frameworks. Organic contents of both MOFs are lower than theoretical predictions after desolvation around 300°C.[44] The mass difference for each framework roughly equals to the absence of 2 linkers per metal cluster. Note, this weight loss metric does not assert mass differences are created purely from missing linker vacancies—metal clusters may be absent from studied samples as well. It should be stated that a *reo* phase, which is indicative of missing zirconium clusters within UiO-66, is not apparent from diffraction data in Figure 4-2a or b.[43]

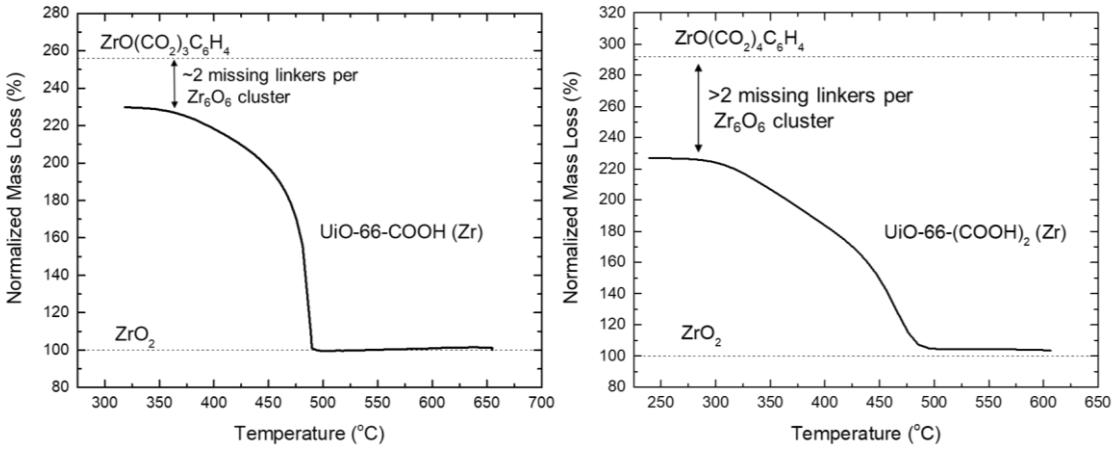

Figure 4-3: TGA curves for UiO-66-COOH (left) and UiO-66-$(COOH)_2$ (right). Solid lines represent sample mass loss. Dashed lines represent normalized end (ZrO_2) and beginning (dehydroxylated formula unit) masses. Mass loss differences are normalized to approximate missing linker amounts.

Clet and coworkers[24] identified the onset of acid anhydrides which form among pendant -COOH groups in UiO-66-COOH and UiO-66-$(COOH)_2$ in close proximity. However, the authors of the previous study utilized a different hydrothermal approach to create the MOFs. So, textural properties may be different from materials synthesized here. Nonetheless, acid anhydride defects were observable for UiO-66-COOH and UiO-66-$(COOH)_2$ synthesized here. Taking UiO-66-$(COOH)_2$ as an example, *in situ* FTIR data in Figure 4-4 evidences the onset of acid anhydride formation as a function of temperature. Resolution limitations under DRIFTS makes it difficult to clearly differentiate carboxyl stretching modes. These are instead supplemented in *ex situ* ATR measurements in Figure A-18. At temperatures exceeding 65°C, strong features corresponding to acid anhydrides become apparent.[45] This was also noted by Clet for UiO-66-COOH and UiO-66-$(COOH)_2$ samples, which was ascribed to dehydration reactions amongst facing carboxylic acid groups.[24] This phenomenon is not unique to UiO-66(Zr)-type frameworks. Acid anhydride formation between pendant -COOH groups localized in micropores also form in MIL-53-COOH(Al) through the same general mechanism.[46] Bridging pendant linker groups strain the MOF lattice, which can hinder pore accessibility. To mitigate the loss of accessible -COOH bonding sites and maintain structural consistency in samples across adsorption measurements, a degas temperature of 65°C was used for UiO-66-COOH and UiO-66-$(COOH)_2$ in all presented experiments. This temperature is notably insufficient to completely evacuate heavier reagent and rinse solvents such as N,N-dimethylformamide and molecular guests (e.g. water vapor).[47] Differences may also result from previously discussed missing linker/cluster defects that effectively remove adsorption surfaces available in defect-free structures for a given volume.

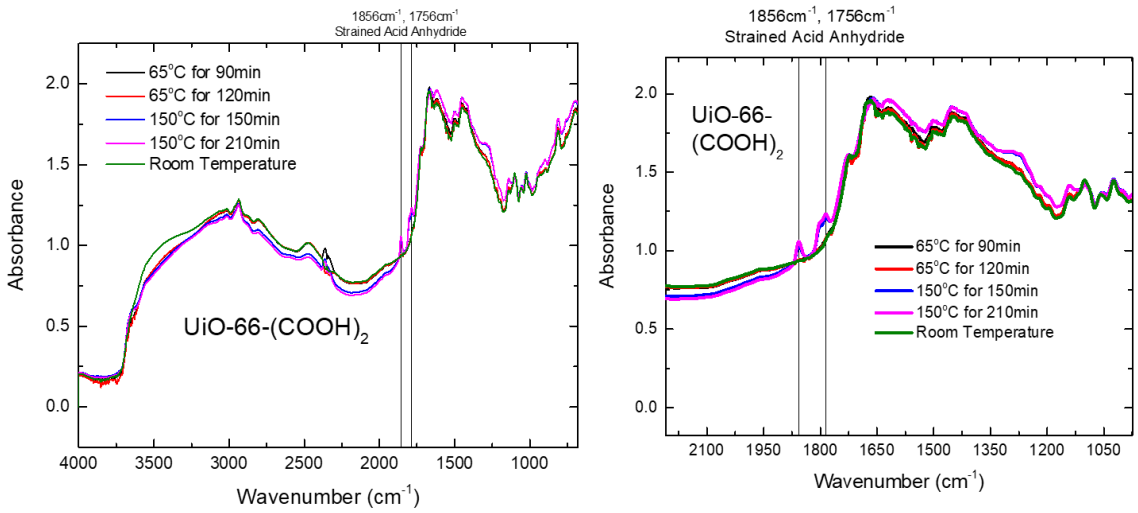

Figure 4-4: *In situ* DRIFTS spectra of UiO-66-$(COOH)_2$ under helium flow at various temperatures—increasing from room temperature. Left-full spectra, right-inset of carboxyl and aromatic stretching regions. Wavenumbers at top identify features corresponding to acid anhydride stretches

Solid state ^{13}C NMR spectra in Figure 4-5 also indicate anhydride features, apparent as weak shoulders around 165ppm for UiO-66-COOH and 155ppm for UiO-66-$(COOH)_2$. Features are in good agreement with previous assignments.[24] Full spectra are presented in Figure A-19 and Figure A-20. Spectral features from 110-140ppm are consistent between both MOFs since they emerge from quaternary and C-H carbon atoms on bridging terephthalate linkers. Unique lineshapes between 170-180ppm for UiO-66-COOH and 160-180ppm for UiO-66-$(COOH)_2$ distinguish carboxylic acid groups in variable electronic environments. Based on prior assignments[24], the lower chemical shift corresponds to metal carboxylate bonds ('COOZr') bridging the framework. Peaks denoted "C-OOH" in Figure 4-5 correspond to uncoordinated carboxylic acid groups, which resonate at higher chemical shifts due to carbon nuclei desheilding from protons on -OH groups. In this way, ^{13}C NMR spectra support the existence of uncoordinated -COOH groups detected by FTIR. Solid state ^{1}H NMR data in Figure A-21 and Figure A-22 also

evidence framework features along with molecular guests retained from low degas temperatures, as apparent from aliphatic and C-C bonding. From ^{1}H NMR data, it is assumed molecules remain entrapped following desolvation procedures, and may affect acid gas capture in UiO-66-COOH and UiO-66-$(COOH)_2$ samples studied here.

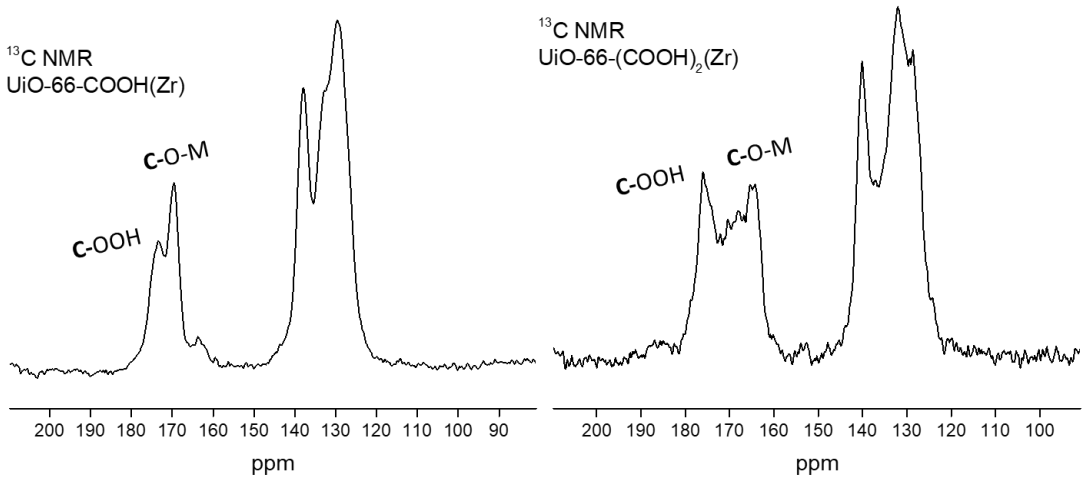

Figure 4-5: Solid state ^{13}C CPMAS spectra for UiO-66-COOH (left) and UiO-66-$(COOH)_2$ (right) samples. Samples were degassed under vacuum at 65°C prior to measurements at room temperature.

4.3.1.3 Acid Gas Adsorption of UiO-66-COOH and UiO-66-$(COOH)_2$

The H_2S and SO_2 adsorption performance of UiO-66-COOH and UiO-66-$(COOH)_2$ was investigated. Equilibrium SO_2 uptake data are presented in Figure 4-6. UiO-66-COOH has a higher SO_2 saturation capacity than UiO-66-$(COOH)_2$, owing to the larger pore volume of UiO-66-COOH. Interestingly, UiO-66-COOH also has a sharper low pressure (< 200mbar) SO_2 uptake profile than UiO-66-$(COOH)_2$. The opposite is expected, since the more restrictive pore environment of UiO-66-$(COOH)_2$[48] should enhance intermolecular interactions and adsorption affinity with pendant ligand functionalities. A

computational study by Li et al.[5] investigating various UiO-66(Zr) functionalized analogs also predicted UiO-66-$(COOH)_2$ to have a greater isosteric heat of adsorption of SO_2 at infinite dilution than UiO-66-COOH, although the calculated difference was only ~1kJ mol^{-1}. The difference in uptake may suggest accessibility issues govern SO_2 adsorption. Transport barriers are likely caused by the greater density of pendent -COOH groups residing in the pore windows of UiO-66-$(COOH)_2$. Demir, Walton, and Sholl predicted PLDs below 0.3nm, as found in UiO-66-$(COOH)_2$ but not with UiO-66-COOH (PLD ≈ 2.2Å and 3.2Å, respectively), would create diffusion limitations for larger adsorbates such as H_2S, and by extension SO_2 (kinetic diameter ≈ 3.6Å).[48,49] Inaccessibility couples with the lower available BET surface area in UiO-66-$(COOH)_2$ for SO_2 adsorption. Structural defects described in 4.3.1.2 may also decrease experimental SO_2 uptakes for UiO-66-$(COOH)_2$. Regardless, both MOFs exhibit fully cyclable SO_2 capacities at all tested pressure ranges following *in situ* regeneration. As hypothesized, SO_2 adsorption is likely governed by reversible binding interactions in both frameworks. Measurements consequently suggest the adsorbents are applicable for regenerative adsorption of SO_2, even at high pressures.

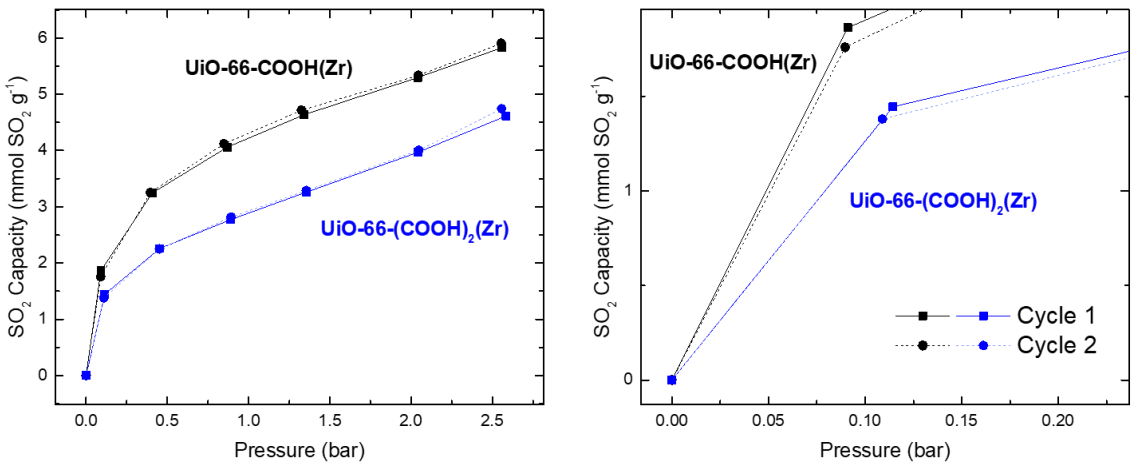

Figure 4-6: SO_2 pressure decay curves for UiO-66-COOH (black) and UiO-66-$(COOH)_2$ (blue). Full data shown on right-hand side, and an inset of the low pressure region is displayed on the left. Solid lines represent the first adsorption cycle, and dashed lines represent a subsequent adsorption cycle after degas

Fixed-bed H_2S and SO_2 adsorption experiments provide insight onto low partial pressure adsorption behaviors. Feed concentrations of approximately 1000ppm SO_2 and 5000ppm H_2S were utilized for respective breakthrough experiments. Kinetic uptake and desorption data are presented in Figure 4-7a for the two samples. Heating and inert purging upon desorption creates sudden, sharp desorption profiles that exceed inlet concentrations, due to large amounts of gas immediately leaving tested adsorbents. This is strongly indicative of physisorption interactions, where adsorbates release easily from porous hosts. Sharper adsorption profiles are apparent for H_2S in both UiO-66-COOH and UiO-66-$(COOH)_2$. This occurs because the test concentration for H_2S is ~5x greater than that for SO_2, accelerating time required for saturation. Kinetic uptake of H_2S in UiO-66-$(COOH)_2$ is notably slower than observed in Figure 4-7a for UiO-66-COOH, although there is no significant difference in H_2S breakthrough times. Gradual gas uptake after breakthrough causes the H_2S adsorption capacity of UiO-66-$(COOH)_2$ to exceed that of UiO-66-COOH,

as shown in Figure 4-7b. Transport hinderance during H_2S adsorption likely creates kinetic limitations for H_2S removal by UiO-66-$(COOH)_2$, and echoes previously discussed uptake impediment in pressure decay measurements. Pore blocking from more pendant -COOH groups would contribute to transport limitations, as the slowed H_2S uptake behavior of UiO-66-$(COOH)_2$ is not observed in UiO-66-COOH. H_2S removal applications generally mandate complete or ppb-ppm level outlet concentrations. As a result, the large difference in adsorption capacity between the tested MOFs in Figure 4-7b does not indicate UiO-66-$(COOH)_2$ is a pragmatically advantageous choice over UiO-66-COOH for H_2S removal.

SO_2 adsorption behaviors are similar for both MOFs in Figure 4-7a. Opposite from H_2S data, UiO-66-COOH has a slightly greater adsorption capacity for UiO-66-$(COOH)_2$ at tested concentrations. This observation is in accord with pressure decay data in Figure 4-6, and is similarly consequent of less adsorption surface accessibility for SO_2 within UiO-66-$(COOH)_2$ in comparison to UiO-66-COOH. Minute molecular differences of guest molecules can create significant binding disparities. It is possible -COOH functional groups are unfavorable SO_2 binding sites at tested pressures, but interact more aggressively with H_2S at 0.5%. This would explain why UiO-66-$(COOH)_2$, which should contain a higher density of -COOH sites, exhibits a higher H_2S capacity than UiO-66-COOH, but similar SO_2 uptake. Experimental and/or theoretical site-specific studies are required to confirm actual binding modes, since various interactions are possible.

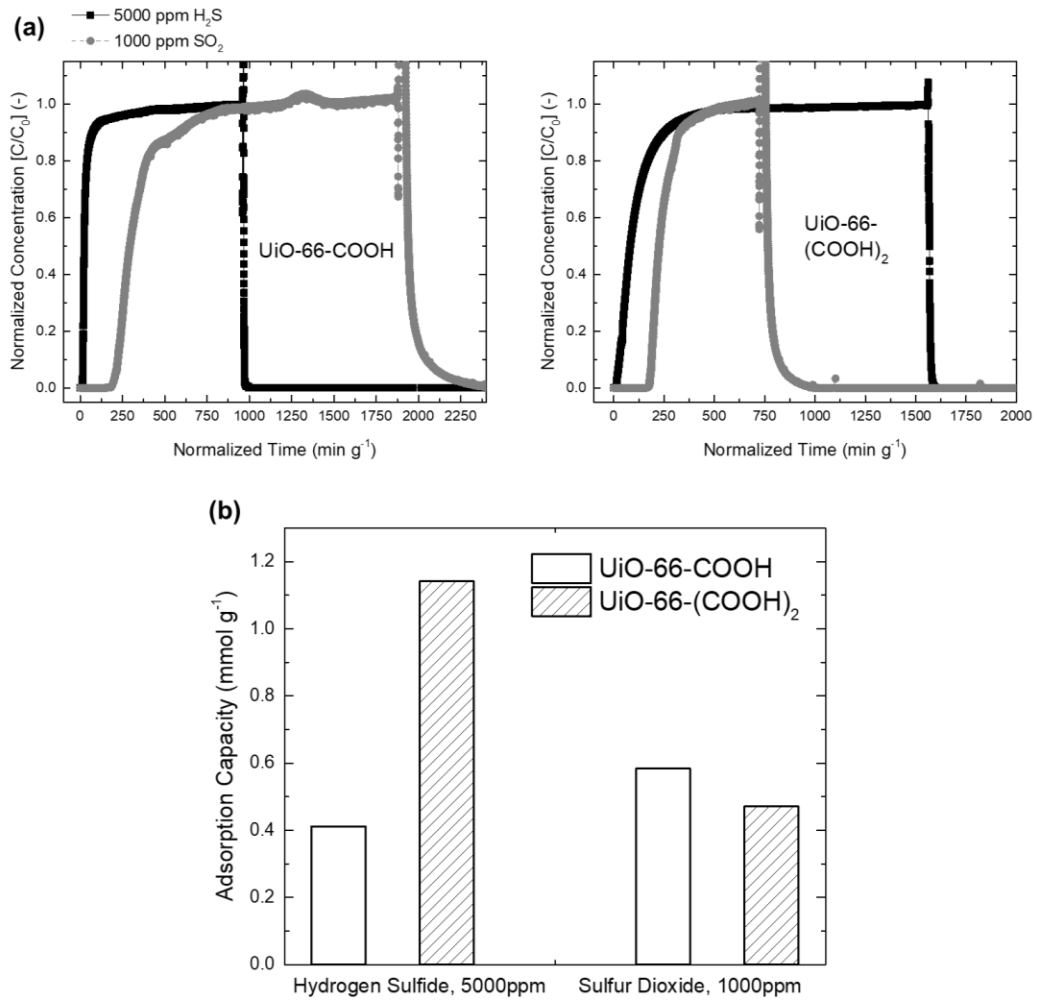

Figure 4-7: Adsorption data for tested frameworks containing pendant -COOH groups. (a) Fixed bed adsorption/desorption curves for UiO-66-COOH (left) and UiO-66-$(COOH)_2$ (right), (b) calculated adsorption capacities for tested samples in H_2S/N_2 and SO_2/N_2 gas mixtures

H_2S capacities for tested frameworks are greater than those measured for UiO-66(Zr)[18] and similar to measurements on UiO-66-NH_2 (~0.5mmol g^{-1} at 1% H_2S, data provided in Figure A-26). Measured SO_2 capacities of UiO-66-COOH and UiO-66-$(COOH)_2$ in Figure 4-7b are similar to other previously investigated MOFs summarized by Jones and coworkers[50] (reproduced in Table A-7 for convenience) considering differences in SO_2 partial pressures used in prior tests. Both MOFs outperform UiO-66(Zr). So, -

COOH groups enhance H_2S and SO_2 uptake. UiO-66-NH_2(Zr), an isostructural framework containing pendant primary amine (-NH_2) functionalities, interestingly displays a higher SO_2 adsorption capacity (> 0.7 mmol g^{-1} at 1000ppm SO_2) in Figure A-27 than UiO-66-COOH and UiO-66-$(COOH)_2$. Primary amines offer similar electrostatic bonding opportunities with SO_2 as carboxylic acids—they are both polar, donate hydrogen bonds, and can share electrons with sulfur through the carbonyl in -COOH and nitrogen in -NH_2 groups. UiO-66-NH_2(Zr) also contains a larger (more accessible) pore limiting diameter than UiO-66-COOH and UiO-66-$(COOH)_2$—over 0.1nm greater than UiO-66-$(COOH)_2$.[48] So aside from possible differences in specific binding strengths, the stronger SO_2 adsorption efficacy of UiO-66-NH_2(Zr) may be consequent of the greater gas accessibility into the pore space and with -NH_2 binding sites.

4.3.1.4 Acid Gas Adsorption Performance of Copper Carboxylate (-COOCu) Containing Frameworks

Reversible acid gas adsorption characteristics of UiO-66-COOH and UiO-66-$(COOH)_2$ are certainly desirable for adsorbent recycling. But, chemical acid gas adsorption is beneficial as well. Irreversible adsorbate retention usually equates to higher uptake capacities and mixture selectivities at low partial pressures, due to stronger thermodynamic binding potentials. Unlike highly-connected UiO-66(Zr), MOFs with unsaturated and accessible metal centers portray strong chemical adsorption interactions with SO_2 and H_2S.[11,18,22,51–53] Binding interactions at metal centers usually come at the cost of degradation, as metal-ligand bonds connecting MOF structures are often displaced by strongly coordinated adsorbates.[54–57] Accordingly, reactive copper carboxylate sites were installed on stable UiO-66(Zr) analogues via post-synthetic modification of uncoordinated

pendant carboxylic acid groups. Syntheses, stability properties, and characterizations of newly made UiO-66-COOCu and UiO-66-$(COOCu)_2$ MOFs are detailed in Chapter 3, Section 3.2.4.

Fixed-bed adsorption experiments were carried out on newly made UiO-66-COOCu and UiO-66-$(COOCu)_2$ frameworks. SO_2 breakthrough data are provided alongside adsorption curves for parent UiO-66-COOH and UiO-66-$(COOH)_2$ in Figure 4-8a. A clear reduction in SO_2 breakthrough time and adsorption capacity is observed for both samples. Relative ranking of SO_2 adsorption performance is preserved from parent frameworks as well: SO_2 capacity of UiO-66-COOCu > UiO-66-$(COOCu)_2$. Measurements indicate introduced copper species are not favorable SO_2 binding sites. Cluster models representative of HKUST-1, whose framework is constructed of accessible copper carboxylate bonds, also found Cu(II)-S interactions were repulsive between SO_2 and copper sites, and only weaker-order bonding with the oxygen species were favorable.[58] Chemisorption was also not apparent in SO_2 pressure decay measurements by Hungerford for MOFs possessing unsaturated copper carboxylates.[59] Decreased breakthrough times from parent MOFs result from increased framework density and/or blocking of accessible adsorption surfaces from copper-based functionalities intruding the pore space. The latter is supported by significantly lower BET surface areas for UiO-66-COOCu and UiO-66-$(COOCu)_2$ in comparison to unmodified frameworks in Chapter 3, Section 3.2.4.

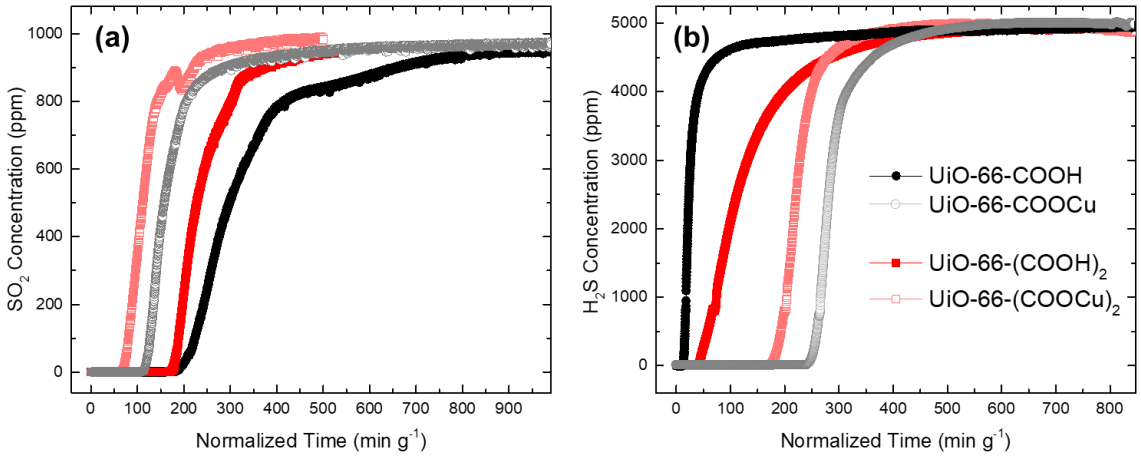

Figure 4-8: Fixed-bed adsorption measurements for tested materials in (a) 1000ppm SO_2/N_2 and (b) 5000ppm H_2S/N_2

While SO_2 capture is hampered by metalation, H_2S uptake markedly improves. Figure 4-8b evidences over 1000% increases in normalized H_2S breakthrough times for both UiO-66-COOCu and UiO-66-$(COOCu)_2$. Cu^{2+}-functionalized UiO-67(bipy) materials similarly displayed large enhancements in H_2S uptake upon metalation, supporting the general reactivity of framework-appended copper metal sites towards H_2S.[60] UiO-66-COOCu displays the highest adsorption capacity for H_2S for all studied frameworks. This may be owed to a greater accessibility of active sites in UiO-66-COOCu in comparison to UiO-66-$(COOCu)_2$. As previously discussed, UiO-66-$(COOH)_2$ displays slow adsorption kinetics for H_2S in fixed-bed experiments. The relatively more obstructed pore network of UiO-66-$(COOH)_2$ from higher -COOH density transfers onto UiO-66-$(COOCu)_2$. Consequently, H_2S molecules may not access -COOCu binding sites in UiO-66-$(COOCu)_2$ as easily as with UiO-66-COOCu during adsorption experiments. Sulfidation is also visually observed. A series of images depicting this chemical change in UiO-66-$(COOCu)_2$ during adsorption experiments is provided in Figure 4-9. As acid gas flows from top-to-bottom of the packed bed, the blue adsorbent becomes black. The color

change is obvious enough that the adsorption front is easily discerned over the course of the experiment. Black coloring results from copper sulfide formation. The chemical change is irreversible under standard MOF degassing after H_2S exposure. Similar color changes were noted by Zou and coworkers after exposing H_2S to HKUST-1 and Cu-BDC(ted)$_{0.5}$, both MOFs comprised of accessible copper carboxylate metal-ligand framework bonds, where color changes were also onset by reaction(s) between sulfur and Cu^{2+} sites.[18] Altogether, frameworks incorporated with copper carboxylate functionalities display strong chemical reactivity with hydrogen sulfide at tested concentrations, but not with sulfur dioxide. The described post-synthetic modification method can therefore be applied to imbue high H_2S uptakes in dilute conditions. However, reactive copper installation is not applicable for all acid gas adsorbates, such as SO_2.

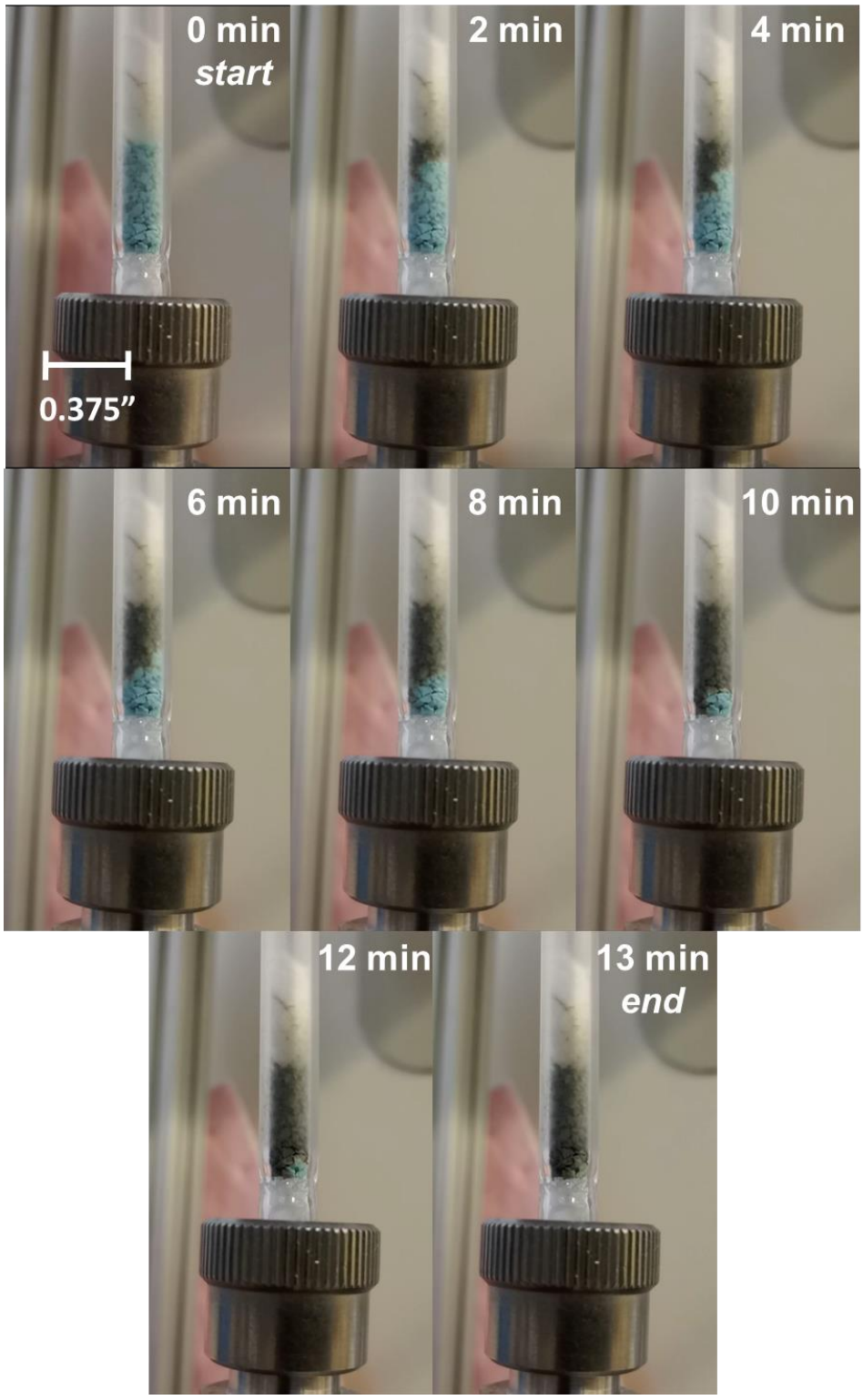

Figure 4-9: Time lapse of 5000ppm H_2S exposure on UiO-66-$(COOCu)_2$. Sample is located inside quartz glass tube in the images. Length scale bar is provided in top left image

Figure 4-10 compares adsorption capacities for all tested materials. As qualitatively apparent from Figure 4-8, MOFs containing -COOCu groups have significantly higher H_2S adsorption capacities than their non-functionalized counterparts. A 615% capacity increase in 0.5mol% H_2S is observed between UiO-66-COOH and UiO-66-COOCu, and a 100% increase results from UiO-66-$(COOH)_2$ to UiO-66-$(COOCu)_2$. Improvements in adsorption capacities of copper carboxylate-containing MOFs importantly arise from matching increases in breakthrough times, and not gradual post-breakthrough adsorption as seen with UiO-66-$(COOH)_2$ in Figure 4-7 and Figure 4-8b. Preventing long times without H_2S elution is desirable for applications mandating high purity outlet streams, as with natural gas and biogas remediation.[61,62] Notably, an uptake capacity of 2.94mmol H_2S g^{-1} for UiO-66-COOCu is competitive with commercial desulfurization media offered by Schlumberger.[63] H_2S capacities also outperform select carbonaceous and MOF-based sulfur scavengers listed in Table A-6, developed in previous literature. On the other hand, metalated frameworks decrease SO_2 adsorption capacity. The contrast between SO_2 and H_2S reactivity is caused by their interactions with accessible copper cations. Lewis acidic Cu^{2+} binding sites cannot interact favorably with the electrophilic sulfur atoms within SO_2. Conversely, sulfur-bound lone pair electrons in H_2S are readily donated to accessible cations, creating strong coordination bonds.

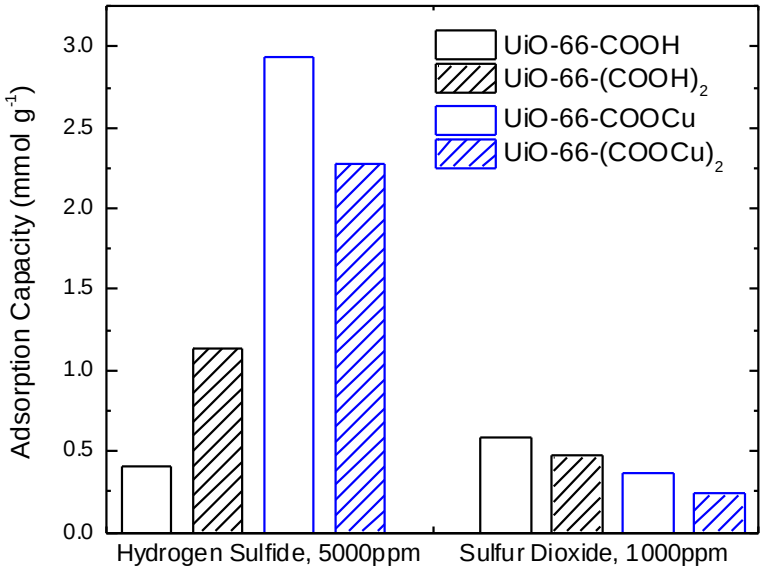

Figure 4-10: Bar graph of adsorption capacities for studied MOFs from fixed-bed experiments. Black bars represent frameworks containing carboxylic acid functionalities, blue bars represent materials containing copper carboxylate sites

4.3.1.5 Summary: Carboxylic Acid Groups Targeting Polar Acid Gas (SO_2, H_2S) Capture

The efficacy of framework -COOH groups as SO_2 and H_2S adsorption sites were evaluated. Multiple material characterization uncovered framework defects that result from UiO-66(Zr) production and integration of reactive -COOH sites. Identification of these defects explains the departure of expected adsorbent properties from predicted acid gas binding interactions and accessible adsorption surface areas in previous theoretical studies. Resulting UiO-66-COOH and UiO-66-$(COOH)_2$ materials displayed reversible acid gas binding interactions, and improved SO_2 and H_2S capture capabilities relative to the unfunctionalized UiO-66(Zr). Therefore, it was determined the introduction of pendant -COOH groups benefits acid gas sequestration.

Uncoordinated carboxylic acid groups in tested adsorbents also enable irreversible H_2S adsorption after conversion to copper carboxylates (-COOCu). UiO-66-COOCu and UiO-66-$(COOCu)_2$ displayed significant improvements in H_2S breakthrough times and adsorption capacities from parent UiO-66-COOH and UiO-66-$(COOH)_2$ materials. Aside from adsorption applications, the apparent color change upon dilute H_2S exposure suggests metalated frameworks may have usefulness in gas sensing applications as well. These functionalities were non-reactive with SO_2 however, and underperformed UiO-66-COOH and UiO-66-$(COOH)_2$ frameworks in SO_2 uptake. Kinetic data suggests framework accessibility dictates adsorption performance amongst evaluated materials, where UiO-66-$(COOH)_2$ and UiO-66-$(COOCu)_2$ exhibit lower breakthrough capacities for probed acid gases at test concentrations than UiO-66-COOH and UiO-66-COOCu, despite their expectedly higher concentration of respective -COOH and -COOCu binding sites. This work provides design heuristics to instill reversible and irreversible acid gas binding in chemically stable MOF systems.

4.3.2 Probing Metal-Organic Framework Design for Adsorptive Natural Gas Purification

4.3.2.1 Primary Amine (-NH_2) Functionalized Frameworks for Sour Gas Remediation

As with pendant -COOH functionalities, primary amines (-NH_2) offer advantageous chemistry for acid gas capture. Amines are famously employed in traditional aqueous scrubbing media.[64] They are also appended onto silicas using aminosilanes[65–67], and more recently MOFs[68,69], to enhance capture of acid gases such as CO_2 and H_2S. In aforementioned studies, amine chains are long and flexible. These traits with primary and

secondary amines facilitate strong CO_2 capture capabilities through carbamate formation via interacting amine chains, and similar reactive H_2S binding.[70] Although beneficial for gas removal, this reactivity hinders H_2S/CO_2 selectivity, especially since typically encountered H_2S concentrations are a magnitude lower than those of CO_2. Primary amines appended on MOF ligands are conversely rigid. This is apparent in the structure of 2-aminoterephthalic acid (BDC-NH_2), a commonly utilized linker to imbue ligand-based amines into frameworks, where *ortho* -NH_2 groups relative to coordinating -COOH functionalities are restrained directly onto the phenyl ring. Amines furthermore become regularly partitioned from one another in the ordered structures of crystalline MOFs. Consequently, ligand-based amines in MOFs cannot freely interact with one another, and are instead relegated to electrostatic interactions with CO_2 and H_2S. Comparing the two adsorbates, the dipole moment and stronger electronegativity of sulfur on H_2S is predicted to outcompete weak CO_2 quadrapole attractions for inflexible primary amine bonding sites.

Through this hypothesis, detailed studies below aim to build upon the presently limited understanding of H_2S removal from natural gas related mixtures using MOFs. Favorable interactions between primary amines and acid gas adsorbates are leveraged to enhance H_2S capture through exploring the effects of linker-based amine (-NH_2)-MOF functionalization on adsorptive sour gas purification. Three well-studied, stable MOFs previously demonstrated to allow functionalization via linker-based amines[31–34] are examined as candidate frameworks: UiO-66(Zr), MIL-101(Cr), MIL-125(Ti). Their respective amine analogues are all constructed using 2-aminoterephalic acid as a framework ligand. Materials were chosen due to their previously reported H_2S stability and facile ability for amine functionalization, making them promising candidate adsorbents for

cyclable H_2S capture. Results from this study will serve to reveal desirable framework qualities for cyclable and selective H_2S removal in MOF-based adsorbent materials.

4.3.2.2 Multicomponent Adsorption Experiments on Candidate Adsorbents

Fixed-bed adsorption experiments for candidate frameworks were first examined using a 1% H_2S/CH_4 challenge gas. Desorption was performed by purging with helium at ambient temperature. Adsorption-desorption cycles for each MOF are presented in Figure A-28 to Figure A-33. All materials exhibit a decrease in uptake capacity following the first cycle. This is likely due to hydrogen sulfide retention between cycles. As previously discussed in Section 3.2.5.1 surface areas and crystalline features of stable materials (UiO-66 and MIL-125) are unchanged after heated activation and vacuum. Subsequently, the initial adsorption capacity losses observed are not indicative of degradation.

Measured uptake capacities for UiO-66(Zr), UiO-66-NH_2(Zr), and MIL-101(Cr) are all lower than previously reported from fixed-bed experiments at the same partial pressure of H_2S by Zou and coworkers,[18] albeit their experiments used balance He carrier gas instead of CH_4. Methane is largely non-adsorbing at room temperature with the selected MOFs, even at its high partial pressure relative to hydrogen sulfide.[7,8,28] Considering this, a comparison of H_2S uptake was performed for using methane and inert carrier N_2 for the same inlet H_2S concentration (1%). Using UiO-66-NH_2(Zr) as an example, the data in Figure A-23 evidences a clear decrease in H_2S adsorption when using CH_4 as a carrier gas, compared to N_2. These observations highlight the importance of evaluating sour gas adsorbents in the presence of even weakly adsorbing natural gas constituents to gauge competitive adsorption effects. The saturation capacity of UiO-66-NH_2(Zr) in 1% H_2S/N_2

(0.576 mmol H_2S g^{-1}) is still less than the 0.909 mmol H_2S g^{-1} capacity reported by Zou and coworkers[18] for a similar mixture. However, it should be noted that the previous study utilized an acid modulator in their synthesis of UiO-66-NH_2(Zr), whereas a non-modulated production scheme was utilized in this study. Comparison of N_2 uptake isotherms at 77K for the MOF between Zou et al. and here in Figure A-14 reveals a higher accessible microporosity for the MOF in the previous report. Modulated UiO-66(Zr) materials are well known to obtain enhanced internal pore volumes and surface areas through induced defects.[36,71–73] So the lower H_2S capacity for UiO-66-NH_2(Zr) in the 1% H_2S/N_2 mixture measured here is consequent of the smaller accessible adsorption surface per mass available for H_2S binding, which is descriptive of the textural properties for the non-modulated MOF utilized in this study. Acknowledging these differences across studies helps provide some metric for expected deviations in adsorption results across disparate processing conditions for MOF-based adsorbents.[74]

Integration of linker-based primary amines enhanced H_2S uptake in the 1% H_2S/CH_4 mixture for all three parent frameworks. The degree to which H_2S uptake increased is dependent on the textural properties of the three frameworks. Breakthrough times for the materials in Figure 4-11a-c reveal MIL-101-NH_2(Cr) alone does not exhibit a significant enhancement in 1% H_2S uptake after the addition of primary linker-based amines, at least in comparison to the other MOFs. This result is attributed to enhanced adsorption interactions of H_2S with the smaller pore environments of UiO-66(Zr) and MIL-125(Ti). Calculated pore sizes from previous studies suggest ranking of MIL-125(Ti) < UiO-66(Zr) < MIL-101(Cr) from smallest to largest pore size—also supported by the pore size distribution in Figure A-15.[8,75,76] In this work, only MIL-101(Cr) MOFs are

mesoporous. Ligand-based binding sites consequently exist in smaller pores within UiO-66(Zr) and MIL-125(Ti) structures. The larger pore diameters and cage sizes of MIL-101(Cr) weaken physisorption interactions between framework $–NH_2$ and –OH functionalities and adsorbed H_2S. It should be restated the previously discussed partial degradation in MIL-101-NH_2(Cr) may also reduce improvement in H_2S breakthrough time, as seen in a similar adsorption study by Peterson *et al.* for HKUST-1 and UiO-66(Zr).[77]

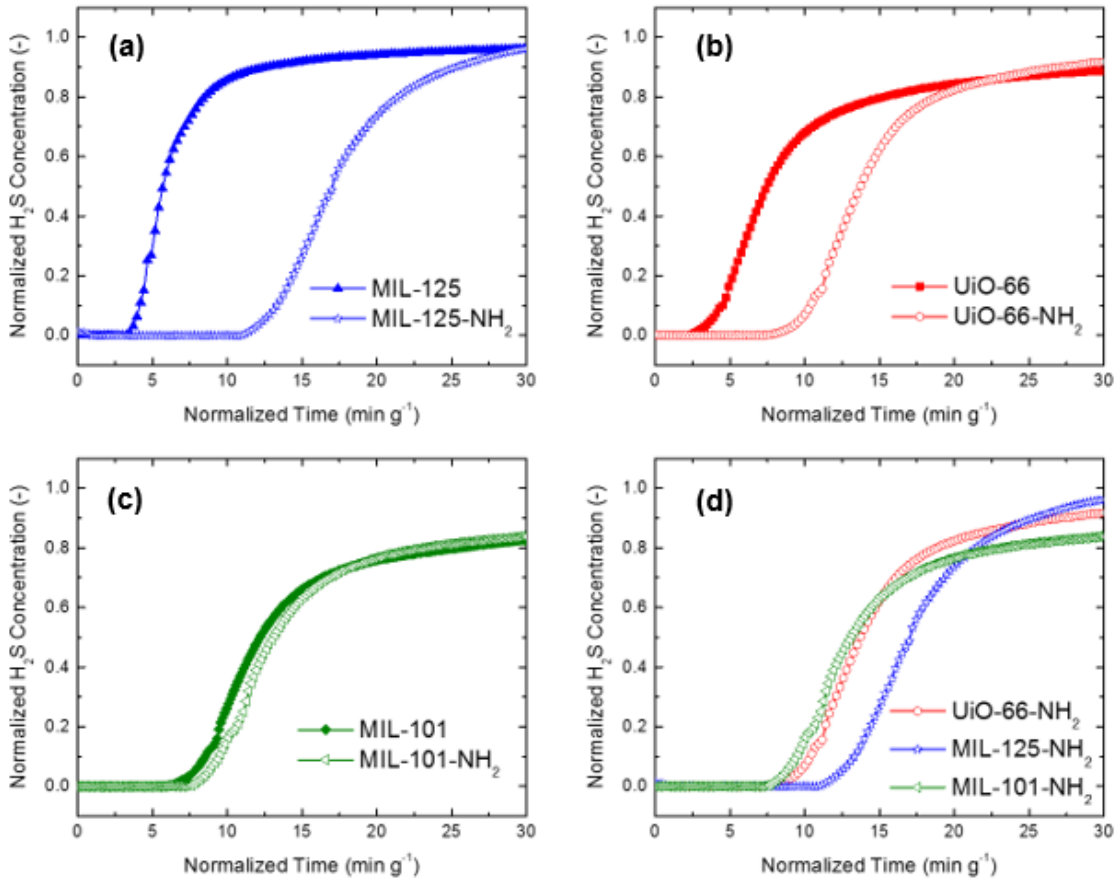

Figure 4-11: 1% H_2S/CH_4 breakthrough curves at 20°C for parent and -NH_2 containing analogues of (a) MIL-125(Ti) (b) UiO-66(Zr) (c) MIL-101(Cr) (d) all –NH_2 functionalized materials

Dynamic adsorption curves for amine-functionalized samples in the 1% H_2S/CH_4 mixture are compared in Figure 4-11d**.** MIL-125-NH_2(Ti) exhibited the greatest H_2S

removal performance amongst candidate MOFs, with a saturation capacity of 0.559 mmol H_2S g^{-1} in the 99% CH_4 mixture. This is also the largest increase (~170%) in H_2S capacity from the parent MOF (unfunctionalized MIL-125) observed in this study. Later discussion on MIL-125-NH_2(Ti) hydroxyl and primary amine site sensitivity to adsorbing H_2S, investigated through *in situ* FTIR experiments, elaborates more on this phenomenon.

Carbon dioxide (CO_2) is another nearly-ubiquitous natural gas constituent. Considering this, mixture complexity was increased to test the candidate MOF adsorbents using a 1% H_2S/10% CO_2/CH_4 challenge gas. Breakthrough curves for all MOFs display a roll-up effect for CO_2 upon adsorption in the new mixture—delineated through Figure A-34 to Figure A-39. Roll-up, especially for heavier components, typically indicates the displacement of a weaker adsorbate by a stronger one in multicomponent, fixed-bed adsorption processes.[78] Uptake curves suggest H_2S preferentially binds to frameworks over CO_2 at the concentrations evaluated in this study. Microporous UiO-66(Zr)-NH_2 and MIL-125-NH_2(Ti) qualitatively exhibit more pronounced roll-up of CO_2 than their parent frameworks, suggesting stronger interactions of H_2S with accessible -NH_2 sites over CO_2. Amine groups facilitate greater CO_2 uptake at low partial pressures. As such, comparatively more adsorbed CO_2 is displaced during roll-up in amine-functionalized samples. The opposite phenomenon is interestingly observed for MIL-101(Cr) and MIL-101-NH_2(Cr). However, the previously discussed degradation for H_2S-exposed MIL-101(Cr) materials reduces pore accessibility and partially destroys the structure—restricting adsorption interactions with–NH_2 and –OH binding sites on MIL-101-NH_2(Cr).

Figure 4-12 illustrates the tendency of MIL-101-NH_2(Cr) to ignore CO_2 competitive adsorption effects. Unlike mesoporous MIL-101-NH_2(Cr), the other two

amine-functionalized frameworks experience more significant losses in H_2S capacity after introduction of CO_2. Adsorption measurements demonstrate the impact of pore environment on integrated linker-based moieties acting as adsorption sites for target molecules. The smaller pores of UiO-66(Zr) and MIL-125(Ti) facilitate CO_2 adsorption at its relatively low partial pressure, enhancing interactions of the adsorbate with framework physisorption sites. Breakthrough behavior of the parent frameworks in Figure 4-13 supports this. The adsorption characteristics of MIL-101(Cr) are largely unchanged with added CO_2, demonstrated by the relatively lower reduction in H_2S breakthrough time in comparison to the microporous frameworks. Hindrance of stronger CO_2 adsorption in the larger pores of MIL-101(Cr) and MIL-101-NH_2(Cr) therefore mitigates more evident adsorption competition experienced with UiO-66(Zr) and MIL-125(Ti) materials. For MOFs containing linker-based amines, the rigidity and regulated partitioning of these functionalities restricts their interactions with molecules like CO_2 to weak physisorption (evidenced later in FTIR experiments), as opposed to the stronger adsorption behavior of CO_2 observed in materials impregnated with flexible primary amines.[69,79–81] Adsorption interactions are further hindered in MOFs with larger pores, as seen across non-functionalized MOFs in Figure 4-13. These observations importantly serve as a design heuristic for integrating gas capture selectivity in MOFs—installation of linker-based functionalities in relatively larger pore environments reduces adsorption competition between adsorbate species.

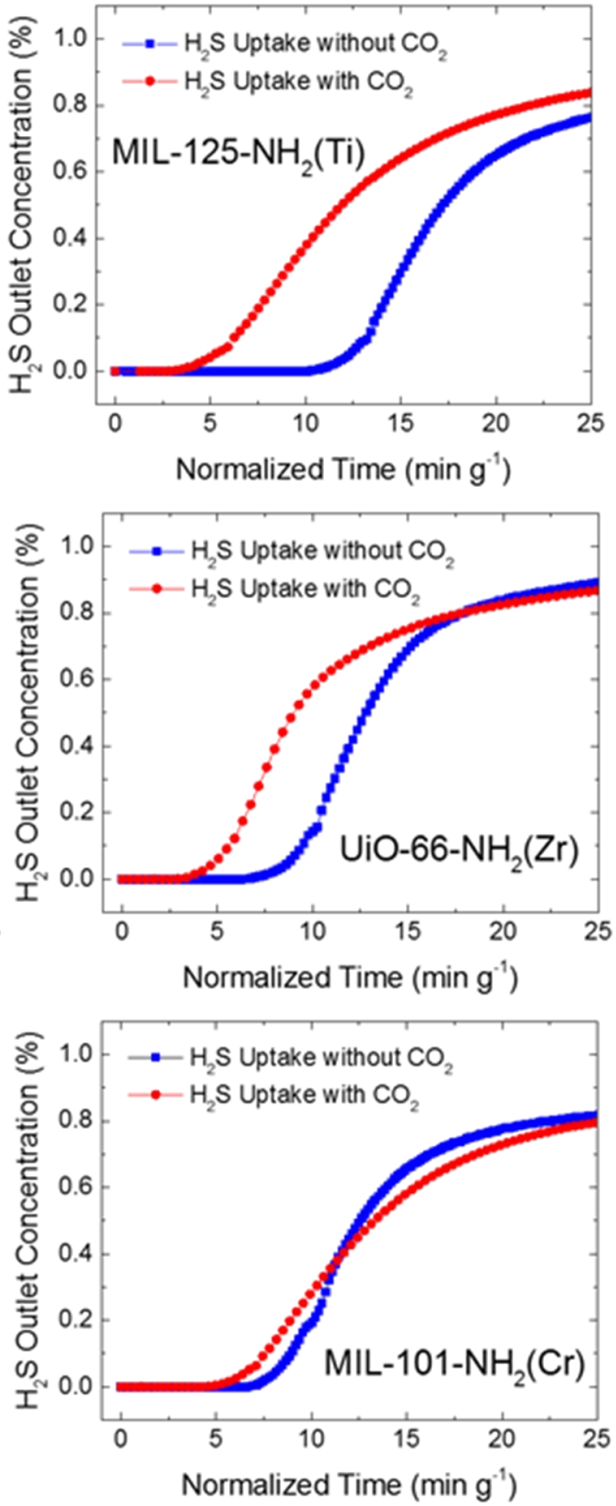

Figure 4-12: H_2S breakthrough curves, organized top-to-bottom by increasing mean cage size, for -NH_2 functionalized materials under 1% H_2S/CH_4 (blue) and 1% H_2S/10% CO_2/89% CH_4 (red) mixtures. Tested at 20°C.

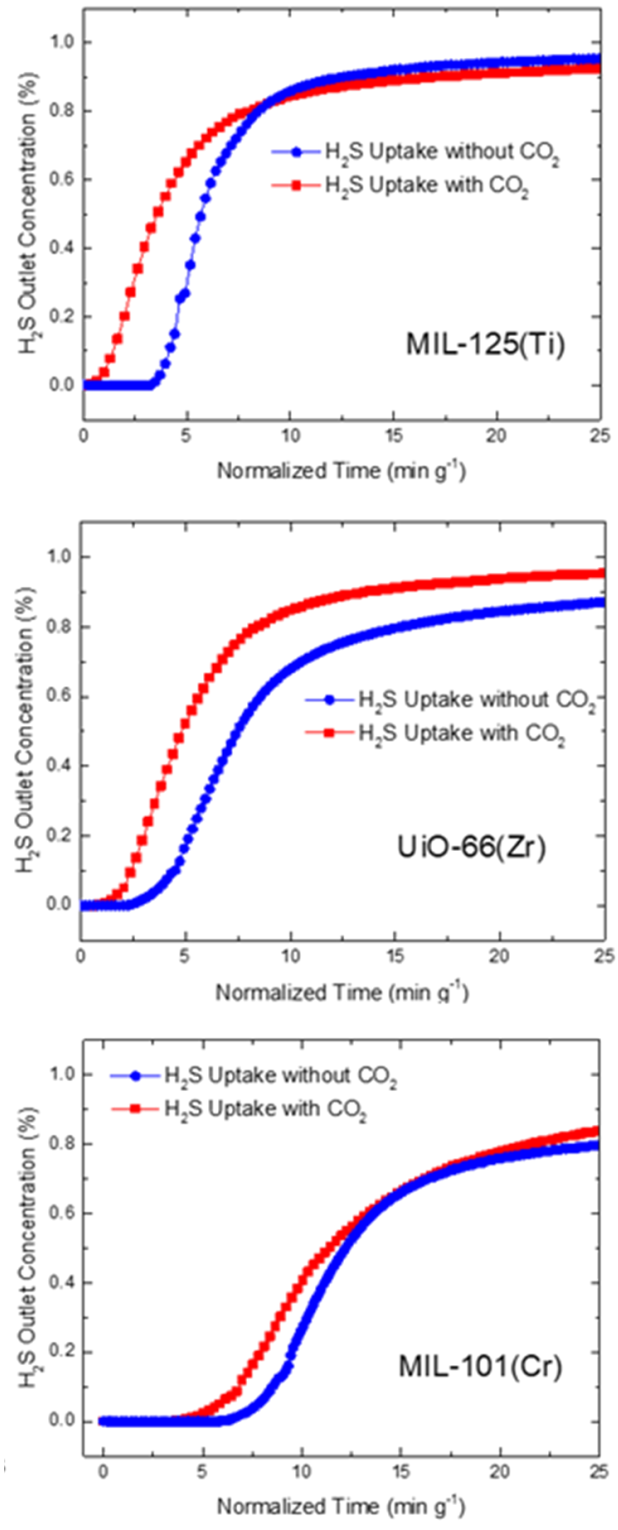

Figure 4-13: H_2S breakthrough curves organized top-to-bottom by increasing mean cage size, for non-functionalized MOF materials under 1% H_2S/CH_4 (blue) and 1% H_2S/10% CO_2/89% CH_4 (red) mixtures. Tested at 20°C.

MIL-125-NH_2(Ti) displaced MIL-101-NH_2(Cr) as the material with the largest H_2S saturation capacity when using the 1% H_2S/10% CO_2/CH_4 mixture. The importance of adding multicomponent complexity is clearly demonstrated by this change in adsorbent ranking. This dynamic is not easily discerned from comparing single-component isothermal uptake measurements, or previous fixed-bed adsorption studies utilizing H_2S mixtures with inert balances (e.g., He, N_2). Saturation capacities for all materials in both 1% H_2S/CH_4 and 1% H_2S/10% CO_2/CH_4 are provided in Figure 4-14. The markedly lower accessible BET surface area of UiO-66-NH_2(Zr) compared to MIL-125-NH_2(Ti) and MIL-101-NH_2(Cr), even after pelletization, likely caused this MOF to possess the lowest H_2S saturation capacity of the primary amine containing adsorbents in both mixtures. H_2S adsorption capacities for MIL-101(Cr) materials in the methane carrier gas here are similar to those reported by Zou and coworkers[18] using 1% H_2S/10% CO_2/89% He breakthrough experiments. Significant methane adsorption competition at low pressures is unexpected in the mesoporous adsorbent, which explains why the fixed-bed results are comparable to those acquired with an inert He carrier gas. Because methane is a major constituent in natural gas, the relative insensitivity of MIL-101(Cr) to methane competition is beneficial for selective H_2S removal. In contrast to MIL-101(Cr), the H_2S capacities measured here for UiO-66-NH_2(Zr) for 1% H_2S/CH_4 and 1% H_2S/10% CO_2/CH_4 mixtures are significantly lower than the 0.909 mmol g^{-1} capacity reported by Zou and coworkers.[18] As previously explained, this is ascribed to synthesis differences with the previous study. Still, the ~50% lower H_2S saturation capacity measured in 1% H_2S/99% CH_4 here suggests competitive binding effects from methane reduce H_2S adsorption performance in small-pore UiO-66-NH_2(Zr). All H_2S saturation capacities exhibit order-of-magnitude agreement

with previous calculations and/or equilibrium H_2S adsorption experiments (previous data not available for MIL-101-NH_2) around $P/P_0 = 0.01$.[5,7,8,18]

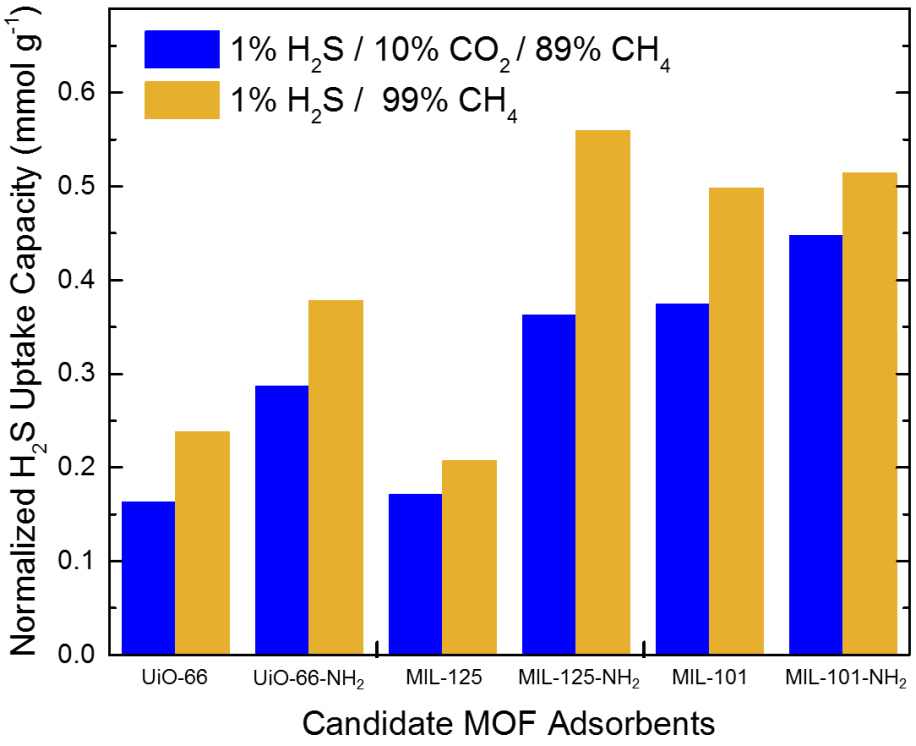

Figure 4-14: Bar graph of H_2S saturation capacities for studied materials under 1% H_2S / 99% CH_4 (gold) and 1% H_2S / 10% CO_2 / 89% CH_4 (blue) challenge mixtures, tested at 20°C.

4.3.2.3 FTIR Investigation of Carbon Dioxide Binding

In situ diffuse reflectance infrared spectroscopy (DRIFTS) experiments in 10% CO_2 and 5000 ppm H_2S environments were conducted to further understand differences in adsorption behavior among –NH_2 functionalized materials. Spectra for MOFs before and after CO_2 adsorption are presented in Figure 4-15. Physisorbed CO_2 is apparent near 2341 cm^{-1} after subtraction of gaseous CO_2.[82] Chemisorbed CO_2 (1800-1300 cm^{-1}) is not evidenced.[70] Interestingly, features in the -OH stretch region for MIL-101-NH_2(Cr) are

greatly varied and low in absorbance intensity following activation, unlike the other two MOFs. The evacuation of capping water molecules from Cr^{3+} metal sites following degas has been previously reported.[83] As a potential binding site for both CO_2 and H_2S, the absence of hydroxyl groups could partially explain the relatively small H_2S uptake change after CO_2 addition shown previously in Figure 4-12. Noticeable changes in the hydroxyl stretches 3800 cm^{-1} to 3600 cm^{-1} for UiO-66-NH_2(Zr) and MIL-125-NH_2(Ti) in Figure 4-16 and Figure A-40 (expanded hydroxyl and amine stretch regions presented from Figure A-41 to Figure A-46 in Appendix A) support this hypothesis. These perturbations again help explain more significant H_2S capacity decreases in the presence of CO_2 for UiO-66-NH_2(Zr) and MIL-125-NH_2(Ti) than observed for MIL-101-NH_2(Cr). Multiple –OH stretches in the FTIR spectrum for UiO-66-NH_2(Zr) indicate either remaining water or linker defects inherently present following synthesis of UiO-66(Zr) type materials.[42,84,85] Primary amine stretches contrastingly remain static following CO_2 exposure. This suggests MOF linker-based amines do not serve as favorable CO_2 physisorption sites at the tested partial pressure. Alternatively, linker-based $–NH_2$ groups are weaker CO_2 physisorption sites than framework hydroxyl groups at tested conditions. A previous study on UiO-66-NH_2(Zr) by Bordiga and coworkers[86] also noted the relative insensitivity of linker-based primary amine stretches to CO_2 binding under IR, despite calculations identifying electronic interactions of the adsorbate with framework $–NH_2$ groups. FTIR results for CO_2 adsorption here are consistent with this previous finding.

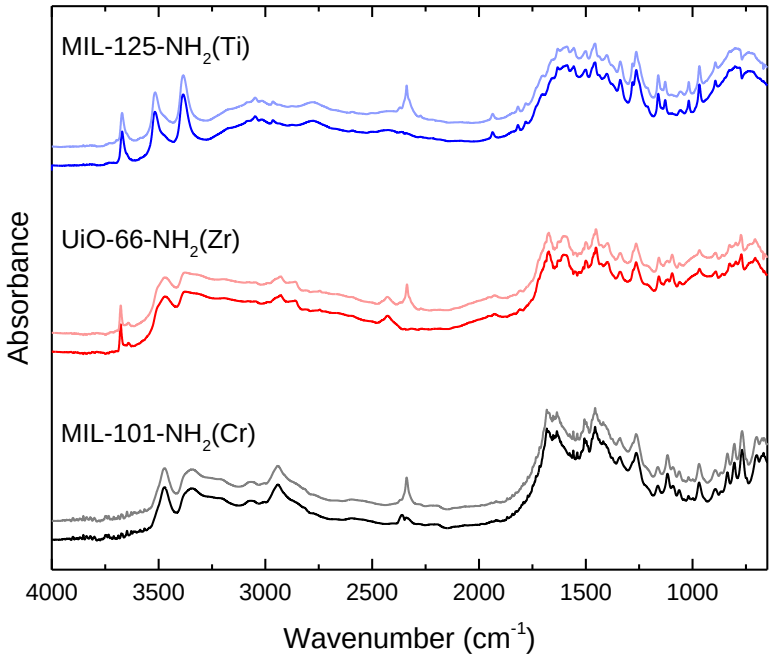

Figure 4-15: DRIFTS measurements collected for activated (bottom) and exposed (top) samples. Spectra were acquired after 15 minutes of 10% CO_2 exposure. Data are shown after gaseous CO_2 subtraction

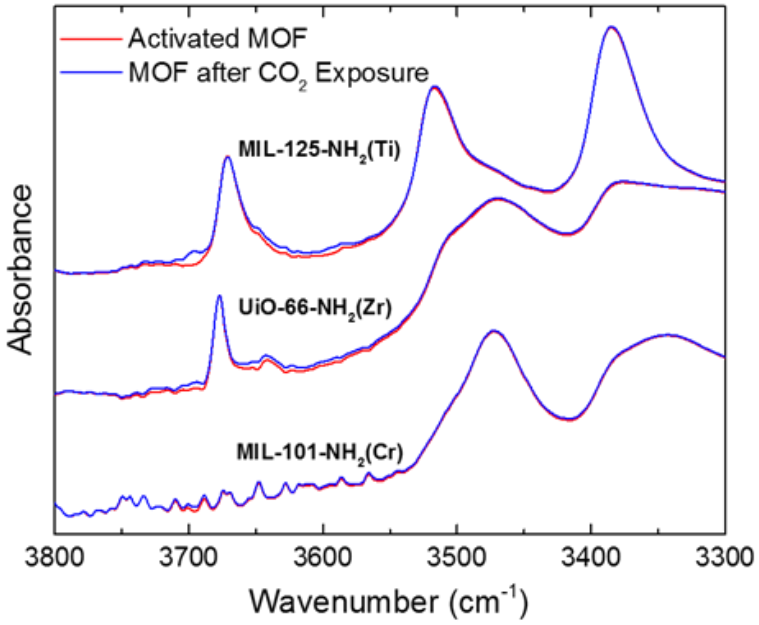

Figure 4-16: FTIR spectra in hydroxyl and primary amine stretching regions for all MOFs before and after 10% CO_2/He exposure

4.3.2.4 FTIR Investigation of Hydrogen Sulfide Binding

Time resolved FTIR spectra over 45 min of H_2S exposure for activated MOFs are illustrated in Figure 4-17. Minor shifts in the hydroxyl and amine stretching regions are observed upon H_2S exposure. In MIL-101-NH_2(Cr), the low absorbance intensity of hydroxyl spectral features makes it unclear if detected changes in Figure 4-17a are representative of lingering hydroxyl groups or other guest molecules (e.g., H_2O, solvents) interacting with adsorbing H_2S. Still, changes in the hydroxyl stretch region are observed for all materials, denoting the importance of these moieties for H_2S binding. Primary amine stretch perturbations in UiO-66-NH_2(Zr) are not evidenced in Figure 4-17b. This may suggest H_2S at tested partial pressures does not significantly interact with linker-based amines in this framework. The small magnitude of changes with $–NH_2$ groups are partially due to resolution limitations in DRIFTS. However, they are also indicative of weak physisorption interactions between H_2S and pendant amine moieties. Slight spectral shifts of $–NH_2$ and –OH stretches observed for the MOFs in the presence of H_2S suggest the increase in H_2S affinity for amine-incorporated materials seen previously in breakthrough experiments are due to H_2S interactions with these framework species. Weak H_2S binding also explains porosity recovery in previously discussed post-exposure N_2 physisorption experiments after degassing under heat and vacuum. These subtle binding interactions with framework groups are expected from previous studies. For instance, weak hydrogen bonding on linker-based $–NH_2$ groups were proposed by Vaesen et al.[8] through similar FTIR experiments and GCMC simulations on MIL-125-NH_2(Ti). The inherent restriction of linker-based amine interactions with H_2S to weak physisorption observed through FTIR measurements is consequent of the inflexible and regularly-partitioned primary amines on

bridging linkers, which discourage stronger cooperative binding interactions among multiple -NH_2 functionalities. This importantly lends potential for cycled, regenerable H_2S adsorption, facilitated by simple MOF construction using modified ligands.

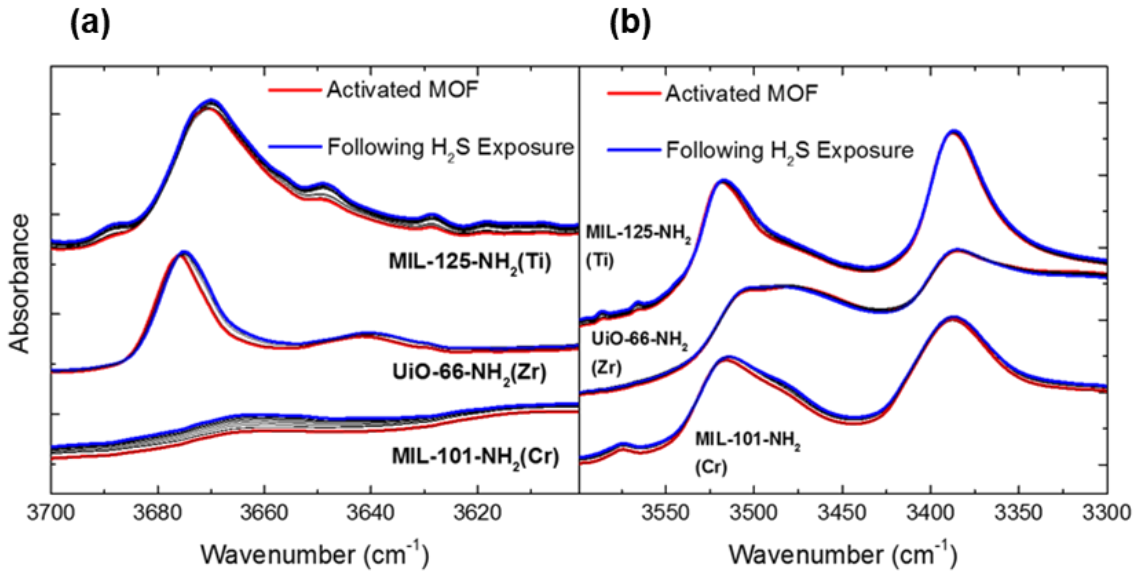

Figure 4-17: FTIR spectra in hydroxyl and primary amine stretching regions for all MOFs (after 0.5 % H_2S/N_2 exposure in (a) hydroxyl (-OH) stretching region and (b) primary amine stretching region.

4.3.2.5 Summary: Probing Metal-Organic Framework Design for Adsorptive Natural Gas Purification

To compare the effectiveness of MOFs for hydrogen sulfide (H_2S) removal from natural gas, the commonly studied frameworks UiO-66(Zr), MIL-125(Ti), MIL-101(Cr), and their amine-functionalized analogues were evaluated for their H_2S stability and removal capacities using fixed-bed experiments with 1% H_2S/99% CH_4 and 1% H_2S/10% CO_2/89% CH_4 test mixtures.

Adsorption experiments revealed linker-based amines enhance the H_2S uptake capacity in all materials. For mixtures containing CO_2, MIL-101-NH_2(Cr) portrayed the greatest H_2S saturation capacity and breakthrough time among studied adsorbents. FTIR measurements demonstrated that –OH groups in microporous materials also behaved as CO_2 physisorption sites, but were absent in activated mesoporous MIL-101-NH_2(Cr).

Adsorption data reported here benchmark selective H_2S removal capabilities from natural gas using MOFs. Linker-based amine functionalization in smaller pore MOFs significantly enhanced H_2S breakthrough time as compared to their respective parent materials. Mitigated H_2S uptake loss with ternary mixtures in mesoporous MIL-101(Cr), as compared to smaller pore (< 1 nm) adsorbents, suggests installation of linker-based amines in larger pore frameworks affords greater H_2S/CO_2 adsorption selectivity in sour gas mixtures. Changes in adsorption performance with mixture complexity also illustrate the importance of screening adsorbents in multicomponent mixtures related to those encountered in well-head natural gas. Future work should conduct multicomponent adsorption investigations with extensions to other common natural gas species (e.g., water vapor, mercaptans, C_2-C_6 hydrocarbons) to discover other favorable design traits in next-generation sour gas adsorbents.

4.4 Chapter 4 References

1. Liu, W., Vidic, R. D. & Brown, T. D. Impact of Flue Gas Conditions on Mercury Uptake by Sulfur-Impregnated Activated Carbon. *Environ. Sci. Technol.* **34**, 154–159 (1999).

2. Hammer, G. *et al.* Natural Gas. *Riegel's Handbook of Industrial Chemistry*, 10th Ed.; 545–569 (Springer: 2003).

3. Al-Jadir, T. & Siperstein, F. Monte Carlo Simulation of Adsorption of Polar and Nonpolar Gases in (FP)YEu Metal–Organic Framework. *J. Chem. Eng. Data* **61**, 4209–4214 (2016).

4. Gutiérrez-Sevillano, J. J., Martín-Calvo, A., Dubbeldam, D., Calero, S. & Hamad, S. Adsorption of hydrogen sulphide on Metal-Organic Frameworks. *RSC Adv.* **3**, 14737–14749 (2013).

5. Li, Z. *et al.* Capture of H_2S and SO_2 from trace sulfur containing gas mixture by functionalized UiO-66(Zr) materials: A molecular simulation study. *Fluid Phase Equilib.* **427**, 259–267 (2016).

6. Hamon, L. *et al.* Molecular Insight into the Adsorption of H_2S in the Flexible MIL-53 (Cr) and Rigid MIL-47 (V) MOFs : Infrared Spectroscopy Combined to Molecular Simulations. *J. Phys. Chem. C* **115**, 2047–2056 (2011).

7. Hamon, L. *et al.* Comparative Study of Hydrogen Sulfide Adsorption in the MIL-53 (Al, Cr, Fe), MIL-47 (V), MIL-100 (Cr), and MIL-101 (Cr) Metal- Organic Frameworks at Room Temperature. *J. Am. Chem. Soc.* **131**, 8775–8777 (2009).

8. Vaesen, S. *et al.* A robust amino-functionalized titanium(IV) based MOF for improved separation of acid gases. *Chem. Commun.* **49**, 10082–10084 (2013).

9. Song, J. *et al.* A Multiunit Catalyst with Synergistic Stability and Reactivity: A Polyoxometalate-Metal Organic Framework for Aerobic Decontamination. *J. Am. Chem. Soc.* **133**, 16839–16846 (2011).

10. Huang, P.-H. Molecular dynamics investigation of separation of hydrogen sulfide from acidic gas mixtures inside metal-doped graphite micropores. *Phys. Chem. Chem. Phys.* **17**, 22686–22698 (2015).

11. Watanabe, T. & Sholl, D. S. Molecular chemisorption on open metal sites in Cu_3 (benzenetricarboxylate)$_2$: A spatially periodic density functional theory study. *J. Chem. Phys.* **133**, 094509 (2010).

12. Nijem, N., Fursich, K., Bluhm, H., Leone, S. R. & Gilles, M. K. Ammonia Adsorption and Co-adsorption with Water in HKUST-1: Spectroscopic Evidence for Cooperative Interactions. *J. Phys. Chem. C* **119**, 24781–24788 (2015).

13. Myers, A. L. & Prausnitz, J. M. Thermodynamics of Mixed-Gas Adsorption. *AIChE J.* **11**, 121–126 (1965).

14. Walton, K. S. & Sholl, D. S. Predicting Multicomponent Adsorption: 50 Years of the Ideal Adsorbed Solution Theory. *AIChE J.* **61**, 2757–2762 (2015).

15. Bhatt, P. M. *et al.* Isoreticular rare earth fcu-MOFs for the selective removal of H_2S from CO_2 containing gases. *Chem. Eng. J.* **324**, 392–396 (2017).

16. Belmabkhout, Y. *et al.* Metal-Organic Frameworks to Satisfy Gas Upgrading Demands: Fine-tuning the soc-MOF platform for the Operative Removal of H_2S. *J. Mater. Chem. A* **5**, 3293–3303 (2017).

17. Liu, G. *et al.* Mixed matrix formulations with MOF molecular sieving for key energy-intensive separations. *Nat. Mater.* **17**, 283–289 (2018).

18. Liu, J., Wei, Y., Li, P., Zhao, Y. & Zou, R. Selective H_2S/CO_2 Separation by Metal−Organic Frameworks Based on Chemical-Physical Adsorption. *J. Phys. Chem. C* **121**, 13249–13255 (2017).

19. Heinen, J., Burtch, N. C., Walton, K. S., Fonseca Guerra, C. & Dubbeldam, D. Predicting Multicomponent Adsorption Isotherms in Open-Metal Site Materials Using Force Field Calculations Based on Energy Decomposed Density Functional Theory. *Chem. - A Eur. J.* **22**, 18045–18050 (2016).

20. Chavan, S. *et al.* Fundamental Aspects of H_2S Adsorption on CPO-27-Ni. *J. Phys. Chem. C* **117**, 15615–15622 (2013).

21. Bobbitt, N. S. *et al.* Metal–organic frameworks for the removal of toxic industrial chemicals and chemical warfare agents. *Chem. Soc. Rev.* **46**, 3357–3385 (2017).

22. Petit, C., Mendoza, B. & Bandosz, T. J. Hydrogen sulfide adsorption on MOFs and MOF/Graphite oxide composites. *ChemPhysChem* **11**, 3678–3684 (2010).

23. Britt, D. K., Tranchemontagne, D. & Yaghi, O. M. Metal-organic frameworks with high capacity and selectivity for harmful gases. *Proc. Natl. Acad. Sci. U. S. A.* **105**, 11623–11627 (2008).

24. Ragon, F. *et al.* Acid-functionalized UiO-66(Zr) MOFs and their evolution after intra-framework cross-linking: structural features and sorption properties. *J. Mater. Chem. A* **3**, 3294–3309 (2015).

25. Wang, S. *et al.* Computational exploration of H_2S/CH_4 mixture separation using acid-functionalized UiO-66(Zr) membrane and composites. *Chinese J. Chem. Eng.* **23**, 1291–1299 (2015).

26. Jasuja, H., Peterson, G. W., Decoste, J. B., Browe, M. a. & Walton, K. S. Evaluation of MOFs for air purification and air quality control applications: Ammonia removal from air. *Chem. Eng. Sci.* **124**, 118–124 (2015).

27. Cmarik, G. E., Kim, M., Cohen, S. M. & Walton, K. S. Tuning the Adsorption Properties of UiO-66 via Ligand Functionalization. *Langmuir* **28**, 15606–15613 (2012).

28. Jasuja, H. & Walton, K. S. Experimental Study of CO_2 , CH_4 , and Water Vapor Adsorption on a Dimethyl-Functionalized UiO-66 Framework. *J. Phys. Chem. C* **117**, 7062–7068 (2013).

29. Hu, Y., Verdegaal, W. M., Yu, S.-H. & Jiang, H.-L. Alkylamine-Tethered Stable Metal-Organic Framework for CO_2 Capture from Flue Gas. *ChemSusChem* **7**, 734–737 (2014).

30. Jiang, Z.-R., Wang, H., Hu, Y., Lu, J. & Jiang, H.-L. Polar Group and Defect Engineering in a Metal-Organic Framework: Synergistic Promotion of Carbon Dioxide Sorption and Conversion. *ChemSusChem* **8**, 878–885 (2015).

31. Peterson, G. W., DeCoste, J. B., Fatollahi-Fard, F. & Britt, D. K. Engineering UiO-66-NH_2 for Toxic Gas Removal. *Ind. Eng. Chem. Res.* **53**, 701–707 (2014).

32. Schoenecker, P. M., Carson, C. G., Jasuja, H., Flemming, C. J. J. & Walton, K. S. Effect of Water Adsorption on Retention of Structure and Surface Area of Metal–Organic Frameworks. *Ind. Eng. Chem. Res.* **51**, 6513–6519 (2012).

33. Jiang, D., Keenan, L. L., Burrows, A. D. & Edler, K. J. Synthesis and post-synthetic modification of MIL-101(Cr)-NH_2 via a tandem diazotisation process. *Chem. Commun.* **48**, 12053–12055 (2012).

34. Zlotea, C. *et al.* Effect of NH_2 and CF_3 functionalization on the hydrogen sorption properties of MOFs. *Dalt. Trans.* **40**, 4879–4881 (2011).

35. Walton, K. S. & Snurr, R. Q. Applicability of the BET method for determining surface areas of microporous metal-organic frameworks. *J. Am. Chem. Soc.* **129**, 8552–8556 (2007).

36. Jiao, Y. *et al.* Heat-Treatment of Defective UiO-66 from Modulated Synthesis: Adsorption and Stability Studies. *J. Phys. Chem. C* **121**, 23471–23479 (2017).

37. Pawley, G. S. Unit-cell refinement from powder diffraction scans. *J. Appl. Crystallogr.* **14**, 357–361 (1981).

38. Biswas, S. *et al.* Enhanced selectivity of CO_2 over CH_4 in sulphonate-, carboxylate- and iodo-functionalized UiO-66 frameworks. *Dalt. Trans.* **42**, 4730–4737 (2013).

39. Biswas, S. & Van Der Voort, P. A general strategy for the synthesis of functionalised UiO-66 frameworks: Characterisation, stability and CO_2 adsorption properties. *Eur. J. Inorg. Chem.* 2154–2160 (2013). doi:10.1002/ejic.201201228

40. Cavka, J. H. *et al.* A new zirconium inorganic building brick forming metal organic frameworks with exceptional stability. *J. Am. Chem. Soc.* **130**, 13850–13851 (2008).

41. Schaate, A. *et al.* Modulated synthesis of Zr-based metal-organic frameworks: from nano to single crystals. *Chem. Eur. J.* **17**, 6643–51 (2011).

42. Fang, Z., Bueken, B., De Vos, D. E. & Fischer, R. A. Defect-Engineered Metal-Organic Frameworks. *Angew. Chemie Int. Ed.* **54**, 7234–7254 (2015).

43. Cliffe, M. J. *et al.* Correlated defect nanoregions in a metal-organic framework. *Nat. Commun.* **5**, (2014).

44. Valenzano, L. *et al.* Disclosing the complex structure of UiO-66 metal organic framework: A synergic combination of experiment and theory. *Chem. Mater.* **23**, 1700–1718 (2011).

45. Lambert, J. B. *Organic Structural Spectroscopy*. (Prentice-Hall, Inc: Upper Saddle River, NJ 1998).

46. Reimer, N., Gil, B., Marszalek, B. & Stock, N. Thermal post-synthetic modification of Al-MIL-53–COOH: systematic investigation of the decarboxylation and condensation reaction. *CrystEngComm* **14**, 4119 (2012).

47. Xiaolong Cui, Guangming Chen, & Han, X. Experimental Vapor Pressure Data and a Vapor Pressure Equation for N,N-Dimethylformamide. *J. Chem. Eng. Data* **51**, 1860–1861 (2006).

48. Demir, H., Walton, K. S. & Sholl, D. S. Computational Screening of Functionalized UiO-66 Materials for Selective Contaminant Removal from Air. *J. Phys. Chem. C* **121**, 20396–20406 (2017).

49. Breck, D. W. *Zeolite Molecular Sieves: Structure, Chemistry, and Use*. (Wiley: New York 1974).

50. Rezaei, F., Rownaghi, A. A., Monjezi, S., Lively, R. P. & Jones, C. W. SO_x /NO_x Removal from Flue Gas Streams by Solid Adsorbents: A Review of Current Challenges and Future Directions. *Energy & Fuels* **29**, 5467–5486 (2015).

51. Ethiraj, J., Bonino, F., Lamberti, C. & Bordiga, S. H_2S interaction with HKUST-1 and ZIF-8 MOFs: A multitechnique study. *Microporous Mesoporous Mater.* **207**, 90–94 (2015).

52. Tan, K. *et al.* Interaction of Acid Gases SO_2 and NO_2 with Coordinatively Unsaturated Metal Organic Frameworks: M-MOF-74 (M = Zn, Mg, Ni, Co). *Chem. Mater.* **29**, 4227–4235 (2017).

53. Kim, K. C. Design strategies for metal-organic frameworks selectively capturing harmful gases. *J. Organomet. Chem.* **854**, 94–105 (2018).

54. Mounfield III, W. P. *et al.* Synergistic Effects of Water and SO_2 on Degradation of MIL-125 in the Presence of Acid Gases. *J. Phys. Chem. C* **120**, 27230–27240 (2016).

55. Han, S. *et al.* MOF stability and gas adsorption as a function of exposure to water, humid air, SO_2, and NO_2. *Microporous Mesoporous Mater.* **173**, 86–91 (2013).

56. Bhattacharyya, S. *et al.* Stability of Zeolitic Imidazolate Frameworks in NO_2. *J. Phys. Chem. C* **123**, 2336–2346 (2019).

57. Bhattacharyya, S. *et al.* Acid Gas Stability of Zeolitic Imidazolate Frameworks: Generalized Kinetic and Thermodynamic Characteristics. *Chem. Mater.* **30**, 4089–4101 (2018).

58. Supronowicz, B., Mavrandonakis, A. & Heine, T. Interaction of Small Gases with the Unsaturated Metal Centers of the HKUST-1 Metal Organic Framework. *J. Phys. Chem. C* **117**, 14570–14578 (2013).

59. Hungerford, J. T. Synthesis and Stability: Metal-Organic Frameworks Exposure to Water, Sulfur Dioxide, Hydrogen Sulfide. PhD Dissertation. (Georgia Institute of Technology, 2019).

60. Nickerl, G. *et al.* Integration of accessible secondary metal sites into MOFs for H_2S removal. *Inorg. Chem. Front.* **1**, 325 (2014).

61. Adcock, R. N. *Determination of H_2S and Total Sulfur in Natural Gas*. SpectraSensors Inc: Houston.

62. *Report to Congress on Hydrogen Sulfide Air Emissions Associated with the Extraction of Oil and Natural Gas.* U.S. Environmental Protection Agency, Research Triangle Park, NC (1993).

63. *Sulfatreat The Original Hydrogen Sulfide Scavenger*. Sulfatreat, Chesterfield MO (2002).

64. Aaron, D. & Tsouris, C. Separation of CO_2 from Flue Gas: A Review. *Sep. Sci. Technol.* **40**, 321–348 (2005).

65. Choi, S., Drese, J. H. & Jones, C. W. Adsorbent Materials for Carbon Dioxide Capture from Large Anthropogenic Point Sources. *ChemSusChem* **2**, 796–854 (2009).

66. Hiyoshi, N., Yogo, K. & Yashima, T. Adsorption characteristics of carbon dioxide on organically functionalized SBA-15. *Microporous Mesoporous Mater.* **84**, 357–365 (2005).

67. Okonkwo, C. N., Okolie, C., Sujan, A., Zhu, G. & Jones, C. W. Role of Amine Structure on Hydrogen Sulfide Capture from Dilute Gas Streams Using Solid Adsorbents. *Energy & Fuels* **32**, 6926–6933 (2018).

68. McDonald, T. M. *et al.* Capture of Carbon Dioxide from Air and Flue Gas in the Alkylamine-Appended Metal–Organic Framework mmen-Mg_2(dobpdc). *J. Am. Chem. Soc.* **134**, 7056–7065 (2012).

69. Darunte, L. A., Oetomo, A. D., Walton, K. S., Sholl, D. S. & Jones, C. W. Direct Air Capture of CO_2 Using Amine Functionalized MIL-101(Cr). *ACS Sustain. Chem. Eng.* **4**, 5761–5768 (2016).

70. Lee, J. J. *et al.* Effect of Humidity on the CO_2 Adsorption of Tertiary Amine Grafted SBA-15. *J. Phys. Chem. C* **121**, 23480–23487 (2017).

71. Vandichel, M. *et al.* Active site engineering in UiO-66 type metal–organic frameworks by intentional creation of defects: a theoretical rationalization. *CrystEngComm* **17**, 395–406 (2014).

72. Hu, Z., Peng, Y., Kang, Z., Qian, Y. & Zhao, D. A Modulated Hydrothermal (MHT) Approach for the Facile Synthesis of UiO-66-Type MOFs. *Inorg. Chem.* **54**, 4862–4868 (2015).

73. Shearer, G. C. *et al.* Defect Engineering: Tuning the Porosity and Composition of the Metal-Organic Framework UiO-66. *Chem. Mater.* **28**, 3749–3761 (2016).

74. Park, J., Howe, J. D. & Sholl, D. S. How Reproducible Are Isotherm Measurements in Metal−Organic Frameworks? *Chem. Mater.* **29**, 10487–10495 (2017).

75. Katz, M. J. *et al.* A facile synthesis of UiO-66, UiO-67 and their derivatives. *Chem. Commun.* **49**, 9449–9451 (2013).

76. Hong, D.-Y., Hwang, Y. K., Serre, C., Férey, G. & Chang, J.-S. Porous Chromium Terephthalate MIL-101 with Coordinatively Unsaturated Sites: Surface Functionalization, Encapsulation, Sorption and Catalysis. *Adv. Funct. Mater.* **19**, 1537–1552 (2009).

77. Peterson, G. W. *et al.* Effects of pelletization pressure on the physical and chemical properties of the metal–organic frameworks $Cu_3(BTC)_2$ and UiO-66. *Microporous Mesoporous Mater.* **179**, 48–53 (2013).

78. Kapoor, A. & Yang, R. T. Roll-up in fixed-bed, multicomponent adsorption under pore-diffusion limitation. *AIChE J.* **33**, 1215–1217 (1987).

79. Goeppert, A. *et al.* Carbon Dioxide Capture from the Air Using a Polyamine Based Regenerable Solid Adsorbent. *J. Am. Chem. Soc.* **133**, 20164–20167 (2011).

80. Holewinski, A. *et al.* Aminopolymer Mobility and Support Interactions in Silica-PEI Composites for CO_2 Capture Applications: A Quasielastic Neutron Scattering Study. *J. Phys. Chem. B* **121**, 6721–6731 (2017).

81. Sakwa-Novak, M. A., Tan, S. & Jones, C. W. Role of Additives in Composite PEI/Oxide CO_2 Adsorbents: Enhancement in the Amine Efficiency of Supported PEI by PEG in CO_2 Capture from Simulated Ambient Air. *ACS Appl. Mater. Interfaces* **7**, 24748–24759 (2015).

82. Stevens, R. W., Siriwardane, R. V & Logan, J. In Situ Fourier Transform Infrared (FTIR) Investigation of CO2 Adsorption onto Zeolite Materials. *Energy & Fuels* **22**, 3070–3079 (2008).

83. Henschel, A., Gedrich, K., Kraehnert, R. & Kaskel, S. Catalytic properties of MIL-101. *Chem. Commun.*, 4192–4194 (2008).

84. McGuire, C. V. & Forgan, R. S. The surface chemistry of metal-organic frameworks. *Chem. Commun.* **51**, 5199–5217 (2015).

85. Jiang, J. & Yaghi, O. M. Brønsted Acidity in Metal–Organic Frameworks. *Chem. Rev.* **115**, 6966–6997 (2015).

86. Ethiraj, J. *et al.* Carbon Dioxide Adsorption in Amine-Functionalized Mixed-Ligand Metal-Organic Frameworks of UiO-66 Topology. *ChemSusChem* **7**, 3382–3388 (2014).

CHAPTER 5. CREATING SUPPORTED AND NON-SUPPORTED FRAMEWORK COMPOSITES WITH INSOLUBLE METAL PRECURSORS

5.1 Introduction

Demonstrations of the landmark gas separation and catalysis potential of metal-organic frameworks (MOFs) have been pervasive in scientific literature for over a decade.[1–5] These materials are promising candidates for addressing today's greatest separation challenges[6], such as petrochemical upgrading/separation[7,8], uranium harvesting from seawater[9], and post-combustion and atmospheric CO_2 capture.[10–12] As a result, companies have formed to produce MOFs for industrial applications.[13,14] Petit recently reported a list of companies which commercialize MOF-based materials, and highlighted the manufacture of both (1) supported and (2) non-supported MOF materials as marketable adsorption media.[15] Porous nanomaterials supported on substrates such as monoliths, fibers, thin films, etc., accommodate end-use applications where structured adsorbent media are desirable.[10,16] Alternatively, non-supported adsorbents are traditionally formed into pellets or granules for use in packed-bed separations.[17]

Both supported and non-supported production strategies are unique from one another. Supported MOF synthesis reports entail multistep pathways, where supporting substrate surfaces are often pretreated through various cleaning, etching, and/or chemical functionalization steps. These preliminary steps facilitate subsequent metal precursor seeding or combinatorial MOF growth reactions involving framework ligands and any

other necessary reagents.[18–21] Typically, non-supported MOFs are instead created through one-step solvothermal pathways. Production schemes commonly employ organic solvents, although solvent-free or water-based approaches are environmentally and economically desirable for large-scale MOF production.[22] Traditional non-supported MOF syntheses lack size and property control unless carefully tuned framework-specific procedures are developed.[23] Merging production methodologies for both supported and non-supported MOF growth can consequently simplify manufacturing strategies for both types of MOFs.

Zhan and Zeng thoroughly detailed how insoluble metal precursors are advantageous for large-scale MOF production.[24] Solid matters are readily accessible raw materials, typically inexpensive, and free of anion and hydrate impurities present with metal salts typically used to generate MOFs. Furthermore, solids can impart unique morphologies, particle sizes, architectures, and patterns for resulting hierarchical composite structures through controlled release of metal cations.[24–27] The enhanced growth control and worldwide economic accessibility of insoluble metal precursors suggests insoluble metal precursors are ideal synthesis reagents. Accordingly, a flexible synthesis scheme to create various supported and non-supported MOFs is proposed here.

Successful production of both supported and non-supported frameworks through this methodology are presented herein. Metallic aluminum was chosen as a candidate solid precursor to allow access to a variety of MOF topologies. Aluminum is the second most abundant metal in the earth's crust and the cheapest metal worldwide, where everyday commercial goods such as aluminum foil and food cans are frequently used around the world.[28] Readers may be even using aluminum-containing products while studying this dissertation chapter. Accordingly, the same items such as commercially purchased

aluminum foil and discarded aluminum cans were converted into highly porous MOF materials. In lieu of using organic solvents typical in MOF syntheses, water is utilized to pursue cheaper, more environmentally friendly hydrothermal production. In the first part of Chapter 5, commercially available aluminum-based products act simultaneously as the support and metal precursor for localized supported MOF growth through a one-step process. In the second half of the text, non-supported MOFs are created through the same synthesis by adding dilute hydrochloric acid, which dissolves the aluminum to create non-supported MOF products. The tunable flexibility of this process to target supported or non-supported MOF fabrication shows how insoluble metals can play a critical role in formulating simple and economical MOF production strategies. Findings from this report are intended to facilitate future MOF manufacturing endeavors through use of insoluble metal precursors, and to bridge disparate synthesis techniques employed for supported and non-supported material generation.

5.2 Materials and Methods

5.2.1 Insoluble Aluminum-containing Reagent Information

5.2.1.1 Aluminum Foil

Reynolds Wrap® brand aluminum foil was purchased from a local grocery store in Atlanta, GA. No pretreatment of the foil was performed prior to reaction. Foil squares of approximately 50mg were cut and placed into reactors prior to MOF syntheses.

5.2.1.2 Aluminum Mesh

200 mesh (0.0021" wire diameter) samples were purchased from TWP Inc. Samples were received as 3"x 3" pieces, but cut into smaller squares to allow the mesh to fit into reactors. After reaction, tweezers were used to recover mesh-MOF composites from the reaction mixture. Mesh samples contain magnesium as well, shown in later EDS data (Figure A-48).

5.2.1.3 Aluminum Tube

A 6ft aluminum tube (1/4" O.D., 0.18"I.D.) was purchased from Grainger. The tube was cut down to a length of about 2" to allow the tube to fit into the reaction vessel.

5.2.1.4 Aluminum Oxide Hollow Fiber Membrane

Alumina hollow fiber membranes were acquired from an external laboratory at Georgia Tech. Please refer to Nair and coworkers[29] for details on fiber production.

5.2.2 Synthesis and Materials Preparation

Below procedures describe methods utilized for conversions of aluminum foil to MIL-53(Al). An example of a foil piece used is depicted in Figure 5-1. However, the same molar ratios were used for experiments utilizing different metallic aluminum precursors and coordinating ligands. Exceptions to methods for specific reactions are described in below sub-sections.

5.2.2.1 Synthesis of Supported Aluminum-based MOFs on Metallic Aluminum

Aluminum foil (1.8mmol, 50mg) and terephthalic acid (5.56mmol, 924mg) were added in a 1:3 molar ratio to deionized (DI) water (555mmol, 10mL). The ratio of ligand-to-solvent was approximately 0.556mmol of ligand per mL water. The foil was placed as a small square (approx. 1" x 1") into the reaction vessel. The solution was sonicated at ambient temperature for 5min to partially dissolve the terephthalic acid into solution. The reagent mixture was then transferred to a 20mL PTFE lined stainless steel autoclave. The sealed reaction vessel was transferred into a preheated oven, held isothermally at 220ºC for 24 hours, and allowed to cool naturally afterwards. The product was carefully recovered from the autoclaves post-reaction with fine-point tweezers, and submerged into N,N-dimethylformamide (DMF), under gentle agitation, for at least 5min to remove uncoordinated ligands. The product was then submerged in fresh methanol to remove the DMF for at least 10min. Composite pieces were dried first in a well-ventilated chemical hood overnight. Degassing was performed at 150°C for 24h under vacuum.

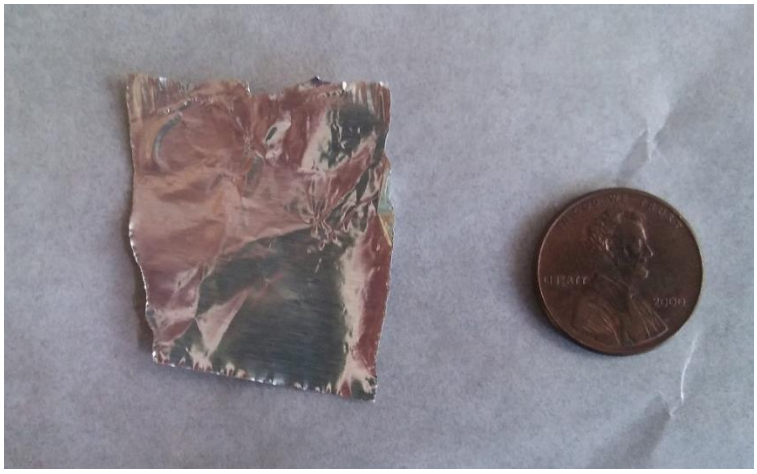

Figure 5-1: Picture of Reynold's Wrap® brand aluminum foil piece used for MOF synthesis. Placed next to U.S. one cent coin for size reference.

5.2.2.2 Synthesis of Supported Aluminum-based MOFs on Aluminum Oxide

Synthesis procedures are consistent with those described in Section 5.2.2.1. Using the same 1:3 molar ratio of aluminium-to-organic linker mentioned in the previous section, mass additions are adjusted when using aluminium oxide. For aluminium oxide precursors, Al_2O_3 stoichiometry is assumed (e.g. molar ratio of 0.5mol Al_2O_3 to 3mol terephthalate linkers).

5.2.2.3 Synthesis of Non-supported Aluminum-based MOFs from Metallic Aluminum

Aluminum foil (1.8mmol, 50mg) was first shredded by hand into small pieces. Metal pieces were placed in a PTFE reactor, along with terephthalic acid (5.56mmol, 924mg) in a 1:3 aluminum-to-ligand molar ratio. Deionized (DI) water (555mmol, 10mL) was also placed in the reaction, making a ratio of 0.556 mmol ligand per mL water. The solution was sonicated for 5min to partially dissolve coordinating ligands in the aqueous solution. In a chemical hood, concentrated hydrochloric acid (HCl, 36% w/w) from Alfa Aesar was introduced to the reaction mixture using a micropipette in additions creating the various molar concentrations of HCl(aq) stated in the text. For the optimized 0.5M HCl reaction, 4.96mmol (152μL) of concentrated HCl(aq) was added. The reactor was quickly sealed and placed in a preheated oven. Different synthesis temperatures and times were utilized, as described in Section 5.3.4.5. All reactions were carried out isothermally. After reaction, the autoclave was cooled naturally in a chemical hood. Resulting solids were filtered, washed three times with both DMF and then methanol, and allowed to dry overnight under ambient conditions. Degassing of dry samples was conducted under vacuum at 150ºC for 24 hours.

5.2.2.4 Synthesis of Non-supported Aluminum-based MOFs from Metal Salts

Aluminum nitrate nonahydrate [$Al(NO_3)_3*9H_2O$] and aluminum chloride hexahydrate [$AlCl_3*6H_2O$] were purchased from Sigma Aldrich, and both used to create frameworks described in the text. HCl(aq) at a concentration of 0.5M was used to create samples of MIL-53(Al) using ionic aluminum salts, mentioned later in the main text. Otherwise, all reagent ratios and procedures as consistent with those listed in Section 5.2.2.3 above.

5.2.3 Sample Characterization Methods

5.2.3.1 ^{27}Al Solution State NMR

^{27}Al solution NMR spectra were recorded using a 400.13 MHz Brucker Avance III 400MHz magnet. Liquid samples were collected immediately after cooling to ambient temperature, and diluted in D_2O. Aliquots were then dispensed in NMR tubes immediately before measurement. Spectra were recorded through 64 scans. 0ppm ^{27}Al signal was standardized to 0.1M $Al(NO_3)$ in D_2O stock solution. Measurements were processed using version 11.0 of MestreNova.

5.2.3.2 ^{27}Al Solid-State Multi-Quantum Magic-Angle Spinning (MQMAS) NMR

Solid state ^{27}Al spectra were measured using a Bruker AV3-400 NMR spectrometer operating at a magnetic field of 9.4T. Spectra were recorded using a magic angle spinning probe operating with 4mm O.D. MAS rotors. The MAS spinning frequency was 14 kHz.

One-dimensional direct polarization spectra were recorded using an excitation with a single pulse with a length of 0.6μs corresponding to a 20° excitation pulse. The repetition delay between scans was 1s. It was verified that this repetition delay is associated with a full recovery of magnetization after each individual scan.

Two-dimensional multi-quantum MAS spectra were recorded using the identical setup. A three quantum MAS pulse sequence with zero quantum filter according to the following scheme was used: excitation pulse – t1 delay (evolution) – conversion pulse - delay (zero quantum filter) – selective 90° pulse – acquisition. Processing of the two-dimensional data, which involves appropriate shearing of the 2D spectra, was executed using the Topspin 3.5 software environment (Bruker).

5.2.3.3 Attenuated Total Reflectance-Fourier Transform Infrared Spectroscopy (ATR-FTIR)

A Thermo Scientific Nicolet iS50 spectrometer coupled with an iS50 ATR module was used to acquire FTIR measurements. The FTIR detector is cooled using liquid nitrogen. Background scans were taken on the blank, clean surface of the ATR probe. Solid aluminum foil and aluminum foil/MOF composites were placed under the ATR probe for data collection. Measurements were acquired through 128 scans, with a data resolution of $0.48 cm^{-1}$.

5.2.3.4 N_2 Adsorption at 77K

Nitrogen physisorption measurements were utilized to examine porosities of produced MOFs. A Quantachrome Quadrasorb SI volumetric system with 5.11

QuadraWin™ software package was used to collect adsorption data. Liquid nitrogen filled dewars kept samples at 77K during experiments. Sample quantities of at least 100mg were tested and degassed under high vacuum at 150°C for 24h prior to measurements in a separate tube degasser.

5.2.3.5 Powder X-ray Diffraction

An X-Pert Pro PANalytical X-ray diffractometer was used to collect PXRD measurements, with a Cu Kα (λ = 1.542 Å) X-ray source. All samples were rotated during data collection. Solid samples were secured flush to a low-background sample holder using tape or putty. Powder samples were placed homogenously into wells on low-background sample holders. For MIL-53(Al) containing samples and aluminum samples, a range of from 2θ = 4° - 45° with 0.02° step size was used; for MIL-96(Al)/MIL-100(Al) samples, 2θ = 2° - 45° with a step size of 0.01° was used; for non-framework alumina materials, 2θ = 10° - 70° with a step size of 0.02° was used.

5.2.3.6 Scanning Electron Microscopy (SEM) and Energy Dispersive Spectroscopy (EDS)

Several microscopes were utilized to collect presented SEM images. Regardless of the microscope, all samples were dispersed directly onto carbon tape prior to analysis. Aluminum hollow fiber membrane composite samples were first pretreated by submerging fibers in hexanes for 5 minutes. Then, fibers were placed one at a time into a dewar filled with liquid nitrogen at 77K for 1min. Afterwards, fine point tweezers were used to break fibers prior to imaging. Accelerating voltage ranges from 2-10keV were utilized when imaging materials.

A Zeiss Ultra60 Field Emission (FE) SEM was utilized to image aluminum foil/mesh-MOF composites, as well as non-supported MIL-53(Al) and MIL-96(Al) samples. EDS mapping was additionally performed using the Zeiss microscope, within a range of 5-10keV.

A LEO 1530 Thermally-Assisted Field Emission (TFE) SEM was also utilized for imaging materials. Images were scanned at an accelerating voltage range of 6-10kV

Finally, focused ion beam (FIB) milling with SEM-EDS was performed utilizing a Nova Nanolab to investigate cross-sections of aluminum foil/MIL-53(Al) composites. Before imaging, a thin layer of colloidal graphite in isopropanol was placed on the top of the samples, in effort to protect MOF crystals from FIB etching and the electron beam. Samples desiccated in a chemical hood for 24h following this treatment. Prior to etching, a μm-scale layer of platinum was deposited on the surface of the material for further protection. Then, a gallium ion beam was utilized to gradually cross-section the aluminum foil/MOF composite, after which ultra-high resolution SEM and EDS data were collected within a voltage range of 2-10keV.

5.2.3.7 Thermogravimetric Analysis with Mass Spectrometer (TG-MS)

TGA data were acquired by a Nietzsche STA 449 F1 Jupiter. A Nietzsche mass spectrometer was coupled on the outlet line to monitor eluting combustion/pyrolysis products from analyzed materials. Samples were held in a ceramic crucible during measurement. Either dry air or helium carrier gas (specified in text) at 20mL min^{-1} were flown over samples during data collection.

5.2.3.8 X-ray Photoelectron Spectroscopy (XPS)

A Thermo K-alpha monochromated Al Kα source with a double-focusing hemispherical analyzer was utilized to collect XPS measurements. Scan parameters used a 0.1eV step size, 50ms dwell time, 50eV pass energy, and 400μm spot size. High resolution spectra were recorded for C 1s, O 1s, and Al 2p.

5.2.4 Cost Analyses

Reagent costs were acquired by averaging metric-ton scale quantities from commercial sources. Prices were acquired between March-July 2018. A previous economic analysis by Veenestra and coworkers[30] was also referenced for material costs relevant to large-scale MOF manufacturing.

Calculations to approximate the materials cost of producing 1kg of non-supported MIL-53(Al) are shown below. Importantly, the calculations reference a lab-scale (< 1g) product yield—production amounts may change significantly in larger productions.

Mass yield assumptions utilized for cost analyses assumed (1) aluminum foil precursors are pure aluminum and (2) 28% of retrievable MOF product by mass is solvent and/or entrapped ligand, as seen through TGA measurements in Figure A-72. Calculations approximating material costs are detailed step-by-step in the Section A.3.3 Cost Analysis Work.

5.3 Results and Discussion

5.3.1 MOF Growth on and from Aluminum Substrates

Reynolds Wrap® brand aluminum foil (Figure 5-1) purchased from a local grocery store was used as an unconventional metal precursor for one-step solvothermal MOF growth. Utilizing terephthalic acid (BDC) as the organic linker, aluminum terephthalate MIL-53(Al) was generated on the surface of the foil. The cartoon in Figure 5-2a visually describes the resulting composite. Epitaxial MIL-53(Al) forms on the uppermost layer of aluminum. Metallic aluminum remains underneath as a supporting structure. The inherent white color of MIL-53(Al) coats the foil following reaction, as seen in Figure 5-2b. Framework formation is affirmed by ATR-FTIR and PXRD measurements in Figure A-49 and Figure 5-3, respectively.[31] The characteristic aluminum (1 1 1) reflection at $2\theta = 38.47°$ (ICDD code: 00-001-1180) in Figure 5-3 verifies the preservation of aluminum in the composite. Diffraction measurements in Figure 5-3 also confirm preferred crystal orientation through the atypically intense reflection of $2\theta \approx 15^{o}$ for MIL-53(Al).[32] Al 2p XPS spectra of the aluminum surface before and after reaction in Figure 5-4 communicate chemical changes in the passive aluminum oxide layer inherently present on aluminum surfaces. Evolved MIL-53(Al) octahedra $AlO_4(OH)_2$ at 74.8eV[33] after reaction dwarfs surface Al(s) and alumina spectral features, asserting MIL-53(Al) as the dominant surface species. EDS mapping of a partially exposed surface in Figure A-50 supports surface-localized MOF growth. TGA measurements in Figure A-51 confirm ~9wt% of the composite mass is MIL-53(Al). Needle-like nanocrystals emerge perpendicular to the foil surface, seen via electron microscopy in Figure 5-2c. This morphology is unique from MIL-53(Al) obtained through conventional syntheses utilizing soluble metal ions.[34]

Interestingly, the same needle-like morphology was observed by Moran et al. when producing MIL-53(Al) from insoluble aluminum carbide, suggesting the altered MOF growth mechanics fostered by insoluble metal precursors influences crystal morphology.[35] To the author's knowledge, this is the first report of supported aluminum MOF growth without requiring any pretreatment or metal seeding step. The insoluble metal reagent acts directly as both the metal source and support. Self-supported growth from metal precursors is fundamentally impossible for conventional, solubilized metal salts dissolved in solvothermal reactions. Monolayer growth control is also conveniently obtained, which typically requires a SAM organic precursor on the surface.[36] Kang et al. observed similar monolayer termination while growing $Ni_2(L\text{-}asp)_2(bipy)$ from a nickel net, similarly indicating the metal source becomes inaccessible for reaction.[37] Focused ion beam (FIB) cross-sectional milling in Figure 5-2d clearly distinguishes crystal growth directly on the aluminum surface. Accompanying SEM and EDS data of the cross-sectioned sample from Figure A-52 to Figure A-54 elucidate framework and unreacted aluminum regions visualized in the Figure 5-2d cartoon (right-hand side of graphic).

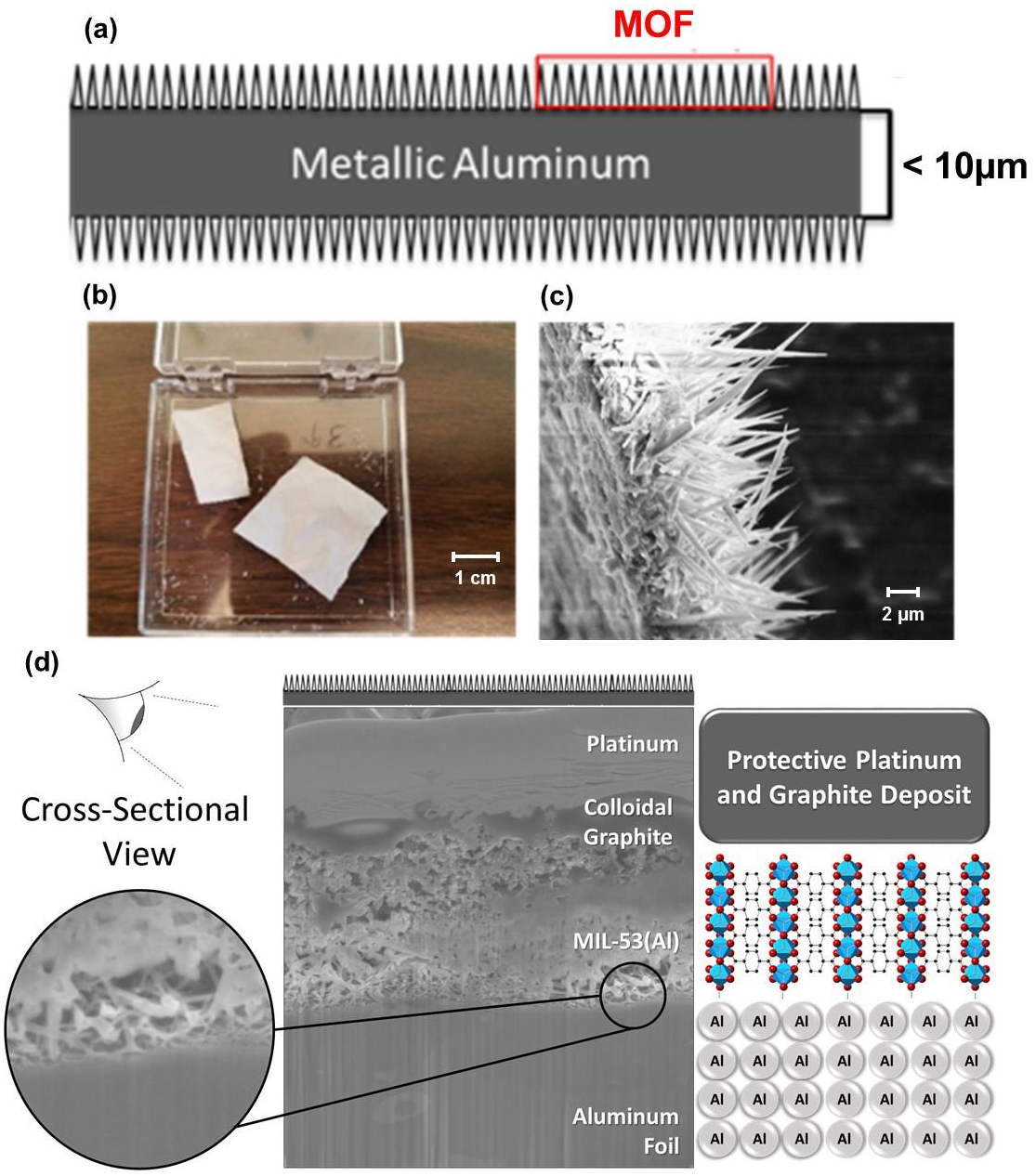

Figure 5-2: One-step hydrothermal production of supported MIL-53(Al) on metallic aluminum foil: (a) Cartoon schematic of needle-like MIL-53(Al) growth on aluminum foil. (b) Image of post-reaction aluminum foil—white coating reflects surface MIL-53(Al) growth. (c) SEM image of perpendicularly-oriented MIL-53(Al) needles grown on post-reaction aluminum foil surface. MOF structures were physically removed from foil surface edge prior to imaging contrast exposed surface with MOF growh. (d) FIB-SEM cross-section of aluminum foil-MOF composite. Circled magnification depicts MOF-metal boundary. Cartoon on right-hand side illustrates components visualized in cross-section

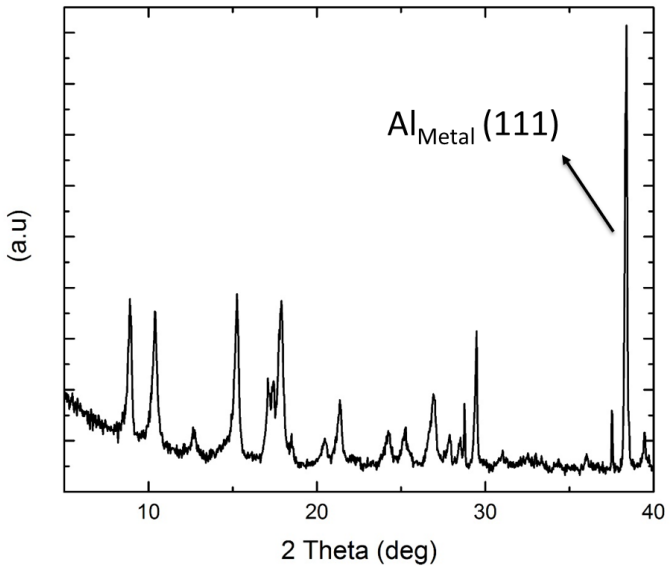

Figure 5-3: X-ray diffraction measurements of supported MIL-53(Al) grown from and on aluminum foil

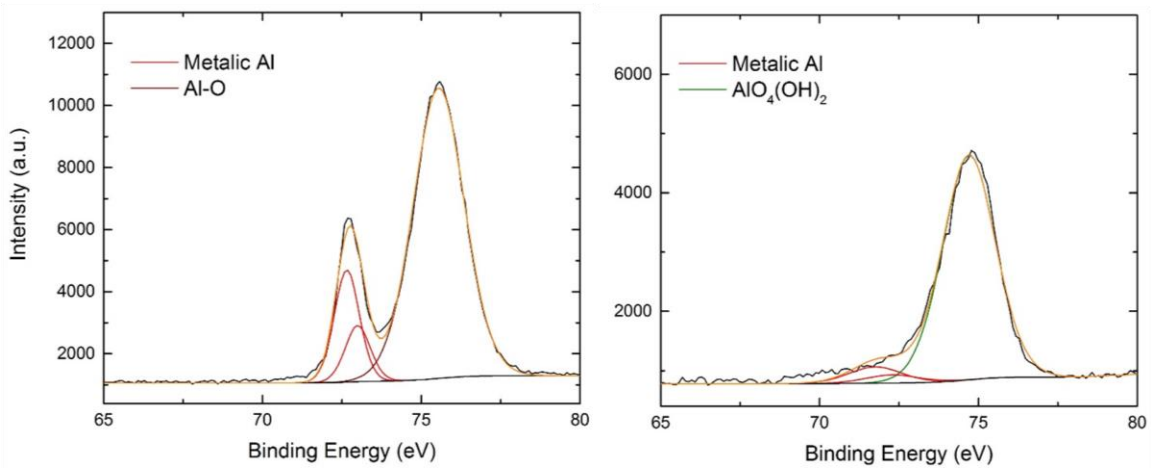

Figure 5-4: High resolution Al 2p XPS scans of aluminum surface before (left) and after (right) supported MIL-53(Al) formation

Interfacial MOF growth through this method is insensitive to substrate geometry. The general production methodology may be used to coat porous nanomaterials onto a variety of metal structures. Since aluminum is already fabricated into a myriad of structured materials, one can easily envision the one-step manufacture of metal substrates integrated

with porous aluminum frameworks. To demonstrate this, standard ¼" aluminum tubing purchased from Grainger® was subjected to the same reaction. As shown, application-based manufacturing flexibility can yield MOF-coatings on substrates with large void volumes such as tubes (exemplified in Figure 5-5), laminates, and monoliths. These structures accommodate separation processes involving large gas flow rates and improve mass transfer for adsorptive separations—desirable in direct-air capture and flue gas remediation operations.[16]

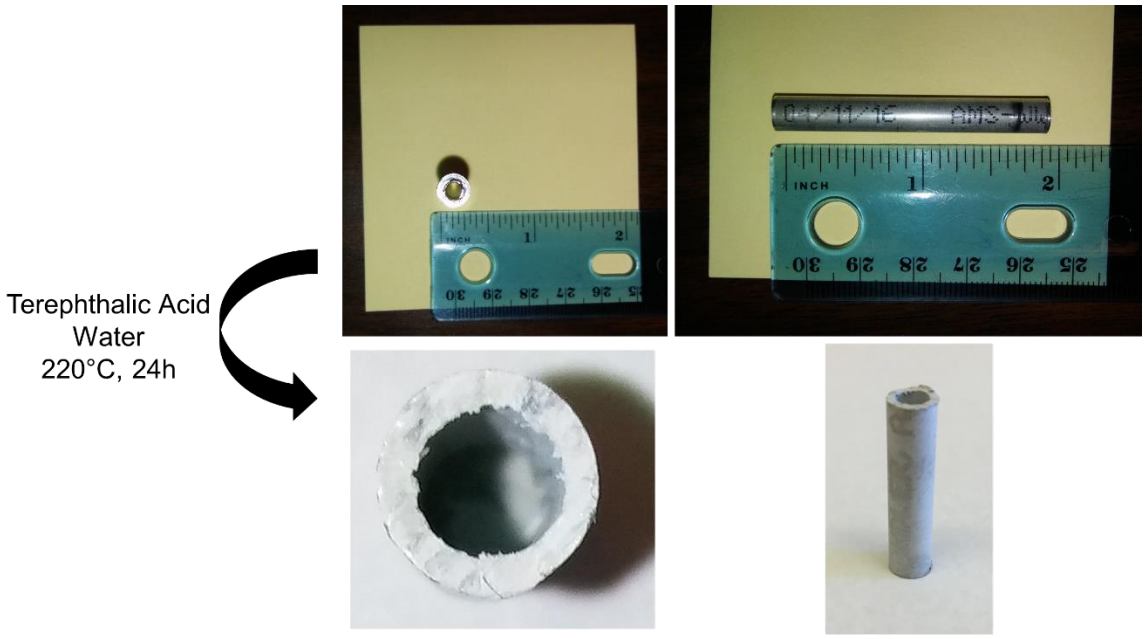

Figure 5-5: Image of 1/4" aluminum tube purchased from Grainger® before (top) and after (bottom) MOF reaction.

5.3.2 Extension of Synthesis to Different Topologies

Supported MOFs have been produced from metals previously.[38–40] The scheme presented here uniquely allows access to different aluminum-based topologies via the same procedure. To establish the flexibility of MOF choice for this reaction methodology,

trimesic acid (BTC) linkers were also used to produce supported porous aluminum trimesates. Diffraction measurements in Figure 5-6 confirm growth of MIL-53(Al) and MIL-96(Al) after reaction with BDC and BTC linkers, respectively. To further showcase metal precursor flexibility, crystals were grown directly from aluminum-based fine mesh (200mesh) supports. Characteristic reflections for metallic aluminum at $2\theta = 38.47°$ and 38.57° persist after MOF formation, evidencing the remaining aluminum backbone underneath newly-formed MOFs. SEM images of the composite formed with BDC in Figure 5-6 again reveal needle-shaped MIL-53(Al) crystals produced from aluminum foil in Figure 5-2c. Aminated terephthalate analogue MIL-53-NH_2(Al) was also created (Figure A-56). Alternatively, 1-5μm dodecahedron MIL-96(Al) crystals densely coat the mesh when BTC linkers were used, also depicted in Figure A-55. Repeating the reaction a second time in the presence of an aluminum salt densifies MOF coverage. SEM images of secondary MIL-53(Al) growth in Figure A-57 show mesh gaps become completely infiltrated with MOF. Resulting MOF-mesh composites have potential use as adsorptive filters and hierarchical sieves. These studies illustrate how novel porous nanomaterials are easily integrated onto accessible and industrially relevant support media, with additional potential for post-synthetic modification such as secondary growth densification treatments.

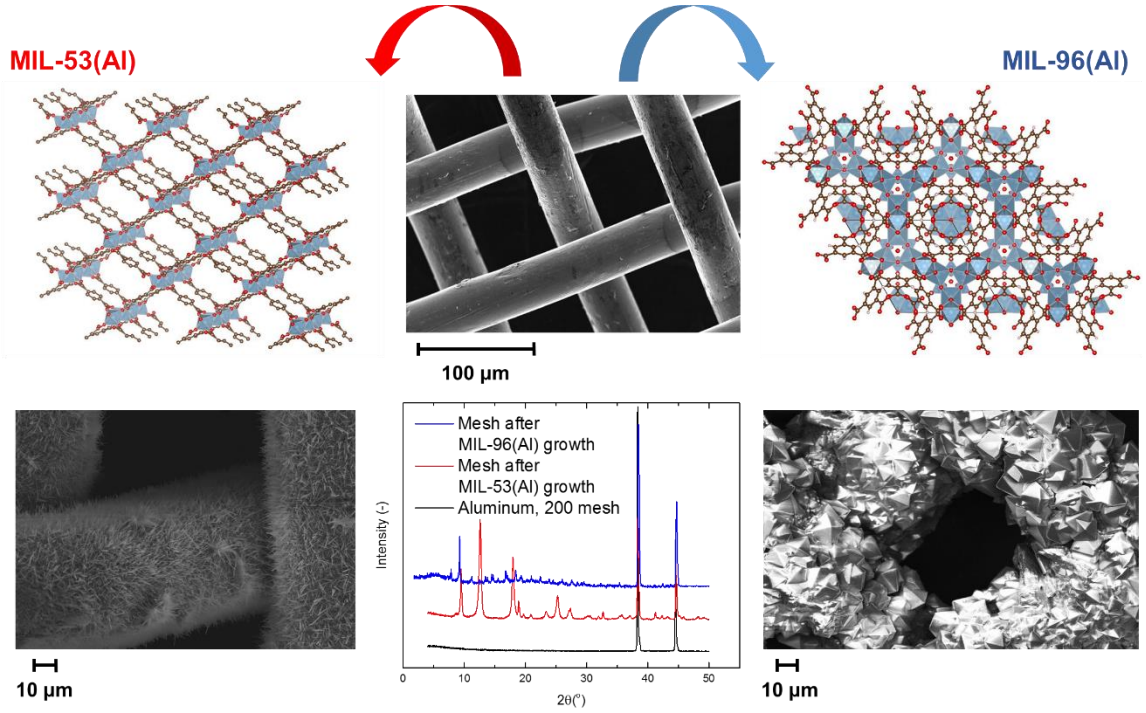

Figure 5-6: SEM images of supported MIL-53(Al) (bottom left) and MIL-96(Al) (bottom right) on 200 aluminum mesh (top, center). PXRD pattern of composites at bottom center. Crystal structure representations of MIL-53(Al) and MIL-96(Al) on top corners of graphic, constructed using previously reported crystallographic data and VESTA visualization software.[32,41,42] Graphics key: blue polyhedrals = metal clusters, red dot = oxygen, grey dot = carbon.

5.3.3 Extension to Aluminum Oxide Hollow Fiber Membranes

Alumina hollow fiber membranes are frequently probed for gas-phase separations.[43,44] Consequently, efforts to adhere MOFs onto hollow fiber membranes are actively investigated to enhance the adsorptive capacities of target species and/or improve process selectivities.[45–48] In our previous work[35], the adaptability of MOF generation from insoluble aluminium sources is amenable to aluminium carbide, as well as metallic aluminium shown here. Aluminum oxide-based membranes therefore present themselves as usable substrates for MOF formation. Uniquely from prior studies, MOFs produced in

this chapter are directly grown *on* and *from* the alumina hollow fiber membrane structures, as opposed to post-MOF formation adhesion methods utilized in prior work.

Alumina hollow fibers were thusly subjected to the same insoluble aluminium reaction scheme (described in Section 5.2.2.2) using terephthalic acid linkers. MOF-alumina fiber structure and porosity data are shown in Figure A-58. PXRD measurements on the crushed sample in Figure A-58a confirm the MIL-53(Al) topology, while N_2 physisorption data in Figure A-58b evidence new microporosity in the sample—supportive of MIL-53(Al) production. Characteristic charging of framework particles under electron irradiation conveniently reveals MOF dispersion on post-reaction fibers in Figure A-59. Visual and spectroscopic mapping of the cross-sectioned product in Figure 5-7 discerns MIL-53(Al) microneedles densely dispersed across the fiber surface, as seen with metallic aluminium precursors. Consequently, the reaction described for metallic aluminium is transferrable to aluminium oxides as well. Quantified elemental dispersion across reacted surfaces in Table 5-1 shows good agreement with the theoretical mass balance of MIL-53(Al). MIL-96(Al) growth is similarly achievable when utilizing trimesic acid. However, post-reaction fiber images in Figure A-60 show MIL-96(Al) growth is significantly less dense than seen with MIL-53(Al) in Figure 5-7. Bulkier trimesic acid linkers likely experience greater mass transfer resistance while diffusing inside axial pores into the central bore of the fiber. Axial transport of reacting ligands through membrane pores is surmised from data presented later in the text.

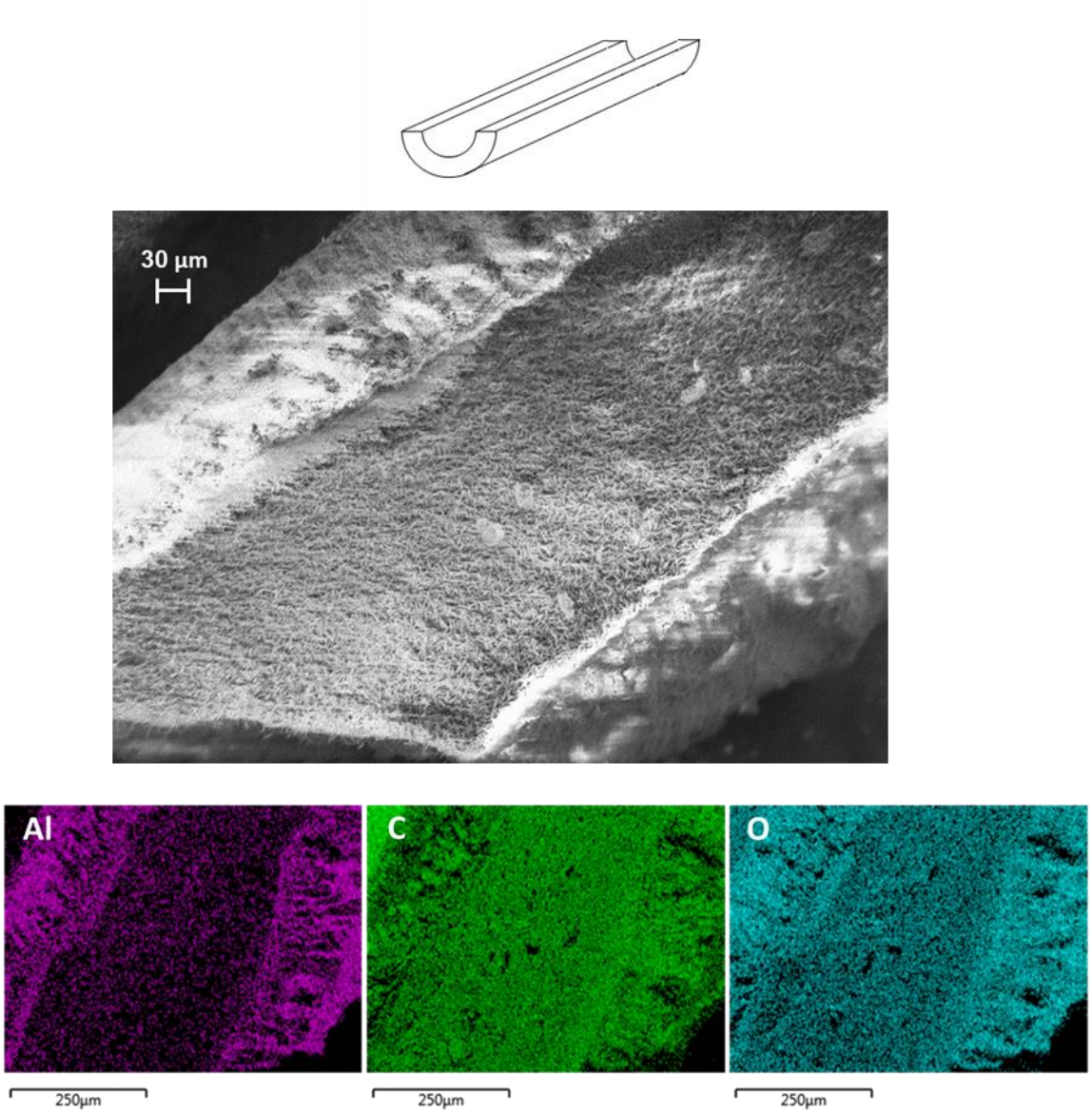

Figure 5-7: Cross-section orientation (top) electron image (middle) and EDS mapping (bottom) of post-reaction alumina hollow fiber membrane with terephthalate ligands.

Table 5-1: Comparison of EDS mapping data of post-terephthalic acid reaction on Al_2O_3 membrane surface with theoretical MIL-53(Al) mass balance

Elements	Elemental Composition of Product Mass Fraction (wt %)	
	[a]Theoretical	From EDS
Aluminum	13.0	16.3
Oxygen	38.5	36.6
[b]Hydrogen	2.5	-
Carbon	46.0	47.1

[a]Calculated from ideal stoichiometric unit of MIL-53(Al): *Al(OH)(O_2C-C_6H_4-CO_2)*
[b]X-ray excitation measurements cannot yield hydrogen detection

In effort to maximize MOF loading on alumina fibers, reagent solvent mixtures were manipulated. Moran et al. showed various ratios of DMF and H_2O in reaction mixtures for growing MIL-53(Al) from insoluble aluminium carbide effected the resulting crystal structure, morphology, and yield of products.[49] Extending this methodology to MIL-53(Al) production from aluminium oxide, utilizing DMF as a solvent instead of water would completely solubilize terephthalic acid ligands. As a result, more terephthalic acid ligands may contact the reacting surfaces of aluminium oxide. Unfortunately, MOF formation from Al_2O_3 does not occur when using 100% DMF—bridging hydroxyl group donation from H_2O is crucial for creating aluminium frameworks from oxide substrates. So instead, 2 vol% DMF was added to the hydrothermal reaction mixture to improve ligand miscibility. TGA results in Figure 5-8 show ~2 wt% greater MOF loadings are acquired when minute amounts of DMF are utilized—a modest increase in yield. But the larger 25vol% DMF detered MOF growth. Testing a range of DMF concentrations between 2-

25vol% DMF, along with other solvents, is required to understand the extent of enhancement in MIL-53(Al) yield through solvent mixing.

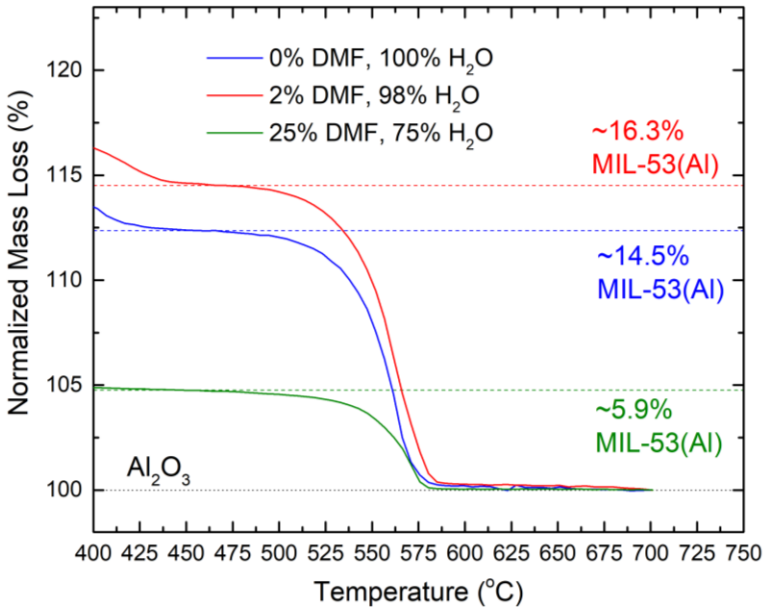

Figure 5-8: TGA results for post-reaction alumina hollow fiber MIL-53(Al) composites formed using various amounts of DMF. Solid lines represent sample mass loss, and dashed lines denote plateau regions used as starting masses. Percent MOF loadings determined from stoichiometry, assuming (1) all mass loss resulted from coordinating terephthalate ligands (O_2C-C_6H_4-CO_2) and (2) the ideal formula unit for MIL-53(Al). Measurements acquired under high purity helium

Maximizing MOF formation across all accessible surfaces would benefit the creation of a purely adsorptive composites. However, the outer surfaces of hollow fiber membranes typically serve as selective barriers for membrane filtration.[45] Developing methods to selectively form MOFs on the outside of hollow fiber membranes would aid creation of potentially gas-selective filtration media. To pursue this, open-bore ends of fiber membranes were wrapped with Teflon tape (picture in Figure A-61) to mitigate ligand transfer directly through the center bores. Imaging into the center bore of a post MIL-96(Al) production reaction fiber (Figure 5-9) evidences greater crystal formation along the

peripheries of the tube, as opposed to the bore-end wrapped with PTFE during reaction. Dense MIL-96(Al) growth is observed in micrographs of exposed surfaces in Figure A-62. However, cross-sectional images of the fiber composite in Figure A-63 still show crystal growth inside the bore, albeit qualitatively less dense than seen with fibers Figure A-60 without PTFE tape capping. It is evident that although blocking the accessible end bores of fibers helped mitigate interior growth, reacting ligands likely still transport through axial membrane pores to access exposed bore surfaces. This is supported by elemental mapping in Figure 5-10 across the membrane layer of the reacted material, which clearly shows carbon deposition from framework ligands along axial pathways. Further material optimization is required to selectively localize supported MOF production on studied membrane materials.

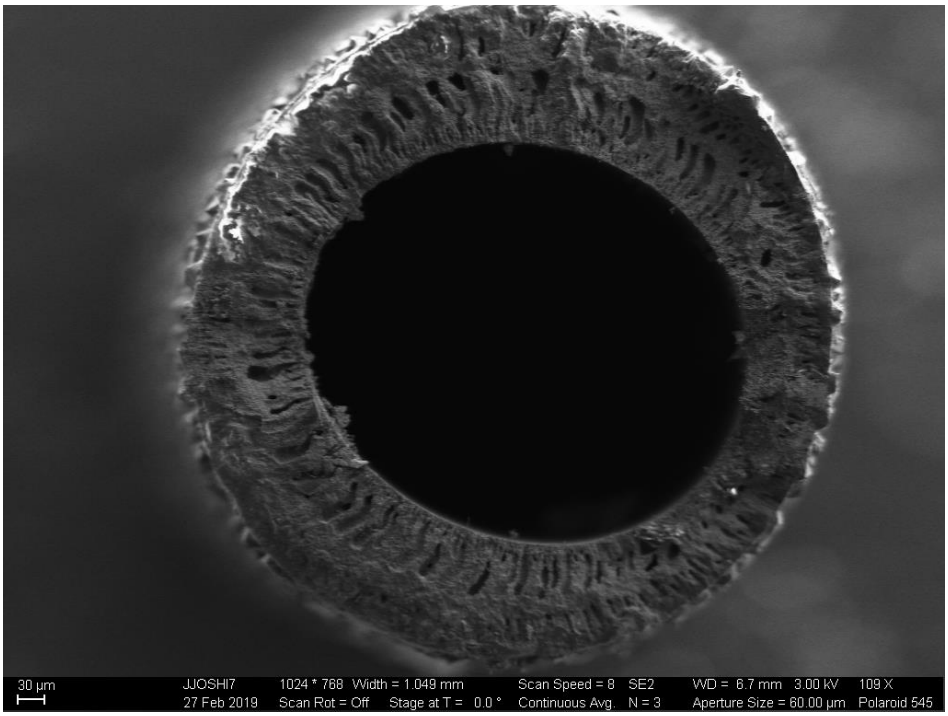

Figure 5-9: Post-reaction alumina fiber with MIL-96(Al) growth on peripheries

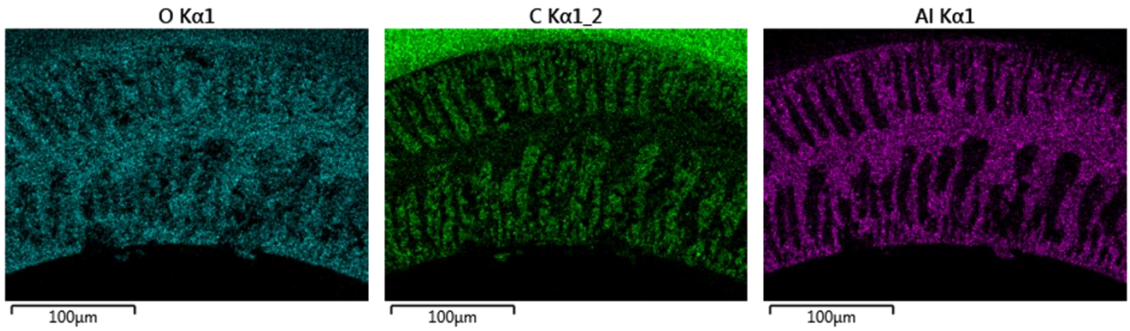

Figure 5-10: EDS mapping of post-reaction fiber (with trimesic acid). Image perspective looking into fiber bore

5.3.4 Non-Supported Aluminum Frameworks from Insoluble Metal Precursors

5.3.4.1 Optimization of Non-supported MIL-53(Al) Production

Metallic aluminum also yields non-supported MOFs through slight alteration of the same reaction scheme. Supported MOF production experiments showed surface aluminum passivated from further conversion after monolayer framework growth was established. Aluminum dissolution would afford continuous MOF formation in the bulk solution until the metal reagent is exhausted. To this end, aqueous hydrochloric acid (HCl) was added to the synthesis mixture to facilitate metal solubilization during reaction. HCl(aq) concentrations were systematically increased from 0.01M to 1M HCl(aq) to optimize MIL-53(Al) yield. Acid concentration directly dictates the relative yield of non-supported MOF. Photographs of the samples in Figure 5-11 show the foil precursor becomes less apparent in post-synthesis precipitate as acid concentration is increased. Foil is not visually observable in the 0.5M HCl(aq) product. Concentrations > 0.5M HCl(aq) failed to produce solid precipitates. Linker deprotonation difficulty in such highly acidic conditions likely prevents metal-ligand coordination. Reactions were also unable to produce MOF when

using DMF as a solvent, due to weak dissociation of HCl(aq) in DMF.[50] Water is therefore crucial for non-supported MOF formation through this method. After conducting the reaction in absence of linker molecules, solution ^{27}Al NMR in Figure A-64 of the post-reaction supernatant confirmed the presence of Al^{3+} cations. This observation is in accord with the initial mechanistic hypothesis for solubilizing metallic aluminum using an etching reagent like HCl(aq). A solid precipitate was also collected from the linker-absent reaction, identified as crystalline boehmite [AlO(OH)] with amorphous alumina via diffraction measurements in Figure A-65. This suggests aluminum MOF formation is thermodynamically favored over other aluminum-based byproducts at tested conditions when coordinating framework ligands are present.

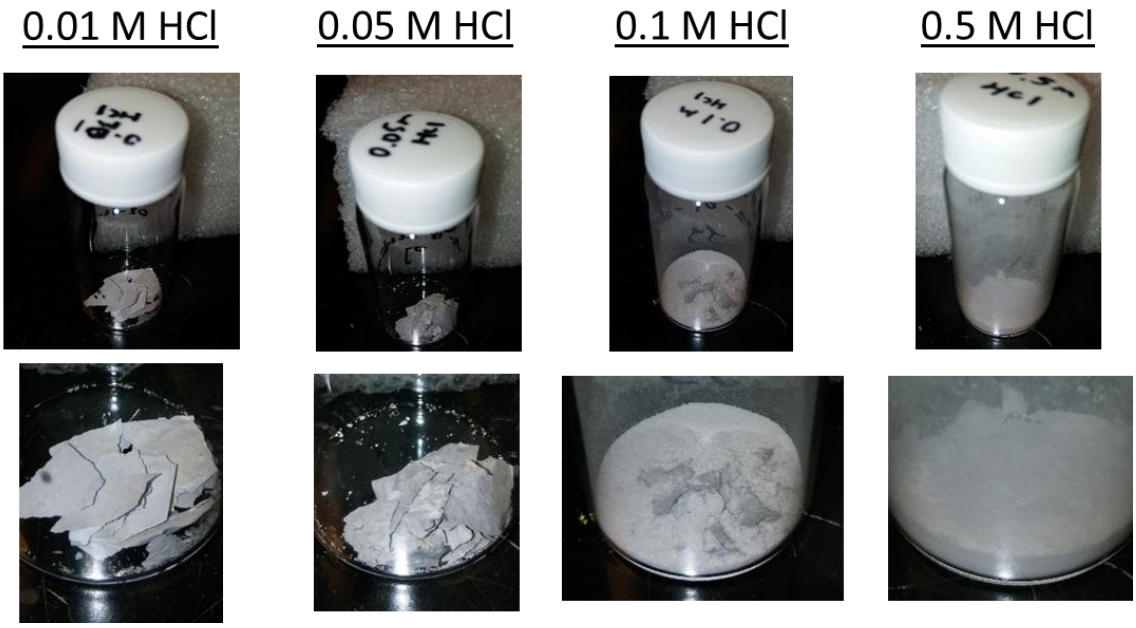

Figure 5-11: Images of MIL-53(Al) products obtained using Reynold's Wrap® brand aluminum foil, while altering hydrochloric acid concentration in the reaction solution. Metallic aluminum is not visually apparent in the 0.5M HCl product.

Powder samples obtained from 0.05M, 0.1M, and 0.5M HCl(aq) syntheses with BDC all portray MIL-53(Al) topologies (Figure A-66). Variations in aluminum environments formed with different HCl(aq) concentrations were evidenced through ^{27}Al multi-quantum magic angle spinning (MQMAS) solid-state NMR experiments. The corresponding MQMAS spectrum in Figure A-67a for MIL-53(Al) produced using 0.1M HCl(aq) unambiguously reveals distinctive aluminum-based species unique from the 0.5M HCl(aq) product in Figure A-67b The 1D spectra in Figure 5-12a shows a strong resonance at 5ppm in the 0.1M HCl(aq) spectrum is diminished when 0.5M HCl(aq) is used. This feature has been previously ascribed to 6-coordinate alumina as a solid intermediate to MIL-53(Al) formation when using insoluble Al_4C_3 precursors, suggesting a similar alumina intermediate exists when using metallic aluminum here.[35] Alumina consumption at higher acid concentrations suggests greater conversion of this intermediate to MIL-53(Al) when using 0.5M HCl(aq) across consistent (24h) reaction times. Alumina intermediate species are surmised to be amorphous, since characteristic crystalline aluminum oxide reflections are absent from collected products in Figure A-66. Other spectral features are consistent with previous reports on the various breathing modes of MIL-53(Al).[32,51] Mounfield and Walton[52] observed the same unique shoulder at -80ppm present in the 0.5M HCl(aq) MIL-53(Al) material. This resonance is attributed to *np*-MIL-53(Al) via PXRD measurements in Figure 5-12b and is present alongside *as*-MIL-53(Al) reflections. These observations suggest multiple pore forms exist simultaneously in the sample. Deviations from expected peak width and positions signify lattice strain resulting from heterogeneous aluminum structural environments. Overall, the results communicate the importance of HCl(aq) concentration in determining both (1) if non-supported MOF is

precipitated and (2) framework properties. Non-supported MOF products described hereafter utilize the optimized 0.5M HCl(aq) reagent concentration.

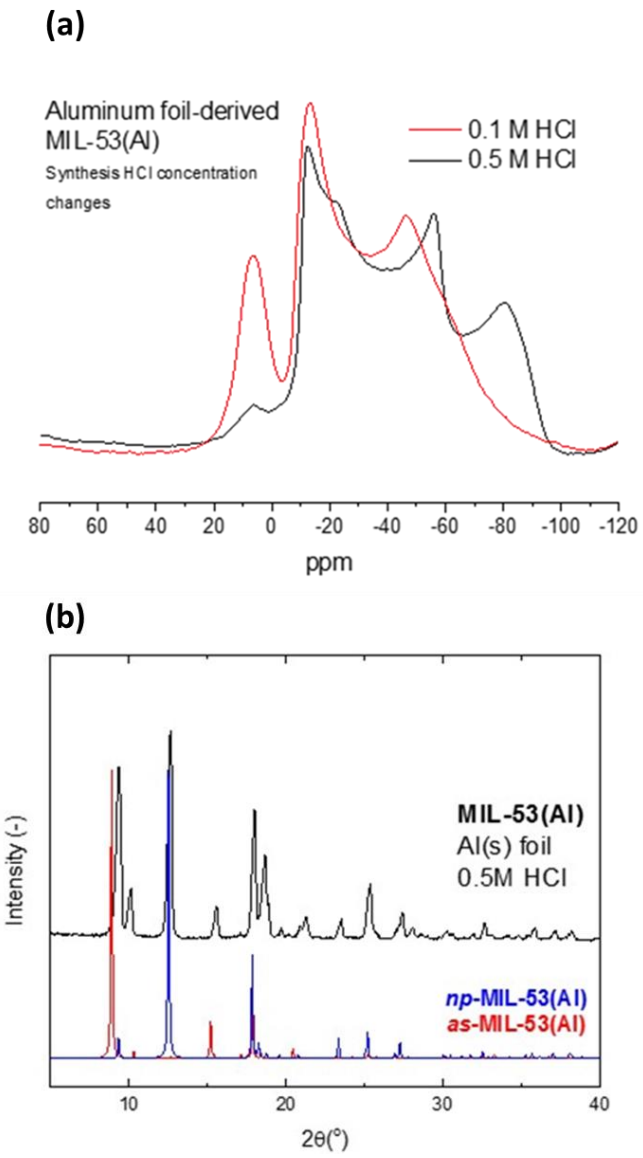

Figure 5-12: Non-supported Al(s)-derived MIL-53(Al) bulk properties (a) ^{27}Al SS MAS spectra of collected powder samples from MIL-53(Al) syntheses using 0.1M HCl(aq) (red) and 0.5M HCl(aq) (black) concentrations, (b) PXRD pattern of MIL-53(Al) generated using 0.5M HCl(aq). Simulated *as*- and *np*- patterns from Loiseau et al.[32]

5.3.4.2 Extension to MIL-53(Al) Topological Analogues

Different linker analogues of MIL-53(Al) may be produced from the same reaction scheme. Precipitates of MIL-53-NH_2(Al) were confirmed through PXRD measurements (Figure 5-13) when utilizing 2-aminoterephthalic acid. Synthesis amounts and procedures when using 2-aminoterephthalic acid in this study are consistent with those described in Section 5.2.2.3. Pre-functionalized ligand use is a proven and simple MOF tuning strategy to enhance the selective adsorptive properties of parent frameworks[53–55], also detailed in Chapter 4. SEM data in Figure A-56 verify 2-aminoterephthalic acid linkers create supported MIL-53-NH_2(Al) crystals on aluminum mesh, as described in Section 5.3.2.

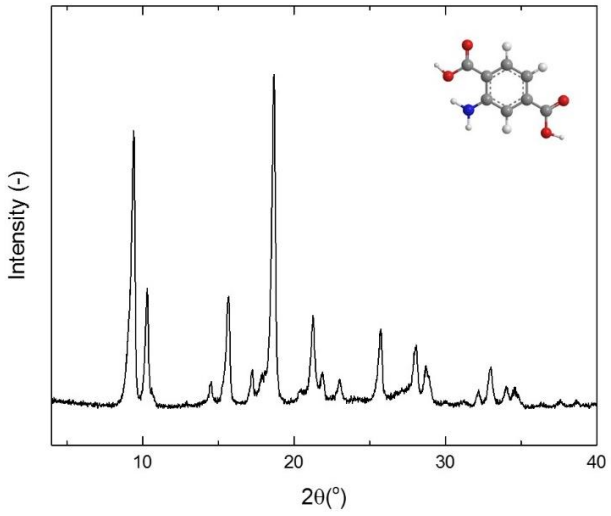

Figure 5-13: PXRD pattern of non-supported as-MIL-53-NH_2(Al) generated from aluminum foil (see synthesis procedures for more details). 2-aminoterepthalate molecule imaged in top right for linker molecule reference, created in ChemDraw.

5.3.4.3 Extension to Non-supported Aluminum Trimesate Frameworks

Non-supported MOF formation is also applicable to non-terephthalate ligands. As with supported MOF growth detailed earlier in this chapter, BTC linkers afforded the

creation of non-supported mesoporous MIL-96(Al), confirmed by characteristic PXRD reflections in Figure 5-14.[41] Broad reflections at 2θ = 3.49° and 4.09° in the diffractogram additionally identify MIL-100(Al) crystalline phases.[56] Previous reports commonly observe mixtures of MIL-100(Al) and MIL-96(Al), as the structures possess isomeric building blocks.[57,58] Interestingly, isolation of the MIL-96(Al) phase typically requires kinetic and/or solvent control, which are not employed here.[57] Subsequently, the insoluble precursor route developed here may provide the ability to mitigate mixed-framework side products encountered in conventional aluminum trimesate production.

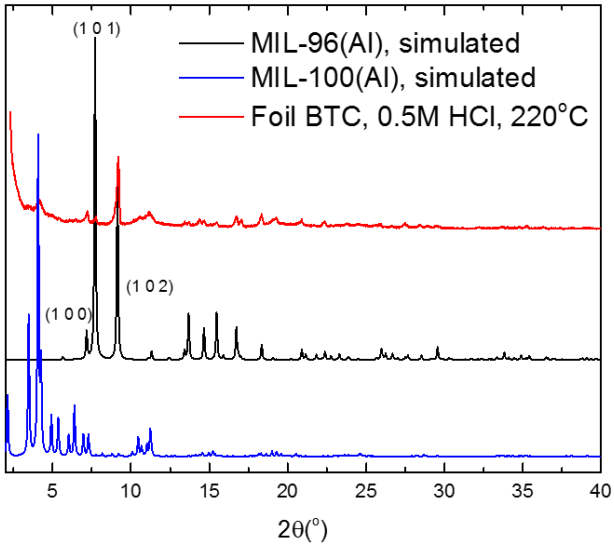

Figure 5-14: PXRD pattern of powder precipitate from foil, BTC, water reaction with 0.5M HCl, overlaid with simulated MIL-100(Al)[56] and MIL-96(Al)[41] crystallographic data

5.3.4.4 Impact of Insoluble Precursor on Growth Kinetics

MIL-96(Al) produced from metallic aluminum displays a unique morphology from conventionally synthesized MIL-96(Al) in previous publications. SEM images in Figure 5-15a and b reveal a dodecahedron morphology, with crystallize sizes from 1-3μm. Liu

and coworkers[59] previously reported the truncation of hexagonal spindle-shaped rod features on MIL-96(Al) crystallites, which correspond to the (1 0 0) plane, when crystal growth rates were decreased. Geometries observed at slower growth rates by Liu are consistent with crystal shapes imaged in this study. Resulting morphologies of MIL-96(Al) crystals strongly suggest a kinetic barrier to MOF growth exists when producing non-supported aluminum frameworks from the method proposed here. Controlled dissolution of metal cations restricts the growth of non-supported MOFs by limiting metal concentration in the bulk solution with respect to time, slowing crystallization. Furthermore, HCl(aq) addition fosters a H^+ concentration barrier which partially hinders linker deprotonation and subsequent MOF growth.

Importantly, this resistance does not prevent MOF formation at time scales relevant for material manufacturing. Non-supported MIL-53(Al) production was observed through the same method in as little as 2h, as shown in Figure 5-15c. To fully probe this behavior, MIL-53(Al) reactions with aluminum foil were exacted for 30min, 1h, 2h, and 4h time frames. Times started when reactant-filled autoclaves were placed inside preheated (220°C) ovens. Reactors were removed at their respective times and cooled to ambient temperature in a chemical hood. Finally, samples were gravity filtered and rinsed with DMF (3x) and methanol (3x). Aluminum foil is visually observable in the 30min and 1h tests. The metal precursor becomes absent at 2h, however. Onset of powder precipitation indicates the insoluble precursor is dissolved by the 0.5M HCl(aq) within 2h of reaction in the non-supported MOF procedure described here. Crystalline diffraction patterns of the 2h and 4h solids presented in Figure 5-15c confirm formation of MIL-53(Al) as early as 2h. Additionally, aluminum reflections are not present. Sharpening of diffraction peaks

from 2h to 4h reaction products evidences continued crystal growth at longer times, and consumption of intermediate and precursor species straining the crystalline lattice.

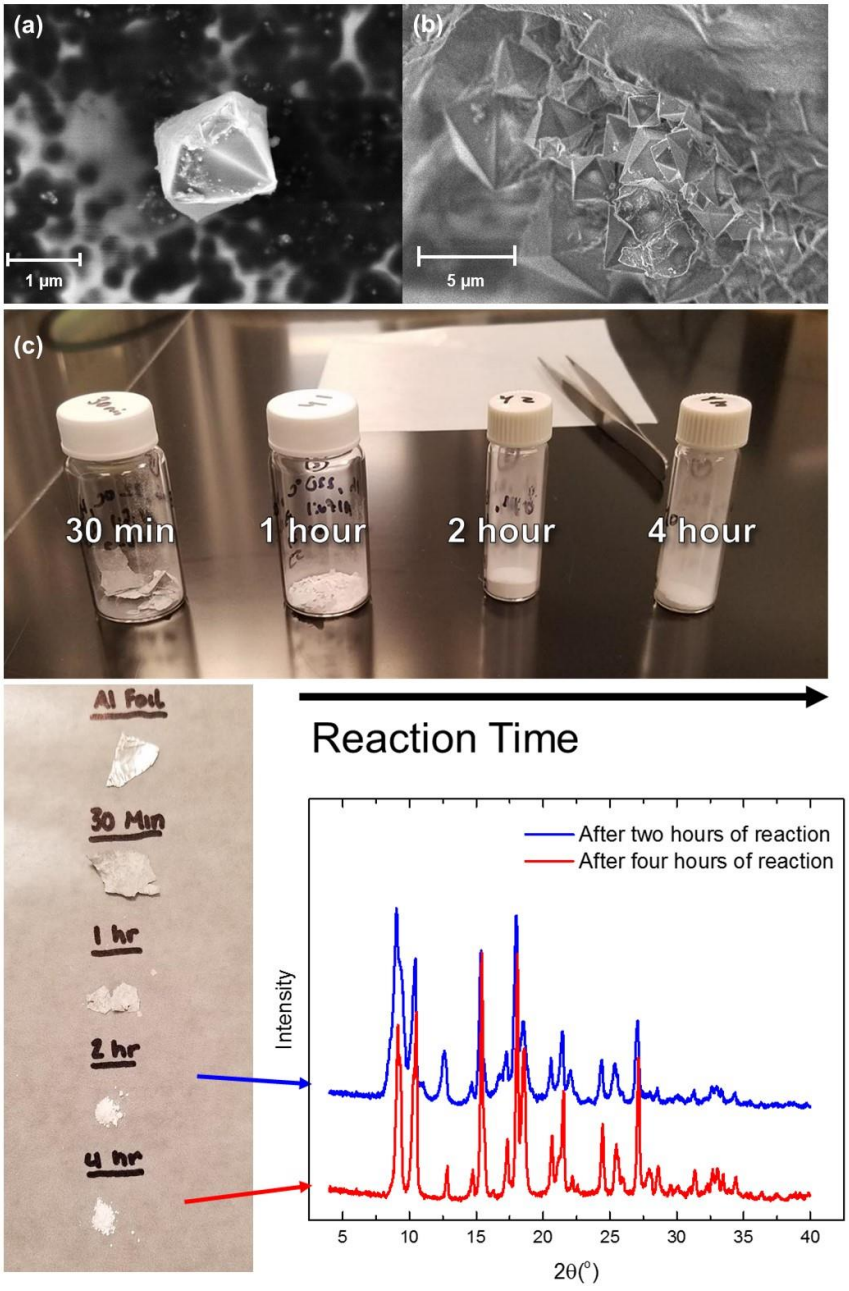

Figure 5-15: Non-supported MOF production from aluminum foil. (a) and (b) SEM images of MIL-96(Al) crystals, (c) time trial samples and measurements for aluminum foil-derived MIL-53(Al) at 220°C. Bottom right depicts powder diffraction data of powders from 2h and 4h experiments.

5.3.4.5 Reaction Temperature Studies on Non-Supported MIL-53(Al) Production

MIL-53(Al) production from aluminum foil occurs at reaction temperatures ≤ 220°C using 0.5M HCl. Pictured reaction precipitates in Figure 5-16 indicate the onset of non-supported MOF recovery at 60°C. Room-temperature MIL-53(Al) production was also attempted, however the aluminum foil did not dissolve. This is visually apparent in Figure 5-16. PXRD measurements of collected and rinsed foil pieces after room temperature reaction in Figure A-68 evidence the (1 1 1) phase of retained aluminum at $2\theta = 38.47°$ and 38.56°, unreacted terephthalic acid at $2\theta \approx 17°$ (ICDD reference code 00-003-0127), and broad scattering from amorphous metal oxide/hydroxide formation.[60]

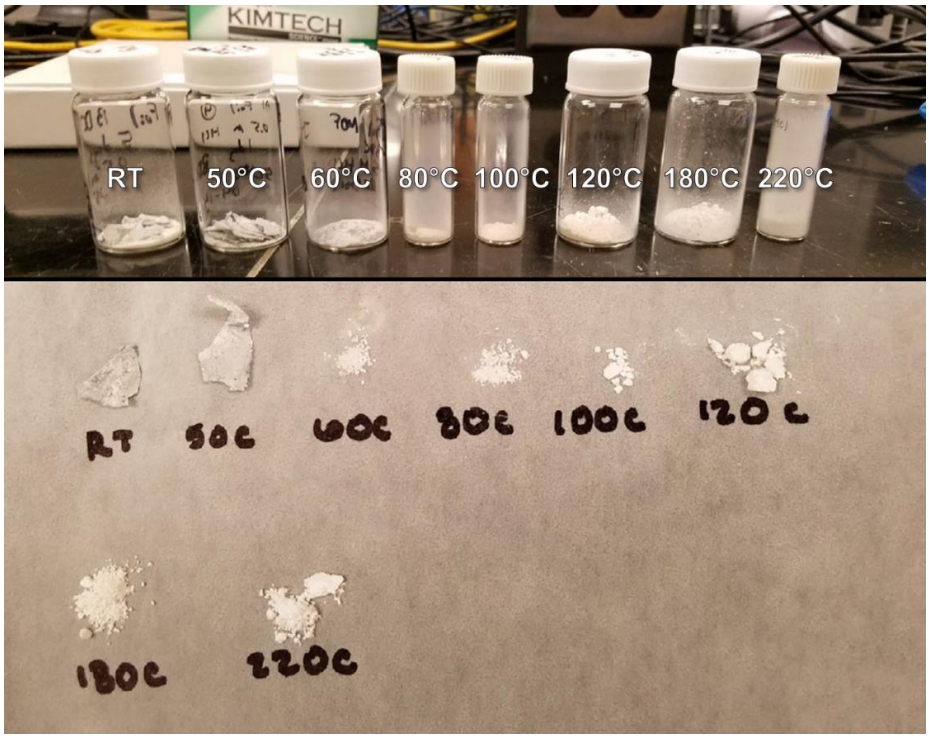

Figure 5-16: Non-supported MIL-53(Al) MOF products acquired after 24h isothermal reaction times at different synthesis temperatures. Top—products in scintillation vials arranged with increasing reaction temperature from left to right. Bottom—total collected solid precipitates from each reaction. Note "free" powder is not obtained in room temperature (RT) and 50°C syntheses.

Figure 5-17a and Figure A-69 show accessible BET surface areas plateau at approximately 1400 m^2 g^{-1} (23% increase from 80°C) at reaction temperatures between 100°C-220°C. To determine whether (1) insoluble aluminum or (2) 0.5M HCl(aq) was responsible for this phenomenon, a control experiment was performed by employing the same non-supported MOF synthesis procedure, but instead replacing insoluble aluminum with $AlCl_3 \times 6H_2O$ and $Al(NO_3)_3 \times 9H_2O$ salts. N_2 adsorption isotherms of acid modulated MIL-53(Al) products are presented alongside uptake data for the MOFs created without HCl(aq) in Figure 5-18. MOF products formed using aluminum nitrate and chloride salt precursors with 0.5M HCl(aq) obtain ~10.7% and ~13.1% enhancements in BET surface area, respectively, from their counterparts formed without acid modulation. This indicates HCl(aq) enhances microporosity in resulting MIL-53(Al) samples; BET surface areas enhancements over 10% in comparison to traditionally synthesized MIL-53(Al) [32,61–63].

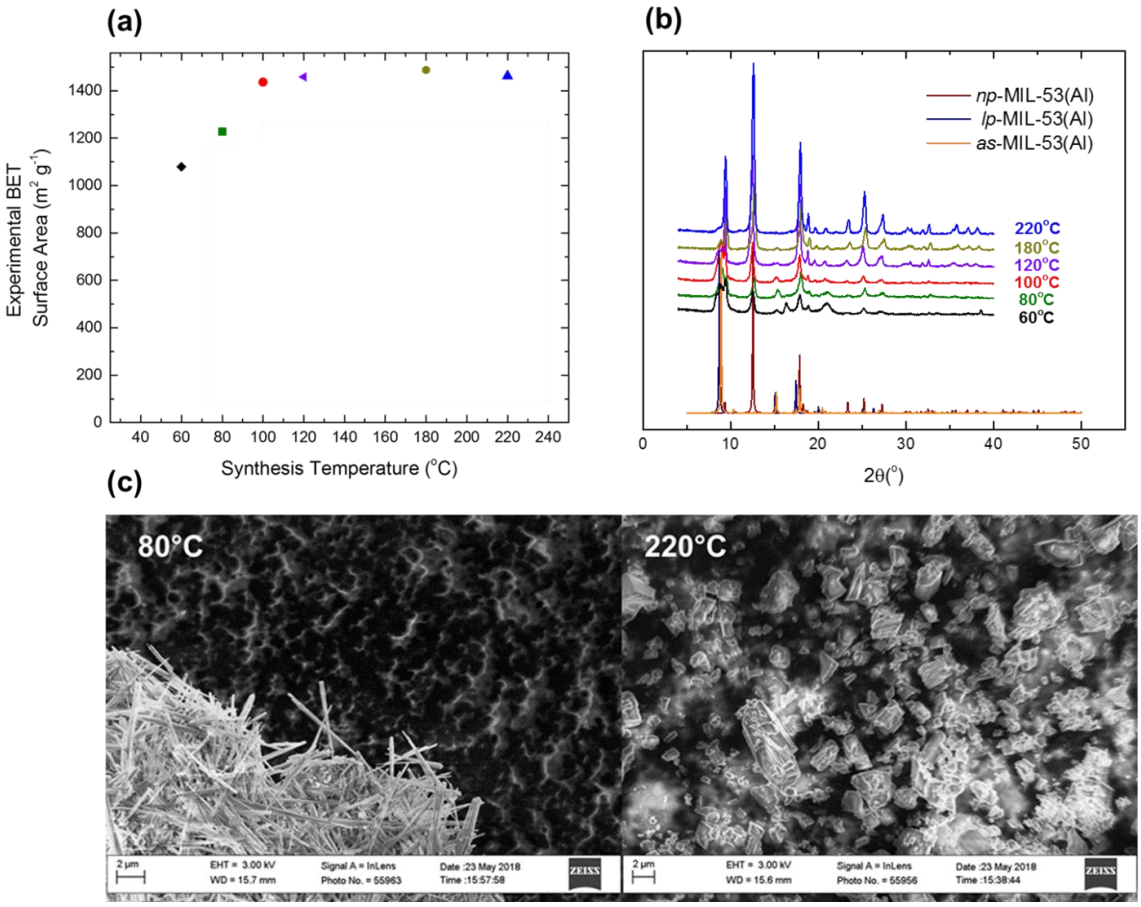

Figure 5-17: Temperature trials for non-supported MIL-53(Al) production from aluminum foil: (a) BET surface areas for MIL-53(Al) samples. (b) PXRD measurements of activated MIL-53(Al) produced using increasing temperatures (bottom to top). Patterns acquired immediately following desolvation are overlaid with crystallographic patterns for three characteristic MIL-53(Al) pore forms.[32] (c) SEM photographs of MIL-53(Al) morphology aluminum at synthesis temperature of 80°C (left) and 220°C (right).

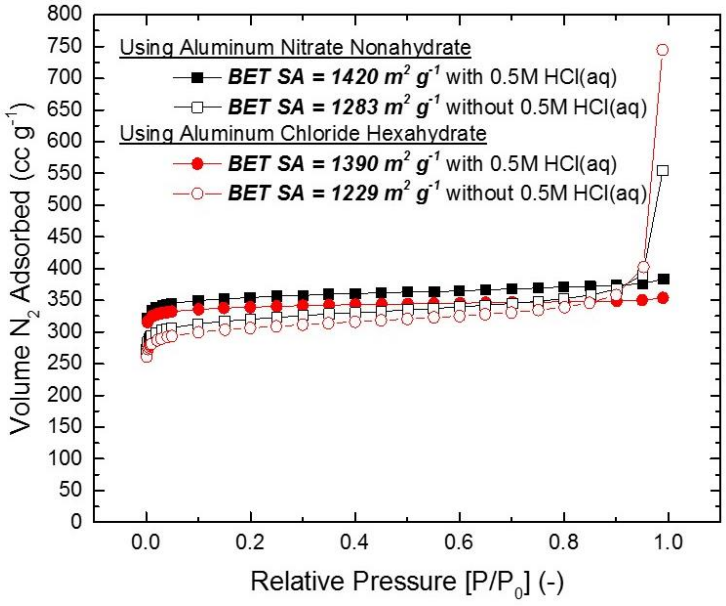

Figure 5-18: N_2 physisorption measurements acquired at 77K. Solid points indicate materials produced via acid modulated non-supported MOF synthesis scheme. Hollow points indicate materials produced without acid modulation (all other synthesis parameters unchanged). BET surface area values calculated using $0.005 < P / P_0 < 0.03$ range.[64]

Structural and morphological MIL-53(Al) features also evolve through increasing synthesis temperatures. Individual diffraction patterns for temperature trial reactions which successfully created non-supported MIL-53(Al) are provided in Figure 5-17b. Diffraction peaks sharpen with increasing reaction temperature, partially reflective of lattice strain and poor crystallinity at low synthesis temperatures. Inspection of the 60°C sample pattern reveals residual Al(s) ($2\theta \approx 38°$) and an unidentified aluminum derivative at $2\theta = 16.2°$, indicating the presence of other side-products. These constituents supplement the comparatively low microporosity illustrated for the sample in Figure 5-17a. Materials display broad, low intensity reflections at $2\theta \approx 8.7°$ and 15.1° at low reaction temperatures which correspond to the *lp*-MIL-53(Al). This gradually disappears with increasing synthesis temperature. Preferred *lp*-MIL-53(Al) pore form at lower reaction temperatures

was also noticed by Mounfield and Walton, although observed phases in the previous report did not possess the simultaneous mixture of *np*- and *lp*- forms seen here.[52] The data suggest higher reaction temperatures encourage *np*-MIL-53(Al) phase homogeneity. Crystal shape is significantly altered with reaction temperature as well. SEM micrographs in Figure 5-17c reveal agglomerated needle-like rod structures ~5μm in length, consistent with those observed for supported MIL-53(Al) growth discussed earlier in Figure 5-2c and d, at 80°C reaction temperatures. MIL-53(Al) obtained at 220°C contrastingly exhibits irregularly-sized rectangular geometries. Figure A-70 illustrates the gradual evolution from rod-to-rectangular MIL-53(Al) structures with increasing reaction temperature. These morphological changes communicate important differences in non-supported MOF formation at various reaction temperatures. Because the solid aluminum dissolution rate (through reaction with hydrochloric acid) is decreased at lower temperatures, MOF nucleation occurs on the exposed surfaces of the solubilizing metal reagent. Consequently, resulting rod-like structures are fostered by initial epitaxial crystal growth along the planes of the insoluble precursor. Conversely, metallic aluminum dissolves rapidly with HCl(aq) at high reaction temperatures. Although thermodynamically less favorable, crystal growth is subsequently forced in the bulk solution. This hypothesis is supported by the similarity of MIL-53(Al) morphologies obtained at high synthesis temperatures (180°C, 220°C) with previous visual observations MIL-53(Al) made with ionic salts, where crystal growth also occurs in the bulk solution.[34] As a process variable, temperature is easily changed in most reaction unit operations. Consequently, the insoluble precursor scheme presented here affords a simple way to tune non-supported MIL-53(Al) crystal size and morphology. Notably, this control is not directly provided by conventional solvothermal syntheses

utilizing ionic salts—dissolution of insoluble aluminum here is critical for directing MOF growth at low synthesis temperatures, and allowing bulk solution crystal formation at high reaction temperatures.

5.3.4.6 Evaluating Unconventional Insoluble Aluminum Sources

This methodology may be extended to a seemingly endless variety of potential aluminum metal precursors for MOF production. Figure 5-19a exemplifies this, where Coca-Cola cans retrieved from a recycling bin were converted into MIL-53(Al) and MIL-96(Al) through the same non-supported MOF reaction scheme. N_2 physisorption measurements of materials in Figure 5-19b verify the creation of highly microporous materials. Clearly, the robust MOF synthesis pathway is not hindered by numerous impurities present in metal precursors such as recycled cans (e.g., epoxy coating, plastic labeling, etc.). Non-aluminum impurities predictably minimize the adsorption properties of resulting materials on a per-mass basis. For example, the BET surface area for MIL-53(Al) generated from Coca-Cola cans is only 800 $m^2 g^{-1}$—30% lower than the 1140 m^2g^{-1} value reported by Loiseau et al. for conventionally-synthesized MIL-53(Al).[32] TGA measurements in Figure 5-19c elucidate resulting residual mass differences between MIL-53(Al) created from aluminum foil (relatively high metal purity) and recycled aluminum cans. Dry air was utilized as a carrier to create Al_2O_3 as the MOF combustion product at 1000°C. The theoretical building unit of MIL-53(Al) [$Al(OH)(C_6H_4\text{-}(COOH)_2$] is stoichiometrically normalized to 100wt% in Figure 5-19c after solvent and entrapped linker evacuation below 400°C. In this way, sample mass changes are compared to the theoretical mass loss of ~75.5wt%. The mass loss of aluminum foil-derived MIL-53(Al) adheres within ~2wt% of expected framework mass. Accordingly, cheap and readily accessible

sources like aluminum present themselves as surprisingly usable precursors to obtain highly ordered, porous, and pure nanomaterials. In contrast, ~38wt% of the Coca-Cola can-derived MOF product is attributed to non-aluminum species (e.g. plastic), explaining its reduced nitrogen uptake in Figure 5-19b.

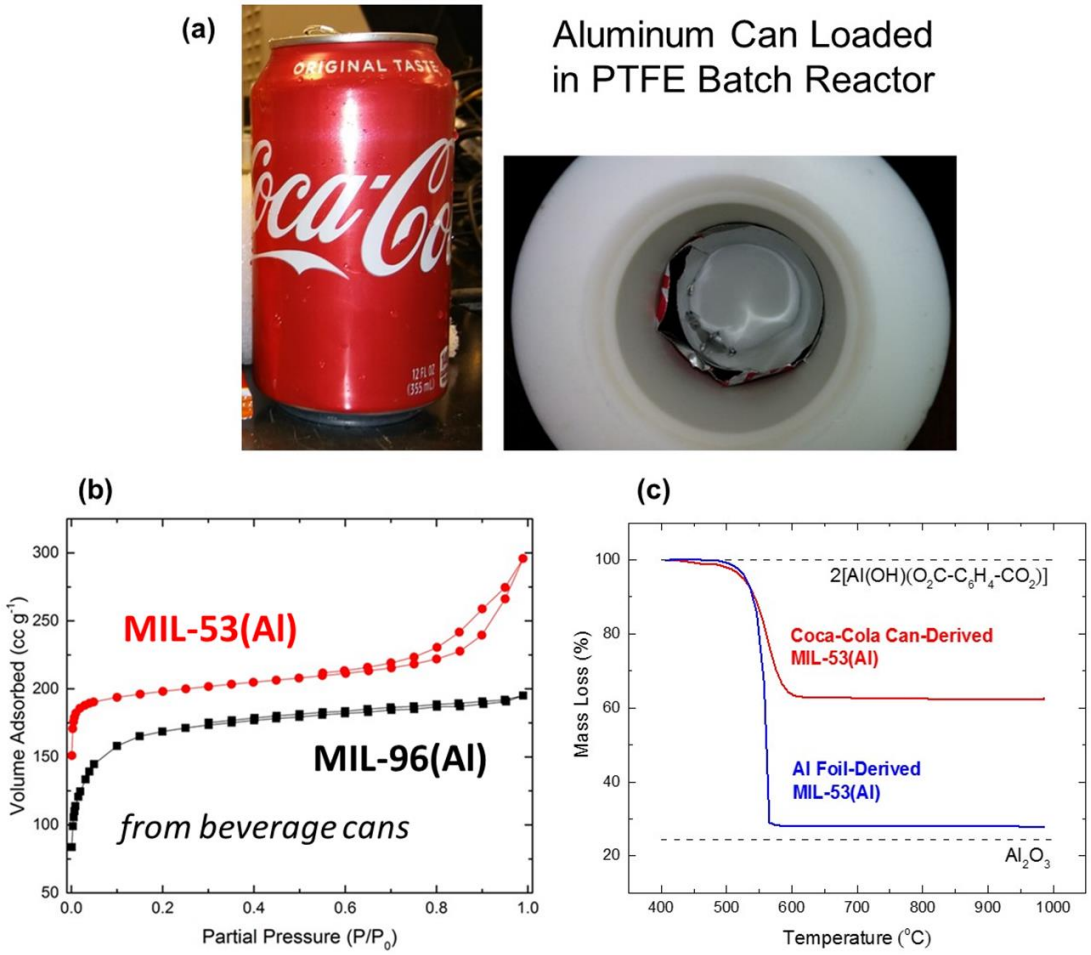

Figure 5-19: Textural properties of MOFs created from unconventional metal precursors: (a) Images of collected aluminum can. Cans were halved and loaded into PTFE liner for batch reaction, due to size restrictions. (b) N_2 uptake measurements at 77K for frameworks produced from a Coca-Cola can using terephthalic acid and trimesic acid linkers. (c) TGA measurements for MIL-53(Al)-derived from a Coca-Cola can (red) and aluminum foil (blue) using air as a carrier. Building unit of MIL-53(Al) normalized as 100% with experimental data after desolvation and removal of entrapped linkers (≥ 400°C), along with stoichiometric combustion product Al_2O_3.

Aluminum-containing metal alloys 6061 and 2024 were also successfully converted to MIL-53(Al), and supplement these findings. Elemental composition of the alloys are reported in Table A-9. PXRD patterns in Figure A-71 from the two alloys and Coca-Cola can-derived product confirm the formation of MIL-53(Al). Fascinatingly, aluminum was selectively converted from the two alloys, demonstrating the chemical specificity of the insoluble aluminum MOF reaction. To elaborate, magnesium and silicon are the other major elements that compose Alloy 6061. Following MIL-53(Al) production and separation, an unreacted non-MOF solid was also recovered containing a pink surface region pictured in Figure 5-20a—reminiscent of magnesium silicate hydroxides, such as montmorillonite.[65] Similarly, the post-reaction copper-rich Alloy 2024 by-product features a blue surface in Figure 5-20b, suggestive of cupric hydroxide formation after hydrothermal treatment. Results prove metallic aluminum purity does not prevent aluminum framework formation. Findings assert strong flexibility in material selection for Al-MOF production through the proposed insoluble aluminum method.

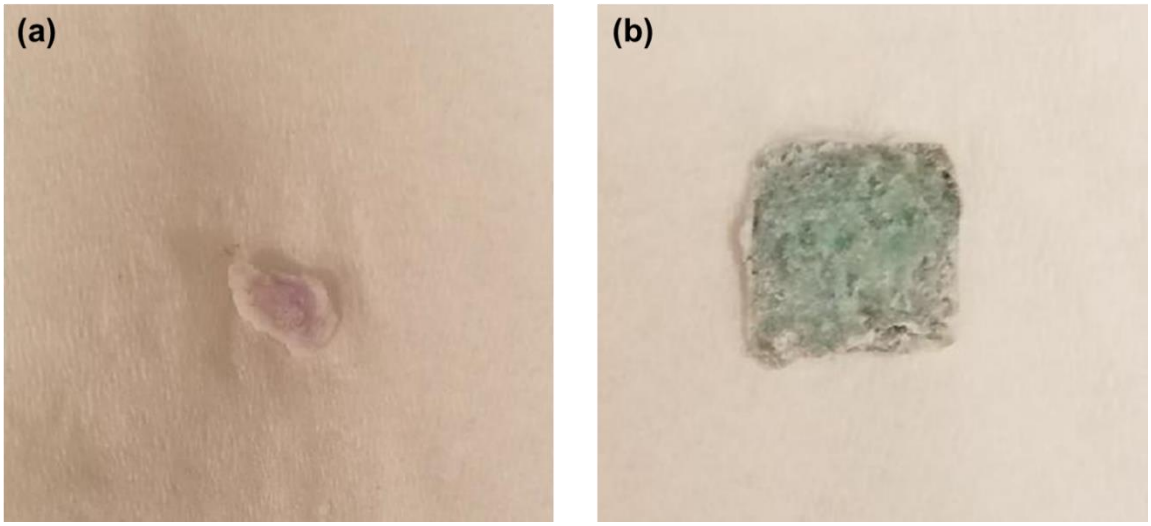

Figure 5-20: Obtained, non-MOF solids following non-supported MIL-53(Al) production using (a) Alloy 6061 and (b) Alloy 2024. Pink region in (a) denotes magnesium silicate hydroxide. blue region in (b) denotes cupric hydroxide

5.3.5 Cost Analysis of MIL-53(Al) Manufacturing from Insoluble Aluminum

A major motivation of pursuing both supported and non-supported aluminum MOF growth strategies here was to communicate how production and engineering of these nanomaterials can be simple and economical. Please refer to the Appendix A.3.3 Cost Analysis Work and Section 5.2.4 for information on cost analyses in this work. The calculated molar yield of MIL-53(Al) produced in this study from commercial aluminum foil was ≈ 83%, accounting for mass impurities examined in Figure A-72. Raw materials utilized in this investigation beneficially lower manufacturing and capital costs for scaled-up nanoporous material fabrication. For example, Table A-10 summarizes averaged, bulk-quantity material costs for synthesis reagents utilized here. These expenses are compared with costs associated with reactants typical for the conventional synthesis of aluminum MOFs: aluminum chloride, aluminum nitrate, and DMF. It is important to recognize that aluminum salts inherently possess a lower $\frac{g\ Al}{g\ material}$ ratio than corresponding metals. So,

larger quantities of metal salts are required to produce similar MOF yields as pure metals, since the bulk of ionic salt masses are often attributed to water and compound anions. Normalizing metal precursor costs by mass of aluminum in Table A-10 divulges the consequent price reduction when using metallic aluminum for MOF production over aluminum salts. The relatively greater market demand for metallic aluminum fosters a ×2.74 and ×11.4 price reduction over commonly reported chloride and nitrate aluminum salts through the same synthesis route, respectively. As a caveat, solvent and/or framework ligand choice often dictates MOF production expenses; these costs are not altered by the reaction scheme shown here. However, presented raw material costs in Table A-10 remain low for terephthalate-based frameworks, which constitute the majority of commonly studied MOFs in the literature (UiO-66, MIL-53, MIL-101, MIL-125, MOF-5, etc.). A materials cost of $3.49 to produce 1kg of non-supported MIL-53(Al) using metallic aluminum was approximated (see Appendix A.3.3 Cost Analysis Work). This estimate is comparable to large-scale MOF production costs reported by PNNL.[66] However, the synthesis route here allows process flexibility through the potential to create supported and non-supported MIL-53(Al), utilizes eco-friendly water and ubiquitously available metallic aluminum, and facilitates low reaction temperatures. As of June 2018, BASF sells MIL-53(Al) (product name Basolite A100) for $5,320 per 500g of material—well over $10,000/kg. Although the price markup for Basolite A100 is likely not close to manufacturing cost (primary market is probably research facilities)[66], the estimated cost of $3.49/kg MIL-53(Al) approximated here greatly undercuts current sale prices. Although other operating expenses and post-synthetic purification steps would be required, the resulting price margin for this order-of-magnitude estimation is > 99%. This strongly

suggests that the methodology presented here can be leveraged for economical MOF production when inexpensive framework ligands are utilized.

5.3.6 Conclusions

Advanced adsorption-based separation methods will certainly require advanced separation materials. Discovering facile routes of generating these materials while keeping production techniques affordable, simple, and accessible are consequently crucial. Findings presented in this study are intended to showcase how these two criteria are not mutually exclusive when producing high-value porous nanomaterials. The general methodology of utilizing insoluble metal precursors shows flexibility in MOF production, where well-known solvothermal reaction pathways were adapted to unconventional precursors. This is specifically relevant for MOF literature as a novel one-step strategy for creating supported frameworks. Discovering analogous reaction pathways for supported frameworks from different metals will greatly diversify the applicability and application of MOFs for separation processes.

Adaptation of non-supported MOF production from insoluble precursors similarly mandate future studies to focus on tuning synthesis chemistry towards generating different MOFs. An unexpected level of porosity, morphology, growth rate, and crystal size control is conveniently afforded by non-supported MOF growth from metallic aluminum. Control over framework by-products, as noticed with MIL-96(Al) production over MIL-100(Al) and MIL-110(Al), may also result from insoluble metal precursors. The authors suggest examining conventional synthesis procedures utilizing ionic salts and replacing them with insoluble metal reagents. Tuning synthesis chemistry thereafter and incorporating etching

agents, as performed here with HCl(aq), can be promising to successfully yield target frameworks.

Metals are ubiquitous in the modern world: present in nature, structure materials, catalysts, supports, and even commodity goods as seen with aluminum foil and cans here. Consequently, insoluble metals are readily attainable precursors for generating high-value materials. It is hoped future investigations into porous material engineering and production will not eschew the notion of looking into unconventional reagent sources to produce advanced materials as highlighted in this report—even if that source happens to be discarded items in a recycling bin.

5.4 Chapter 5 References

1. Yuan, S. *et al.* Stable Metal–Organic Frameworks: Design, Synthesis, and Applications. *Adv. Mater.* **30**, 1704303 (2018).

2. Schroder, M. *Functional Metal-Organic Frameworks: Gas Storage, Separation and Catalysis*. (Springer, 2010).

3. Gascon, J., Corma, A., Kapteijn, F. & Llabrés i Xamena, F. X. Metal Organic Framework Catalysis: Quo vadis? *ACS Catal.* **4**, 361–378 (2014).

4. Zhou, H.-C., Long, J. R. & Yaghi, O. M. Introduction to Metal–Organic Frameworks. *Chem. Rev.* **112**, 673–674 (2012).

5. Corma, A., García, H. & Llabrés i Xamena, F. X. Engineering Metal Organic Frameworks for Heterogeneous Catalysis. *Chem. Rev.* **110**, 4606–4655 (2010).

6. Sholl, D. S. & Lively, R. P. Seven chemical separations to change the world. *Nature* **532**, 435–437 (2016).

7. Liu, G. *et al.* Mixed matrix formulations with MOF molecular sieving for key energy-intensive separations. *Nat. Mater.* **17**, 283–289 (2018).

8. Bloch, E. D. *et al.* Hydrocarbon Separations in a Metal-Organic Framework with Open Iron(II) Coordination Sites. *Science* **335**, 1606–1610 (2012).

9. Chen, L. *et al.* Ultrafast and Efficient Extraction of Uranium from Seawater Using an Amidoxime Appended Metal–Organic Framework. *ACS Appl. Mater. Interfaces* **9**, 32446–32451 (2017).

10. Sanz-Peez, E. S., Murdock, C. R., Didas, S. A. & Jones, C. W. Direct Capture of CO_2 from Ambient Air. *Chem. Rev.* **116**, 11840–11876 (2016).

11. McDonald, T. M. *et al.* Capture of Carbon Dioxide from Air and Flue Gas in the Alkylamine-Appended Metal–Organic Framework mmen-Mg_2(dobpdc). *J. Am. Chem. Soc.* **134**, 7056–7065 (2012).

12. Choi, S., Watanabe, T., Bae, T.-H., Sholl, D. S. & Jones, C. W. Modification of the Mg/DOBDC MOF with Amines to Enhance CO_2 Adsorption from Ultradilute Gases. *J. Phys. Chem. Lett.* **3**, 1136–1141 (2012).

13. Frameworks for commercial success. *Nat. Chem.* **8**, 987 (2016).

14. Urquhart, J. World's first commercial MOF keeps fruit fresh. *Chemistry World* (Sept. 2016).

15. Petit, C. Present and future of MOF research in the field of adsorption and molecular separation. *Curr. Opin. Chem. Eng.* **20**, 132–142 (2018).

16. Rezaei, F. & Webley, P. Structured adsorbents in gas separation processes. *Sep. Purif. Technol.* **70**, 243–256 (2010).

17. Akhtar, F., Andersson, L., Ogunwumi, S., Hedin, N. & Bergström, L. Structuring adsorbents and catalysts by processing of porous powders. *J. Eur. Ceram. Soc.* **34**, 1643–1666 (2014).

18. Darunte, L. A. *et al.* Monolith-Supported Amine-Functionalized Mg_2(dobpdc) Adsorbents for CO_2 Capture. *ACS Appl. Mater. Interfaces* **9**, 17042–17050 (2017).

19. Shekhah, O. Layer-by-Layer Method for the Synthesis and Growth of Surface Mounted Metal-Organic Frameworks (SURMOFs). *Materials (Basel).* **3**, 1302–

1315 (2010).

20. Liu, J. & Woll, C. Surface-supported metal-organic framework thin films: fabrication methods, applications, and challenges. *Chem. Soc. Rev.* **46**, 5730–5770 (2017).

21. Yoon, S. M., Park, J. & Grzybowski, B. A. Large-Area, Freestanding MOF Films of Planar, Curvilinear,or Micropatterned Topographies. *Angew. Chemie Int. Ed.* **56**, 127–132 (2017).

22. Rubio-Martinez, M. *et al.* New synthetic routes towards MOF production at scale. *Chem. Soc. Rev.* **46**, 3453–3480 (2017).

23. Stock, N. & Biswas, S. Synthesis of Metal-Organic Frameworks (MOFs): Routes to Various MOF Topologies, Morphologies, and Composites. *Chem. Rev.* **112**, 933–969 (2012).

24. Zhan, G. & Zeng, H. C. Alternative synthetic approaches for metal-organic frameworks: transformation from solid matters. *Chem. Commun.* **53**, 72–81 (2017).

25. Zhang, Y. *et al.* Constructing Free Standing Metal Organic Framework MIL-53 Membrane Based on Anodized Aluminum Oxide Precursor. *Sci. Rep.* **4**, 4947 (2014).

26. Reboul, J. *et al.* Mesoscopic architectures of porous coordination polymers fabricated by pseudomorphic replication. *Nat. Mater.* **11**, 717–723 (2012).

27. Li, Z. *et al.* The Metal–Organic Framework MIL-53(Al) Constructed from Multiple Metal Sources: Alumina, Aluminum Hydroxide, and Boehmite. *Chem. – A Eur. J.* **21**, 6913–6920 (2015).

28. Pappas, S. Facts About Aluminum. *Live Science* (2014). Available at: https://www.livescience.com/28865-aluminum.html. (Accessed: 27th June 2018)

29. Kwon, Y. H. *et al.* Ion-Exchanged SAPO-34 Membranes for Krypton–Xenon Separation: Control of Permeation Properties and Fabrication of Hollow Fiber Membranes. *ACS Appl. Mater. Interfaces* **10**, 6361–6368 (2018).

30. DeSantis, D. *et al.* Techno-economic Analysis of Metal−Organic Frameworks for Hydrogen and Natural Gas Storage. *Energy & Fuels* **31**, 2024–2032 (2017).

31. Andonova, S., Ivanova, E., Yang, J. & Hadjiivanov, K. Adsorption Forms of CO_2 on MIL-53(Al) and MIL-53(Al)−OH x As Revealed by FTIR Spectroscopy. *J. Phys. Chem. C* **121**, 18665–18673 (2017).

32. Loiseau, T. *et al.* A Rationale for the Large Breathing of the Porous Aluminum Terephthalate (MIL-53) Upon Hydration. *Chem. – A Eur. J.* **10**, 1373–1382 (2004).

33. Alqadami, A. A., Naushad, M., Alothman, Z. A. & Ghfar, A. A. Novel Metal−Organic Framework (MOF) Based Composite Material for the Sequestration of U(VI) and Th(IV) Metal Ions from Aqueous Environment. *ACS Appl. Mater. Interfaces* **9**, 36026–36037 (2017).

34. Isaeva, V. I., Tarasov, A. L., Chernyshev, V. V. & Kustov, L. M. Control of morphology and size of microporous framework MIL-53(Al) crystals by synthesis procedure. *Mendeleev Commun.* **25**, 466–467 (2015).

35. Moran, C. M., Joshi, J. N., Marti, R. M., Hayes, S. E. & Walton, K. S. Structured Growth of Metal–Organic Framework MIL-53(Al) from Solid Aluminum Carbide Precursor. *J. Am. Chem. Soc.* **140**, 9148–9153 (2018).

36. Shekhah, O. *et al.* Layer-by-Layer Growth of Oriented Metal Organic Polymers on a Functionalized Organic Surface. *Langmuir* **23**, 7440–7442 (2007).

37. Xue, S. M. *et al.* "Single nickel source" in situ fabrication of a stable homochiral MOF membrane with chiral resolution properties '"Single nickel source"' *in situ* fabrication of a stable homochiral MOF membrane with chiral resolution properties. *Chem. Commun* **49**, 10569–10571 (2013).

38. Li, Z. *et al.* Platinum–nickel frame within metal-organic framework fabricated in situ for hydrogen enrichment and molecular sieving. *Nat. Commun.* **6**, 8248 (2015).

39. Tanihara, Y., Nozaki, A., Kuwahara, Y., Mori, K. & Yamashita, H. Fabrication of Densely Packed HKUST-1 Metal Organic Framework Thin Layers on a Cu Substrate through a Controlled Dissolution of Cu. *Bull. Chem. Soc. Jpn.* **89**, 1048–1053 (2016).

40. Luz, I., Loiudice, A., Sun, D. T., Queen, W. L. & Buonsanti, R. Understanding the Formation Mechanism of Metal Nanocrystal@MOF-74 Hybrids. *Chem. Mater.* **28**, 3839–3849 (2016).

41. Loiseau, T. *et al.* MIL-96, a Porous Aluminum Trimesate 3D Structure Constructed from a Hexagonal Network of 18-Membered Rings and μ_3-Oxo-Centered Trinuclear Units. *J. Am. Chem. Soc.* **128**, 10223–10230 (2006).

42. Momma, K. & Izumi, F. *VESTA 3* for three-dimensional visualization of crystal, volumetric and morphology data. *J. Appl. Crystallogr.* **44**, 1272–1276 (2011).

43. Bernardo, P., Drioli, E. & Golemme, G. Membrane Gas Separation: A Review/State of the Art. *Ind. Eng. Chem. Res.* **48**, 4638–4663 (2009).

44. Nicolas, C. & Pera-Titus, M. Nanocomposite MFI-Alumina Hollow Fiber Membranes: Influence of NO_x and Propane on CO_2 /N_2 Separation Properties. *Ind. Eng. Chem. Res.* **51**, 10451–10461 (2012).

45. Liu, X., Demir, N. K., Wu, Z. & Li, K. Highly Water-Stable Zirconium Metal–Organic Framework UiO-66 Membranes Supported on Alumina Hollow Fibers for Desalination. *J. Am. Chem. Soc.* **137**, 6999–7002 (2015).

46. DeWitt, S. J. A., Rubiera Landa, H. O., Kawajiri, Y., Realff, M. & Lively, R. P. Development of Phase-Change-Based Thermally Modulated Fiber Sorbents. *Ind. Eng. Chem. Res.* **58**, 5768-5776 (2019)

47. Pimentel, B. R. & Lively, R. P. Propylene Enrichment via Kinetic Vacuum Pressure Swing Adsorption Using ZIF-8 Fiber Sorbents. *ACS Appl. Mater. Interfaces* **10**, 36323–36331 (2018).

48. DeWitt, S. J. A. *et al.* Critical Comparison of Structured Contactors for Adsorption-Based Gas Separations. *Annu. Rev. Chem. Biomol. Eng.* **9**, 129–152 (2018).

49. Moran, C. M. Disordered and Ordered Derivatives of Carbides for Acid Gas Adsorption. PhD Dissertation. (Georgia Institute of Technology, 2018).

50. Chan, S. C. & Valleau, J. P. Ultrasonic study of hydrochloric acid association in N,N-dimethylformamide. *Can. J. Chem.* **46**, 853–858 (1968).

51. Giovine, R. *et al.* NMR crystallography to probe the breathing effect of the MIL-53(Al) metal–organic framework using solid-state NMR measurements of ^{13}C– ^{27}Al distances. *Acta Crystallogr. Sect. C Struct. Chem.* **73**, 176–183 (2017).

52. Mounfield III, W. P. & Walton, K. S. Effect of synthesis solvent on the breathing behavior of MIL-53(Al). *J. Colloid Interface Sci.* **447**, 33–39 (2015).

53. Cmarik, G. E., Kim, M., Cohen, S. M. & Walton, K. S. Tuning the Adsorption Properties of UiO-66 via Ligand Functionalization. *Langmuir* **28**, 15606–15613 (2012).

54. Lin, X. *et al.* High Capacity Hydrogen Adsorption in Cu(II) Tetracarboxylate Framework Materials: The Role of Pore Size, Ligand Functionalization, and Exposed Metal Sites. *J. Am. Chem. Soc.* **131**, 2159–2171 (2009).

55. Jasuja, H. & Walton, K. S. Experimental Study of CO_2 , CH_4 , and Water Vapor Adsorption on a Dimethyl-Functionalized UiO-66 Framework. *J. Phys. Chem. C* **117**, 7062–7068 (2013).

56. Volkringer, C. *et al.* Synthesis, Single-Crystal X-ray Microdiffraction, and NMR Characterizations of the Giant Pore Metal-Organic Framework Aluminum Trimesate MIL-100. *Chem. Mater.* **21**, 5695–5697 (2009).

57. Haouas, M., Volkringer, C., Loiseau, T., Ferey, G. & Taulelle, F. In Situ NMR, Ex Situ XRD and SEM Study of the Hydrothermal Crystallization of Nanoporous Aluminum Trimesates MIL-96, MIL-100, and MIL-110. *Chem. Mater.* **24**, 2462–2471 (2012).

58. Qiu, M., Guan, Q. & Li, W. Controllable Assembly of Al-MIL-100 via an Inducing Occupied Effect and Its Selective Adsorption Activity. *Cryst. Growth Des.* **16**, 3639–3646 (2016).

59. Liu, D. *et al.* Size- and morphology-controllable synthesis of MIL-96 (Al) by hydrolysis and coordination modulation of dual aluminium source and ligand systems. *Dalt. Trans.* **44**, 16421–16429 (2015).

60. Wyckoff, R. W. G. Crystal Structures, Vol. 1; (John Wiley: New York 1963).

61. Férey, G. *et al.* Hydrogen adsorption in the nanoporous metal-benzenedicarboxylate

M(OH)(O_2C–C_6H_4–CO_2) (M = Al^{3+}, Cr^{3+}), MIL-53. *Chem. Commun.* 2976–2977 (2003).

62. Rallapalli, P. *et al.* Sorption studies of CO_2, CH_4, N_2, CO, O_2 and Ar on nanoporous aluminum terephthalate [MIL-53(Al)]. *J. Porous Mater.* **18**, 205–210 (2011).

63. Ma, S. & Zhou, H.-C. Gas storage in porous metal–organic frameworks for clean energy applications. *Chem. Commun.* **46**, 44–53 (2010).

64. Walton, K. S. & Snurr, R. Q. Applicability of the BET method for determining surface areas of microporous metal-organic frameworks. *J. Am. Chem. Soc.* **129**, 8552–8556 (2007).

65. Huat, B. B. K., Toll, D. G. & Prasad, A. *Handbook of Tropical Residual Soils Engineering*. (Taylor & Francis, 2012).

66. Liu, J., Thallapally, P. K., McGrail, B. P., Brown, D. R. & Liu, J. Progress in adsorption-based CO_2 capture by metal–organic frameworks. *Chem. Soc. Rev.* **41**, 2308 (2012).

CHAPTER 6. MOF-DERIVED STRUCTURED METAL OXIDE COMPOSITES FROM INSOLUBLE PRECURSORS

6.1 Introduction

Nanoscale structural control has experienced decades of interest in the scientific community.[1] The ability to harness tight control over pore size distribution, accessibility, and surface chemistry of porous substrates and composites directly dictates their performance and applicability in catalysis and adsorption applications.[2–4] As an example, one-dimensional growth and structure control has yielded significant enhancements in material development related to optics and electronics (e.g. carbon nanotubes).[5–9] Facile methods for enacting geometry, pore chemistry, and structure control over commonly employed porous substrates such as metal oxides and carbons foster broad impacts on materials science. For example, desirable electrochemical working potential and capacitance in reported MOF-derived oxide composites create interesting opportunities in battery power.[10–12]

The extensive library of exotic microstructures provided by metal-organic frameworks (MOFs) provides the opportunity to transfer many unique MOF architectures to derived metal oxide-based composites across the periodic table. MOF-derived oxides and carbons are commonly obtained through combustion or pyrolysis of the framework. The process expels organic linkers, but leaves behind metal oxide building blocks from original MOF structures, along with agglomerated carbon. Previous reports discuss the "structural memory" of MOF-derived oxides/carbons—metal composition and

morphological features in MOF precursors are easily transitioned onto resulting metal oxides/carbonaceous materials.[13–15] MOFs derived from insoluble metal precursors, such as metals, carbides, and hydroxides, have not yet been converted into MOF-derived media in literature reports however. Chapter 5 and previous literature show MOFs derived from insoluble matter adapt unconventional morphologies, and are patterned and positioned directly onto substrates in one step without modulation or structure-directing agents.[16,17] Converting insoluble precursor-derived MOFs into then derived oxide/carbon media therefore imparts their unique structures onto porous oxide-based materials, while still preserving underlying supports. This is not possible with previous MOF-to-oxide/carbon treatments, which utilize non-supported MOFs grown from ionic salts as precursors. In short—the unique features of these MOFs are instilled into metal oxides and porous carbons as well. Chapter 6 consequently extends application of subset "insoluble metal precursor-synthesized MOFs" to derived oxide materials. Highly accessible alumina-based microstructures are developed from previously reported Al_4C_3-derived MIL-53(Al)[18], which exhibits self-supported microneedle structures. The newly-produced metal oxide composite, referred to as *MIL-53(Al)-oxide* in the text, adapts interesting textural properties for MOF chemistry and potential catalysis/adsorption applications, as described herein.

6.2 Materials and Methods

6.2.1 Synthesis and Materials Preparation

MIL-53(Al) produced from insoluble aluminum materials was used to create derived oxide/carbon composites in this study. Specifically, MIL-53(Al) derived from aluminum carbide (Al_4C_3, Strem Chemicals 98% purity 325 mesh) and

aluminum/magnesium alloy mesh purchased from TWC Inc. was utilized to create *MIL-53(Al)-oxide*. Both MOFs and MOF-derived composites were degassed under vacuum at 150°C for 24h before all analyses and synthesis procedures. All other reagents were acquired commercially without further purification.

6.2.1.1 *MIL-53(Al)-oxide* Preparation

300 mg of Al_4C_3-derived MIL-53(Al) was loaded onto a silica boat. The boat was then placed in a 20" long, 1" O.D. quartz tube. The assembly was inserted into a horizontal tube furnace, described previously by Moran et al.[19] The tube was evacuated with argon (Airgas 99.999%) at a flow rate of 150mL min^{-1} for at least 30 minutes to purge out air trapped in the tube. Then, the sample was heated to 600°C with a ramp rate of 5°C/min. MIL-53(Al) pyrolyzed isothermally at 600°C for 8h. Leftover powder then cooled naturally in the tube under dry argon flow. After cooling, the assembly was deconstructed, and newly-synthesized *MIL-53(Al)-oxide* powder was collected. Yields were assessed by weighing the loaded silica boat before and after pyrolysis to quantify mass loss.

6.2.1.2 Iron Oxide-Impregnated *MIL-53(Al)-oxide*

Impregnated was based on the incipient wetness method. First, 300 mg of Al_4C_3-derived MIL-53(Al) was degassed and placed in a 20mL scintillation vial. Simultaneously, 7.86g of 99% purity iron (III) nitrate nonahydrate, purchased from Acros, was mixed into 10mL of DI water in a 20mL scintillation vial with magnetic stirring. The mixture was agitated at room temperature until the solute completely dissolved. Based on the estimated pore volume of Al_4C_3-derived MIL-53(Al) (~0.28 cc g^{-1}), 3.5x the volume of the available pore volume of the MOF (84µL × 3 = 294µL) was assumed to supersaturate the pore space.

Accordingly, 294μL of the iron nitrate solution was dispensed onto the MOF through 5 additions (59μL each) using a micropipette. Between each addition, the powder slurry was quickly mixed with a dry glass rod while sonicating the entire vial to promote infiltration. After salt impregnation, the powder was dried for ~10min in a chemical hood, and was then added to a silca boat for pyrolysis. MOF pyrolysis thereafter was carried out in the same manner as described in Section 6.2.1.1.

6.2.1.3 MIL-53(Al) Cyclic Regrowth Syntheses

MIL-53(Al) growth cycles from *MIL-53(Al)-oxide* were carried out by repeating two general steps:

1. Pyrolysis of Al_4C_3-derived MIL-53(Al)
2. Solvothermal growth of MIL-53(Al) from *MIL-53(Al)-oxide*

Step (2) was achieved using the same general procedure described for Al_4C_3-derived MIL-53(Al) growth by Moran et al., but instead assumes the metal precursor has a stoichiometry of Al_2O_3 (also detailed in Chapter 5).[18] As an example, for Cycle 1 36.9mg of *MIL-53(Al)-oxide* was placed in a stainless steel-lined 20mL PTFE reactor with 361.1mg of terephthalic acid (98% from Sigma Aldrich) and 3.9mL DI water. The reactor was then sealed and heated isothermally at 220°C for 24h. After cooling, the precipitates were separated through gravity filtration, and washed with N,N-dimethylformamide and then methanol three time each. The filtered Cycle 1 MOF was then allowed to dry in a chemical hood overnight. Finally, powder products were collected and stored in a cool, dry location.

6.2.2 Sample Characterization Methods

6.2.2.1 Nitrogen Physisorption at 77K

A Quantachrome Quadrasorb SI volumetric system with 5.11 QuadraWin™ software package was used to collect nitrogen adsorption data at 77K. Sample quantities between 50-100mg (after degassing) were utilized in measurements. BET surface area measurements were approximated using a pressure range of P/P_0 = 0.005–0.03.[20] Total pore volumes are reported at P/P_0 = 0.8 to avoid over-approximation from N_2 condensation at high pressures at 77K.

Quenched Solid Density Functional Theory (QSDFT) was utilized through QuadraWin™ to create pore size distributions for MOF-derived oxide-based composites. To account for the surface heterogeneity and multimodal pore systems apparent in *MIL-53(Al)-oxide*, an adsorption branch slit/cylindrical pore model was assumed using a N_2 adsorbate and carbon adsorbent.

6.2.2.2 Powder X-ray Diffraction

PXRD data was acquired using an X'Pert X-ray PANalytical diffractometer. Cu Kα radiation (λ = 1.5418 Å) source was utilized. Powder samples were first gently ground and packed tightly onto low-intensity background holders. These holders were then rotated during data collection. Scans were carried out at room temperature with a range of 2θ = 4° - 60° and step size of 0.02°.

6.2.2.3 Scanning Electron Microscopy (SEM)/Energy Dispersive Spectroscopy (EDS)

A Zeiss Ultra 60 Field Emission (FE) SEM was used to acquire electron images. Samples were placed onto carbon tape secured on stands prior to imaging. Accelerating voltage down to 1keV was used to image nanorod surface features depicted in this report for *MIL-53(Al)-oxide*. A range of voltages from 1-20keV was used to image materials.

EDS measurements were attained using the same apparatus. An accelerating voltage of at least 10keV was utilized while collecting EDS data, with a working distance of ~8.7mm. AZtec software was used to process EDS data, quantify compositions, and create elemental mapping reports.

6.2.2.4 Inductively Coupled Plasma Optical Emission Spectroscopy (ICP-OES)

Aluminum, iron, and sulfur mass fractions were determined in part through ICP-OES measurements. About 75 mg of tested sample batches were divided into three portions (25 mg each) to provide repeat measurements on each batch. Powder samples were then dissolved through high temperature alkali fusion with sodium carbonate. After fusion, the material was dissolved in a 6N hydrochloric acid solution. Dissolved aliquots were then analyzed with a Perkin Elmer Optima 3000 DV ICP Emission Spectrometer.

Acquired sulfur loadings are assumed to be stoichiometrically related to hydrogen sulfide degradation through a 1:1 molar ratio.

6.2.2.5 X-ray Photoelectron Spectroscopy (XPS)

A Thermo K-alpha was used to collect XPS measurements. The instrument utilizes a monochromated Al Kα source, with a double-focusing hemispherical analyzer. High resolution spectra were acquired and presented here for sulfur and iron. Measurement

parameters include 50ms dwell time, 50eV pass energy, a 0.1eV step size, and 400μm diameter spot size.

6.2.3 Hydrogen Sulfide Uptake Experiments

A fixed-bed apparatus was used to collect hydrogen sulphide adsorption (H_2S) adsorption data. The setup is described in 2.3.2.1.

Humid H_2S mixtures were created by mixing the following streams, where both gases were sourced from cylinders purchased from Airgas without further purification:

1. Dry hydrogen sulfide (~4988ppm) with balance nitrogen
2. Ultra Zero grade air (dry air was passed through a sealed stainless steel vessel containing DI water)

Approximately 150-200mg of samples were first placed in a fritted thermal desorption tube. The tube was attached to the fixed bed apparatus. Simultaneously, stream (2) was allowed to equilibrate through a separate purge line (not entering the bed) for about 90min, reaching a relative humidity of ~85%. Samples were pre-conditioned under flow of the humidified air stream at 50mL min^{-1} for 1h, while heating to 200°C using insulated heat tape. The sample was then allowed to cool to 20°C, measured with a thermocouple.

To start the experiment, stream (1) was mixed with (2). Gases were mixed in a 4:1 volumetric ratio of acid gas-to-humidified air— 40mL min^{-1} (1) and 10mL min^{-1} (2). Upon mixing, the combined streams were sent to the sample bed. Exposure tests at 20°C were terminated after 3h, and samples were flushed with dry air for 30min afterwards to purge

out and oxidize residual H_2S. Powder samples were then collected and degassed at 200°C under vacuum prior to other measurements described in this work.

6.3 Results and Discussion

6.3.1 MOF-derived Oxide Characterization

Previously reported aluminum carbide and metallic aluminum sources for structured MIL-53(Al) formation were utilized as growth precursors.[17,18] In contrast to conventionally-synthesized MIL-53(Al), these crystallites extend perpendicular from underlying insoluble metal precursors, forming a densely-packed monolayer of crystalline microneedles. Figure 6-1 illustrates the procedure of converting insoluble aluminum-based media to MIL-53(Al), and then to nanorod-shaped Al_2O_3 composites. MIL-53(Al) thermally degrades at temperatures >400°C in inert atmospheres.[21] Accordingly, MOFs were pyrolyzed at 600°C (see Section 6.2.1.1) to completely destroy the framework and produce a MIL-53(Al)-derived aluminum oxide-based composite. For brevity, the composite material obtained from pyrolysis of Al_4C_3-derived MIL-53(Al) is named *MIL-53(Al)-oxide* in this chapter. It should be noted that a templating procedure was not utilized in either step. The one-directional growth inherent from using the insoluble precursor-derived MIL-53(Al) is passed on to *MIL-53(Al)-oxide*.

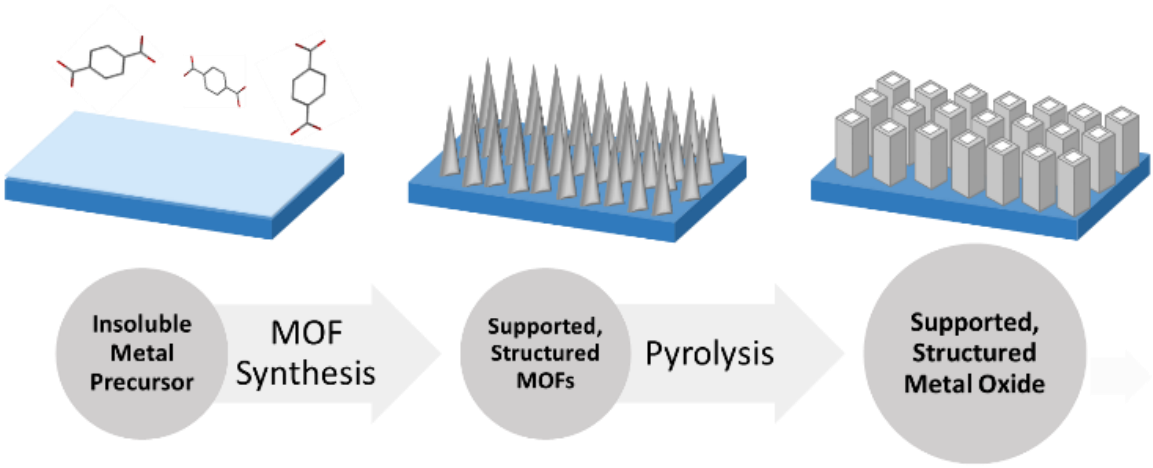

Figure 6-1: Schematic of metal-organic framework (middle) and subsequent MIL-53(Al)-oxide (right) formation using insoluble metal precursors (left). Dark blue rectangle represents the insoluble metal precursor, where the lighter blue region is intended to illustrate the uppermost monolayer in which structure formation occurs. Grey geometries represent the MOF and resultant oxide-based composite.

Before and after pyrolysis images of the porous materials are depicted in Figure 6-2. MIL-53(Al) precursors grown on Al_4C_3 and aluminum foil are shown for reference in Figure 6-2a and b, respectively. MIL-53(Al) microneedles transform into porous nanotubes after pyrolysis. Figure 6-2c & d reveal the formation of elongated, rod-like particles in *MIL-53(Al)-oxide*. Figure A-73 and Figure A-74 confirm the same results for pyrolyzed MIL-53(Al) grown on and from aluminum alloy mesh. EDS data in Figure A-74 reveals the existence of a carbonaceous surface dispersed throughout the mesh-based composite. Carbon deposition is expected from previous MOF degradation studies in inert environments, and results from pyrolyzed terephthalate linkers leaving behind non-combusted carbon.[14] Needle apexes of the MOF precursor truncate after pyrolysis, suggesting they were composed primarily of organic linkers in MIL-53(Al). Uniaxial orientation of alumina rods in *MIL-53(Al)-oxide* suggests the one-dimensional aluminum oxide backbone of MIL-53(Al), which extends along the *a* axis, grows parallel to insoluble

precursor surface and exfoliates. Evolved aluminum oxide-based nanorods in Figure 6-1 showcase “structural memory” from their consistent structural orientation with MIL-53(Al) precursors. Approximately 220nm openings are positioned at the outer ends of the tubular structures. The large central cavity in Figure 6-2d penetrates downwards through the tube, and appears to connect inner void space. Li and coworkers remarked lack of order and interconnectivity is a frequent limitation of MOF-derived porous media.[13] Therefore, this observation constitutes an important novelty in migrating the connectivity of MOFs to their respective derived composites. Distinguishable ridge-like features and openings along the sides of the nanorods in Figure 6-2c and d indicate a heterogeneous pore structure characterized later in this report through porosity measurements. Figure 6-2e generalizes the dimensionality of *MIL-53(Al)-oxide*, where nanorods extend a few microns from the underlying surface, and retain uniform shape and size to one another across studied particle aggregates. Framework destruction results in a 78% decrease of accessible BET surface area and 44% decrease in total measured pore volume, detailed in Figure 6-2f. This is due to the evacuation of bridging framework ligands that generate large adsorption surfaces throughout the MIL-53(Al) precursor. The residual BET surface area of 250.9 $m^2 g^{-1}$ shows *MIL-53(Al)-oxide* still possesses microporosity on the upper-end of typical observations for alumina-based materials, while maintaining a broad spectrum of pore sizes.[22–25] A 61% mass loss is observed after pyrolysis. This mass change agrees well with the reported 64% mass loss from TGA data of Al_4C_3-derived MIL-53(Al) in an inert atmosphere.[18]

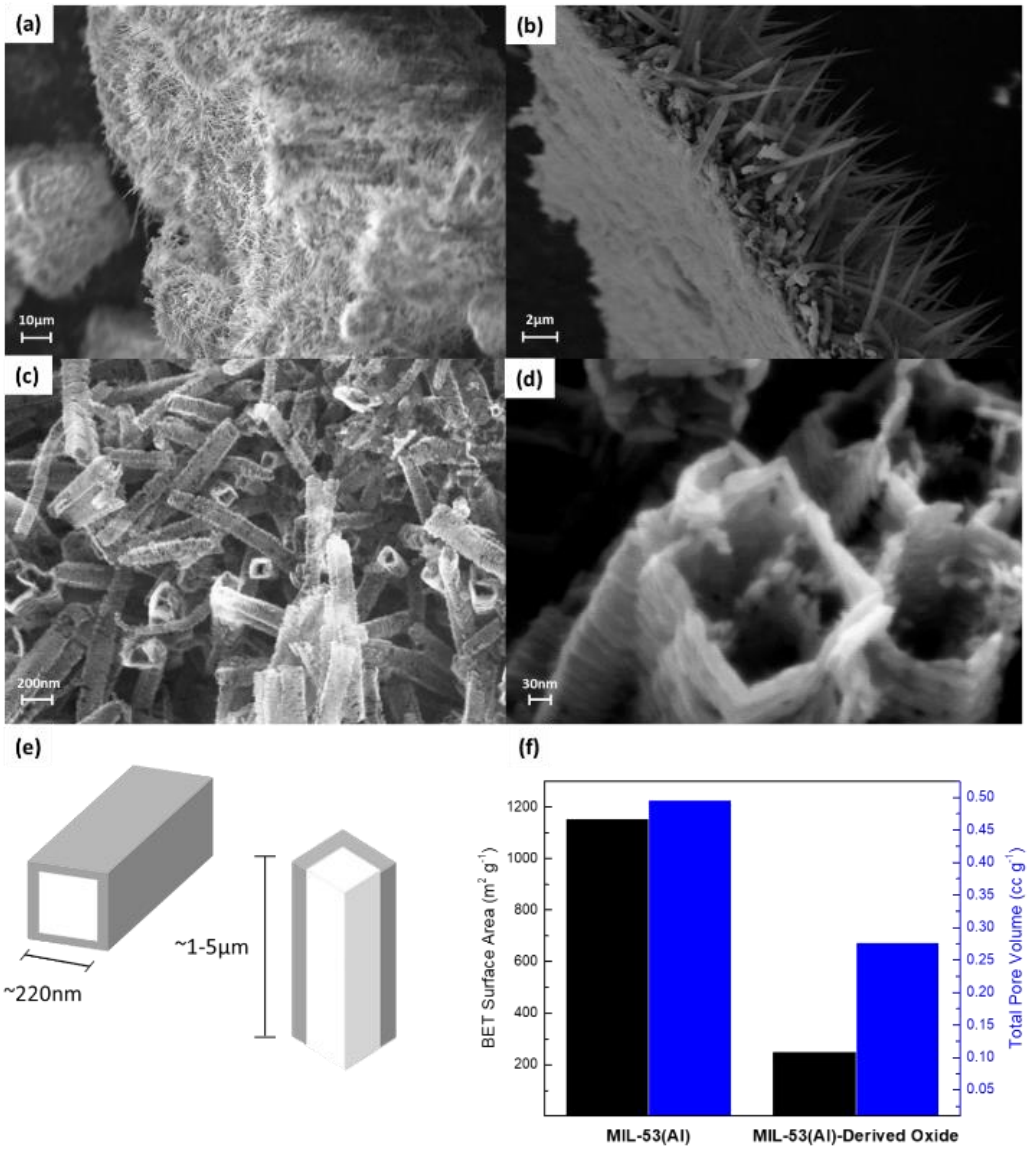

Figure 6-2: Characterization of *MIL-53(Al)-oxide*. SEM images of MIL-53(Al) precursor derived from (a) aluminum carbide (Al_4C_3) and (b) metallic aluminum (foil) are presented for reference, (c-d) shows derived alumina-based nanorod structures from pyrolysis of Al_4C_3-derived MIL-53(Al), (e) cartoon depicting average dimensions of evolved nanorod structures, (f) changes in porosity from Al_4C_3-derived MIL-53(Al) precursor and subsequent *MIL-53(Al)-oxide*, calculated from N_2 physisorption data at 77K.

6.3.2 Leveraging the Unique Textural Properties of MIL-53(Al)-oxide

Studies on structured aluminum oxide growth already exist.[26–29] MOF-derived oxide templating methods however offer a uniform synthesis methodology for creating

these materials—the same general steps can produce carbon/metal oxide-based materials for a variety of different framework architectures. Yamauchi and coworkers exemplify this in their development of similar fibular structures through carbonizing Al-PCP rod-shaped crystals.[14] *Two possible applications of MIL-53(Al)-oxide presented here exemplify the possible uses of MOF-derived oxides from insoluble precursors:* (1) MOFs can be regrown onto derived-oxide structures, and (2) mixed-metal oxide composites can be generated by manipulation of the MOF precursor.

6.3.2.1 Cyclic MOF Regrowth

MOF repair and regrowth strategies generate interesting material property solutions. The SACRed procedure for healing ZIF-8 crystals by Nair and coworkers[30] was hypothesized to possibly enhance ZIF-based filtration and membrane media lifetimes when employed in corrosive environments. Multiple MOF growth cycles were also exacted to create stable and selective catalyst media, by "sandwiching" encapsulate active sites between framework layers.[31,32] Through such studies, chemists garner simple treatments to recycle MOF materials and significantly extend their usable lifetimes, or add further complexity to MOF products in a facile and stepwise manner.

Structured aluminum oxide tubes examined on *MIL-53(Al)-oxide* uniquely serve as a scaffold and aluminum metal center source for MIL-53(Al) regrowth. The regenerability of MIL-53(Al) was demonstrated by repeating two steps (1) thermal degradation of Al_4C_3-derived MIL-53(Al) to produce *MIL-53(Al)-oxide*, and (2) regrowth of MIL-53(Al) on and from *MIL-53(Al)-oxide* via hydrothermal reaction. The reaction used for MIL-53(Al) regrowth is the same used to make the original Al_4C_3-derived MIL-53(Al) precursor, but

assumes the derived oxide has stoichiometry of Al_2O_3 to determine linker and DI water amounts (details in Section 6.2.1.3). A general scheme of cyclic MOF production is presented in Figure 6-3a. MIL-53(Al) growth was cycled twice in succession, where resulting products are named Cycle 1 and Cycle 2, respectively. Micrographs in Figure A-75 evidence reformed MIL-53(Al) crystals after one and two pyrolysis-growth cycles. Regenerated microneedles in Cycles 1 and 2 are uniform in appearance with each other and the original Al_4C_3-derived MIL-53(Al). Impressively, N_2 physisorption measurements at 77K (Figure 6-3b) show Cycle 1 and Cycle 2 completely recover porosity. BET surface areas derived from N_2 adsorption data in Table 6-1 are consistent for regenerated MOFs amongst each regrowth cycle and with Al_4C_3-derived MIL-53(Al). A modest increase in surface area is even observed for regrowth cycles, which may be attributed to accumulated microporous materials between pyrolysis runs. Mesopores in regenerated MIL-53(Al) samples are qualitatively apparent by capillary condensation behavior (positive slope past $P/P_0 = 0.40$) in N_2 adsorption curves in Figure 6-3b. This is distinct from the strictly microporous original MIL-53(Al) precursor, and creates increased pore volumes for regrowth Cycles 1 and 2 in Table 6-1.[33] Residual mesoporous structures from *MIL-53(Al)-oxide* growth precursors manifest in regenerated MOFs, uniquely instilling mesoporosity in resulting MIL-53(Al). PXRD data in Figure 6-3c confirm reappearance of the MIL-53(Al) crystal phase for Cycle 1 and Cycle 2. Crystalline microstrain is clearly visible in the broadened reflections within diffraction patterns for regenerated products. Because MOF growth localizes on alumina nanorods, ligand accessibility and coordination hindrance from particle aggregation and surface heterogeneity likely introduce lattice strain in the final products. Diffraction measurements show the existence of pyrolytic carbon

(ICDD no. 01-083-6084) and aluminum (ICDD no. 00-001-1180), but do not reveal any long-range order for the aluminum oxide structures. The Al_2O_3 phase is subsequently assumed to be amorphous, as was seen through previous measurements on MIL-53(Al) prepared from insoluble metal precursors.[34]

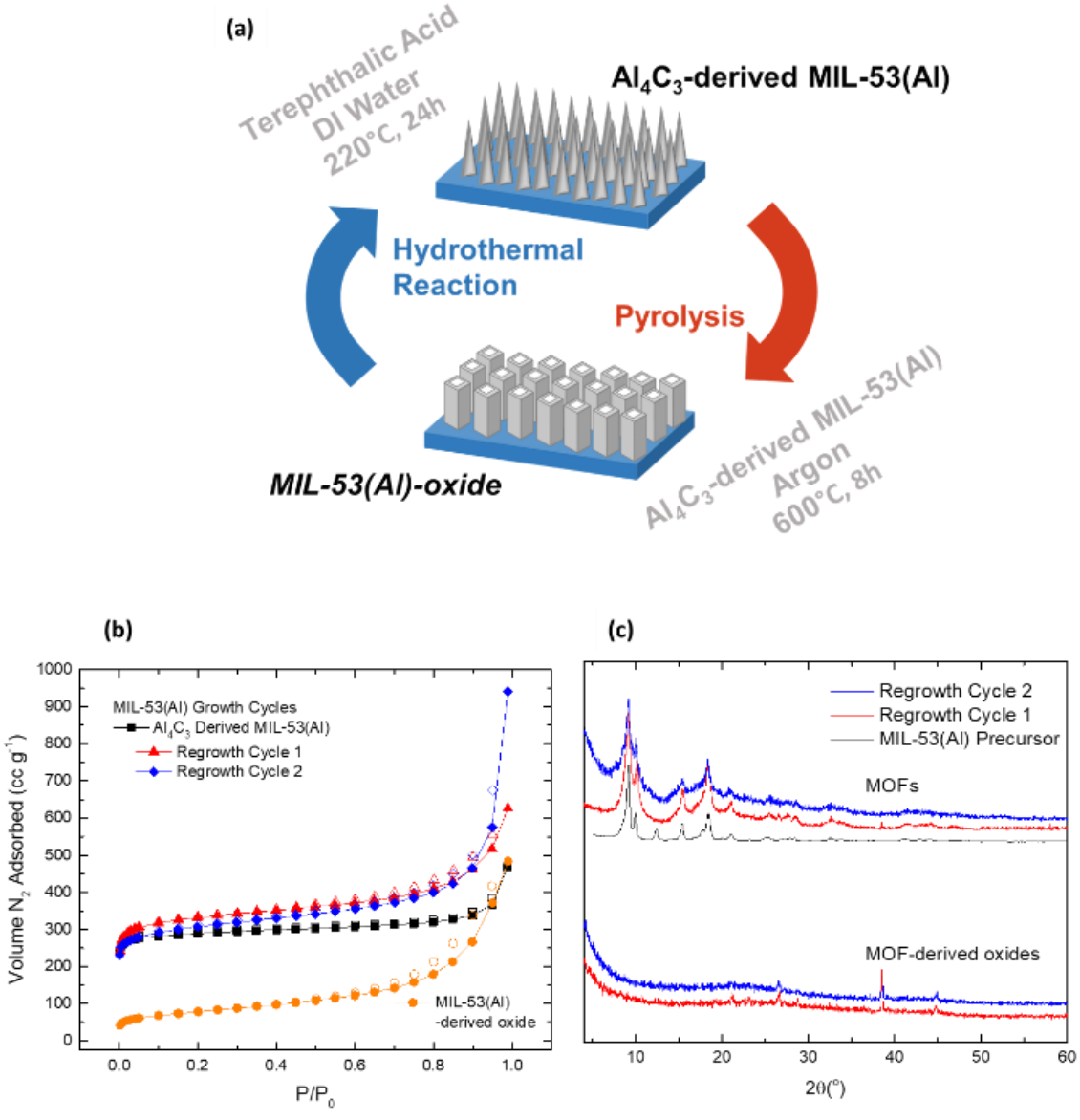

Figure 6-3: Characterization of MIL-53(Al) growth cycle products and derived oxides. (a) Scheme of growth cycle reactions, (b) N_2 physisorption at 77K, and (c) powder X-ray diffraction measurements of regeneration cycle materials.

Table 6-1: Porosity data from MIL-53(Al) growth cycles

MIL-53(Al)	BET Surface Area (m^2 g^{-1})	[a]Total Pore Volume (cc g^{-1})
[b]Parent MOF	1154.2	0.50
Regrowth Cycle 1	1277.7	0.63
Regrowth Cycle 2	1162.3	0.62

[a]Pore volume calculated from N_2 adsorption data at 77K at $P/P_0 = 0.80$
[b]Parent MOF refers to Al_4C_3-derived MIL-53(Al) precursor

MOF regeneration reports already exist in the literature. Earlier investigations on MOF-5 and HKUST-1 by Han and Lah[35] also recover the porosity of their original frameworks after regeneration. Several critical differences are noted here however. Hazardous acidic and/or alkaline modulators used in previous MOF regrowth literature are not necessary for the multiple MIL-53(Al) growth cycles demonstrated from *MIL-53(Al)-oxide*. Additionally because material architectures are supported, the spatial positions of microneedles and rods are affixed (e.g. aluminum carbide, aluminum mesh, etc.) when cycling between MIL-53(Al) and *MIL-53(Al)-oxide*, respectively. Consequently, microneedles are forced to reconstruct on the same locations from which they were destroyed during pyrolysis. Memory of growth location is inherently not possible with non-supported MOF growth techniques, but is attained here without structure direction or templates during regrowth cycles. Results extend MOF recycling to MOF-based composites, devices, and hierarchical media, where spatial growth is consistent between cycles. Furthermore, this methodology allows the generation of consistent and homogeneous porous structures.

6.3.2.2 Mixed-metal oxide composites for hydrogen sulfide removal

Hydrogen sulfide (H_2S) is a pervasive contaminant in many fuel streams.[36] The vapor is oftentimes encountered at low concentrations (< 1%), but still complicates processes due to its high toxicity and corrosive nature.[37,38] Development of H_2S scavengers that function effectively at low gas concentrations can greatly facilitate energy-related remediation operations. Methods of leveraging the well-known chemical degradation of H_2S over inexpensive iron oxide (Fe_2O_3) are explored in literature, were Fe_2O_3 is commonly integrated into commercial desulfurization media.[39] Moreover, the employ of adsorption-based H_2S removal more simple and inexpensive than common amine-based scrubbing technologies.[39,40] Efficient integration of iron oxide chemisorbants can form H_2S-removal products capable of high active site accessibility while stabilizing Fe_2O_3-impregnate particles.

Accordingly, iron oxide composites were formed with *MIL-53(Al)-oxide*. Al_4C_3-derived MIL-53(Al) was first utilized as the precursor for Fe_2O_3 impregnation and subsequently pyrolyzed (sample preparation is detailed in Section 6.2.1.2). The hierarchical pore structure of impregnated *MIL-53(Al)-oxide* is characterized by pore size distributions in Figure 6-4. Well-defined micropores between 10-13Å are apparent for parent and impregnated *MIL-53(Al)-oxide*. In addition to the 220nm macropore in *MIL-53(Al)-oxide* discovered via electron imaging, N_2 data reveals an array of mesopores ranging from under 5nm to around 30nm. The mixture of macropores, mesopores, and micropores together in a single phase is rare; Bruce and coworkers claimed to develop the first reported material (an α-MnO_2 solid) to display such behavior in 2013, and not many more are reported thereafter.[41,42] For aluminum oxides specifically, meso- and micropores

are only observed for γ-Al_2O_3 phases, and bimodal macroporous-mesoporous aluminas require surfactants and/or growth templates.[43,44] MOF-derived oxides naturally attain these qualities however, as Mounfield III et al. noticed similar attributes in MIL-125(Ti)-derived titania.[45] Multimodal pore systems are advantageous in separations limited by sieving effects and other transport phenomena. These textural insights highlight the novelty and intricacy of *MIL-53(Al)-oxide* and other structured MOF-derived oxides. Pore accessibility unsurprisingly decreases after impregnation. Microporosity is largely retained, but mesopores from 10-20nm become absent. These differences may result from the iron oxide aggregates simply occupying larger pore spaces. The impregnate can additionally change how MIL-53(Al) pyrolyzes—minimizing the propagation of mesopores throughout the substrate. Decorated pores along the sides of the MIL-53(Al)-oxide tubes, as illustrated in Figure 6-2c, facilitate guest molecule accessibility throughout the bulk. SEM micrographs in Figure A-76 confirm the morphology of the impregnated samples is consistent with unmodified *MIL-53(Al)-oxide* presented in Figure 6-2.

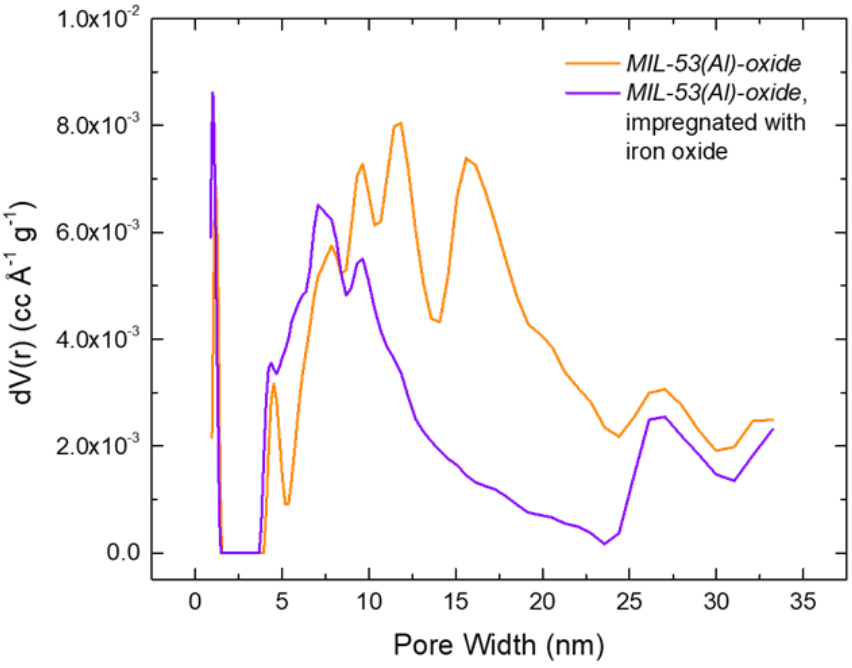

Figure 6-4: Pore size distributions from N_2 measurements at 77K for unmodified and impregnated *MIL-53(Al)-oxide*.

Humid hydrogen sulfide exposures were conducted on *MIL-53(Al)-oxide* with and without iron oxide impregnation (see Section 6.2.3 experimental details). SEM-EDS measurements of the iron-oxide impregnated composite in Figure 6-5a validate homogenous iron dispersion across the sample. Average weight percents of iron and aluminum from EDS data are 15.4% and 28.4%, respectively. Sulfur deposits consistently across particle surfaces. Distributions are likely consequent of the large iron oxide loading and dispersion across the sample, supplying numerous adsorption sites for H_2S. High resolution S2p XPS data in Figure A-77 confirm reactive degradation of H_2S over iron oxide. Species around 168-170eV correspond well with iron sulfates ($FeSO_4$, $Fe_2(SO4)_3$) formed via H_2S oxidation.[46] A small presence of iron(II) sulfite is detected at 162eV, while significant features from elemental sulfur (S_8) in $S2p_{3/2}$ and $S2p_{1/2}$ scans at 164eV are consistent with H_2S decomposition over iron oxides.[46,47] Figure A-78 provides a $Fe2p_{1/2}$

information from 724eV-726eV and a $Fe2p_{3/2}$ peak at 711eV supporting the existence of iron sulfates, as observed with sulfur data in Figure A-77. [46] Unconverted iron oxide(s) in $Fe2p_{1/2}$ measurements around 720eV suggest some iron oxide surfaces were inaccessible to H_2S, or simply arise from oxide detection underneath sulfated monolayers. It should be noted the elemental mapping and XPS information may not represent bulk distribution due to depth resolution limits.

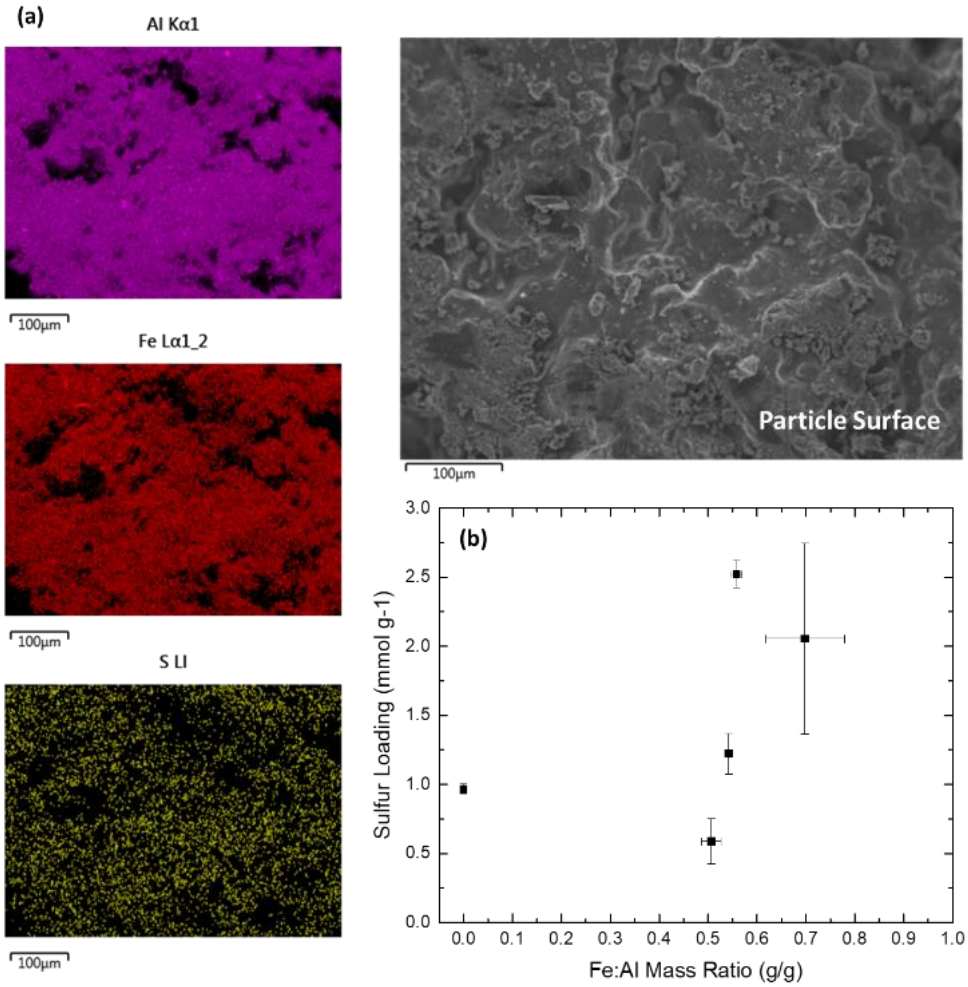

Figure 6-5: Elemental analysis of iron oxide-impregnated *MIL-53(Al) oxide* following H_2S exposure. (a) SEM-EDS mapping of aluminum, iron, and sulfur across particle surface and (b) sulfur loadings on unmodified and impregnated *MIL-53(Al)*, as determined by ICP-OES. Each square in (b) represents a unique sample batch, and error bars describe data ranges from redundant ICP measurements on each sample

Variance in desulfurization performance across evaluated iron oxide-impregnated MOF-derived alumina composites become apparent after determining iron and sulfur loadings via ICP-OES. Figure 6-5b illustrates fairly consistent iron loadings across batches of impregnated *MIL-53(Al)-oxide*. ICP and previously mentioned EDS data both estimate average iron loadings around 15wt% among investigated samples. This is expected, as impregnate amounts are restricted by available substrate pore volume in the incipient wetness method, which is uniform in the highly ordered Al_4C_3-derived MIL-53(Al) precursor. Sulfur uptakes on non-impregnated samples range from 0.93-1 mmol S g^{-1}. XPS experiments at Brookhaven detected H_2S dissociation and possible chemisorption on alumina surfaces at 300K (albeit at higher gas concentrations), in S2p peak positions from 162-162.5eV, although markedly weaker than other metal oxides.[48] Their observations still suggest irreversible H_2S adsorption is possible on alumina *MIL-53(Al)-oxide* surfaces. Primarily, H_2S uptake in non-impregnated *MIL-53(Al)-oxide* is more likely attributed to micropore adsorption. Sulfur loadings are conversely quite different among the four iron oxide impregnated *MIL-53(Al)-oxide* exposure batches. One of the tested samples even has a lower sulfur uptake than the non-impregnated control sample. This loss is likely due to hindered pore accessibility, particularly into micropores. Simultaneously, H_2S loadings improve up to 2.5x for other samples. Figure 6-5b clearly demonstrates H_2S degradation is not dictated by iron oxide loading. It is more likely determined by the relative accessibility of iron oxide active sites between samples. Distribution and size of iron oxide aggregates are not controlled through incipient wetness impregnation. So, relative differences in iron oxide surface accessibility create disparity in sulfur uptake.

Analyses of impregnated *MIL-53(Al)-oxide* illustrate a facile method to imbue heterogeneous surface chemistry into aluminum oxide structures. High impregnate infiltrations are achieved by loading the MOF precursor instead of the aluminum oxide support directly—taking advantage of the markedly greater pore volume inherent of MOFs. This method may be extended to any desired impregnate species for loading onto Al-MOF-derived media (multiple Al-MOF precursors can be produced from work in Chapter 5).

6.4 Conclusions

This report demonstrates the facile construction of *MIL-53(Al)-oxide*: a supported composite containing self-oriented aluminum oxide-based nanorods. The tubular structure was transitioned from MIL-53(Al), which naturally acquires one-dimensional crystal growth when fabricated from insoluble metal precursors—not afforded by conventional syntheses. Derived nanorods retain growth orientation, relative size dimensions, and support material (carbonized Al_4C_3, metallic aluminum, etc.) from which MIL-53(Al) precursors were grown. Produced architectures display a wide range of macro-, meso-, and micropores, and obtain material characteristics unique from conventional porous aluminas.

The supported nature of *MIL-53(Al)*-oxide instilled unique capabilities for MOF regeneration. MIL-53(Al) microneedles were regrown twice from *MIL-53(Al)-oxide* with full porosity recovery. Spatial regrowth control, not possible in previous regrowth strategies using non-supported MOFs, is demonstrated here for the first time. This control stems from insoluble metal precursor support structures, which scaffold alumina-based nanorods serving as regrowth templates between multiple MOF growth cycles. In effect, MOFs grow on the exact locations they were pyrolyzed from in previous cycles.

Additionally, mixed-metal oxide synthesis was explored by metal impregnation of the MIL-53(Al) precursor and subsequent pyrolysis. Accessible and well-dispersed iron oxide was easily attained on *MIL-53(Al)-oxide*, where Fe_2O_3 active sites displayed reactivity with hydrogen sulfide at 0.5%. This result affirms MOF-derived composites are applicable support media for impregnate-based adsorption/catalysis applications. Although these applications have been explored similarly in prior work, the unique MOF-derived composite here affords advances in material growth control. By taking advantage of this hierarchical support structure manufacturing strategy, scientists can construct a platform towards integrating Al_2O_3 media onto devices, monoliths, membranes, and other media.

6.5 Chapter 6 References

1. Iijima, S. Helical microtubules of graphitic carbon. *Nature* **354**, 56–58 (1991).
2. Trimm, D. L. & Stanislaus, A. The control of pore size in alumina catalyst supports: A review. *Appl. Catal.* **21**, 215–238 (1986).
3. Taguchi, A. & Schüth, F. Ordered mesoporous materials in catalysis. *Microporous Mesoporous Mater.* **77**, 1–45 (2005).
4. Corma, A. From Microporous to Mesoporous Molecular Sieve Materials and Their Use in Catalysis. *Chem. Rev.* **97**, 2373–2420 (1997).
5. Wang, X. & Han, G.-R. Fabrication and characterization of anodic aluminum oxide template. *Microelectron. Eng.* **66**, 166–170 (2003).
6. Gudiksen, M. S., Lauhon, L. J., Wang, J., Smith, D. C. & Lieber, C. M. Growth of nanowire superlattice structures for nanoscale photonics and electronics. *Nature* **415**, 617–620 (2002).
7. Lauhon, L. J., Gudiksen, M. S., Wang, D. & Lieber, C. M. Epitaxial core–shell and core–multishell nanowire heterostructures. *Nature* **420**, 57–61 (2002).
8. Dai, H. Carbon nanotubes: opportunities and challenges. *Surf. Sci.* **500**, 218–241 (2002).
9. Martin, C. R. Nanomaterials: a membrane-based synthetic approach. *Science* **266**, 1961–1966 (1994).

10. Li, Y. *et al.* MOF-Derived Metal Oxide Composites for Advanced Electrochemical Energy Storage. *Small* **14**, 1704435 (2018).

11. Xia, W. *et al.* High-Performance Energy Storage and Conversion Materials Derived from a Single Metal–Organic Framework/Graphene Aerogel Composite. *Nano Lett.* **17**, 2788–2795 (2017).

12. Qu, C. *et al.* Nickel-based pillared MOFs for high-performance supercapacitors: Design, synthesis and stability study. *Nano Energy* **26**, 66–73 (2016).

13. Shen, K., Chen, X., Chen, J. & Li, Y. Development of MOF-Derived Carbon-Based Nanomaterials for Efficient Catalysis. *ACS Catal.* **6**, 5887–5903 (2016).

14. Salunkhe, R. R. *et al.* Asymmetric Supercapacitors Using 3D Nanoporous Carbon and Cobalt Oxide Electrodes Synthesized from a Single Metal–Organic Framework. *ACS Nano* **9**, 6288–6296 (2015).

15. Kaneti, Y. V. *et al.* Nanoarchitectured Design of Porous Materials and Nanocomposites from Metal-Organic Frameworks. *Adv. Mater.* **29**, 1604898 (2017).

16. Zhan, G. & Zeng, H. C. Alternative synthetic approaches for metal-organic frameworks: transformation from solid matters. *Chem. Commun.* **53**, 72–81 (2017).

17. Kim, J., Lee, S., Kim, J. & Lee, D. Metal-Organic Frameworks Derived from Zero-Valent Metal Substrates: Mechanisms of Formation and Modulation of Properties. *Adv. Funct. Mater.* 1808466 (2019).

18. Moran, C. M., Joshi, J. N., Marti, R. M., Hayes, S. E. & Walton, K. S. Structured Growth of Metal–Organic Framework MIL-53(Al) from Solid Aluminum Carbide Precursor. *J. Am. Chem. Soc.* **140**, 9148–9153 (2018).

19. Moran, C. M., Marti, R. M., Hayes, S. E. & Walton, K. S. Synthesis and characterization of aluminum carbide-derived carbon with residual aluminum-based nanoparticles. *Carbon N. Y.* **114**, 482–495 (2017).

20. Walton, K. S. & Snurr, R. Q. Applicability of the BET method for determining surface areas of microporous metal-organic frameworks. *J. Am. Chem. Soc.* **129**, 8552–8556 (2007).

21. Patil, D. V *et al.* MIL-53(Al): An Efficient Adsorbent for the Removal of Nitrobenzene from Aqueous Solutions. *Ind. Eng. Chem. Res.* **50**, 10516–10524 (2011).

22. Pines, H. & Haag, W. O. Alumina: Catalyst and Support. I. Alumina, its Intrinsic Acidity and Catalytic Activity. *J. Am. Chem. Soc.* **82**, 2471–2483 (1960).

23. Morris, S. M., Fulvio, P. F. & Jaroniec, M. Ordered Mesoporous Alumina-

Supported Metal Oxides. *J. Am. Chem. Soc.* **130**, 15210–15216 (2008).

24. Zhang, S. *et al.* Anodic aluminum oxide with fine pore size control for selective and effective particulate matter filtering. *Mater. Res. Express* **3**, 74004 (2016).

25. Goldberg, S., Lebron, I., Suarez, D. L. & Hinedi, Z. R. Surface Characterization of Amorphous Aluminum Oxides. *Soil Sci. Soc. Am. J.* **65**, 78–86 (2001).

26. Bocchetta, P., Sunseri, C., Chiavarotti, G. & Di Quarto, F. Microporous alumina membranes electrochemically grown. *Electrochim. Acta* **48**, 3175–3183 (2003).

27. Kelly, P. J. & Arnell, R. D. Control of the structure and properties of aluminum oxide coatings deposited by pulsed magnetron sputtering. *J. Vac. Sci. Technol. A Vacuum, Surfaces, Film.* **17**, 945–953 (1999).

28. Keller, F., Hunter, M. S. & Robinson, D. L. Structural Features of Oxide Coatings on Aluminum. *J. Electrochem. Soc.* **100**, 411–419 (1953).

29. Belwalkar, A., Grasing, E., Van Geertruyden, W., Huang, Z. & Misiolek, W. Z. Effect of processing parameters on pore structure and thickness of anodic aluminum oxide (AAO) tubular membranes. *J. Memb. Sci.* **319**, 192–198 (2008).

30. Jayachandrababu, K. C., Bhattacharyya, S., Chiang, Y., Sholl, D. S. & Nair, S. Recovery of Acid-Gas-Degraded Zeolitic Imidazolate Frameworks by Solvent-Assisted Crystal Redemption (SACRed). *ACS Appl. Mater. Interfaces* **9**, 34597–34602 (2017).

31. Zhao, M. *et al.* Metal–organic frameworks as selectivity regulators for hydrogenation reactions. *Nature* **539**, 76–80 (2016).

32. Huo, F. A new breakthrough in selective catalysis: metal-organic framework nanocomposites with sandwich structure. *Sci. Bull.* **61**, 1726–1727 (2016).

33. J. Rouquerol *et al.* Recommendations for the Characterization of Porous Solids. *Pure Appl. Chem.* **66**, 1739–1758 (1994).

34. Zhang, Y. *et al.* Constructing Free Standing Metal Organic Framework MIL-53 Membrane Based on Anodized Aluminum Oxide Precursor. *Sci. Rep.* **4**, 4947 (2014).

35. Han, S. & Lah, M. S. Simple and Efficient Regeneration of MOF-5 and HKUST-1 via Acid− Base Treatment. *Cryst. Growth Des.* **15**, 5568–5572 (2015).

36. Manning, F. S. & Thompson, R. E. *Oilfield Processing of Petroleum: Natural Gas*. (PennWell Books: Tulsa, OK 1991).

37. Reiffenstein, R. J., Hulbert, W. C. & Roth, S. H. Toxicology of Hydrogen Sulfide. *Annu. Rev. Pharmacol. Toxicol.* **32**, 109–134 (1992).

38. Hessel, P. A., Herbert, F. A., Melenka, L. S., Yoshida, K. & Nakaza, M. Lung health in relation to hydrogen sulfide exposure in oil and gas workers in Alberta, Canada. *Am. J. Ind. Med.* **31**, 554–557 (1997).

39. Abatzoglou, N. & Boivin, S. A review of biogas purification processes. *Biofuels, Bioprod. Biorefin.* **3**, 42–71 (2009).

40. Wang, X., Ma, X., Xu, X., Sun, L. & Song, C. Mesoporous-molecular-sieve-supported polymer sorbents for removing H_2S from hydrogen gas streams. *Top. Catal.* **49**, 108–117 (2008).

41. Ren, Y. *et al.* A solid with a hierarchical tetramodal micro-meso-macro pore size distribution. *Nat. Commun.* **4**, 2015 (2013).

42. Zhou, W. *et al.* Toward Scalable Fabrication of Hierarchical Silica Capsules with Integrated Micro-, Meso-, and Macropores. *Small* **12**, 1797–1805 (2016).

43. Wilson, S. J. & Stacey, M. H. The porosity of aluminum oxide phases derived from well-crystallized boehmite: Correlated electron microscope, adsorption, and porosimetry studies. *J. Colloid Interface Sci.* **82**, 507–517 (1981).

44. Yuan, Z.-Y., Ren, T.-Z., Azioune, A., Pireaux, J.-J. & Su, B.-L. Self-Assembly of Hierarchically Mesoporous−Macroporous Phosphated Nanocrystalline Aluminum (Oxyhydr)oxide Materials. *Chem. Mater.* **18**, 1753–1767 (2006).

45. Mounfield III, W. P. *et al.* Role of defects and metal coordination on adsorption of acid gases in MOFs and metal oxides: An in situ IR spectroscopic study. *Microporous Mesoporous Mater.* **227**, 65–75 (2016).

46. Descostes, M., Mercier, F., Thromat, N., Beaucaire, C. & Gautier-Soyer, M. Use of XPS in the determination of chemical environment and oxidation state of iron and sulfur samples: constitution of a data basis in binding energies for Fe and S reference compounds and applications to the evidence of surface species of an oxidized py. *Appl. Surf. Sci.* **165**, 288–302 (2000).

47. Huang, G. *et al.* Synthesis and Characterization of γ-Fe_2O_3 for H_2S Removal at Low Temperature. *Ind. Eng. Chem. Res.* **54**, 8469–8478 (2015).

48. Rodriguez, J. A., Chaturvedi, S., Kuhn, M. & Hrbek, J. Reaction of H_2S and S_2 with Metal/Oxide Surfaces: Band-Gap Size and Chemical Reactivity The adsorption and dissociation of H_2S and S_2 on a series of oxides. *J. Phys. Chem. B* **102**, 5511–5519 (1998)

CHAPTER 7. CONCLUSIONS AND RECOMMENDATIONS

7.1 Conclusions

The work described in this document attempts to communicate studies focusing on how porous materials, particularly metal-organic frameworks, can be utilized for acid gas adsorption. Two major questions guided the contents of work described herein:

(1) *How* can MOFs be tailored for acid gas removal?

(2) *How* can manufacturing methods yield accessible and simple adsorbent design?

Experimental evaluation of several framework adsorbents were performed to address these questions. For the first point, adsorbent stability parameters relevant to environments containing acid gases were examined for candidate frameworks. Acid gas selectivity and reversible uptake were enhanced through MOF ligand functionalization by introducing (a) carboxylic acid and (b) primary amine pendant functionalities. Irreversible acid gas adsorption was similarly fostered through ligand-functionalized copper binding sites. For addressing the second question listed above, a novel MOF manufacturing technique for directly producing both supported and non-supported MOF media from insoluble aluminum sources was developed. The method allows production of aluminum-based framework adsorbents directly *on* and *from* pre-fabricated structured contactors through one step. Garnered materials also serve as templates for MOF-derived (oxide/carbon) media, which inherit unique textural properties from supported MOF precursors that enable new material applications.

7.1.1 Synthesis and Processing Impacts on Framework Stability (Chapter 3)

7.1.1.1 Chapter 3 Conclusions

Effects of framework production and processing on chemical stability were probed in Chapter 3. Three main areas were investigated: (1) defect incorporation, (2) reactive adsorption site integration, and (3) adsorbent pelletization.

For the first time, a defect modulation strategy was implemented for titanium-based frameworks. This technique was directly extended from zirconium-framework literature onto the titanium MIL-125(Ti) system, for the first time. This demonstrates the adaptability of acid modulation as a defect-modification method towards chemically-similar framework systems. Point defect incorporation control via modulator acidity, size, and amount is observed. Chemical properties of MIL-125-NH_2(Ti), such as stability and hydrophilicity, are importantly altered through defect incorporation, and they change in distinctly from previously-studied materials (e.g. UiO-66). While methods of defect incorporation are consistent with other MOF systems, their impacts on framework properties are not.

Reactive metal sites were integrated onto framework ligands and for the first time were utilized in acid gas capture. This method requires an otherwise stable MOF platform—UiO-66(Zr) was chosen here. As predicted from previous studies, scaffolded -COOCu sites strong chemisorption reactions without generating framework instability. This behavior is distinct from MOFs that typically enable gas chemisorption reactions localized on MOF metal center sites. Results demonstrate how integrating ligand-based irreversible binding sites for acid gases preserves stability in chemical environments which may otherwise destroy framework adsorbents.

Finally, relationships between the mechanical and chemical integrity of candidate framework systems were exhumed by pelletizing several MOFs prior to acid gas exposure. All non-pelletized ("pristine") chromium-, zirconium-, and titanium-based materials showed negligible changes in porosity and structure through H_2S exposures. However, chromium MIL-101(Cr) adsorbents suffered structural damage upon pelletization, which led to subsequent erasure of crystalline features after H_2S exposure. Mechanical stresses exacted on MOF adsorbents through standard powder processing procedures can therefore foster acid gas instability. This effect is notably ignored in prior studies advertising H_2S stability of MIL-101(Cr). Degradation is framework-dependent, and not observed for all MOFs investigated here. Therefore, mechanical stability should be considered as a selection parameter for MOF-based acid gas adsorbents.

7.1.1.2 Chapter 3 Recommendations

For studies on MIL-125-NH_2(Ti), water vapor was utilized to gauge defective MOF stability. Although a useful probe molecule, stability experiments utilizing acid gases described throughout this text (H_2S, SO_2) should still be pursued. Additionally, the exact method of degradation for defective MIL-125-NH_2(Ti) in the presence of humidity was not ascertained. Theoretical modelling of H_2O(v) interactions with plausible defective unit cells (e.g. containing varying amounts of missing linker and/or cluster defects) may elucidate degradation mechanisms. Quantitative TGA and NMR data *may* be helpful for in approximating relative defect "amounts" based on coordinated modulators. If these experiments are performed, it is suggested benzoic acid-modulated MIL-125-NH_2(Ti) be considered, as benzoic acid modulators were effectively incorporated into defective frameworks.

Ligand-based reactive metal sites are extendable to MOFs others than UiO-66(Zr). The method only requires frameworks containing inert metal centers, of which there are many. Additionally, Lewis basic sites such as pyridine on framework linkers can also serve as coordination sites for metal cations, other than -COO^-.

As mentioned in Chapter 3, impacts of pre-processing steps on MOF stability are rarely examined. So, a large knowledge gap exists concerning effects powder processing on MOF chemical properties. Only one pelletization pressure was evaluated for MOFs here. Testing more pelletization pressures, particularly for MIL-101(Cr), could reveal pressure ranges which do not onset H_2S instability. Pelletized MOFs should also be subjected to other acid gases, such as SO_2 and NO_2, to acquire stability data relevant to flue gas remediation. Aside from just pelletization, the impacts of other powder processing steps, such as MOF integration onto hierarchical substrates and binder mixing, may also impact acid gas stability. So all future work studying "non-pristine" MOF powders should lend special attention to framework property changes through required processing steps.

7.1.2 Targeted Acid Gas Removal Through Framework Functionalization (Chapter 4)

7.1.2.1 Chapter 4 Conclusions

Pre-functionalized MOF ligands imparted acid gas adsorption affinity. First, carboxylic acid groups installed onto UiO-66(Zr) promoted electronic adsorption interactions with polar acid gases SO_2 and H_2S. Structural characterization of resulting materials UiO-66-COOH and UiO-66-$(COOH)_2$ evidenced various structural defects, but also confirmed the preservation of appended -COOH groups after MOF synthesis. Carboxylic acid moieties enhanced SO_2 and H_2S uptake in comparison to parent UiO-

66(Zr). UiO-66-$(COOH)_2$ and UiO-66-COOH displayed similar H_2S breakthrough times. UiO-66-COOH outperforms UiO-66-$(COOH)_2$ for SO_2 uptake—likely due to accessibility issues in UiO-66-$(COOH)_2$. Scaffolded -COOH groups were transformed into copper carboxylates (-COOCu) to facilitate chemisorption of target acid gas species, in contrast to the physical adsorption displayed by -COOH functionalities. SO_2 retention decreases post-metalation. However, H_2S adsorption capacities in resulting UiO-66-COOCu and UiO-66-$(COOCu)_2$ composites were significantly higher than parent UiO-66-COOH and UiO-66-$(COOH)_2$ precursors. Increased H_2S uptake was coupled by visually observable H_2S degradation during adsorption breakthrough and EDS measurements. Results from this study show significant enhancements in reversible *and* irreversible acid gas capture are easily imbued into frameworks through coordinating ligand integration and modification.

To enhance H_2S removal uptake and selectivity from representative sour natural gas mixtures, primary amines (-NH_2) were functionalized on terephthalate-based linkers of three candidate MOF systems. Amine containing MIL-101-NH_2(Cr), MIL-125-NH_2(Ti), and UiO-66-NH_2(Zr) materials displayed higher H_2S uptake than parent MOF analogues in binary H_2S/CH_4 and ternary $H_2S/CO_2/CH_4$ test mixtures. Smaller pore sizes in tested frameworks fostered greater relative increases in H_2S breakthrough capacities between parent and amine-functionalized materials. However, larger pore sizes mitigated adsorption competition from CO_2 and CH_4. *In situ* FTIR measurements confirmed the absence of acid gas chemisorption by framework -NH_2 functional groups, supporting H_2S adsorption cyclability observed through fixed-bed experiments. Subsequently, ligand functionalization enhances H_2S adsorption uptake and selectivity. The extent of improvement depends strongly on respective MOF pore environments.

7.1.2.2 Chapter 4 Recommendations

Copper carboxylates constitute just one of many possible appended chemisorption sites. Other metals can promote irreversible acid gas adsorption. For instance, Zn^{2+} portrays well-known sulfur scavenging capabilities in oxides, even at room temperature. Although -COOCu sites were non-reactive towards SO_2, other metallics such as ceria display chemisorption potential for the gas at various conditions. It is recommended that metals with 2+ oxidation states are prioritized for functionalization *if* using $-COO^-$ sites. Higher valency cations such as Fe^{3+} may experience difficulty coordinating to -COOH binding sites due to charge-balancing, unless reduced during reaction. Reactivity of ligand-based metal carboxylates importantly was consistent with MOFs containing the same unsaturated metal centers (i.e. here -COOCu and Cu^{2+} metal centers of HKUST-1 are reactive with H_2S and inert towards SO_2). So, the reactivity of unsaturated MOF metal centers with acid gases may guide the effectiveness of metal carboxylates for acid gas capture. As an example, high SO_2 uptakes in Mg-MOF-74, which are not observed in Zn-IRMOF-3, may suggest hypothetical SO_2 binding affinities of -COOMg > -COOZn. Of course, this depends on other framework properties, and is merely suggests as a rule-of-thumb. Computational screening of plausible metal carboxylates for acid gas affinity would provide more accurate rankings.

Multicomponent adsorption tests at the end of Chapter 4 demonstrate the importance of mixture complexity on measured adsorption capacities. Inclusion of methane and carbon dioxide strongly altered H_2S uptake performance among studied materials. But even ternary test mixtures are drastic oversimplifications of sour natural gas. Including other relevant constituents, such as mercaptans or hydrocarbons C_2-C_6, would

more accurately benchmark adsorbents in realistic processing conditions. Additionally, the study showed ligand-based primary amines facilitate regenerative H_2S adsorption. Integrating amines on other framework topologies may create efficient sour gas remediation media. Terephthalate-based MOFs are particularly actionable, since the same 2-aminoterephthalic acid reagent can be used to install amines. Design heuristics from this study help determine the desired pore environment for aminated MOF adsorbents—larger pore sizes mitigate competition under high mixture complexity and alternatively microporous systems encourage high uptake for relatively less diverse gas compositions, such as tail gas.

7.1.3 Creating Supported and Non-supported Framework Composites with Insoluble Metal Precursors (Chapter 5)

7.1.3.1 Chapter 5 Conclusions

A novel MOF production strategy utilizing insoluble metal precursors facilitated creation of both supported and non-supported porous crystal growth. Metallic aluminium yielded aluminium-based frameworks from foil, mesh, tubes, and other media. Several MIL-53(Al) analogues and MIL-96(Al) trimesates are successfully produced through the same hydrothermal method. Growth planes supplied by insoluble aluminium impart morphologies in resultant crystals that are unique from conventionally-synthesized materials. This method provides a simple, one-step process to produce porous materials both *on* and *from* support media, instead of traditional multistep processes entailing higher complexities and capital costs. Non-supported MOFs are created through the same method by adding of hydrochloric acid to dissolve the metal precursor during reaction. Porous

powders were retrieved at reaction temperatures as low as 60°C, and microscopy show manufacturers can manipulate MIL-53(Al) morphologies, porosities, and breathing modes with reaction temperature. Impure aluminium sources, such as beverage cans and metal alloys, successfully yield MOF products—demonstrating the robust nature of the insoluble precursor approach. Material cost estimations over non-supported MIL-53(Al) production suggest competitive production costs are attainable through the described methodology.

The same growth technique was applied to create MOF composite material with alumina hollow fiber membranes. Microscopy confirmed growth of MIL-53(Al) and MIL-96(Al) frameworks both on and from aluminium oxide fiber surfaces. Introducing varying amounts of DMF to the hydrothermal reaction provide slight control over MOF yield by manipulating ligand miscibility. Capping fiber ends before reaction mitigates MOF growth inside the membrane bore, but does not prevent it altogether. This work supports efforts in synthesis design of MOF membrane composites, and provides strategies for establishing framework growth control on hierarchical porous support media.

7.1.3.2 Chapter 5 Recommendations

Aluminum is one of many metals utilized to grow metal-organic frameworks. Other metals should be probed as insoluble precursors. Iron is particularly interesting, due to its similar omnipresence in fabricated materials (tubes, filters, etc.), low cost, worldwide accessibility, and propensity to create the same MOF systems available with aluminum (e.g. MIL-53, MIL-100, etc.). These similarities between iron and aluminum suggest their MOF synthesis chemistries from insoluble precursors may be similar as well.

Additionally, many other prefabricated aluminum supports may be exploited for MOF growth using synthesis techniques developed here. It is strongly suggested that future work focuses on identifying aluminum-based MOFs that are advantageous for select gas separations. Then, identified frameworks should be produced on and from aluminum-based support material to directly generate macroscopic adsorption media tailored for given applications. Work remains on optimizing MOF growth on aluminum hollow fiber membranes as well. For increasing MOF loadings, evaluating more solvent mixtures, increasing reaction temperatures, or elongating reaction times can be explored. Location-selective growth requires a separate treatment altogether. A flow reactor, where perhaps MOF reagents are contacted with only the outer layer of hollow fibers, may afford selective and efficient MOF growth.

On a higher level, the work in Chapter 5 fosters unique growth properties onto already-produced frameworks. Applying the insoluble precursor approach allows researchers to create the same, well-known framework topologies with completely new porosities, crystal phases, production parameters, costs, architectures, and underlying supports (if desired). This was clearly demonstrated for MIL-53(Al) and MIL-96(Al) here. Desirable framework properties may result from this. So, it is recommended to extend this methodology towards other framework systems (starting with Al-MOFs will probably afford more direct implementation of synthesis procedures described here).

Finally, Al-MOFs grown in Chapter 5 only grow on aluminum. This is most apparent from reactions with beverage cans and metal alloys. The chemical specificity allows tight locational growth control. So, aluminum can be adhered onto desired substrate surface, and even specific locations within the structures. Then, exacting the insoluble

precursor reaction would produce frameworks on desired areas that were coated with aluminum. This general strategy should facilitate patterning and geometric control over all kinds of macroscopic materials.

7.1.4 MOF-derived Structured Metal Oxide Composites from Insoluble Precursors (Chapter 6)

Structured aluminium-based MOFs derived from insoluble metal precursors described in Chapter 5 were transformed into derived porous oxide/carbon media. Resulting oxide structures remained scaffolded on underlying aluminium-based support media. Conversion was achieved through one step, regardless of insoluble aluminum precursor. MOF-derived media created in Chapter 6 possesses multimodal pore size distributions, one-directional architectures, and accessible surface areas distinct from conventional porous aluminas. The needle-like morphology of insoluble aluminium-derived MIL-53(Al) fostered nanorod structures in resulting MIL-53(Al)-derived composites (*MIL-53(Al)-oxide)* developed here. Macropores cap ends of evolved nanorods, while meso- and micropores decorate tube surfaces, providing high internal accessibility Size and spatial homogeneity are attained from the highly-structured MOF precursor, in contrast to previously studied MOF-derived oxides utilizing non-supported aggregates.

New material applications become available with MOF-derived aluminium oxide structures created here. First, metal oxide nanorods are used as MOF precursors for cyclic MOF regrowth. MIL-53(Al) was grown on and from derived oxide nanostructures. Nanorods allow regrown MOFs to assume their distinctive needle-like structures upon regeneration. Porosity is completely recovered for MOFs over two separate regrowth-

pyrolysis cycles. However, N_2 adsorption at 77K evidences the integration of mesoporosity in regenerated frameworks—residual from derived aluminium oxide precursors. Cyclic acquisition of parent MOF architecture and porosity from derived oxides has not been previously demonstrated. This work delineates the construction and regeneration of porous materials on hierarchical support structures while retaining spatial growth memory.

The broad pore size distribution of *MIL-53(Al)-oxide* elucidates its high internal accessibility. Subsequently, porous alumina structures were integrated with iron (III) oxide (Fe_2O_3) reaction sites to promote H_2S degradation properties. Iron nitrate-impregnated MIL-53(Al), derived from insoluble Al_4C_3, was pyrolyzed to create Fe_2O_3/*MIL-53(Al)-oxide* composites. Humid hydrogen sulfide streams (~0.5%) were reactively desulfurized using resulting materials. EDS and ICP-OES measurements confirmed sulfur deposition and retention on samples post-exposure. Formation of iron-sulfur species and elemental sulfur are observed through XPS scans, which confirm the reactive degradation of H_2S over reaction sites. Impregnate accessibility appears to dictate sulfur uptake, which does correlate with iron loadings. Results outline the extension of acid gas removal techniques described throughout this dissertation to MOF-derived media, where H_2S chemisorption is imparted onto highly accessible oxide media.

Chapter 6 builds upon the impact of materials designed and tested in Chapter 5. The unique chemical and physical properties of crystalline frameworks grown from insoluble metal precursors are extended to derived metal oxides. These advents broaden the applicability of materials studied here, where MOF derived oxide/carbon materials lend desirable qualities in situations where MOFs may be inappropriate, such as chemical and

thermal stability in harsh environments. New applications, such as the cyclic regrowth and impregnation schemes, also become available.

7.1.4.1 Chapter 6 Recommendations

Materials developed in Chapter 6 extend a general concept of Chapter 5—where framework-derived media can be grown directly on and from support media in addition to MOFs. To produce viable separation media, researchers can create MOF-derived oxide/carbon media that instill desirable acid gas separation properties onto macroscale objects through this scheme.

MOF-derived media typically acquire the morphology of precursor frameworks. However, MOFs grown from insoluble media in Chapter 5 adopt architectures that are unique from their conventionally-grown counterparts. So, previously inaccessible structural attributes are easily imparted onto porous carbonaceous oxide media through the pyrolysis scheme presented in Chapter 6.

A final recommendation is to consider how derived materials maintain their spatial distribution on support structures. This is easily seen in pyrolyzed MOF/mesh composites. When converting non-supported MOFs into derived oxides/carbons, particles agglomerate and acquire heterogeneous particle sizes and geometries. But supported MIL-53(Al)-derived materials examined in Chapter 6 remain uniform, homogenously distributed, and orient similarly to one-another. They cannot agglomerate, since they are affixed to their respective locations. Spatial control at the nanoscale is inherently imparted, since microstructures transition directly from MOF precursor locations. A major aspect of both Chapters 5 and 6 is that nanoscale location and structure control is afforded, where often

complex procedures are traditionally required to achieve the same product qualities. So, the recommendation is to spatially control MOF growth on substrate locations using techniques outlined in Chapter 5 (e.g. coating specific parts of a support material with aluminum to localize Al-MOF production). Then convert frameworks to carbonaceous oxide materials, if desired.

APPENDIX A. SUPPORTING INFORMATION

A.1 Chapter 3: Synthesis and Processing Impacts on Framework Stability

A.1.1 Supporting and Raw Data: Defect Engineering in MIL-125-NH_2(Ti)

Table A-1: Acid modulator quantities for 30 : 1 modulator to metal precursor molar ratio experiments.

Acid Modulator	**Amount (30 : 1 Molar Ratio with metal precursor)**
Benzoic Acid	1.84 g
Glacial Acetic Acid	0.86 mL
Formic Acid	0.57 mL
Trifluoroacetic Acid	1.15 mL
Hydrochloric Acid	0.45 mL

Table A-2: Example modulator quantities in varied benzoic and acetic acid modulation experiments.

	Modulator Amount	
Modulator Molar Ratio to Titanium Precursor	Benzoic Acid (mg)	Acetic Acid (mL)
15	915.9	0.43
30	1,831	0.86
60	3,663	1.72
120	7,327	3.43
240	14,654	6.86

Table A-3: Organic acid pK_a values for MOF synthesis reagents. Modulator pK_a values from *CRC Handbook of Chemistry and Physics*

2-Aminoterephthalic Acid	Benzoic Acid	Acetic Acid	Formic Acid	Trifluoroacetic Acid	Hydrochloric Acid
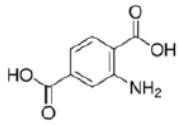	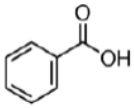	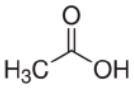	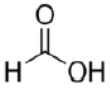	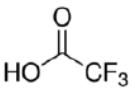	
pK_a:	**3.95[a]**	**4.756**	**4.204**	**3.750**	**0.520**	**-7.000**

Increasing Acidity

[a]pK_a value for BDC-NH_2 from Delori and Jones

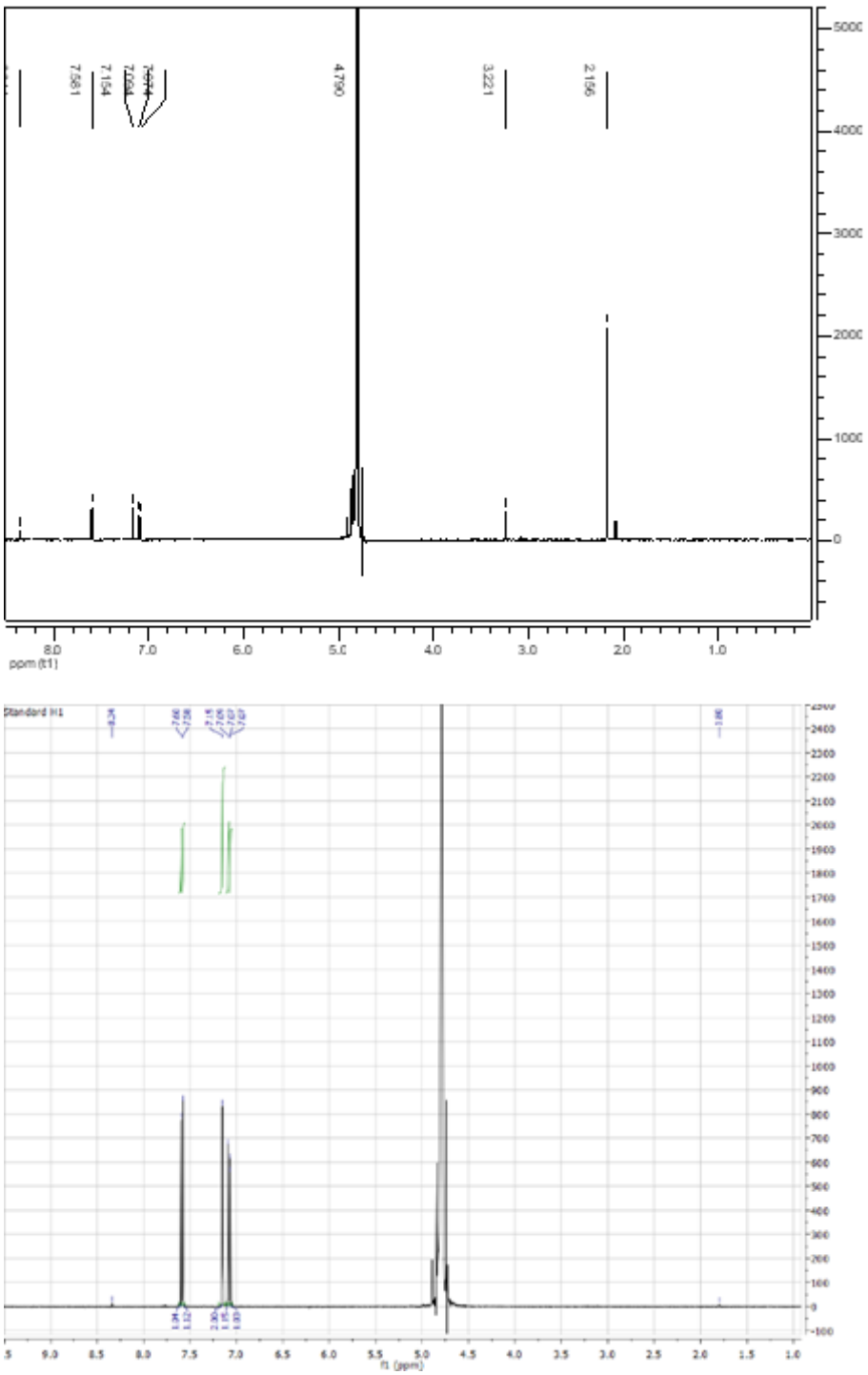

Figure A-1: Full ^{1}H NMR spectra of (top) solvated parent MIL-125-NH$_2$(Ti) and (bottom) 2-aminoterephthalic acid in 1M NaOH/D$_2$O

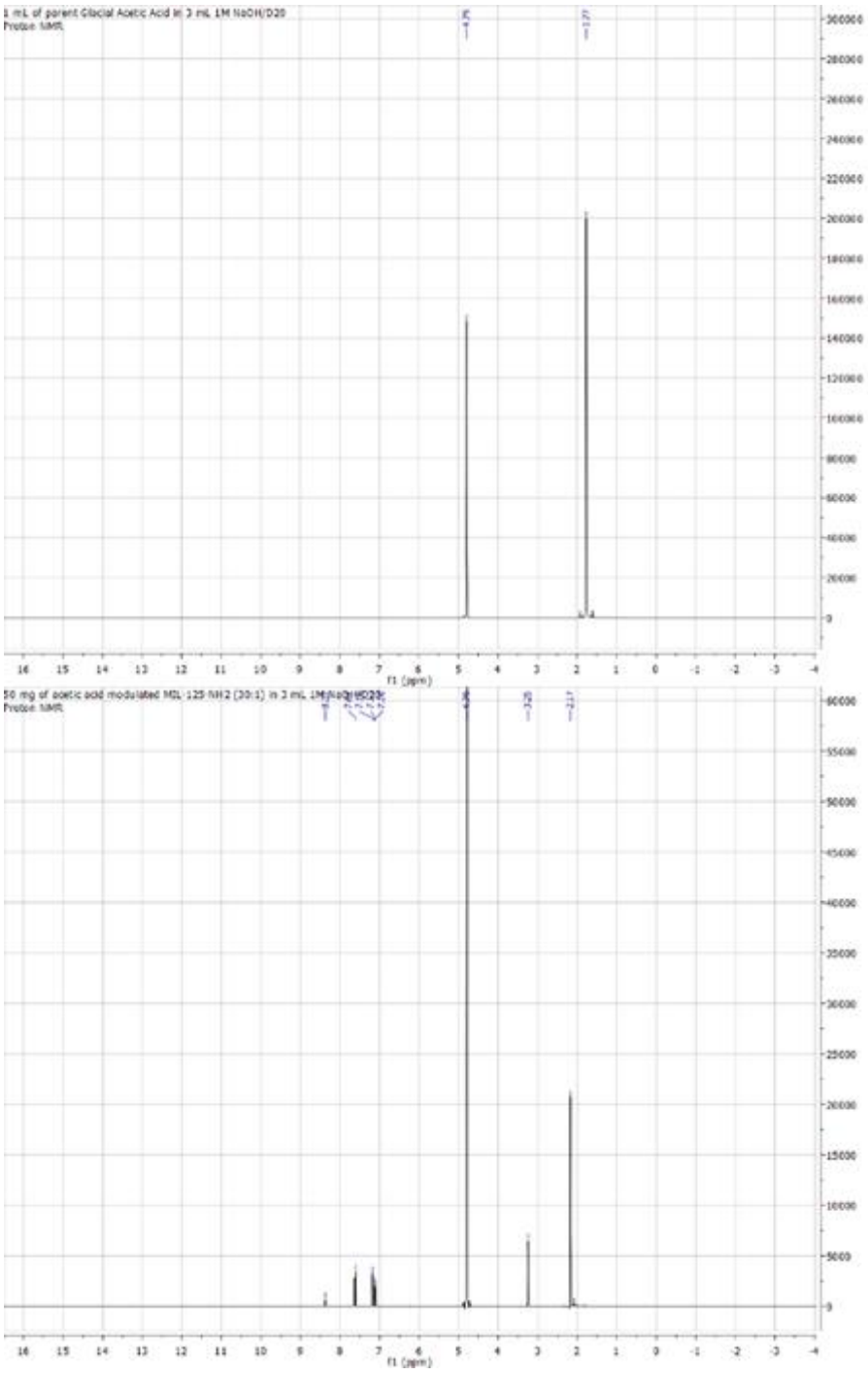

Figure A-2: Full ^{1}H NMR spectra of (top) glacial acetic acid (~33 vol%) and (bottom) 30:1 acetic acid modulated MIL-125-NH_2(Ti)

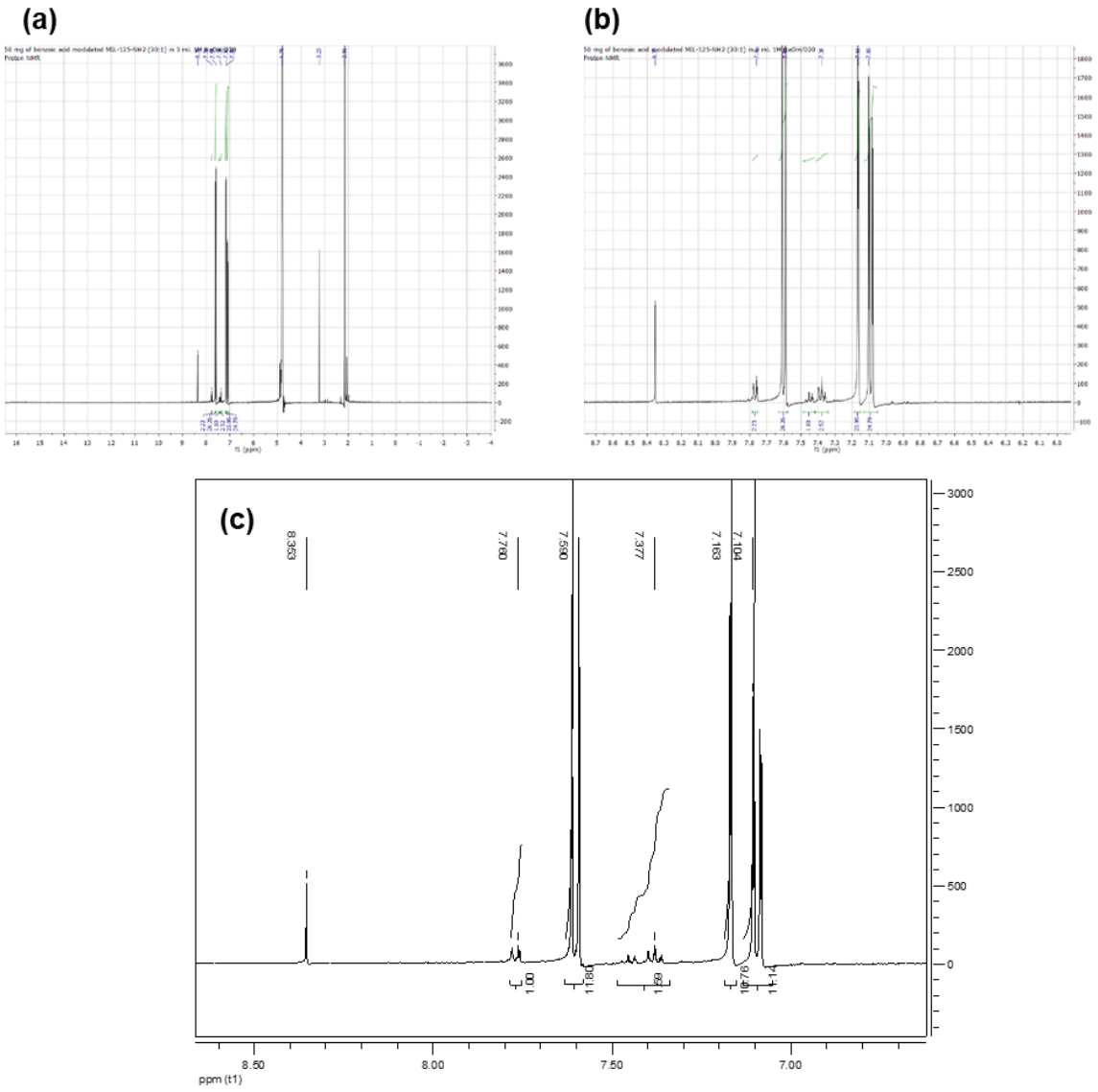

Figure A-3: ^{1}H NMR measurements of 30:1 benzoic acid modulated MIL-125-NH$_2$(Ti). a) Full data, b) inset of phenyl ring and carboxylic acid proton resonances, c) peak integration between framework ligand and benzoic acid ^{1}H peaks

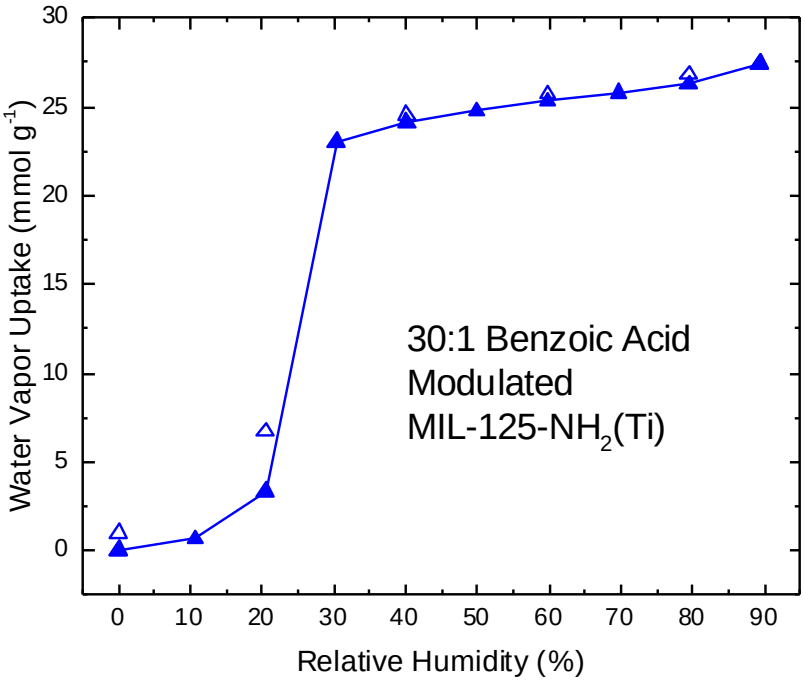

Figure A-4: Water vapor adsorption measurements on benzoic acid-modulated MIL-125-NH_2(Ti) at a 30:1 modulator-to-metal precursor molar ratio. Taken at 25°C. Hollow points denote desorption measurements, while solid points show adsorption. Line is only intended to guide the eye

A.1.2 Supporting and Raw Data: Stable Acid Gas Chemisorption Sites Through Ligand-based Carboxylic Acid Metalation

Experimental synthesis procedures adapted from Joshi et al.[1]

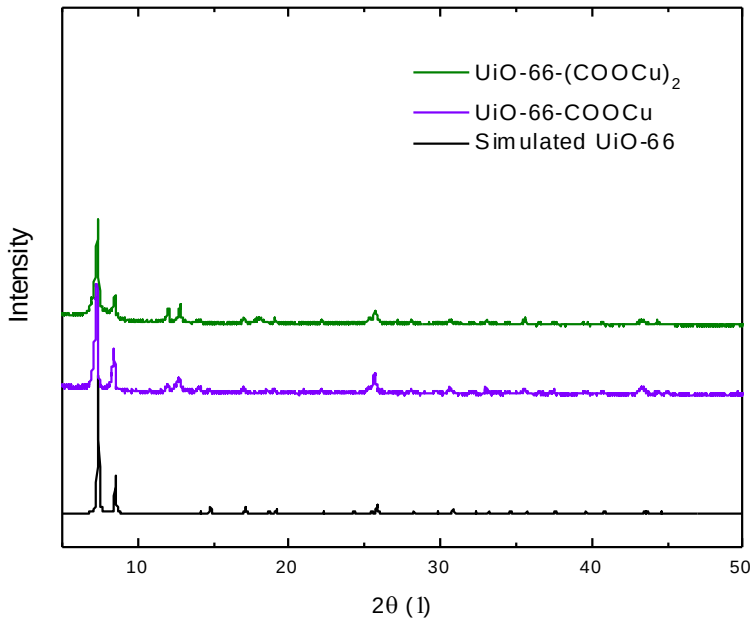

Figure A-5: PXRD patterns of UiO-66-COOCu and UiO-66-(COOCu)$_2$. Simulated pattern from Cavka et al.[2]

Table A-4: FTIR Peak Assignments for UiO-66-(COOH)$_2$ and UiO-66-(COOCu)$_2$. ATR data presented in Figure 3-10

Chemical Functionality	Wavenumber (cm^{-1})
C=O	1653
Asymmetric COO^-	1582
Aromatic C-C	1499
In-plane –OH	1425
Symmetric COO^-	1383
Aliphatic ($-CH_3$)	1380-1360
Aliphatic Ether (C-O-C)	1128

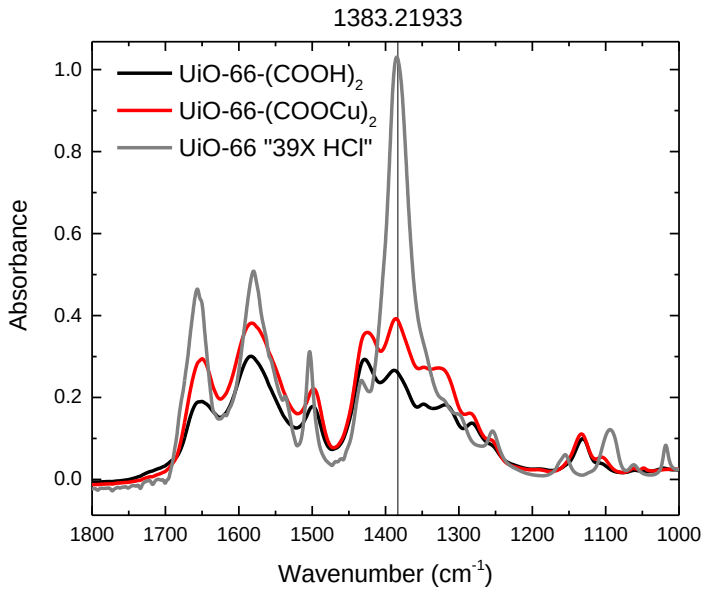

Figure A-6: Inset of ATR-FTIR spectra for UiO-66-(COOH)$_2$ before (black) and after (red) copper coordination, and parent UiO-66(Zr) (grey). Denoted 1383cm^{-1} wavenumber is intended to identify the common -COO$^-$ stretching mode assignment

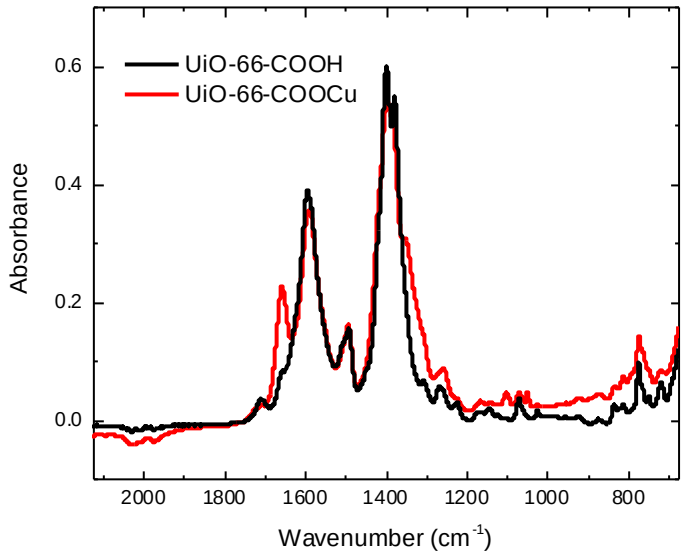

Figure A-7: Inset of ATR-FTIR spectra for UiO-66-COOH before (black) and after (red) copper coordination

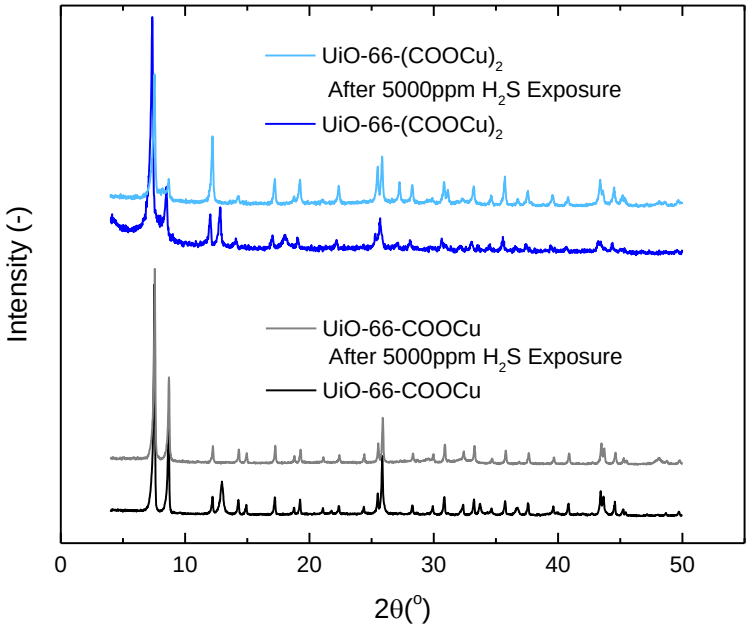

Figure A-8: PXRD patterns for UiO-66-COOCu and UiO-66-(COOCu)$_2$ before and after exposure to 5000ppm H_2S at 25°C

A.1.3. Supporting and Raw Data: Relationships Between MOF Mechanical and Chemical Stability Towards Hydrogen Sulfide

Data are reproduced and adapted from Joshi et al.[3]

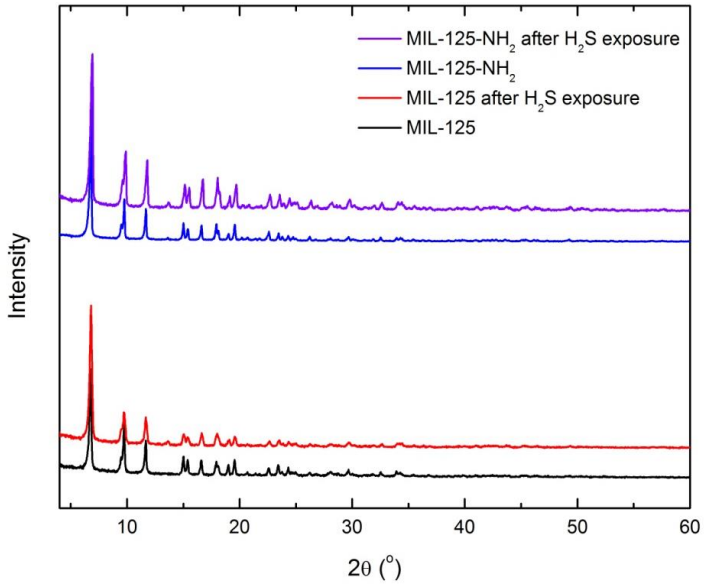

Figure A-9: PXRD of pelletized MIL-125-NH_2(Ti) before and after H_2S exposure

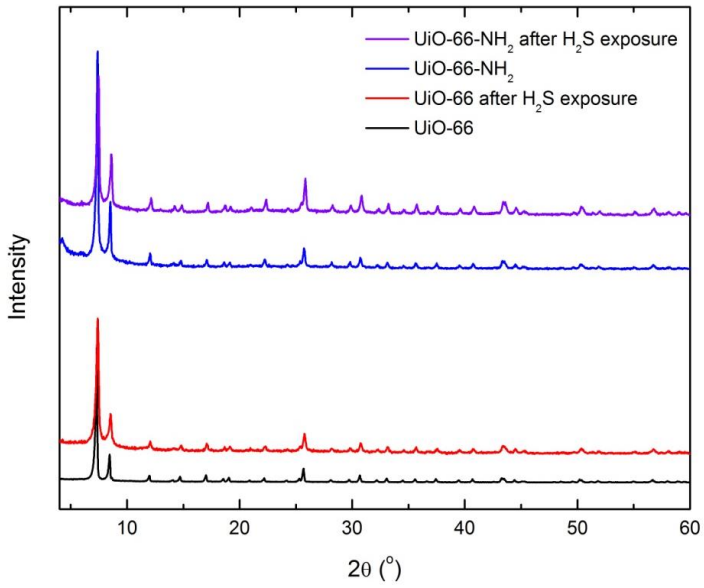

Figure A-10: PXRD of pelletized UiO-66-NH_2(Zr) before and after H_2S exposure

Table A-5: BET surface areas for activated MOFs before and after 1% H_2S exposure, at ambient conditions. N_2 physisorption experiments performed at 77 K

[a]MOF	BET Surface Area (m^2 g^{-1})		
	Before H_2S	After H_2S	Percent Loss (%)
UiO-66(Zr)	1114	1111	-
UiO-66-NH_2(Zr)	963	940	**2**
MIL-125(Ti)	1639	1622	**1**
MIL-125-NH_2(Ti)	1612	1609	-
MIL-101(Cr), **pristine**	3409	3361	**1**
MIL-101(Cr)	2261	2033	**10.0**
MIL-101-NH_2(Cr), **pristine**	2096	2039	**3**
MIL-101-NH_2(Cr)	1288	1238	**3**

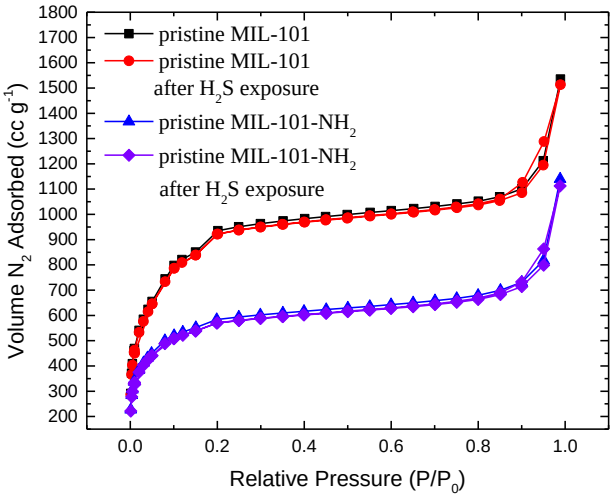

Figure A-11: N_2 adsorption isotherms at 77K for MIL-101(Cr) and MIL-101-NH_2(Cr), before and after H_2S adsorption experiments

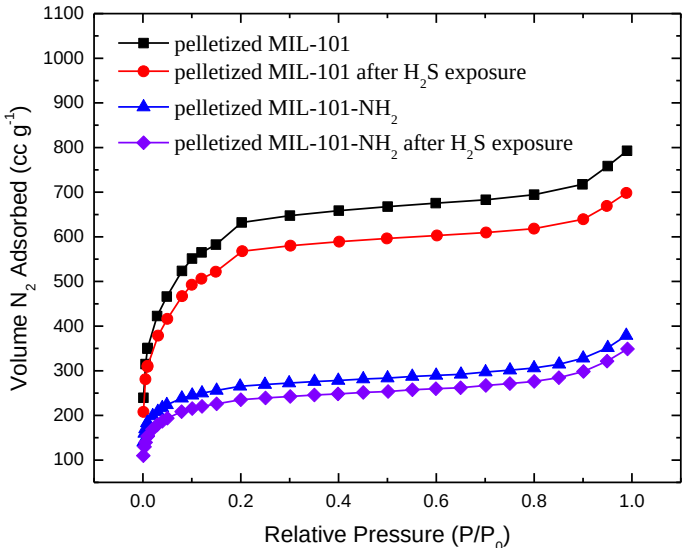

Figure A-12: N_2 adsorption isotherms at 77K for pelletized MIL-101(Cr) and MIL-101-NH_2(Cr), before and after H_2S adsorption experiments

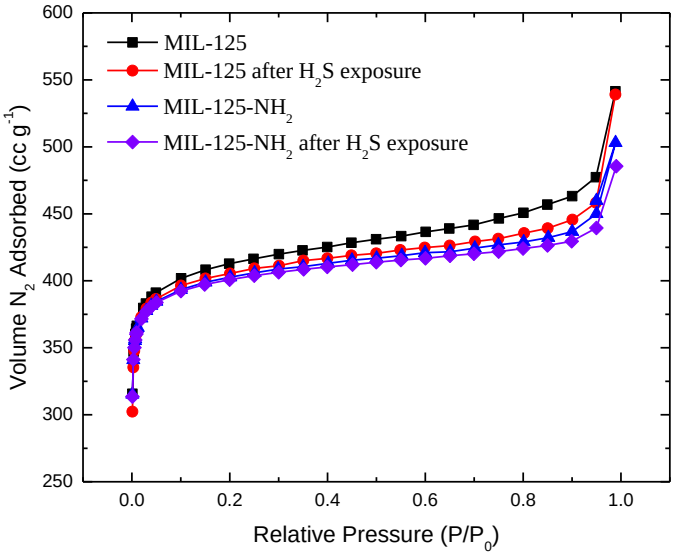

Figure A-13: N_2 adsorption isotherms at 77K for pelletized MIL-125(Ti) and MIL-125-NH_2(Ti), before and after H_2S adsorption experiments

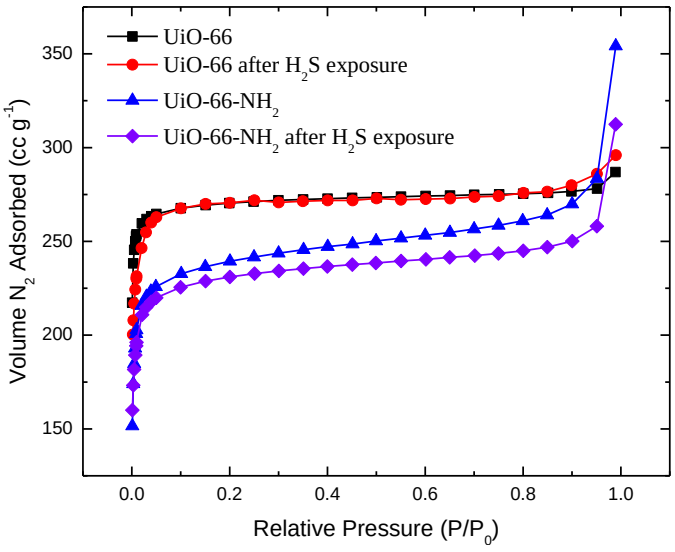

Figure A-14: N_2 adsorption isotherms at 77K for pelletized UiO-66(Zr) and UiO-66-NH_2(Zr), before and after H_2S adsorption experiments.

Accompanying pore size distributions for the materials as provided below. Data were modeled using non-local density functional theory (NLDFT), assuming carbon surface with cylindrical pores.[4] Please note that no general pore size distribution model exists for MOF N_2 adsorption measurements. Consequently, the distributions are not intended to communicate quantitative changes in textural properties.

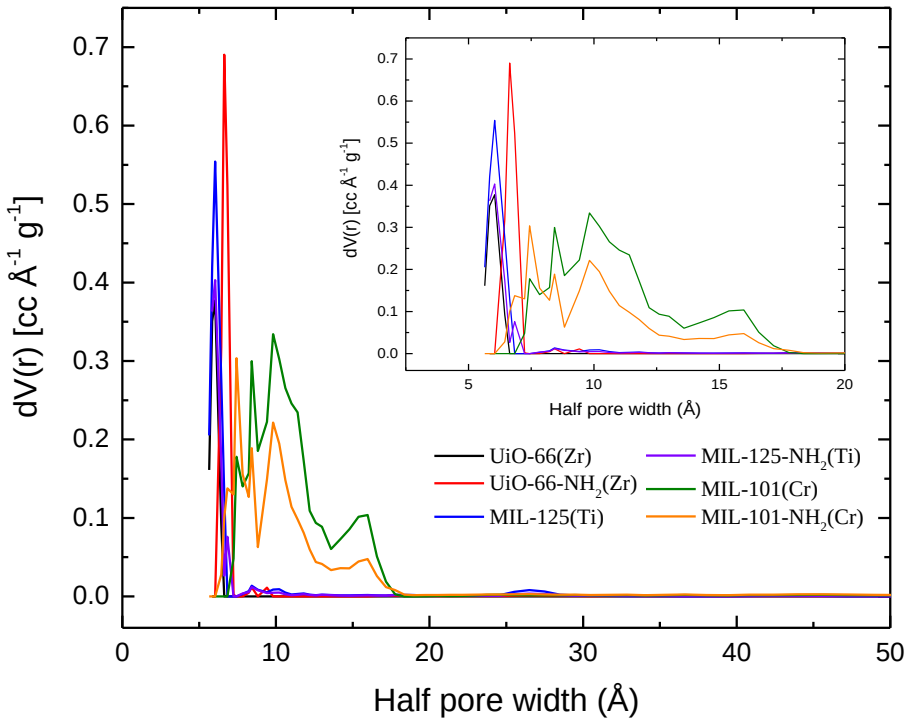

Figure A-15: Pore size distribution for investigated MOFs. Utilizing N_2 adsorption data collected at 77K. Modeled with non-local density functional theory (NLDFT) assuming carbon, cylindrical pores.

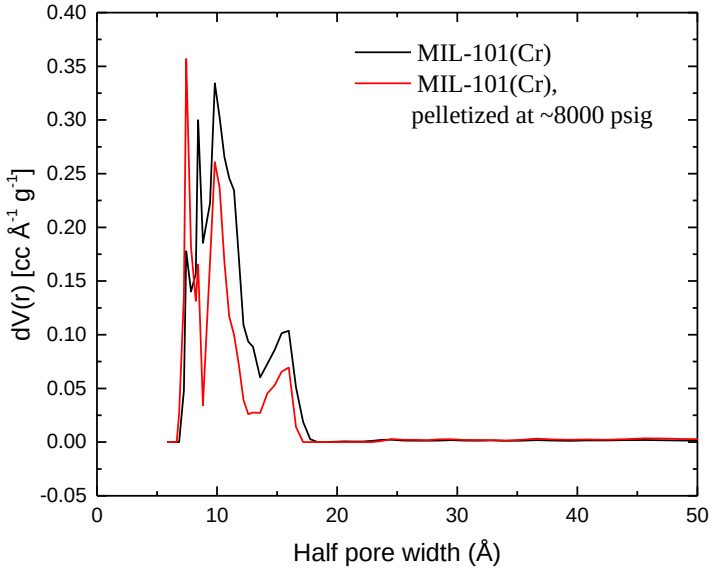

Figure A-16: Pore size distribution for MIL-101(Cr) before and after pelletization, utilizing N_2 adsorption data collected at 77K. Modeled with non-local density functional theory (NLDFT) assuming carbon, cylindrical pores.

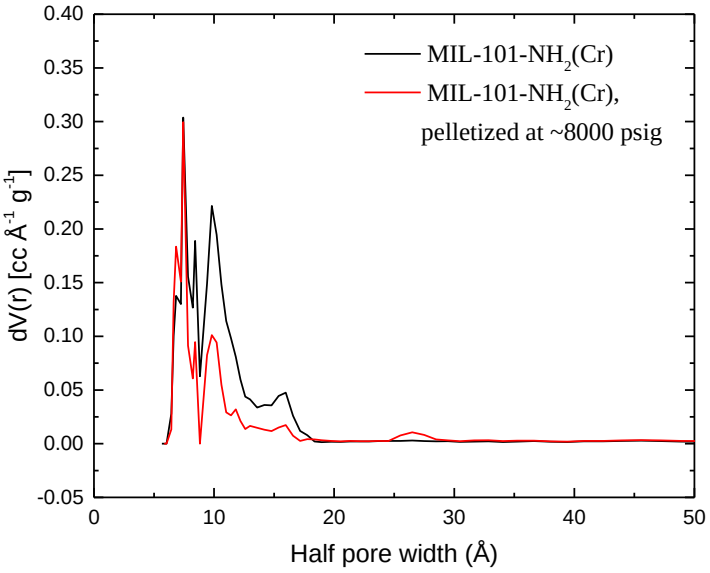

Figure A-17: Pore size distribution for MIL-101-NH_2(Cr) before and after pelletization, utilizing N_2 adsorption data collected at 77K. Modeled with non-local density functional theory (NLDFT) assuming carbon, cylindrical pores.

A.2 Chapter 4: Targeted Acid Gas Removal Through Framework Functionalization

A.2.1. Supporting and Raw Data: Carboxylic Acid Groups Targeting Polar Acid Gas (SO_2, H_2S) Capture

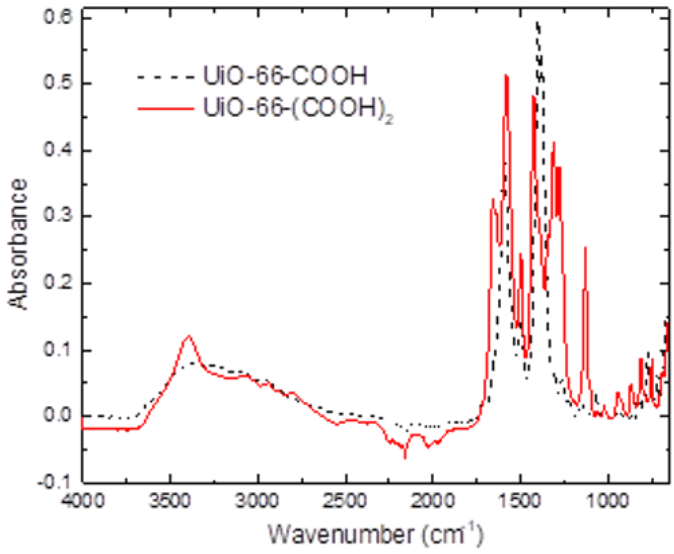

Figure A-18: ATR measurements of UiO-66-COOH (dashed black line) and UiO-66-(COOH)$_2$ (solid red line)

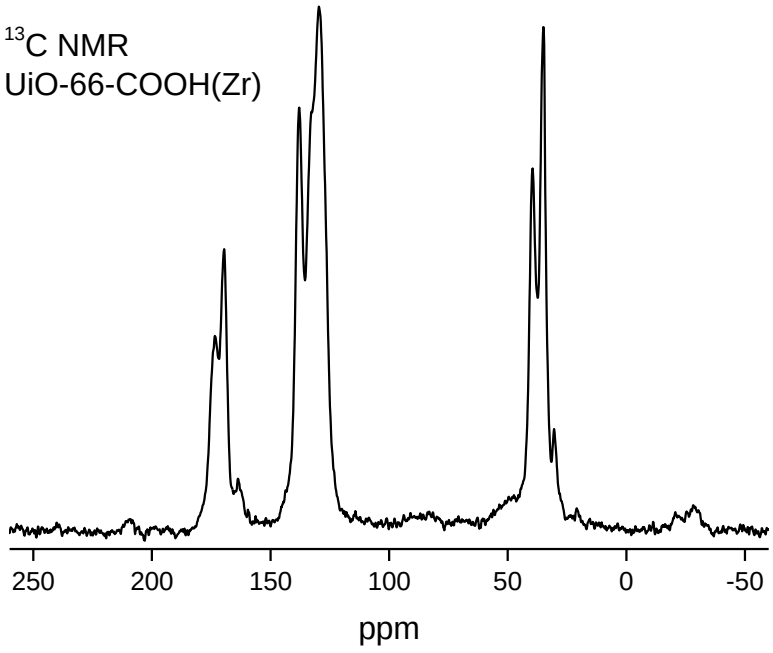

Figure A-19: ^{13}C solid-state NMR measurements of UiO-66-COOH

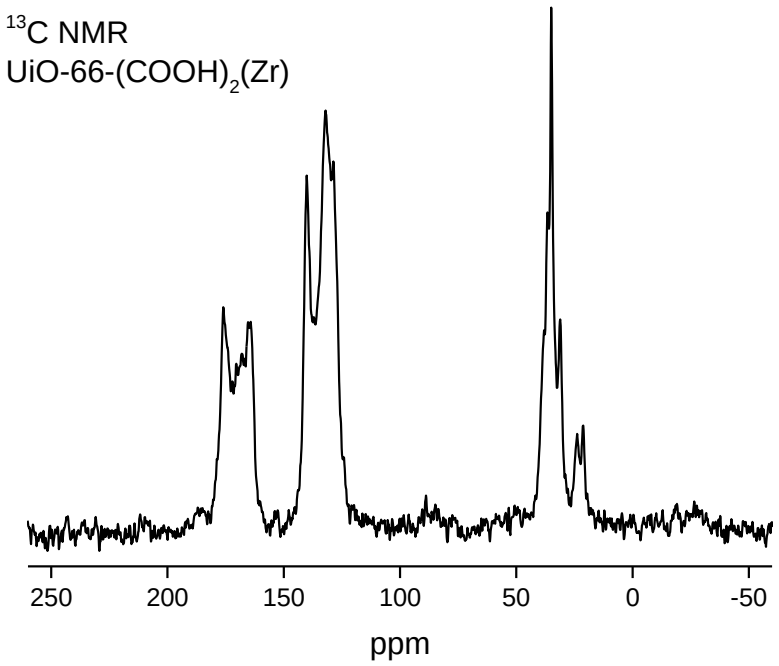

Figure A-20: ^{13}C solid-state NMR measurements of UiO-66-(COOH)$_2$

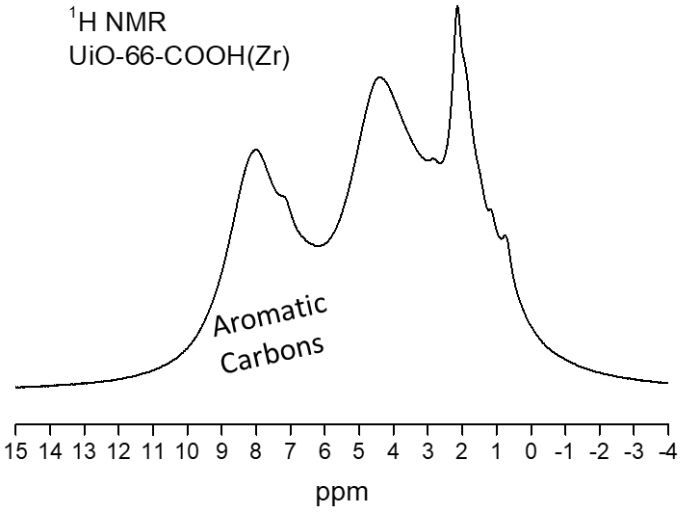

Figure A-21: ^{1}H solid-state NMR measurements of UiO-66-COOH. Text label intended to discern phenyl ring resonances

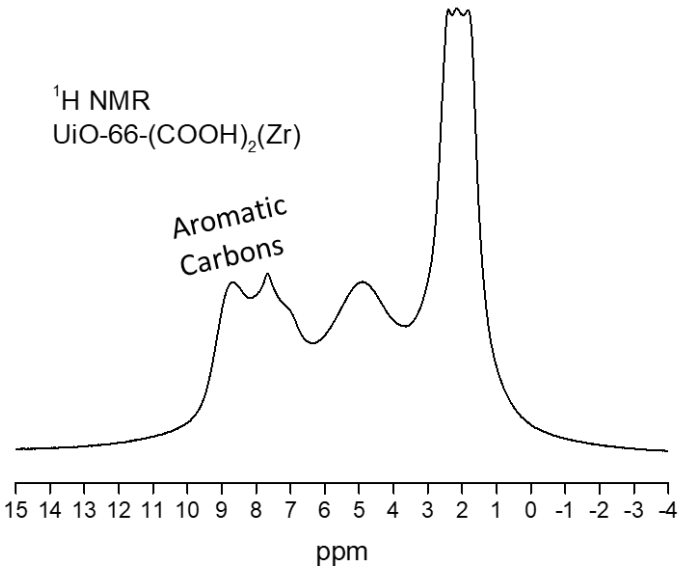

Figure A-22: ^{1}H solid-state NMR measurements of UiO-66-(COOH)$_2$. Text label intended to discern phenyl ring resonances

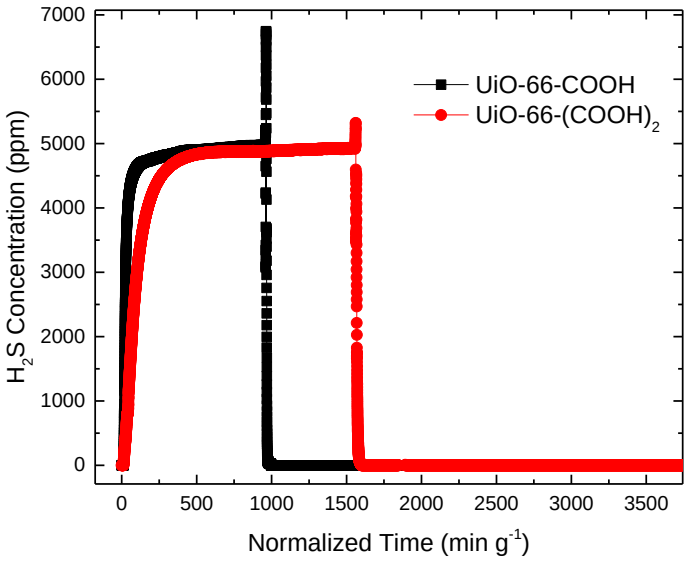

Figure A-23: 5000ppm H_2S breakthrough and desorption curves for UiO-66-COOH and UiO-66-(COOH)$_2$

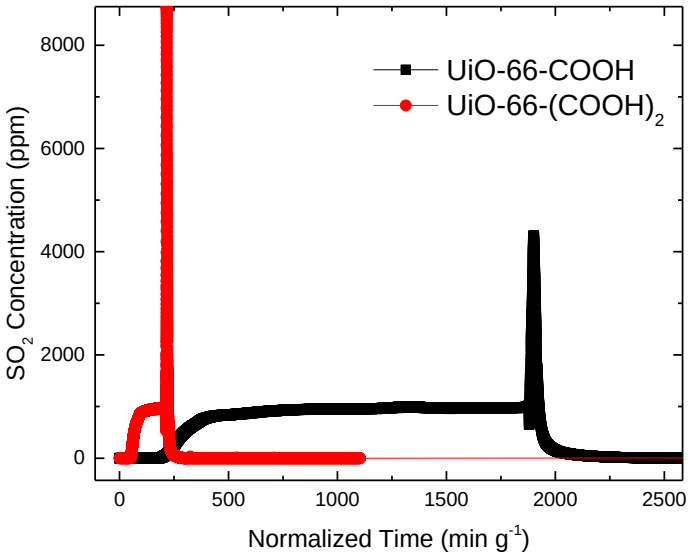

Figure A-24: 1000ppm SO_2 breakthrough and desorption curves for UiO-66-COOH and UiO-66-(COOH)$_2$

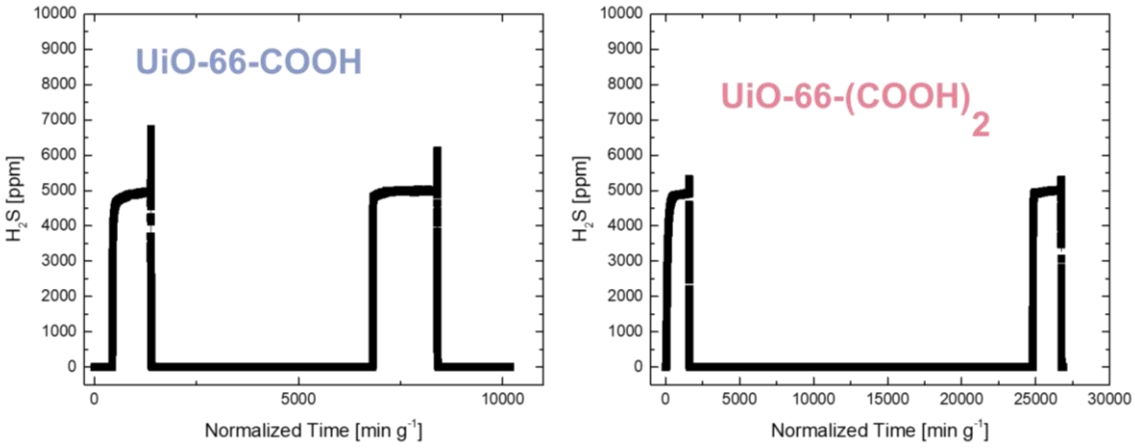

Figure A-25: Cyclic H_2S adsorption-desorption measurements for UiO-66-COOH (left) and UiO-66-(COOH)$_2$ (right)

Table A-6: Uptake capacities for select H_2S and CO_2 removal media

Adsorbent	Adsorbent Type	H_2S Uptake [mmol / g]	CO_2 Uptake [mmol / g]	Source
GC Sulfursorb Plus	Activated Carbon	14.7	-	5
Perilla	Biochar	0.537	2.312	6
Korean oak	Biochar	0.178	0.597	

Japanese oak	Biochar	0.167	0.379	
Soybean stover	Biochar	0.308	0.707	
Y-FTZB-fcu-MOF	MOF	0.9	0.22	
Y-fum-fcu-MOF	MOF	1.1	0.17	[7]
Y-1,4-NDC-fcu-MOF	MOF	1.5	0.24	
ACF10	Activated Carbon Fibers	0.042	-	
ACF20	Activated Carbon Fibers	0.064	-	[8]
ACF 25	Activated Carbon Fibers	0.078	-	

Table A-7: List of reported acid gas adsorption capacities and experimental conditions of MOFs evaluated in the literature. Data table reproduced from Rezaei et al.[9]

Adsorbent	Gas Mixture (vol %)	System	Temperature (°C)	Adsorption Capacity (mmol g^{-1})
Ba/Cu-BTC	50 ppm SO_2/6% O_2/He	plug flow reactor	<400	2.4
FMOF-2	0.5 bar SO_2	volumetric system	25	1.4
MOF-5	1% SO_2/N_2	fixed-bed reactor	25	1
MOF-74	1% SO_2/N_2	fixed-bed reactor	25	3
MOF-177	1% SO_2/N_2	fixed-bed reactor	25	<1.0
MOF-199	1% SO_2/N_2	fixed-bed reactor	25	0.5
IRMOF-3	1% SO_2/N_2	fixed-bed reactor	25	6
IRMOF-62	1% SO_2/N_2	fixed-bed reactor	25	<1.0
Cu-BTC/graphite oxide	1000 ppm NO2/N2	fixed-bed reactor	25	2.1
CPO-27-Ni	1 bar pure NO	gravimetric system	25	7

Cu-BTC	1 bar pure NO	gravimetric system	25	3
MIL-88A(Fe)	1 bar pure NO	gravimetric system	30	2.5
UiO-66	1000 ppm NO_2/N_2	fixed-bed reactor	25	1.1
UiO-67	1000 ppm NO_2/N_2	fixed-bed reactor	25	1.8
Cu-BTC/graphite oxide	1000 ppm NO_2/N_2	fixed-bed reactor	25	1.8
Cu-BTC	1000 ppm NO_2/N_2	fixed-bed reactor	25	1.7

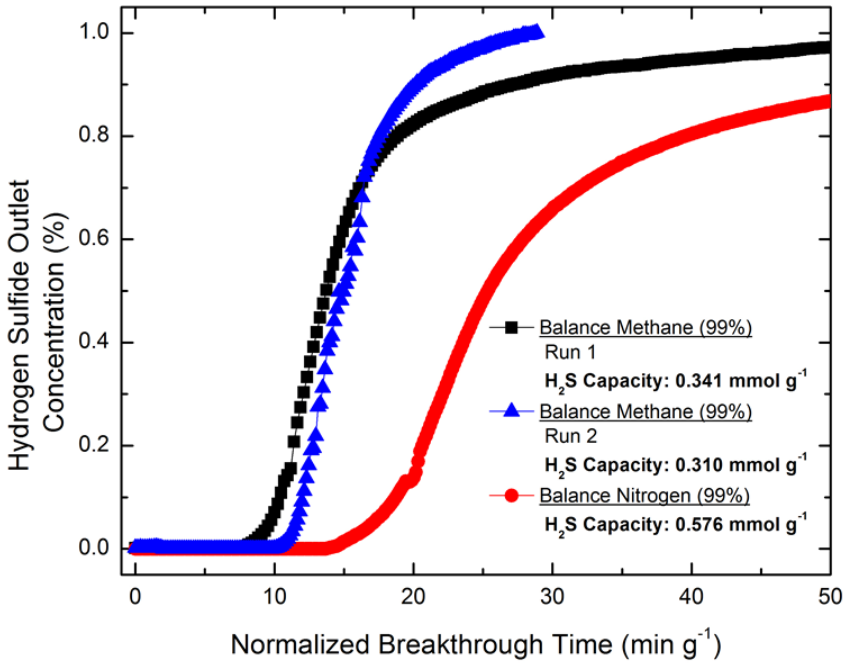

Figure A-26: 1% H_2S/N_2 and 1% H_2S/CH_4 breakthrough curves and H_2S saturation capacities for UiO-66-NH_2(Zr)

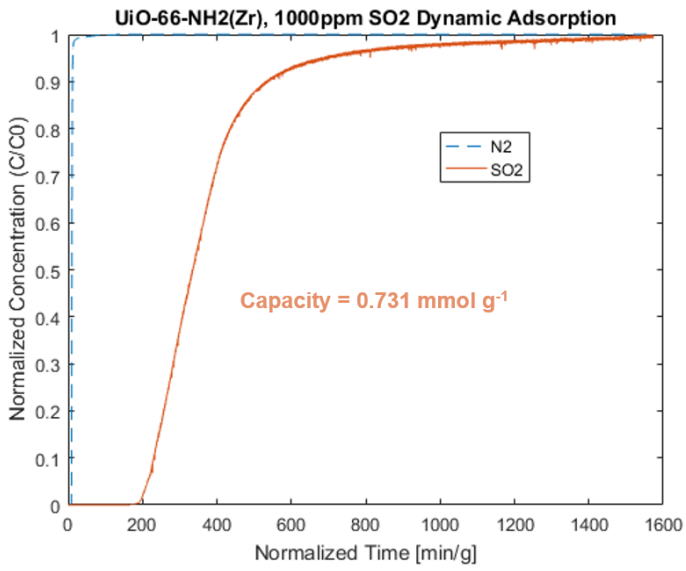

Figure A-27: 1000 ppm SO_2/N_2 adsorption breakthrough curve. Solid orange line denotes kinetic SO_2 uptake, dashed blue line denotes kinetic N_2 uptake. Calculated uptake capacity based on adsorption data listed in graphic

A.2.2 Supporting and Raw Data: Probing Metal-Organic Framework Design for Adsorptive Natural Gas Purification

Data reproduced from Joshi et al.[3]

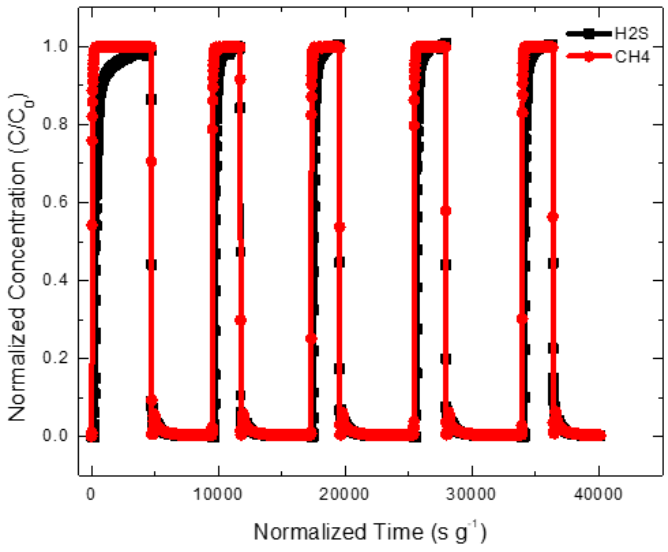

Figure A-28: 1% H_2S/CH_4 fixed-bed experiments for MIL-125(Ti)

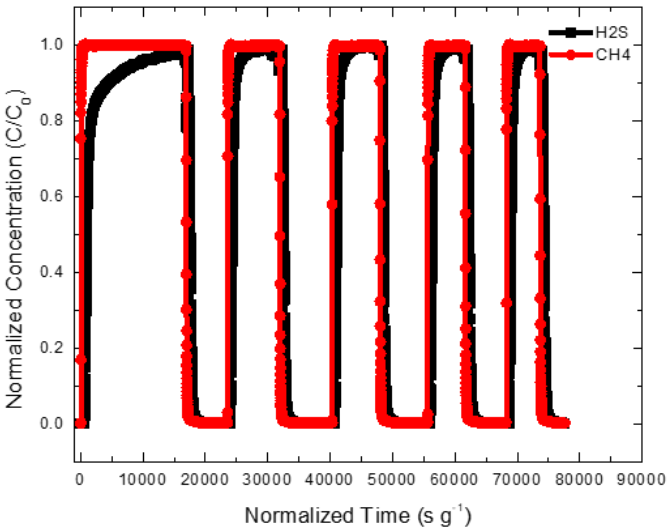

Figure A-29: 1% H_2S/CH_4 fixed-bed experiments for MIL-125-NH_2(Ti)

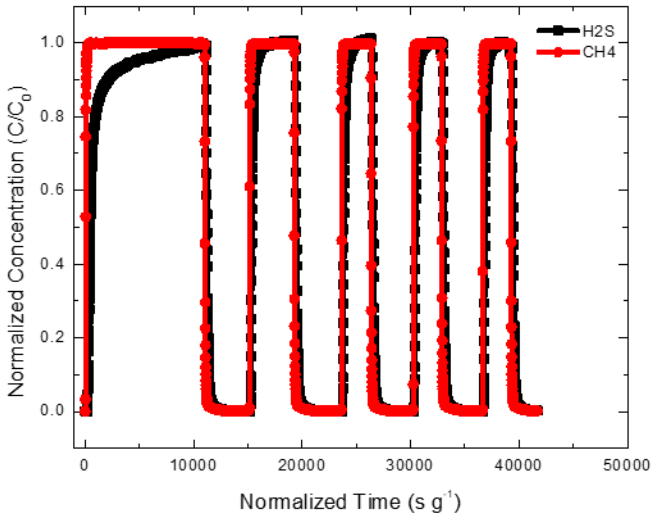

Figure A-30: 1% H_2S/CH_4 fixed-bed experiments for UiO-66(Zr)

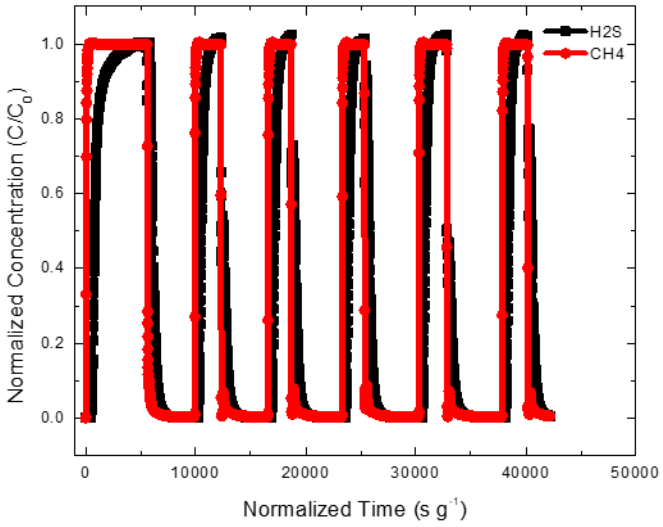

Figure A-31: 1% H_2S/CH_4 fixed-bed experiments for UiO-66-NH_2(Zr)

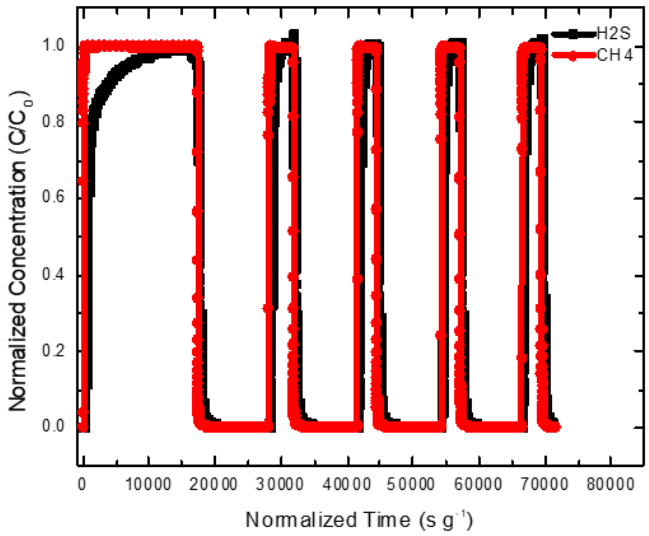

Figure A-32: 1% H_2S/CH_4 fixed-bed experiments for MIL-101(Cr)

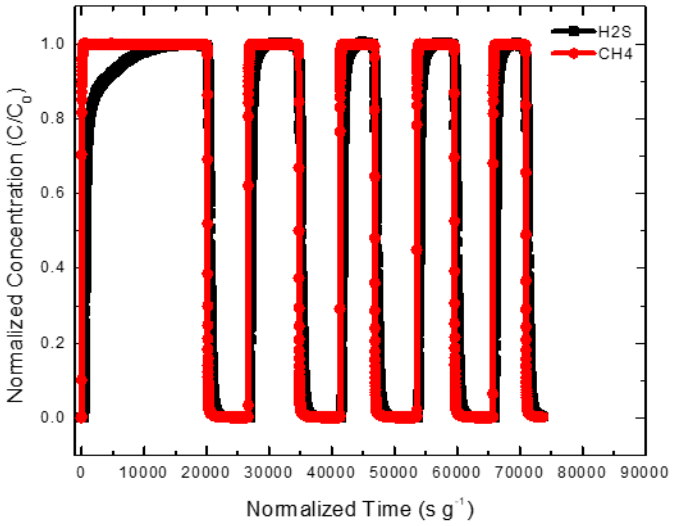

Figure A-33: 1% H_2S/CH_4 fixed-bed experiments for MIL-101-NH_2(Cr)

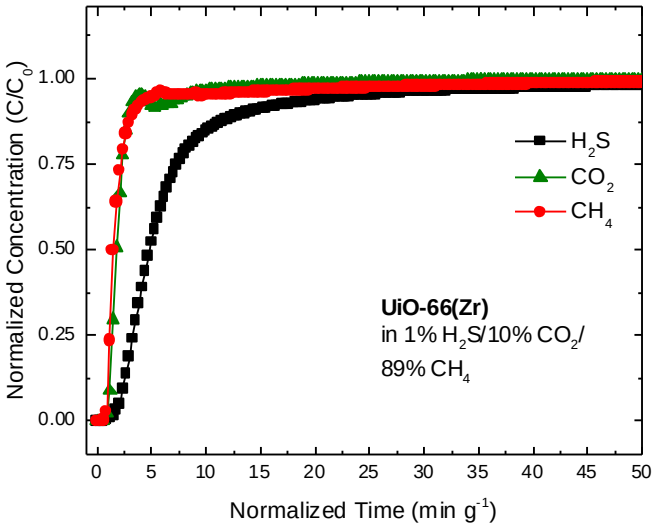

Figure A-34: UiO-66(Zr) breakthrough curves using 1% H_2S/10% CO_2/89% CH_4 mixture at ambient conditions

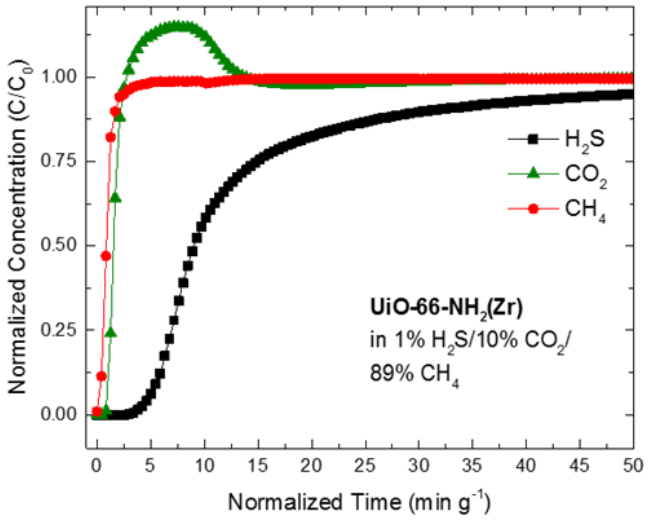

Figure A-35: UiO-66-NH_2(Zr) breakthrough curves using 1% H_2S/10% CO_2/89% CH_4 mixture at ambient conditions

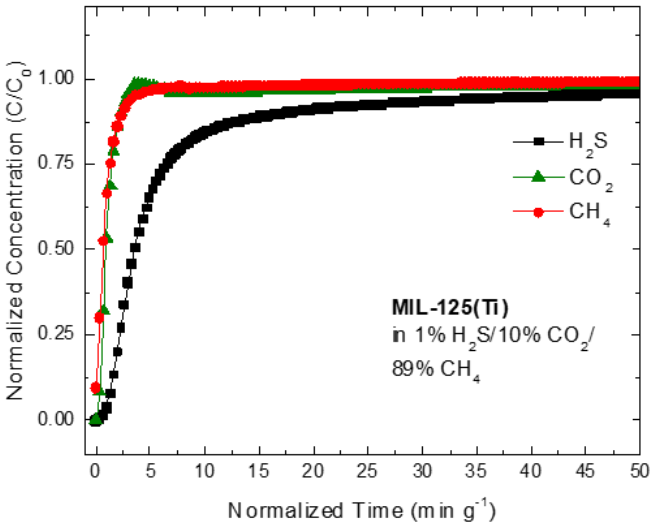

Figure A-36: MIL-125(Ti) breakthrough curves using 1% H_2S/10% CO_2/89% CH_4 mixture at ambient conditions

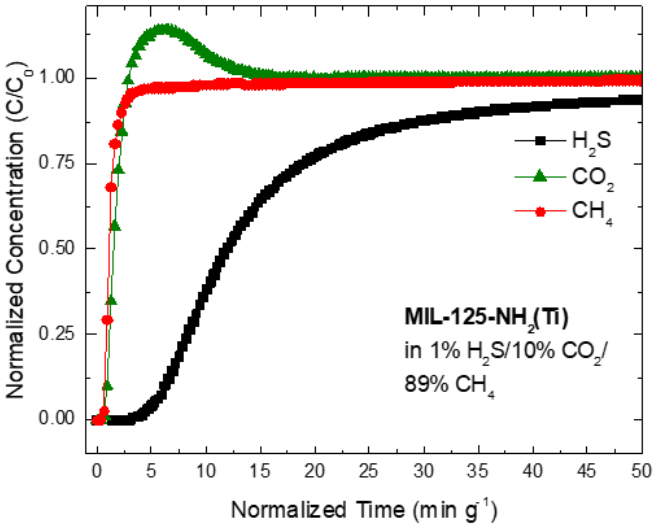

Figure A-37: MIL-125-NH_2(Ti) breakthrough curves using 1% H_2S/10% CO_2/89% CH_4 mixture at ambient conditions

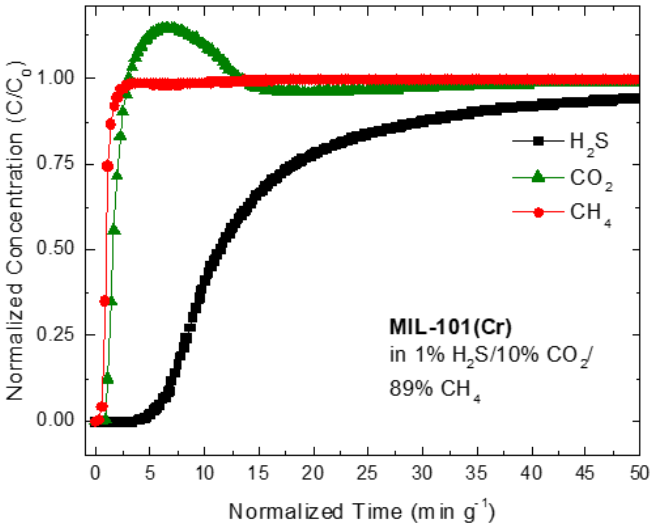

Figure A-38: MIL-101(Cr) breakthrough curves using 1% H_2S/10% CO_2/89% CH_4 mixture at ambient conditions

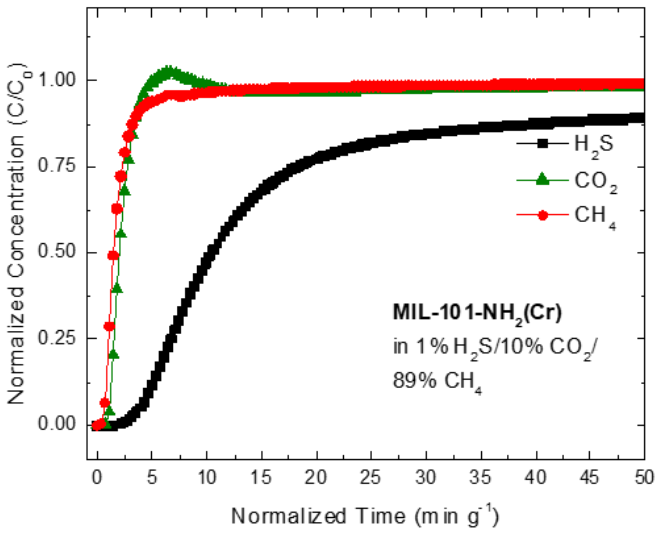

Figure A-39: MIL-101-NH_2(Cr) breakthrough curves using 1% H_2S/10% CO_2/89% CH_4 mixture at ambient conditions

Table A-8: Referenced literature H_2S uptake capacities.

MOF	[a]Estimated H_2S Uptake Capacity (mmol g^{-1})	Manuscript Reference Number	Notes
UiO-66(Zr)	< 0.5	13	GCMC simulated H_2S uptake at 303K
UiO-66-NH_2(Zr)	0.95	23	Fixed-bed saturation uptake, 1%H_2S/10%CO_2/89%He challenge gas
MIL-125(Ti)	<0.5	16	GCMC simulated H_2S uptake at 303K
MIL-125-NH_2(Ti)	0.5-0.8	16	GCMC simulated H_2S uptake at 303K
MIL-101(Cr)	0.5-1	15	Experimental H_2S uptake at 303.1K
MIL-101-NH_2(Cr)	Does Not Exist	-	-

[a]Note single component H_2S uptake measurements are not directly comparable to capacities determined in multicomponent mixtures here. Estimated capacities were approximated from literature isothermal uptake curves.

A.2.1.1. Supplemental Information for FTIR Studies

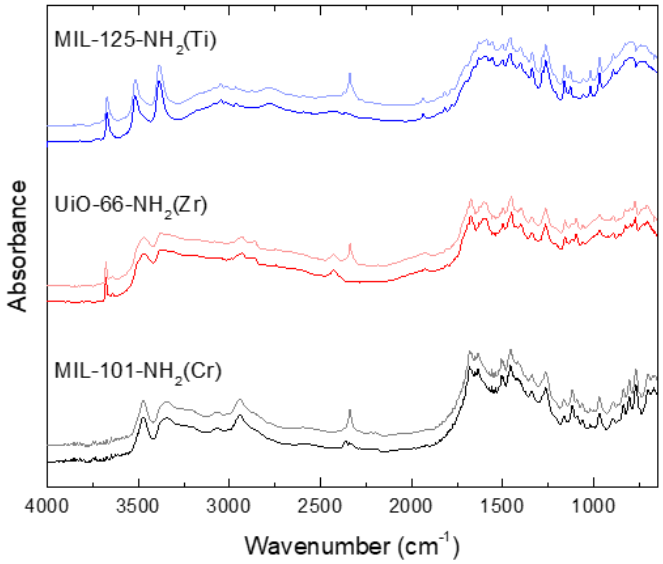

Figure A-40: FTIR spectra collected through DRIFTS for activated (bottom) and exposed (top) samples. Exposure spectra were acquired after 15 minutes of 10% CO_2 exposure. Data are shown after subtraction of gaseous CO_2.

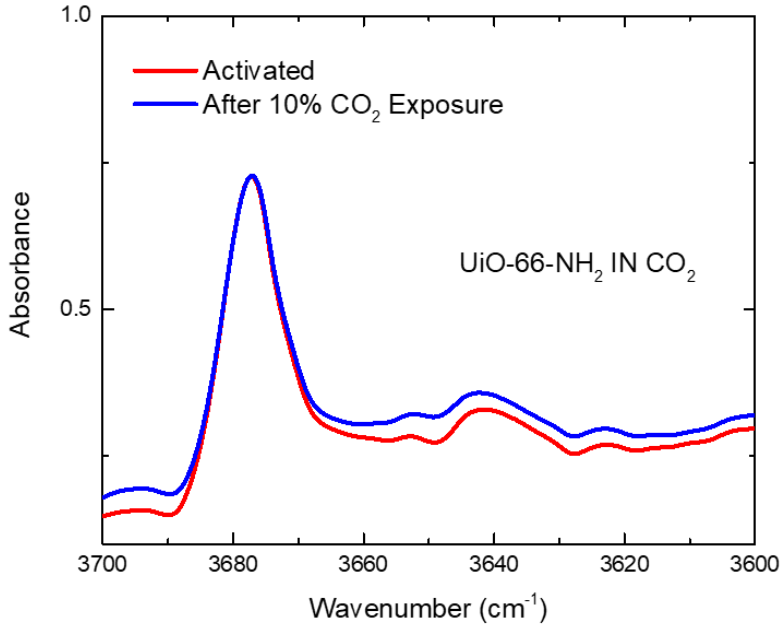

Figure A-41: Hydroxyl stretch region of FTIR spectra for activated and 10% CO_2/He exposed UiO-66-NH_2(Zr)

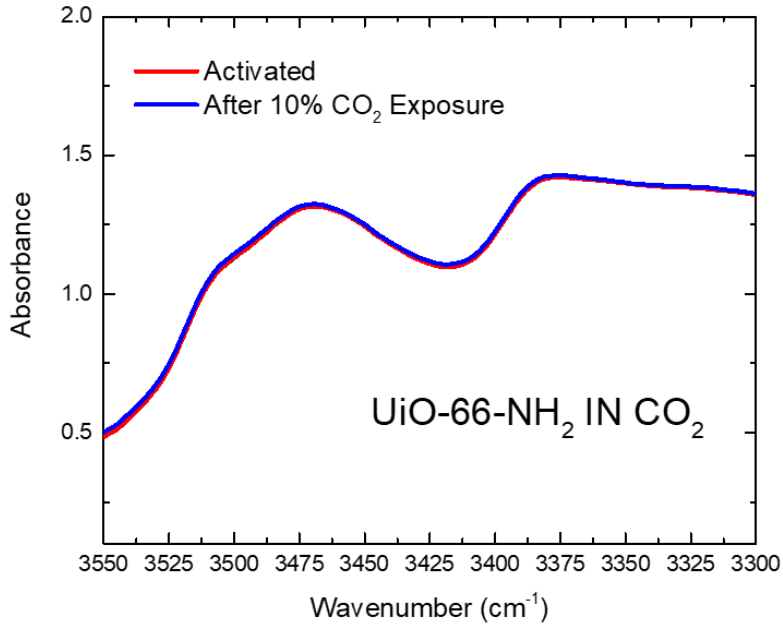

Figure A-42: Primary amine stretch region of FTIR spectra for activated and 10% CO_2/He exposed UiO-66-NH_2(Zr)

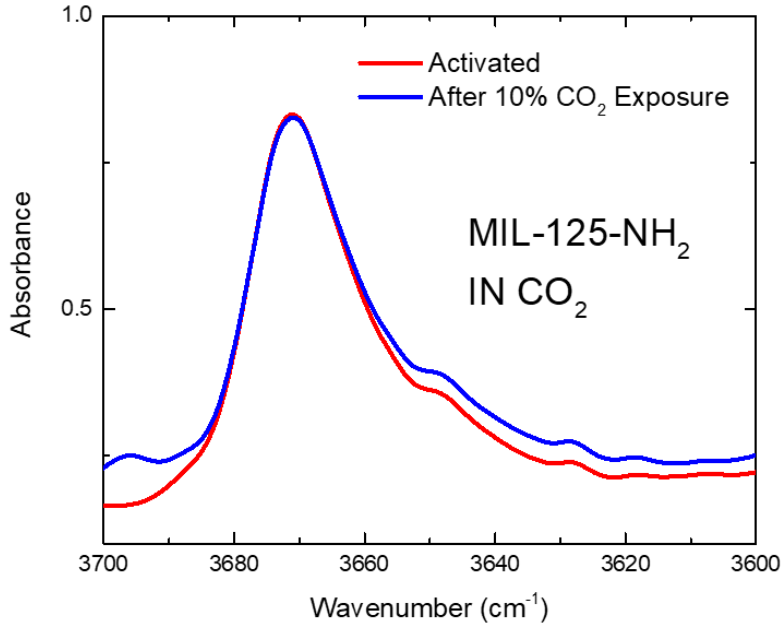

Figure A-43: Hydroxyl stretch region of FTIR spectra for activated and 10% CO_2/He exposed MIL-125-NH_2(Ti)

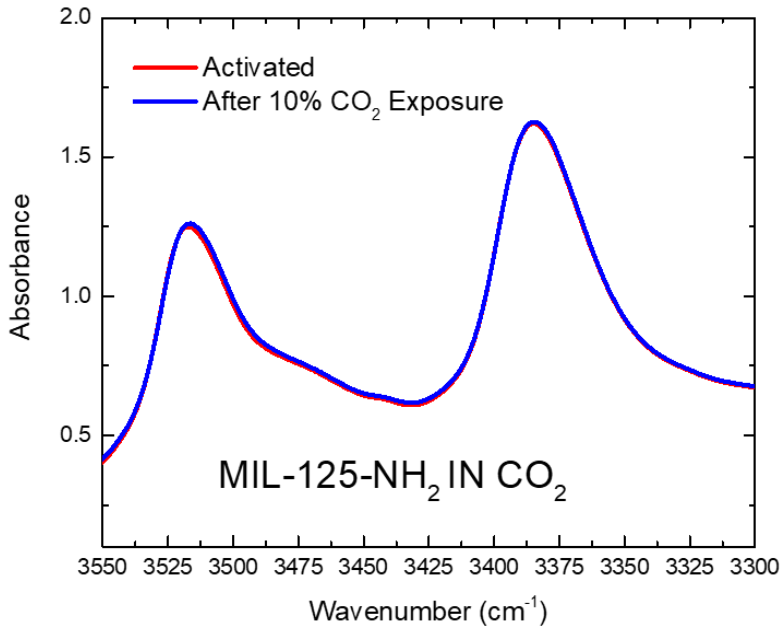

Figure A-44: Primary amine stretch region of FTIR spectra for activated and 10% CO_2/He exposed MIL-125-NH_2(Ti)

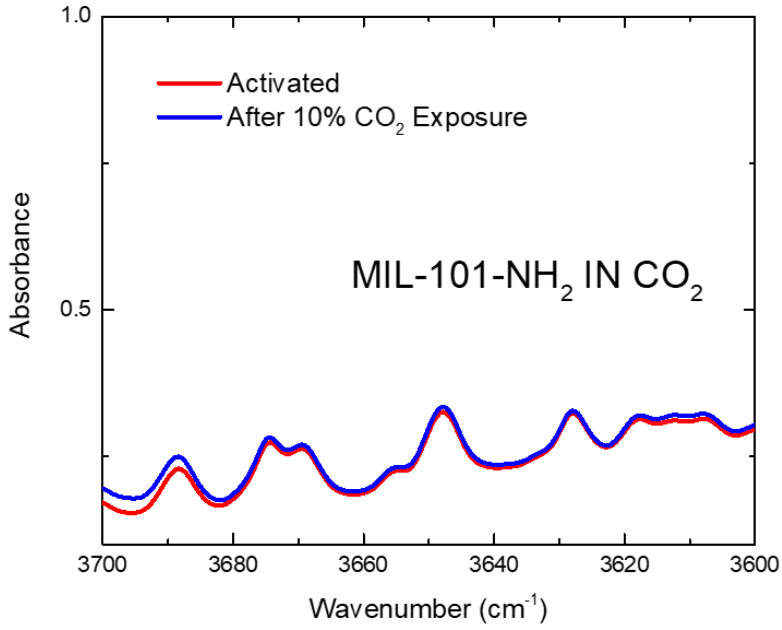

Figure A-45: Hydroxyl stretch region of FTIR spectra for activated and 10% CO_2/He exposed MIL-101-NH_2(Cr)

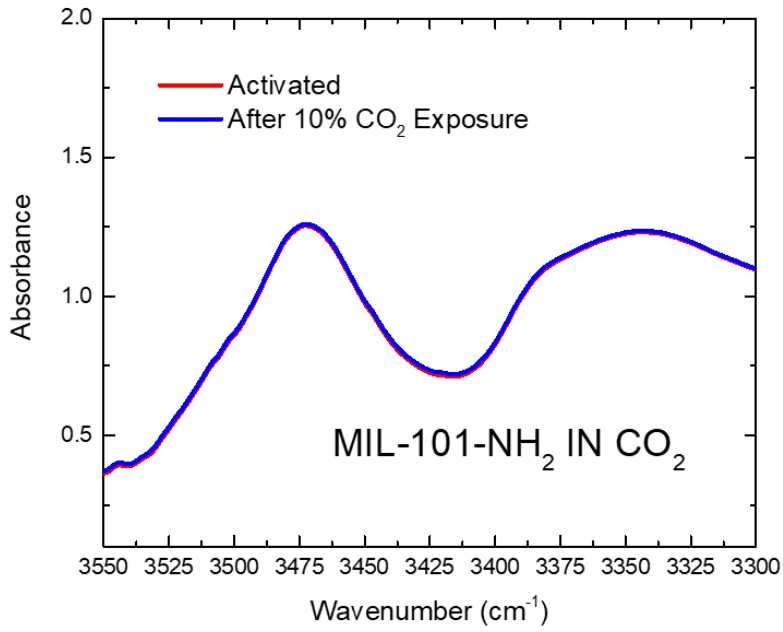

Figure A-46: Primary amine stretch region of FTIR spectra for activated and 10% CO_2/He exposed MIL-101-NH_2(Cr)

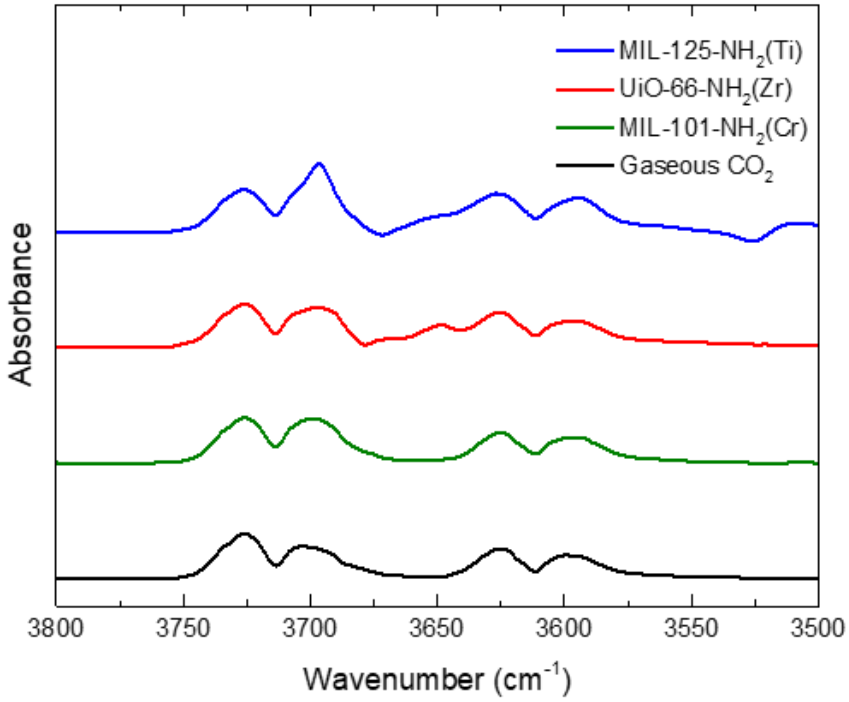

Figure A-47: MOF FTIR spectra without gaseous CO_2 subtraction, overlaid with spectrum of gaseous CO_2.

A.3 Chapter 5: Creating Supported and Non-Supported Framework Composites with Insoluble Metal Precursors

A.3.1. Supplemental Information for Supported Aluminum MOF Growth

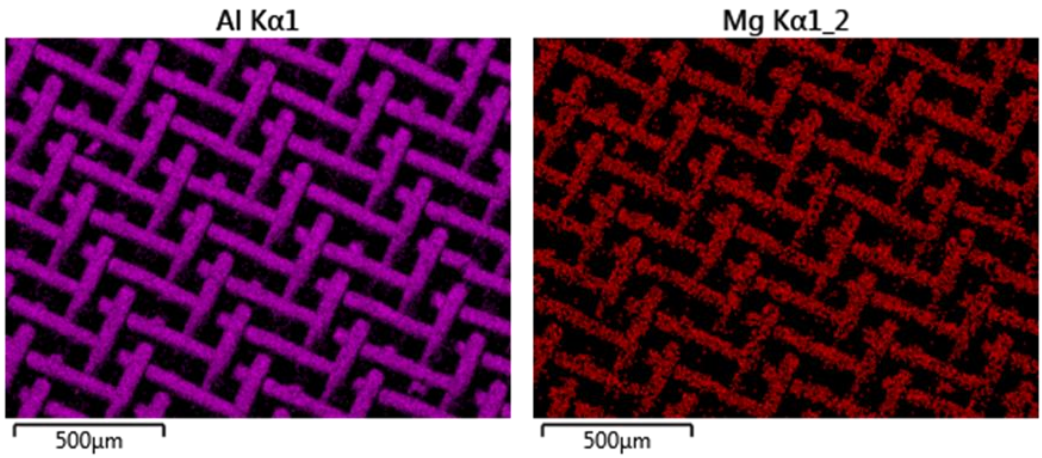

Figure A-48: EDS measurement on aluminum alloy mesh reagent detecting aluminum (left) and magnesium (right)

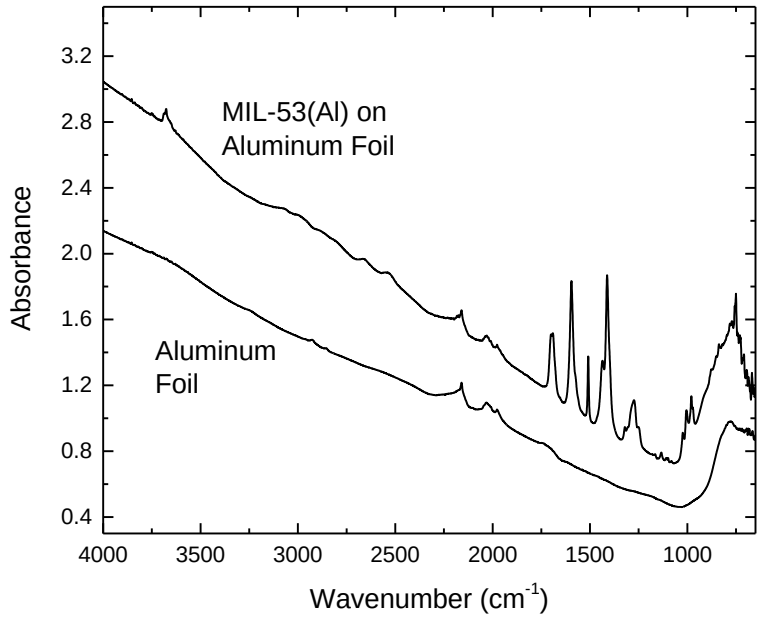

Figure A-49: ATR-FTIR spectra of bare aluminum foil (bottom) and aluminum foil coated with MIL-53(Al) (top).

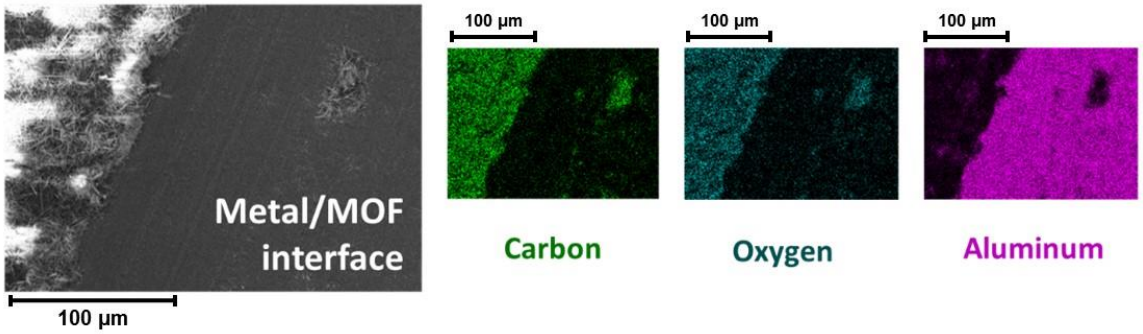

Figure A-50: Surface of aluminum foil-MIL-53(Al) composite. MOF was physically scraped away on right-hand side before imaging. Corresponding EDS mapping exposes location of preserved MOF on left-hand side (carbon & oxygen from linkers), where sub-surface aluminum is confirmed on the right (magnesia).

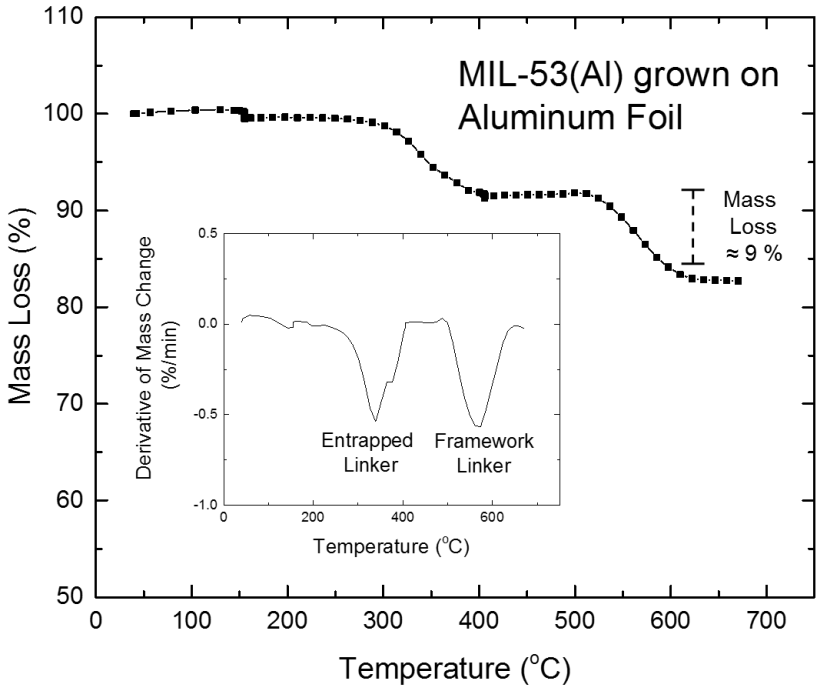

Figure A-51: TGA data for supported MIL-53(Al) grown on aluminum foil. Using helium carrier gas. Inset provides first derivative mass loss data to help differentiate non-coordinated and coordinated linker mass loss.

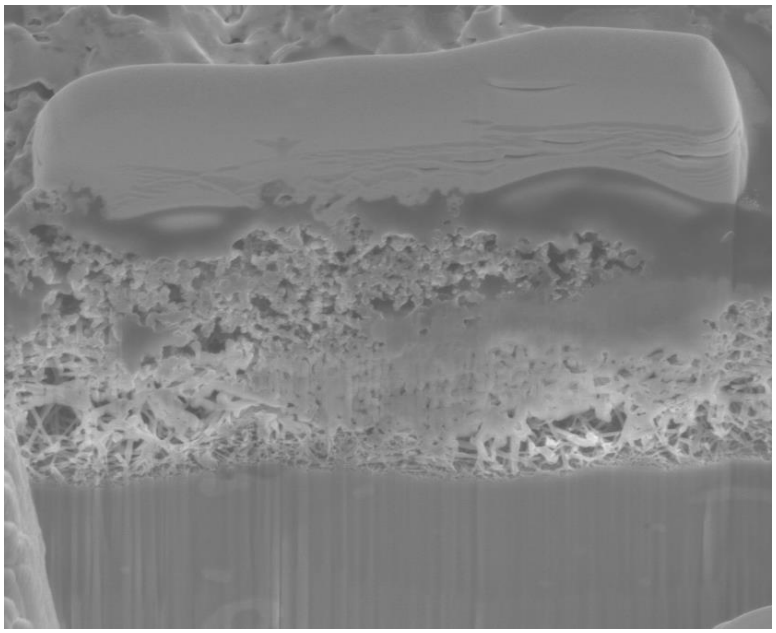

Figure A-52: Zoomed-out FIB-SEM image of supported MIL-53(Al) growth on metallic aluminum (accompanies Figure 5-2d in main text).

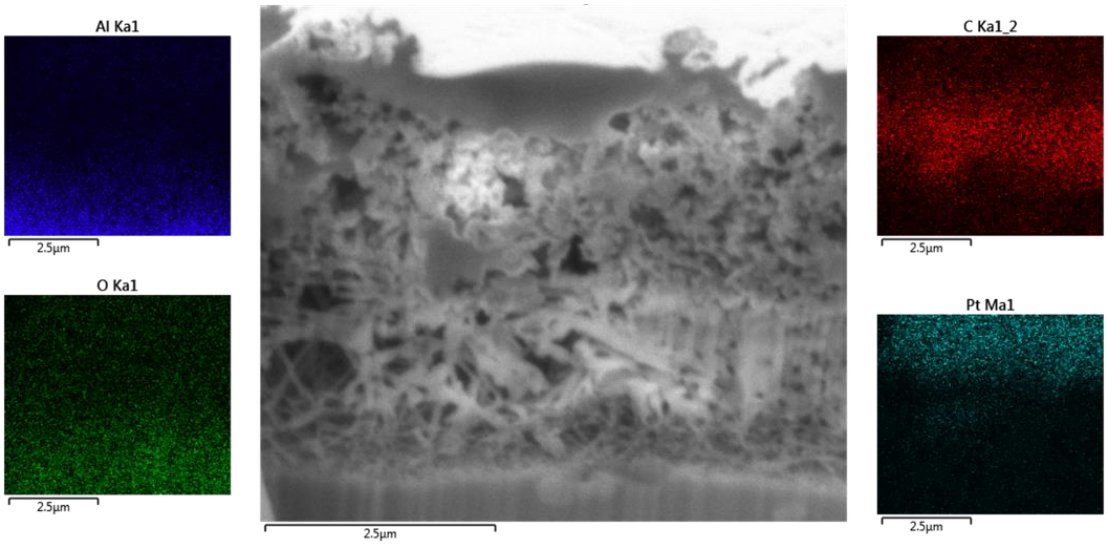

Figure A-53: FIB-SEM/EDS mapping. Middle selection of supported MIL-53(Al) composite on aluminum foil (accompanies Figure 5-2d in main text).

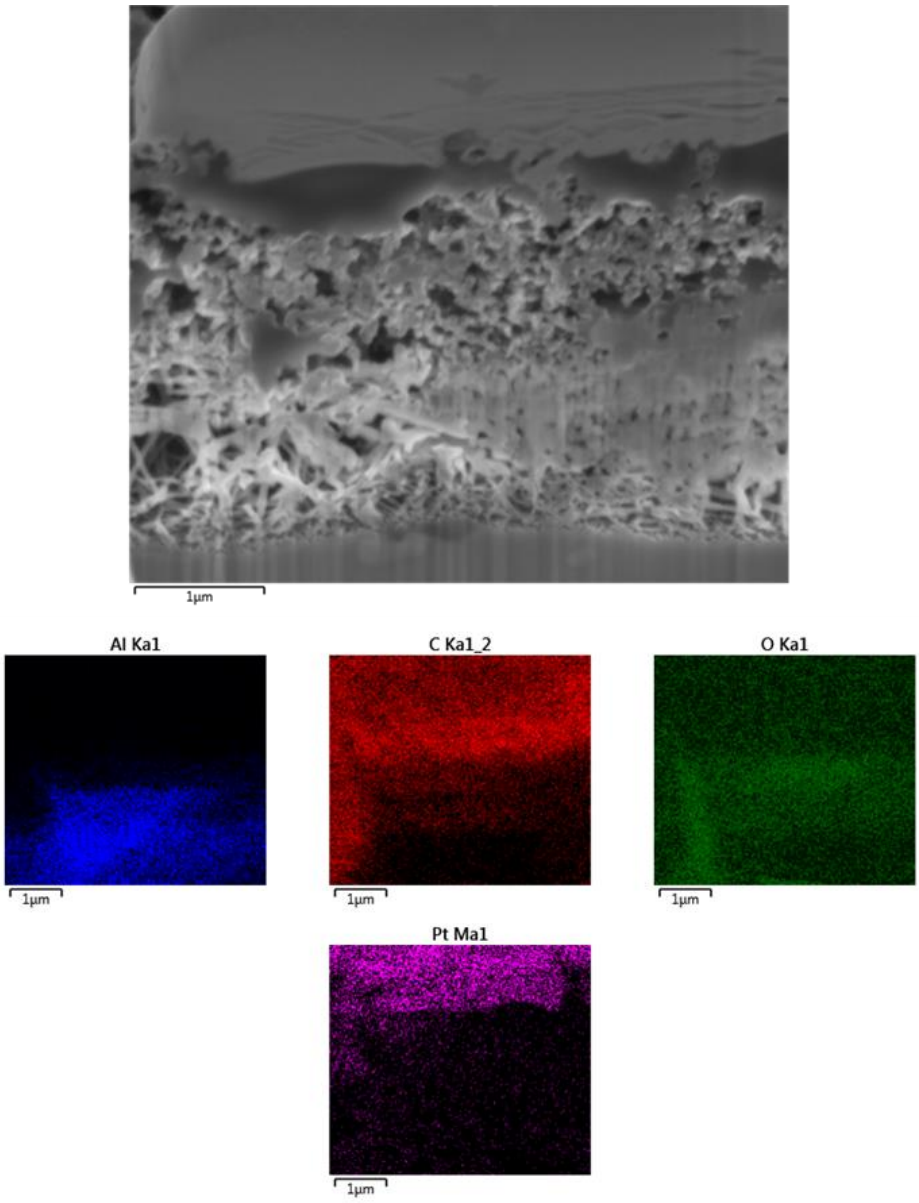

Figure A-54: FIB-SEM/EDS mapping. Top selection of supported MIL-53(Al) composite on aluminum foil (accompanies Figure 5-2d in main text).

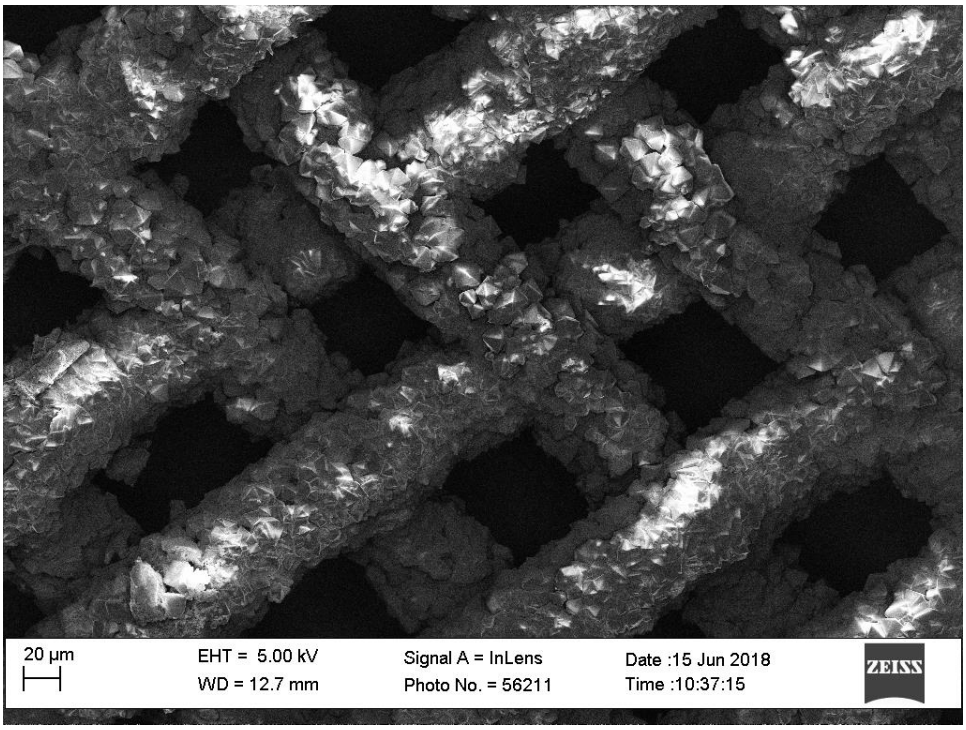

Figure A-55: Electron image of MIL-96(Al) growth on aluminum alloy mesh

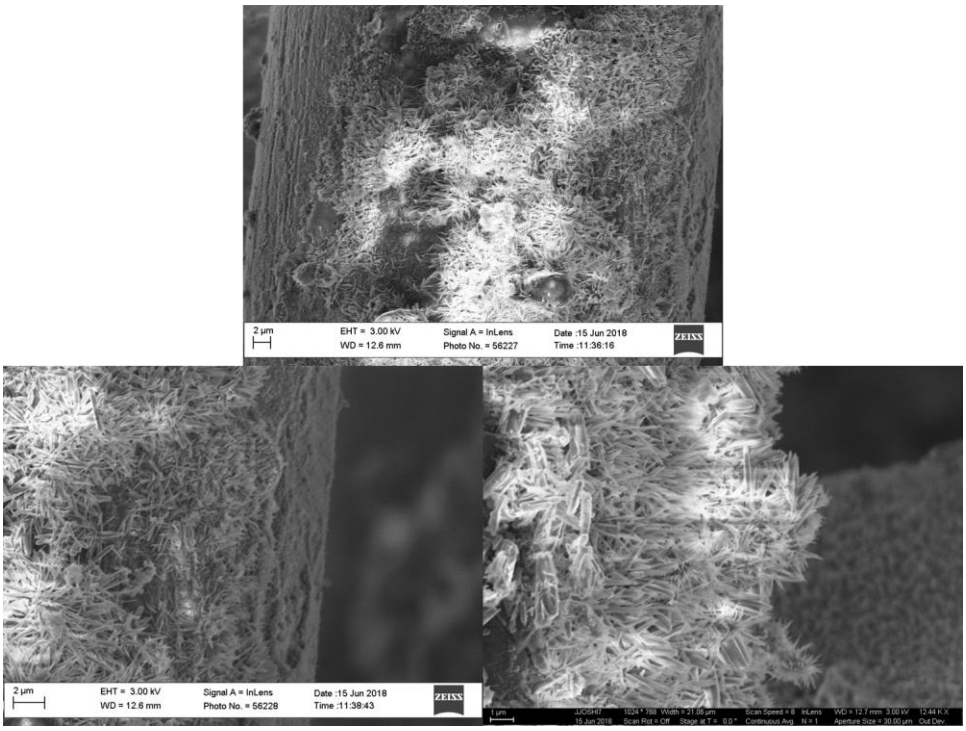

Figure A-56: Imaging of MIL-53-NH_2(Al) growth on aluminum alloy mesh

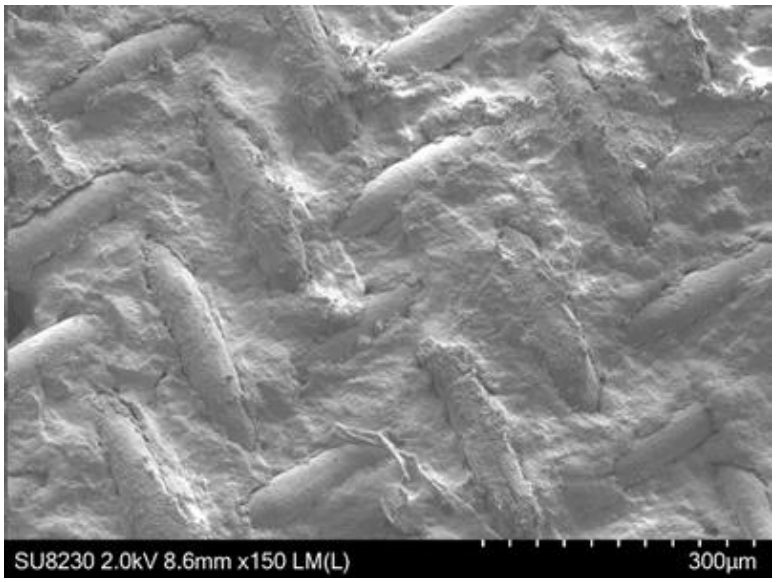

Figure A-57: SEM image of aluminum mesh-MOF composite after secondary growth. Secondary growth achieved by repeating same MOF growth procedures described in Chapter 5 on MOF composite

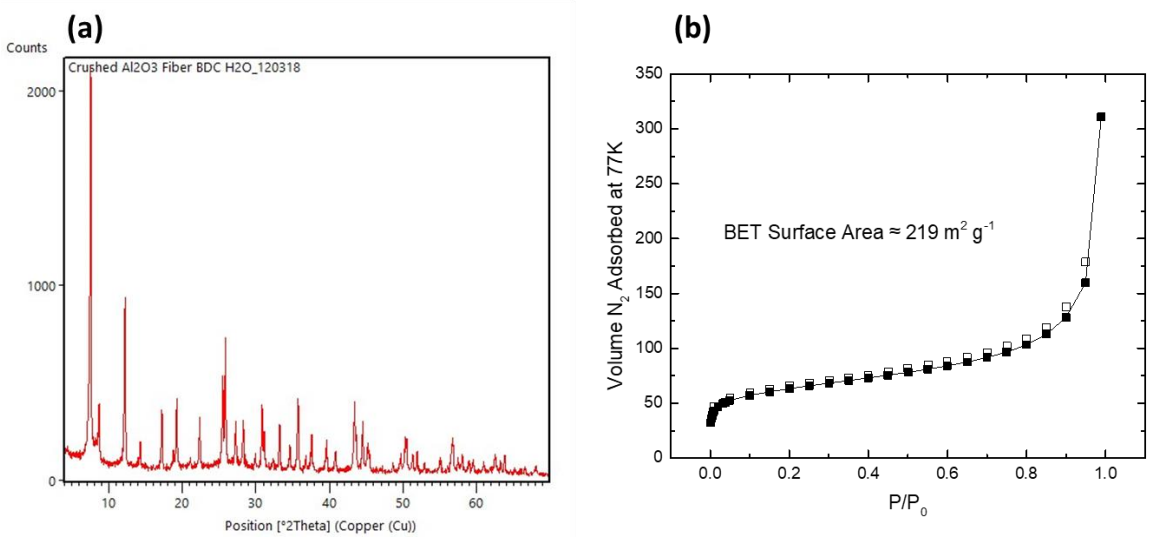

Figure A-58: Materials characterization data on post-MIL-53(Al)/aluminum oxide hollow fiber membrane composite. (a) PXRD acquired after gently crushing sample with mortar and pestle and (b) N_2 measurements on fiber composite at 77K

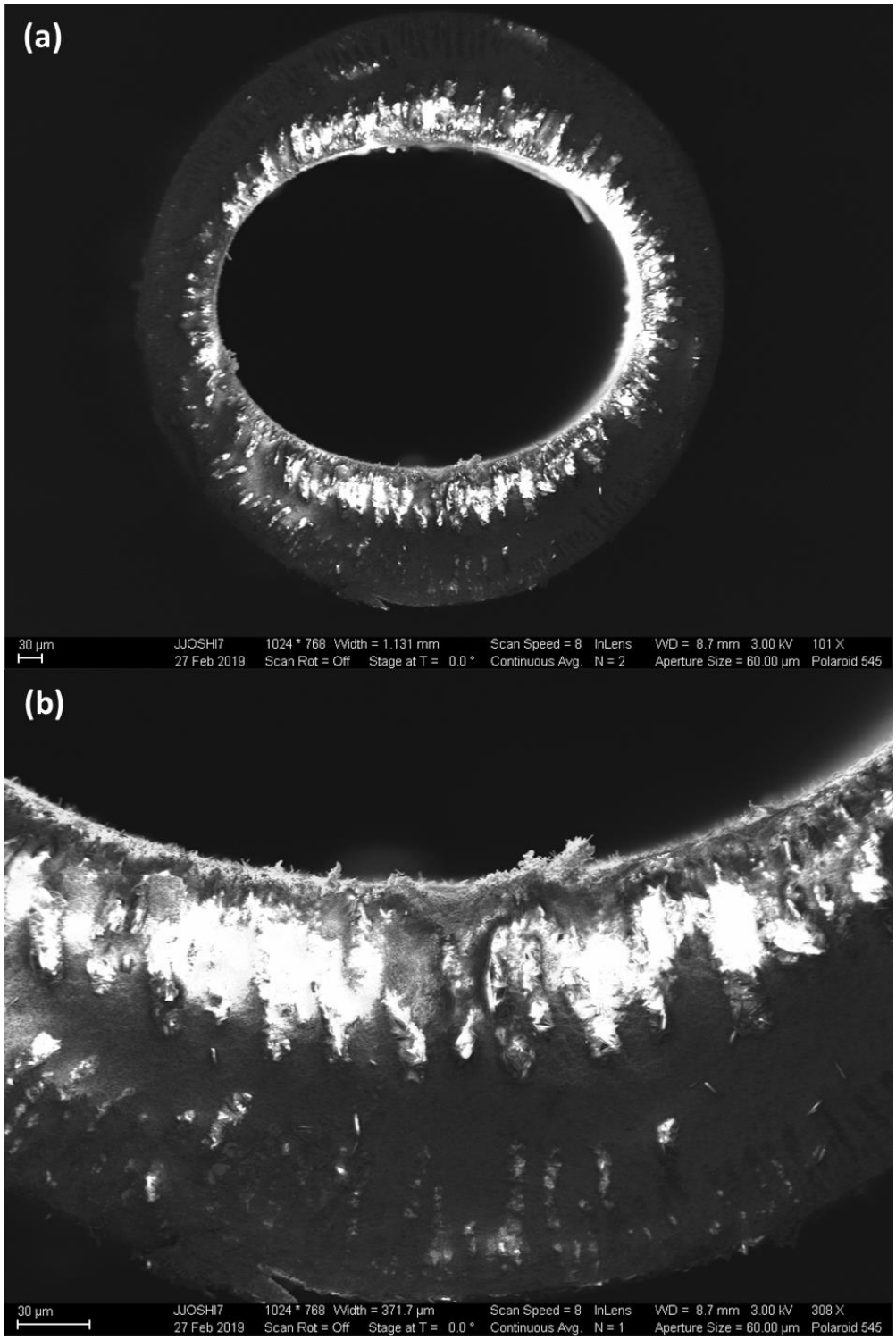

Figure A-59: High contrast electron images of post-reaction MOF/aluminum oxide hollow fiber composite. Localized charge densities (lighter areas) after 1min of electron beam exposure denote MIL-53(Al) distribution in (a) full and (b) magnified top-down fiber images

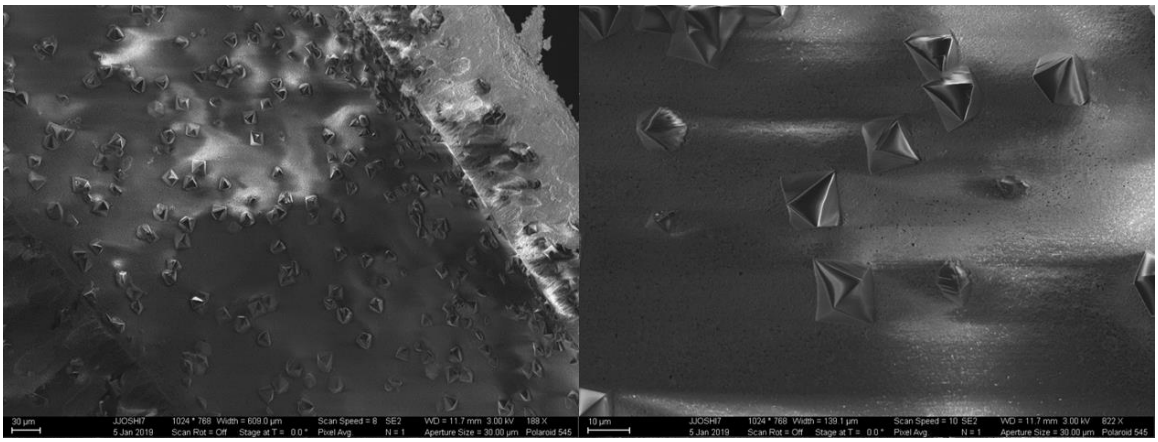

Figure A-60: MIL-96(Al)/aluminum oxide hollow fiber composite (a) full and (b) magnified cross-section

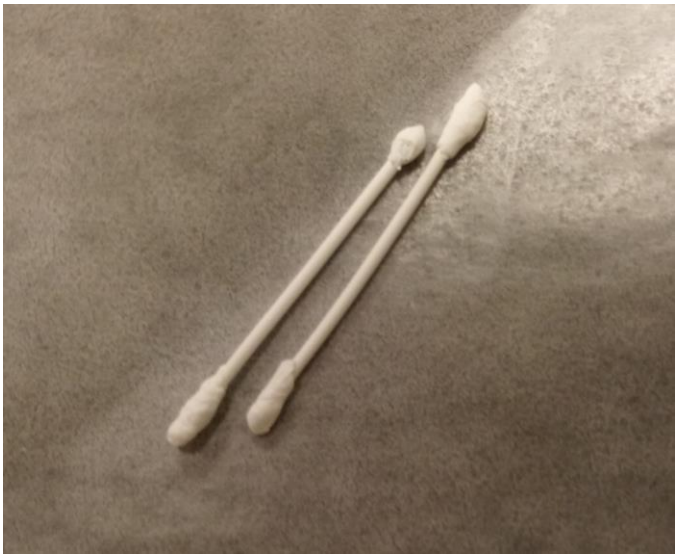

Figure A-61: Image of alumina hollow fibers before reaction. Ends are wrapped with PTFE tape to mitigate ligand transport through fiber bores on either end.

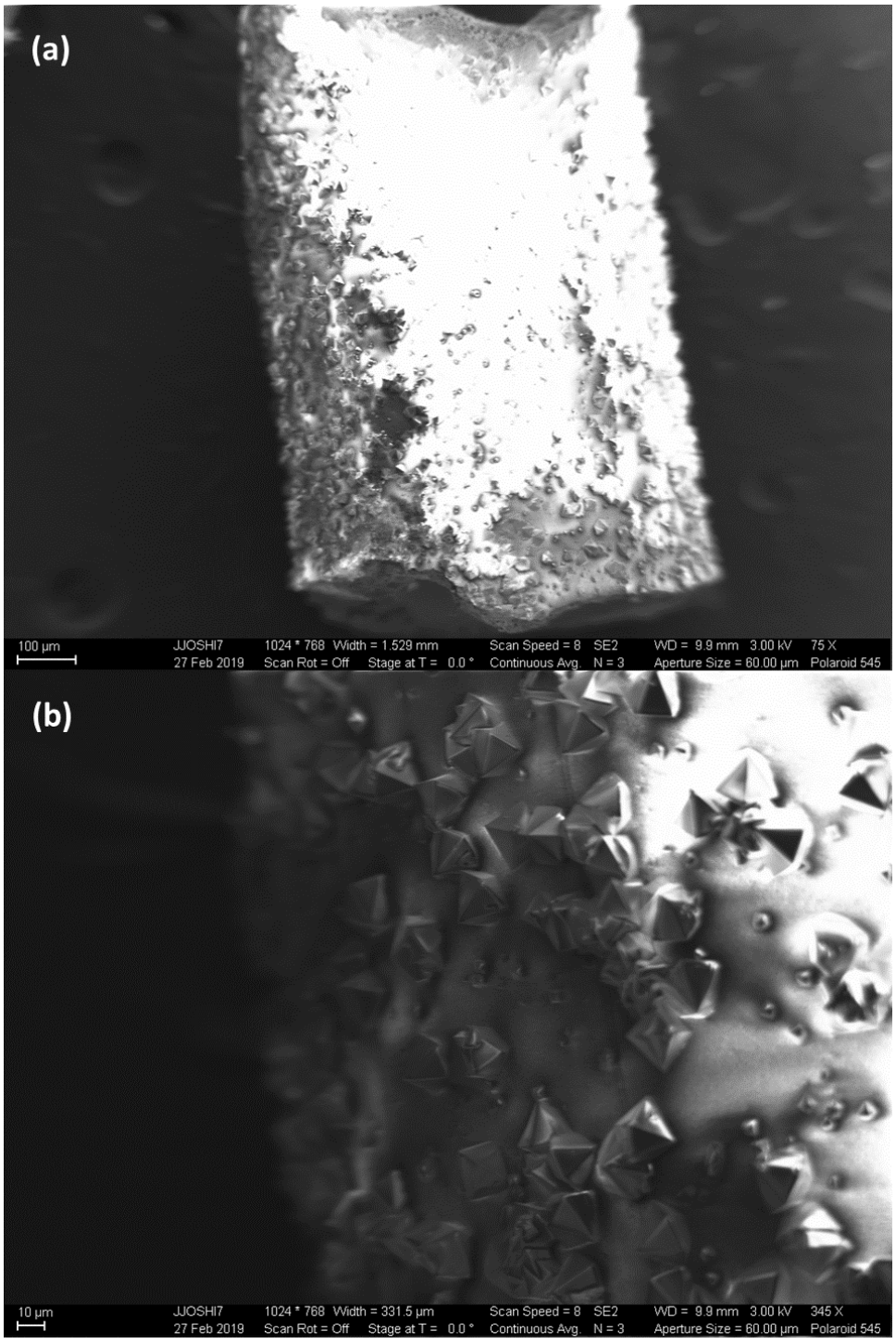

Figure A-62: Electron images of (a) outer fiber surface and (b) zoomed-in fiber surface post-MIL-96(Al) growth

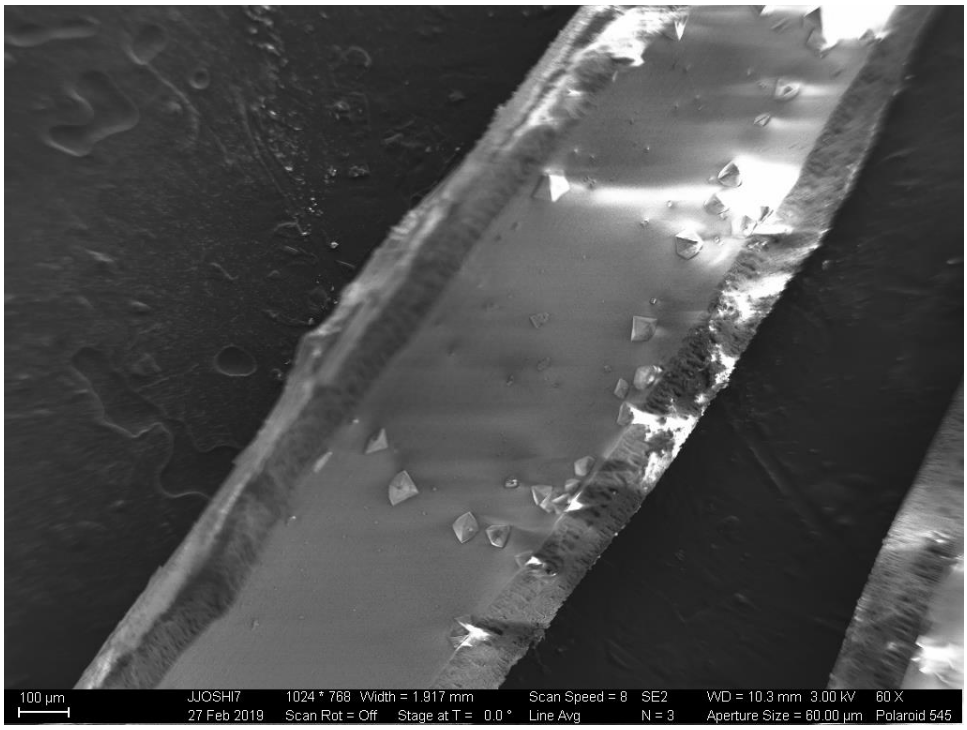

Figure A-63: Cross-sectional SEM image inside bore of alumina hollow fiber-post MIL-96(Al) production.

A.3.2 Supplemental Information for Non-supported Aluminum MOF Growth

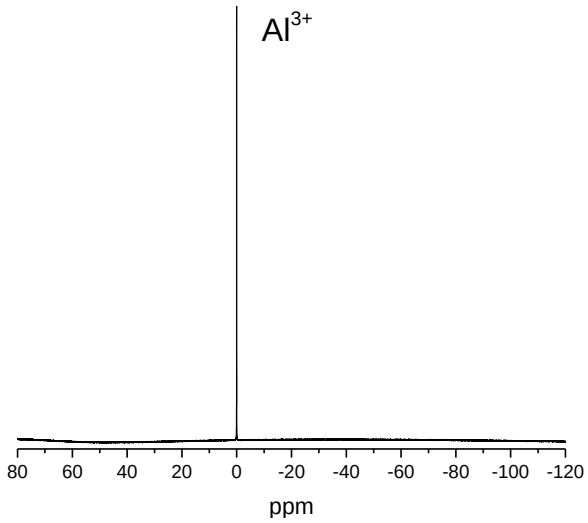

Figure A-64: ^{27}Al solution NMR spectrum of solution supernatant, diluted in D_2O. Supernatant was collected after non-supported MIL-53(Al) synthesis in absence of linker reagent (refer to experimental methods).

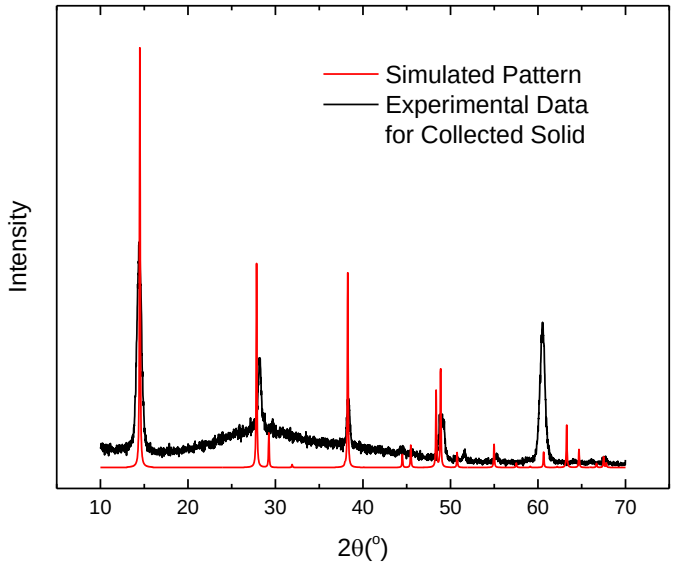

Figure A-65: PXRD data for collected solid precipitate from non-supported MIL-53(Al) synthesis in absence of linker reagent (refer to experimental methods). Simulated crystallographic data for boehmite (AlO(OH)) from Navarrete and coworkers.[10]

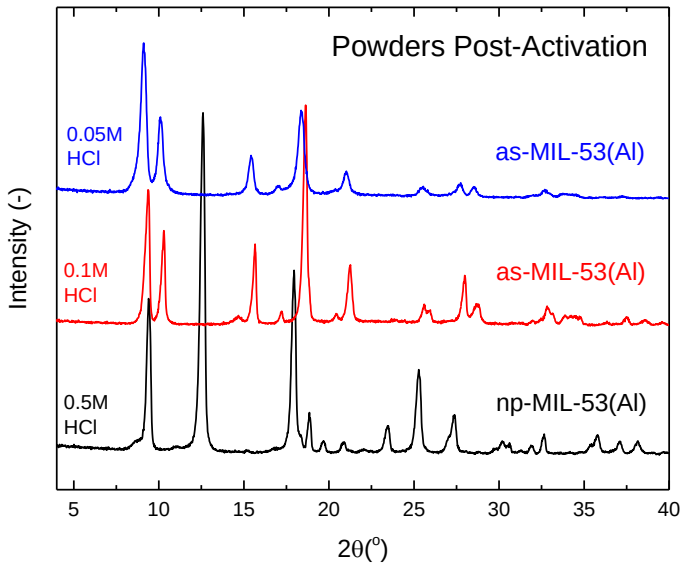

Figure A-66: PXRD data for powders obtained from non-supported MIL-53(Al) reactions utilizing 0.05M (blue), 0.1M (red), and 0.5M (black) HCl(aq). Labels distinguish as-synthesized (*as*-) and narrow pore (*np*-) breathing forms of MIL-

53(Al). Patterns were acquired within 24h of entrapped ligand evacuation and framework desolvation.

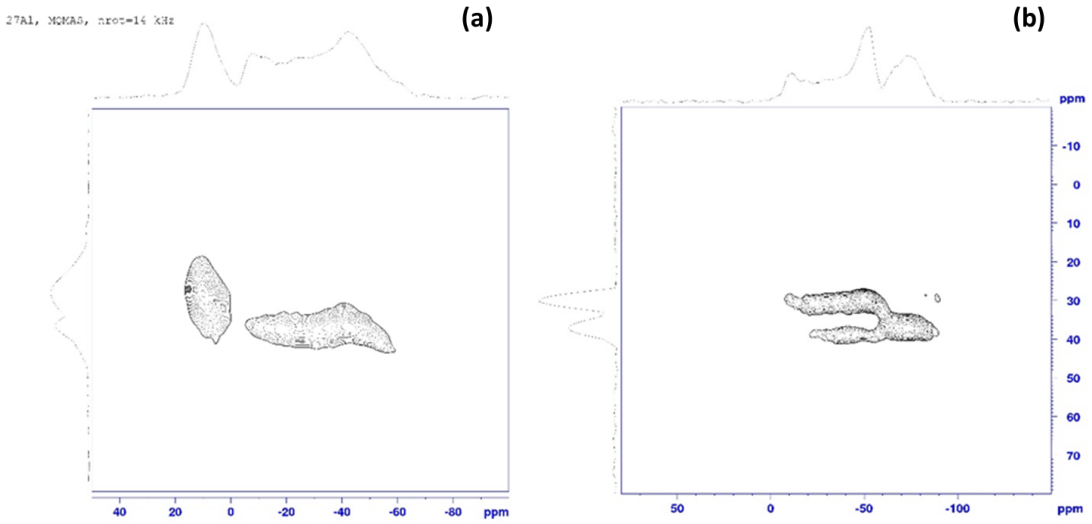

Figure A-67: ^{27}Al SS MQ NMR spectrum for MIL-53(Al) obtained using HCl modulator concentrations of (a) 0.1M and (b) 0.5M

A.3.2.1. Supplemental information for time-trial studies on non-supported MIL-53(Al) production

The synthesis procedure described in "*Synthesis of Non-supported Aluminum-based MOFs from Metallic Aluminum* (p.3) was exacted for 30min, 1h, 2h, and 4h time frames to approximate the required duration to produce MIL-53(Al). Times started when reactant-filled autoclaves were placed inside the preheated (220°C) ovens. Reactors were removed at their respective times, and cooled to ambient temperature in a chemical hood. Finally, samples were gravity filtered and rinsed with DMF (3x) and methanol (3x).

Collected samples at the four tested times are pictured in Figure 3c of the main text. Aluminum foil is visually observable in the 30min and 1h tests. The precursor becomes

absent at 2h, however. This shows that the insoluble precursor is dissolved by the 0.5M HCl(aq) within 2h of reaction in the non-supported MOF procedure described here. Crystalline diffraction patterns of the 2h and 4h solids presented in Figure 3c confirm the formation of MIL-53(Al) in as early as 2h. Additionally, aluminum reflections are not present. Sharpening of diffraction peaks from 2h to 4h reaction products evidences continued crystal growth at longer times, and the likely removal of intermediate and precursor species straining the crystalline lattice.

A.3.2.2. Supplemental information for temperature-trial studies for non-supported MIL-53(Al) production

Room-temperature MIL-53(Al) production was also attempted, however the aluminum foil did not dissolve. This is visually apparent in Figure 5-16.

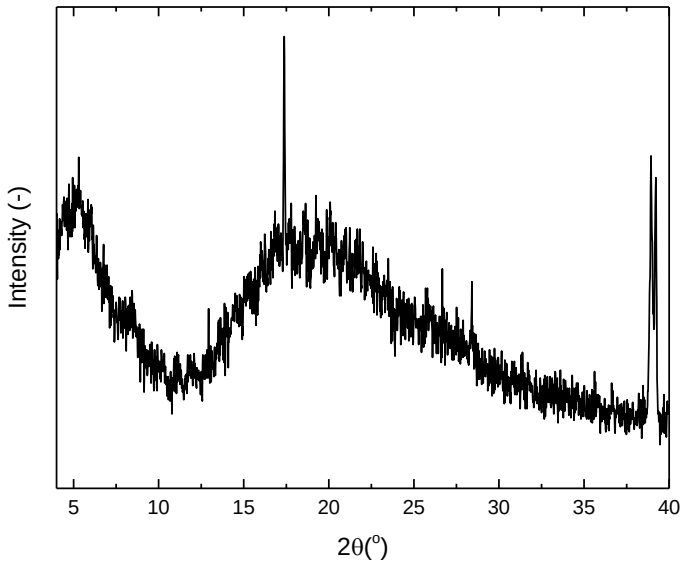

Figure A-68: PXRD measurements for aluminum foil piece after room temperature non-supported MIL-53(Al) reaction using 0.5M HCl for 5 days.

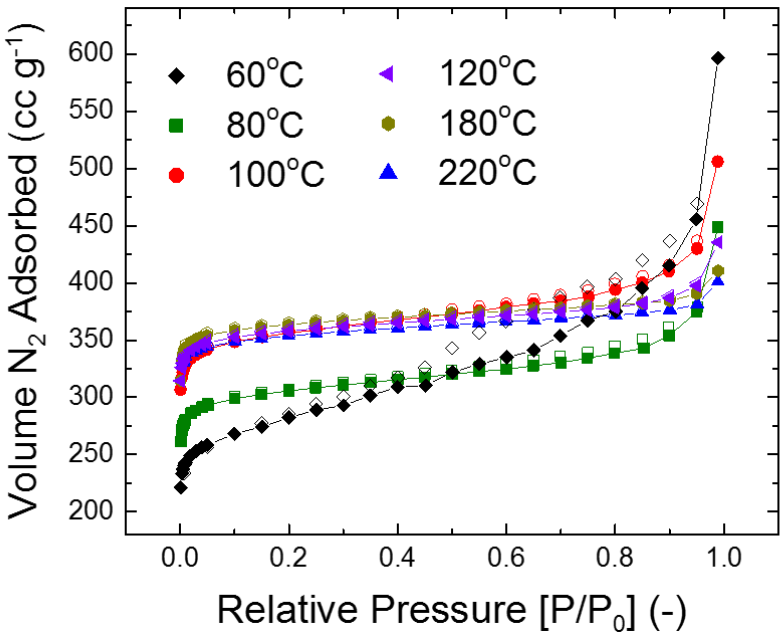

Figure A-69: N_2 physisorption measurements at 77K of non-supported MIL-53(Al) produced from aluminum foil at different temperatures.

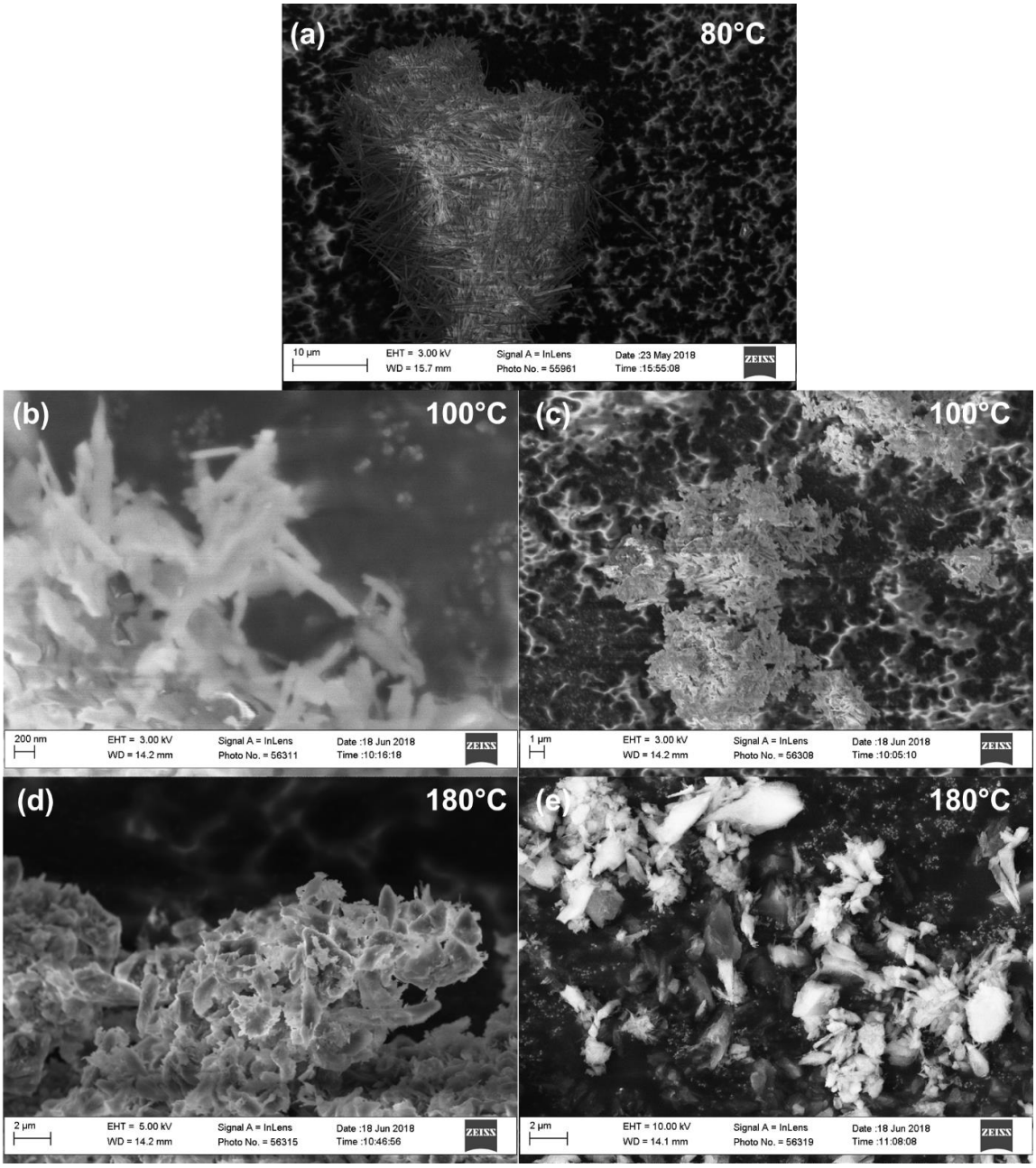

Figure A-70: SEM micrographs of non-supported MIL-53(Al) samples produced at (a) 80°C, (b&c) 100°C, and (d&e) 180°C

Table A-9: Estimated composition of aluminum alloys utilized for MOF growth in Chapter 5. Averages are reproduced from United Aluminum[11,12]

Elements	Alloy Composition(wt%)	
	6061	2024
Cr	0.04-0.35	0.10
Cu	0.15-0.40	3.8-4.9
Fe	0.7	0.50
Mg	0.8-1.2	1.2-1.8
Mn	0.15	0.3A-0.9
Si	0.4A-0.8	0.50
Ti	0.15	0.15
Others-Total	0.15	0.15
Al	Balance	Balance

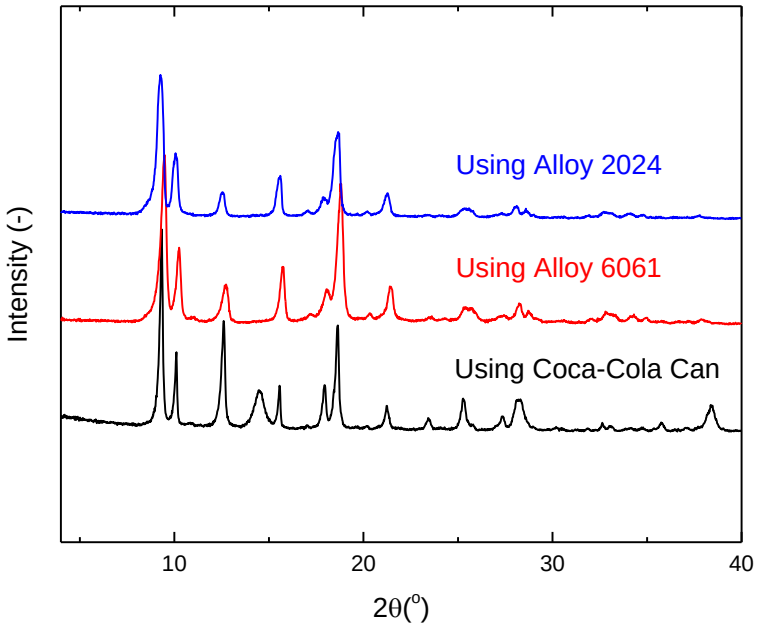

Figure A-71: Powder X-ray diffraction patterns of *as*-MIL-53(Al) produced from Alloy 2024 (top), Alloy 6061 (middle), and a Coca-Cola Can retrieved from a recycling bin (bottom)

A.3.3 Cost Analysis Work

Reagent costs in Table A-10 were acquired by averaging metric-ton scale quantities from commercial sources. Prices were acquired between March-July 2018. A previous economic analysis by Veenestra and coworkers[13] was also referenced for material costs relevant to large-scale MOF manufacturing.

Table A-10: Averaged reagent costs for aluminum MOF production. Yellow highlighted rows denote materials utilized in new MOF synthesis route presented here.

Reactant Material		[a]Averaged Material Cost
[b]**Metal Precursor**	Aluminum Chloride Hexahydrate	$2.91
	Aluminum Nitrate Nonahydrate	$12.08
	Metallic Aluminum	$1.06
[c]**Solvent**	N,N-Dimethylformamide	$1.64
	Water	$0.00045
[c]**Linker**	Terephthalic Acid	$1.04
	Trimesic Acid	$33.67
Reagent Modulator	Hydrochloric Acid, technical grade	$0.50

[a]Prices normalized per kilogram for solid materials and per liter for liquid solutions
[b]Price normalized as $/kg Al
[c]Originally reported by Veenstra and coworkers[13]

Calculations to approximate the **materials cost** of producing 1kg of non-supported MIL-53(Al) are shown below. Importantly, the calculations reference a lab-scale (< 1g) product yield—production amounts may change significantly in larger productions:

Obtained 462.7mg product from 46.4mg aluminum foil

-Assume aluminum foil is pure aluminum

-Assume from TGA measurements in Figure A-72 that **28%** of the product is solvent + entrapped ligand

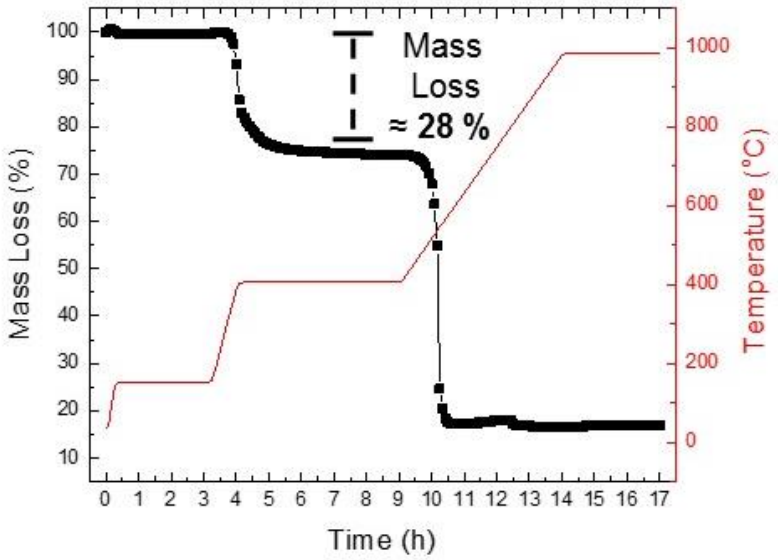

Figure A-72: TGA curve of non-supported MIL-53(Al) produced from aluminum foil (utilizing 0.5M HCl reagent). Measured mass loss of entrapped linker and solvent denoted with text label.

$$462mg\ product\ \times 0.72 = \mathbf{332.64mg\ MOF}$$

Required reagent amounts to make 1kg of MIL-53(Al)

Use 3:1 BDC to Al molar ratio, 92.4mg/mL solution ratio, and 0.5M HCl(aq) from technical grade (33wt%) HCl solution

Metallic aluminum

$$\frac{332.64mg\ MOF}{46.4\ mg\ Al} = \frac{1 \times 10^6 mg\ MOF}{x\ mg\ Al}$$

$$\boldsymbol{x = 0.139 kg\ Al(s)}$$

Terephthalic Acid (BDC)

$$139.4g\ Al\left(\frac{mol\ Al}{26.98g\ Al}\right)\left(\frac{3\ mol\ BDC}{1\ mol\ Al}\right)\left(\frac{166.13g\ BDC}{mol\ BDC}\right) = 2575.1g = \boldsymbol{2.575 kg\ BDC}$$

Water

Assume "non-DI water" may be sourced

$$2575.1g\ BDC\left(\frac{1000mg}{g}\right)\left(\frac{mL\ H_2O}{92.4mg\ BDC}\right)\left(\frac{L\ H_2O}{1000mL}\right) = \boldsymbol{27.9 L\ H_2O}$$

Hydrochloric Acid (HCl)

Use system of equations to determine total solution volume (T) and HCl volume (H), in liters (L)

Assume density of HCl solution is 1.2 g/mL

$$(1)\ H + 27.9L\ H_2O = T$$

$$2)\ H = T\left(\frac{0.5\ mol\ HCl}{L\ solution}\right)\left(\frac{36.46g\ HCl}{mol}\right)\left(\frac{1\ g\ solution}{0.33\ g\ HCl}\right)\left(\frac{mL\ solution}{1.2g}\right)\left(\frac{L\ solution}{1000mL}\right)$$

$$(2)\ H = \boldsymbol{0.046T}$$

Insert (2) into (1)

$$0.046T + 27.9L\ H_2O = T$$

$$T = 29.2L\ solution$$

$$H = \mathbf{1.3}\boldsymbol{L\ HCl(aq), technical\ grade}$$

Costs to produce 1kg of MIL-53(Al)

Using referenced material costs in **Table S1** above

Metallic Aluminum

$$0.139kg\ Al(s)\left(\frac{\$1.06}{kg\ Al(s)}\right) = \$\mathbf{0.15}\ \boldsymbol{for\ Al(s)}$$

Terephthalic Acid

$$2.575kg\ BDC\left(\frac{\$1.04}{kg\ BDC}\right) = \$\mathbf{2.68}\ \boldsymbol{for\ BDC}$$

Water

$$27.9L\ H_2O\left(\frac{1kg\ H_2O}{L}\right)\left(\frac{\$0.00045}{kg\ H_2O}\right) = \$\mathbf{0.01}\ \boldsymbol{for\ H_2O}$$

HCl(aq), technical grade

$$1.3L\ HCl(aq), technical\ grade\left(\frac{\$0.50}{L\ HCl(aq)}\right) = \$\mathbf{0.65}\ \boldsymbol{for\ HCl(aq)}$$

$$Total\ Material\ Cost = \$\mathbf{3.49}$$

A.4 Chapter 6: MOF-Derived Structured Metal Oxide Composites from Insoluble Precursors

Some experimental procedures and data reproduced from Moran et al.[14]

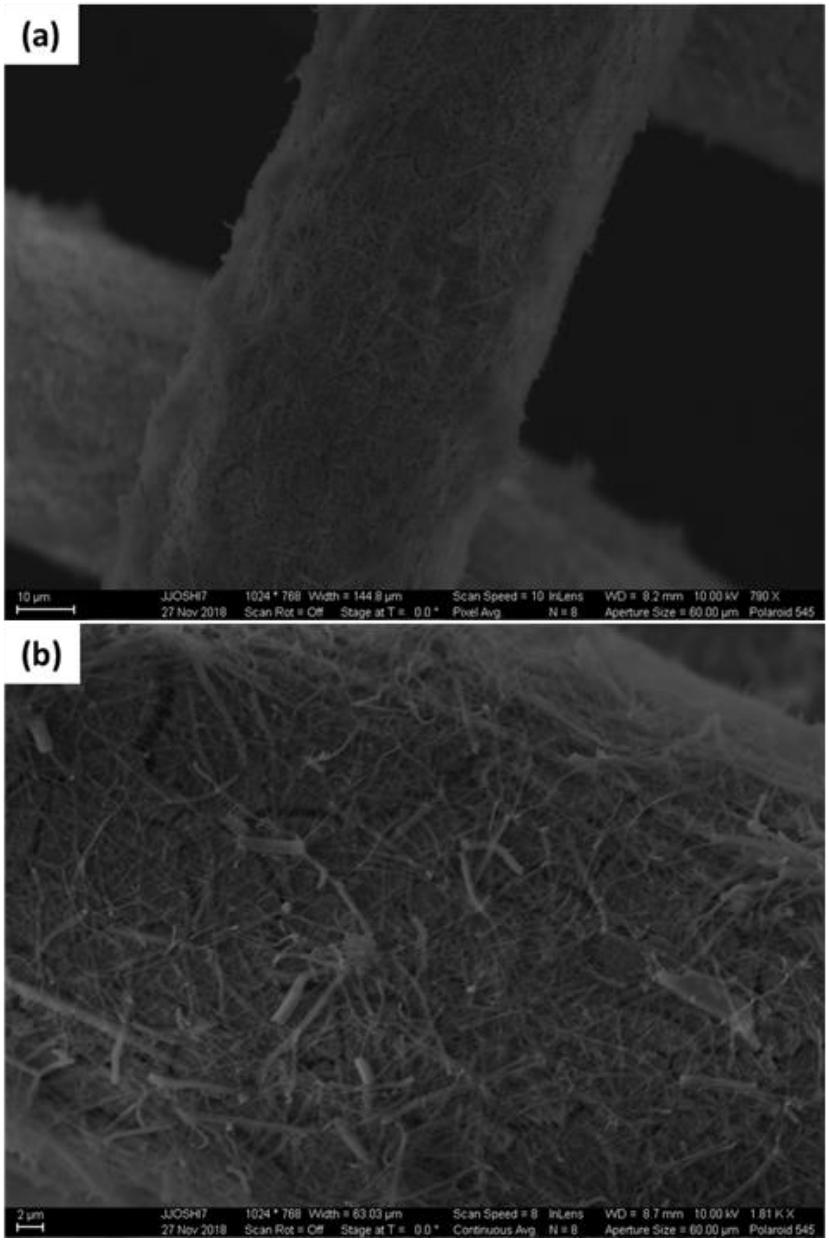

Figure A-73: Pyrolyzed MIL-53(Al) derived from aluminum mesh at (a) 790X and (b) 1810X magnification

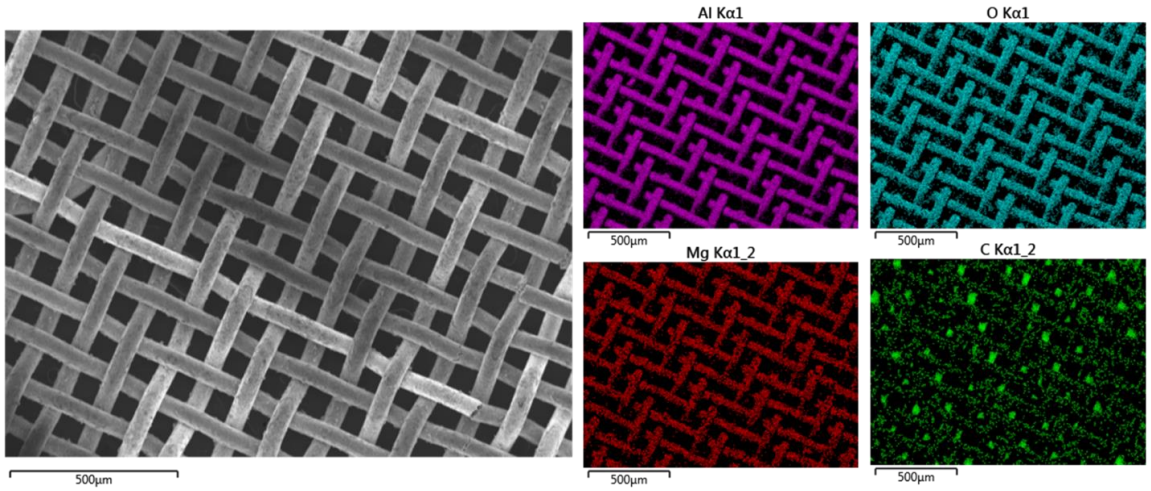

Figure A-74: Elemental mapping of aluminum mesh-derived MIL-53(Al) after pyrolysis. C Kα data confirm residual carbon from pyrolyzed linker remains on surface. Magnesium detection results from presence of the element in the original alloy.

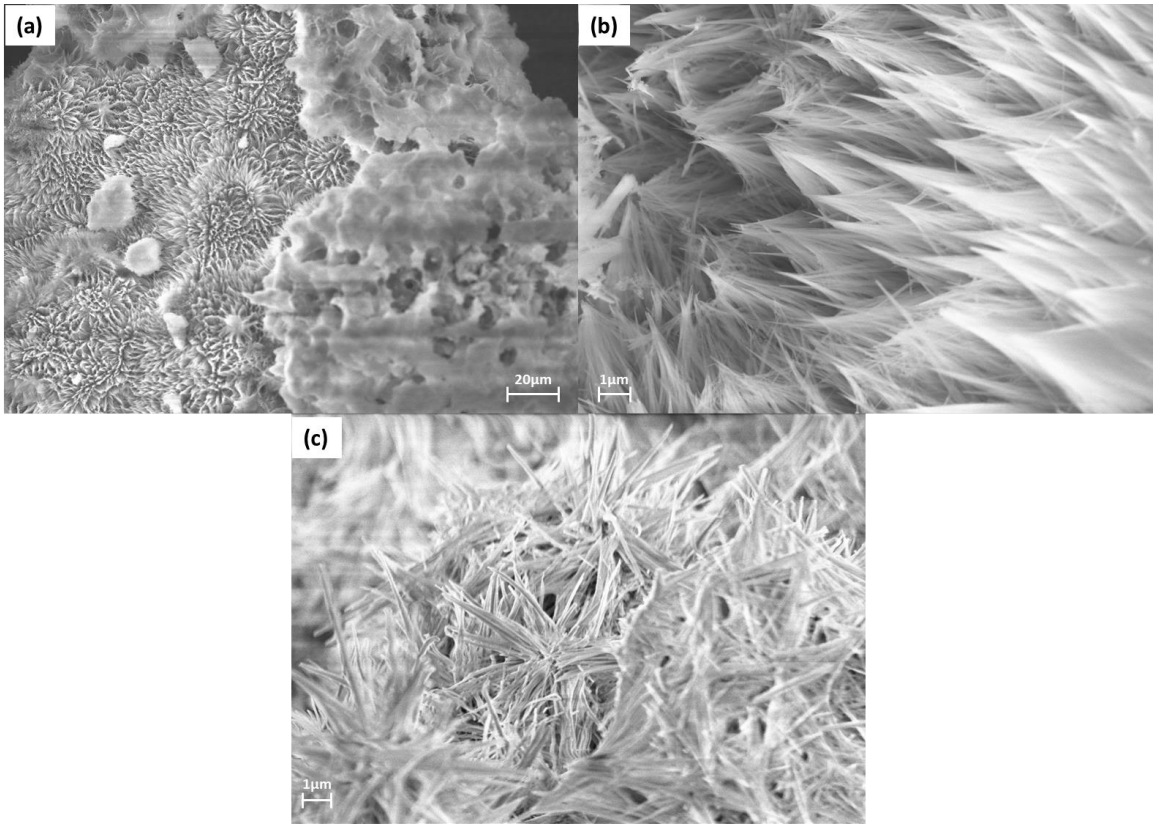

Figure A-75: Images of regrown MIL-53(Al) from MIL-53(Al)-oxide in (a-b) one and (c) two growth cycles

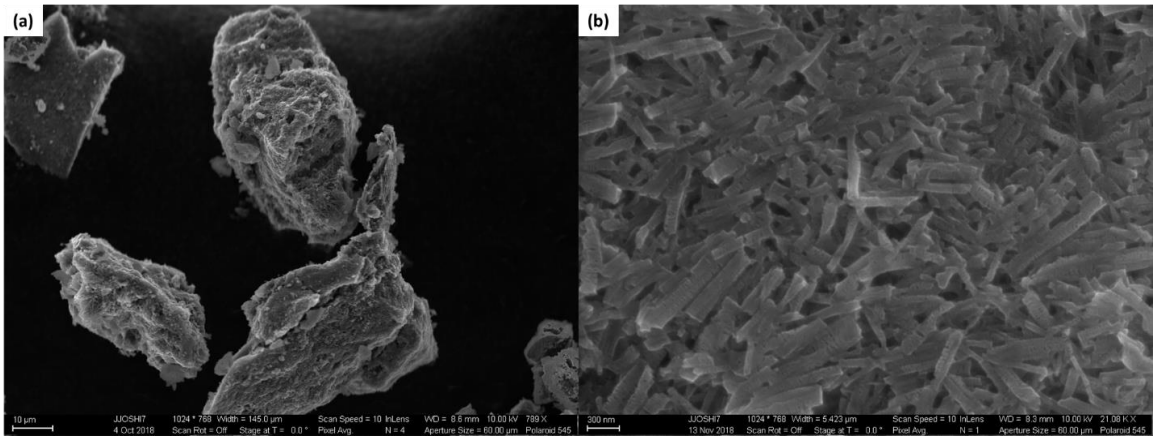

Figure A-76: SEM images of MIL-53(Al)-derived oxide impregnated with iron oxide

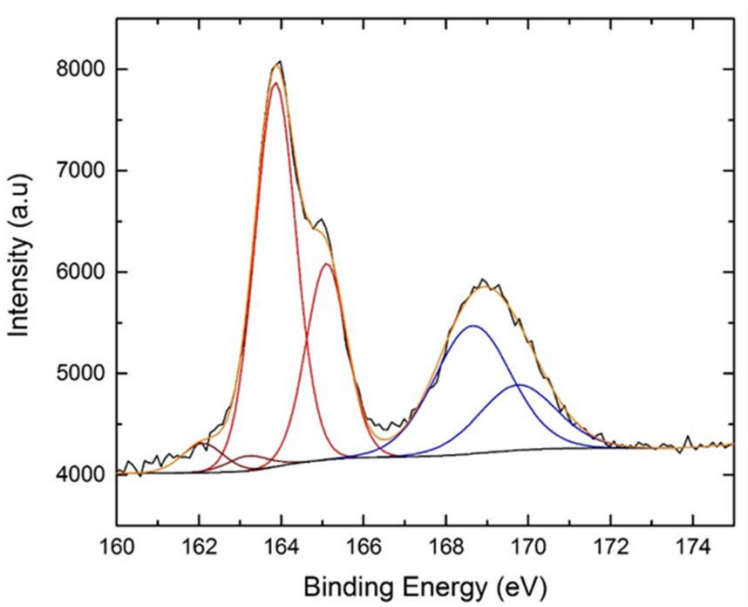

Figure A-77: Fitted S2p XPS data of iron oxide-impregnated MIL-53(Al)-oxide, following humid 0.5% H_2S exposure. Fitted sulfur species are color-coded: red—elemental sulfur and sulfide species, blue—metal sulfates

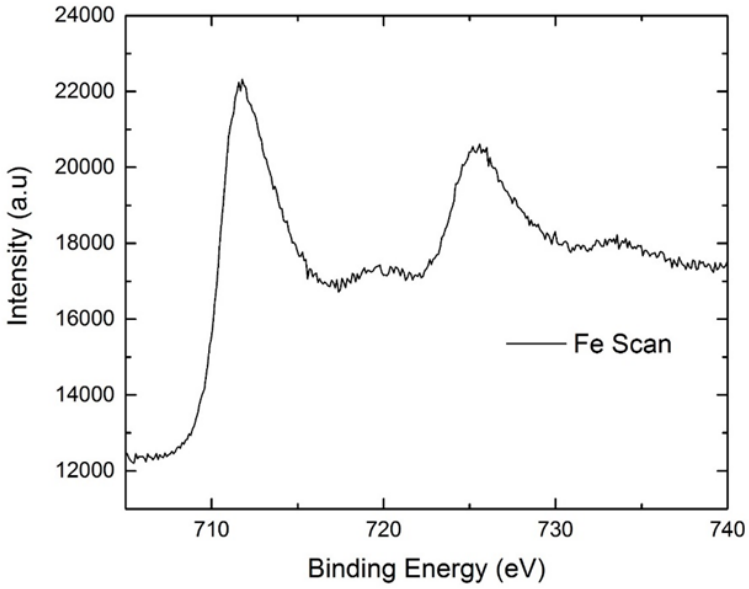

Figure A-78: Fe 2p XPS spectrum of iron oxide-impregnated MIL-53(Al)-oxide, following humid 0.5% H_2S exposure

A.5 Appendix A References

1. Joshi, J. N., Garcia-Gutierrez, E. Y., Moran, C. M., Deneff, J. I. & Walton, K. S. Engineering Copper Carboxylate Functionalities on Water Stable Metal-Organic Frameworks for Enhancement of Ammonia Removal Capacities. *J. Phys. Chem. C* **121**, 3310–3319 (2017).

2. Cavka, J. H. *et al.* A new zirconium inorganic building brick forming metal organic frameworks with exceptional stability. *J. Am. Chem. Soc.* **130**, 13850–13851 (2008).

3. Joshi, J. N. *et al.* Probing Metal–Organic Framework Design for Adsorptive Natural Gas Purification. *Langmuir* **34**, 8443–8450 (2018).

4. Jiao, Y. *et al.* Heat-Treatment of Defective UiO-66 from Modulated Synthesis: Adsorption and Stability Studies. *J. Phys. Chem. C* **121**, 23471–23479 (2017).

5. *GC Sulfursorb Plus*. General Carbon Corp: Patterson, NJ

6. Sethupathi, S. *et al.* Biochars as potential adsorbers of CH_4, CO_2 and H_2S. *Sustainability* **9**, 121 (2017).

7. Bhatt, P. M. *et al.* Isoreticular rare earth fcu-MOFs for the selective removal of H_2S

from CO_2 containing gases. *Chem. Eng. J.* **324**, 392–396 (2017).

8. Wenguo Feng, Seokjoon Kwon, Eric Borguet, and & Radisav Vidic. Adsorption of Hydrogen Sulfide onto Activated Carbon Fibers: Effect of Pore Structure and Surface Chemistry. *Environ. Sci. Technol.* **39**, 9744–9749 (2005).

9. Rezaei, F., Rownaghi, A. A., Monjezi, S., Lively, R. P. & Jones, C. W. SO_x /NO_x Removal from Flue Gas Streams by Solid Adsorbents: A Review of Current Challenges and Future Directions. *Energy & Fuels* **29**, 5467–5486 (2015).

10. Bokhimi, X. *et al.* Dependence of Boehmite Thermal Evolution on Its Atom Bond Lengths and Crystallite Size. *J. Solid State Chem.* **161**, 319–326 (2001).

11. Aluminum Alloy 6061 - Information and Specifications. *United Aluminum Corporation* (2015). Available at: https://www.unitedaluminum.com/united-aluminum-alloy-6061/. (Accessed: 13th April 2019)

12. Aluminum Alloy 2024. *United Aluminum Corporation* (2015). Available at: https://www.unitedaluminum.com/united-aluminum-alloy-2024/. (Accessed: 13th April 2019)

13. DeSantis, D. *et al.* Techno-economic Analysis of Metal−Organic Frameworks for Hydrogen and Natural Gas Storage. *Energy & Fuels* **31**, 2024–2032 (2017).

14. Moran, C. M., Joshi, J. N., Marti, R. M., Hayes, S. E. & Walton, K. S. Structured Growth of Metal–Organic Framework MIL-53(Al) from Solid Aluminum Carbide Precursor. J. Am. Chem. Soc. 140, 9148–9153 (2018).

APPENDIX B. DEVELOPMENT OF IRON OXIDE-MOF COMPOSITE FOR HYDROGEN SULFIDE DEGRADATION

B.1 Motivation

B.1.1. Iron Oxide-based Hydrogen Sulfide Scavengers

Hydrogen sulfide may be oxidized through routes other than gas flaring or the Claus process. Ferric oxides, commonly called iron sponge, have been historically used for H_2S degradation.[1] H_2S is reported to react with iron (III) oxides according to Equation B.1, where iron sulfide is evolved, and water is released.[2] The regeneration of iron sponge is also shown, where iron sulfide oxidizes under air flow and produces elemental sulfur (Equation B.2). The reaction occurs at ambient conditions.[2] Sulfur caking on the metal oxide unfortunately hinders reactivity of reused material.[1] Also, reaction site accessibility on iron sponge is a major limitation, where the low porosity limits the availability of bulk iron oxide species for hydrogen sulfide to react with. Utilizing nanoscale materials is a well known method for markedly increasing the surface area to volume ratio of particles, and may address this problem. Additionally, Bandosz[3] reports mechanistic observations for H_2S oxidation in reactive carbon materials (e.g. Midas® carbon), where generated elemental sulfur migrates from reaction sites to nearby pores until saturation. This phenomenon renews access to oxidation sites. Sulfur migration is not beneficial in iron sponge since it can only migrate to another oxide surface. In this way, utilizing reactive materials in composites are desired to mitigate the immediate capping of surface sites that would occur when using only bulk reactive media. Incorporating iron oxide nanoparticles

in adsorbent supports is subsequently a promising strategy to pursue in sour gas refinement. Hu and coworkers[4] showed this by doping carbon nanofilament supports with various amounts of iron oxide nanoparticles. Hydrogen sulfide breakthrough experiments revealed some composites greatly exceeded the 0.15 g/g H_2S capacity of the commercial standard adsorbent Sulfatreat. Manipulation of nanoparticle loading in the materials was also observed to dictate the breakthrough capacity of the composite.

$$Fe_2O_3 + 3H_2S \rightarrow Fe_2S_3 + 3H_2O \quad \text{(B.1)}$$

$$2Fe_2S_3 + 3O_2 \rightarrow 2Fe_2O_3 + 6S \quad \text{(B.2)}$$

Iron sponge contains iron (III) oxides: hematite (α-Fe_2O_3), maghemite (γ-Fe_2O_3), and magnetite (Fe_3O_4), although magnetite gradually converts to maghemite through contact with oxygen. Hematite is typically considered for reactive H_2S conversion in the literature.[5,6] But, Chen and coworkers[7] observed maghemite sulfur capacities through reaction with H_2S to be ~1-2% higher than hematite particles at room temperature, indicating more of the gas reacted with maghemite. It should be noted that hematite grain sizes in the study were ~5x larger than maghemite nanoparticles used, lending to lower accessibility of surface sites per mass for hematite particles. This likely explains the small reported difference in capacities. Nevertheless, because it is unclear which oxide may be more reactive with H_2S, both maghemite and hematite nanoparticles will be used in this study to make encapsulated MOF composites.

B.1.2. Impregnation/Encapsulation of Adsorption Sites

Membrane and zeolite materials have been doped with various metals to enhance the chemical affinities of the substrates towards target adsorbate species.[8,9,10,11] This methodology has been extended to the incorporation of metal guest species into MOFs.[12] An obvious advantage to using MOFs as supports is that the MOF itself can interact with adsorbate species via functional groups, defect sites, etc., to generate possibly cooperative adsorption interactions with incorporated guests as part of composite. Metal incorporation into MOFs is typically achieved through either impregnation or encapsulation. The cartoon in Figure B-1 depicts their formative and structural differences. Impregnation describes the creation of nanoparticles within the pores of the framework. This is usually carried out through wet impregnation, which entails dissolving a metal precursor in solution with the MOF such that the metal ions penetrate the pore space. Metal salts can then be decomposed through heating to produce oxide particles.[13] This been done in MIL-125-NH_2 using cobalt, which induced photocatalytic hydrogen production properties in the framework.[14] Encapsulation involves growing MOF around pre-made nanoparticles. Huo and coworkers[15] reported MOF encapsulation techniques for a myriad of metal nanoparticles using ZIF-8. TEM images in the study reveal the particles to be encapsulated by ZIF-8 crystals. This imparted molecular sieving behavior, as only species that pass through the pores could interact with the metal nanoparticles. Previous use of MIL-125-NH_2 for metal incorporation, electrostatic anchoring effects between amine functionalities and metal nanoparticles[11], and purported framework stability in the presence of H_2S and other acid gases, makes this MOF an appropriate candidate for iron oxide nanoparticle incorporation.[16]

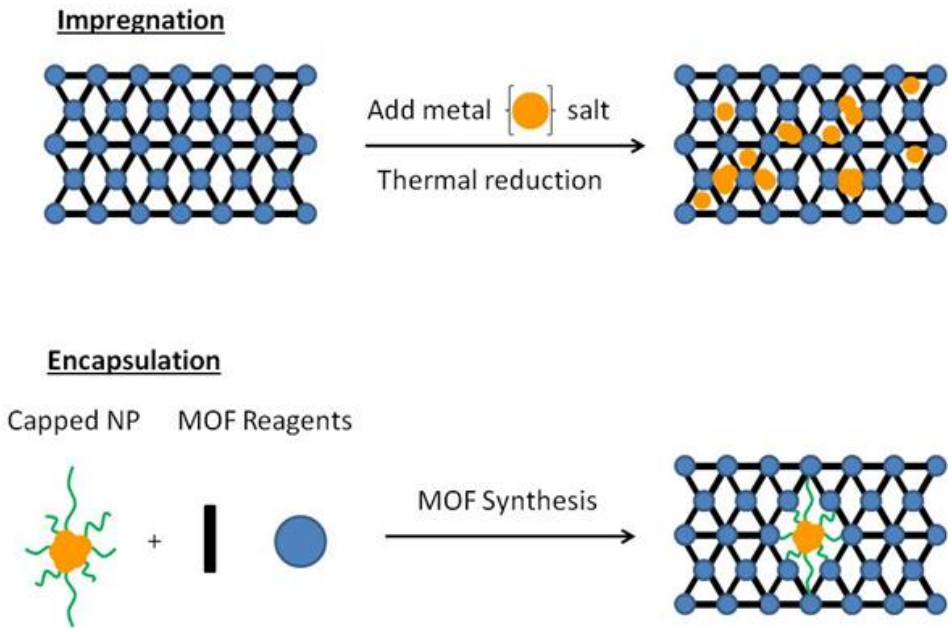

Figure B-1: Comparison of impregnation and encapsulation in a model framework. Blue spheres-framework metal centers, black lines-organic framework ligands, gold spheres-metal nanoparticles, green lines-nanoparticle surfactant (encapsulation only)

Both strategies offer different attributes in resultant MOF composites. Impregnation affords some control over metal loading, and allows for inclusion of guest species after MOF synthesis reactions, which may contain harsh reagents or reaction conditions (i.e. low pH) that decompose or chemically alter impregnates. But, the inherent lack of control over the mass transfer of metal guests in impregnation can lead to poor distribution within the framework pores and surface, as well as particle agglomeration.[12] Also, the small pores and cages (~1nm) will likely hinder access to impregnates in the pore space. Alternatively, encapsulation offers size control, minimizes cage accessibility issues, and avoids agglomeration by surrounding a few particles with MOF crystals. There may be complications though if the nanoparticles are affected by MOF synthesis conditions. An example of this was encountered by Tulig and Walton[17], where HCl formation in the synthesis of UiO-66 prevented the encapsulation of gold nanoparticles, mandating use of

an alternative synthesis route. Consequently, it is necessary to study the effects of both methods on nanoparticle loading and hydrogen sulfide removal. Especially for impregnation, greater framework accessibility makes choosing larger pore MOFs typically more appropriate over the microporous MIL-125-NH_2(Ti). However, these MOFs often suffer from chemical instability, and some have already been found to degrade in the presence of H_2S.[18] This behavior comes from the low connectivity and/or complex linkers usually necessary to produce such frameworks. Exotic linkers in some large pore MOFs also makes them more expensive alternatives to ones utilizing BDC ligands. So, the stable MIL-125-NH_2 is a more reasonable choice, where pore blocking effects will be managed by controlling metal loading in impregnation experiments.

B.2 Synthesis Methods

B.2.1. MOF Composite Syntheses

B.2.1.1. MIL-125-NH_2(Ti)

A 1:2 metal precursor to organic linker molar ratio was used: 150 µL of titanium (IV) isopropoxide (0.5 mmol) and 180 mg of 2-aminoterephthalic acid (BDC-NH_2) (1 mmol) were transferred to a 20 mL scintillation vial containing equal volumetric portions of N,N-dimethylformamide (DMF) and methanol (4.15 mL). The reaction vessel was heated in an oil bath at 120°C for 24 hours. The product was then filtered and rinsed three times each with DMF, followed by methanol. Sample activation was carried out under vacuum for 24 h at 110°C.

B.2.1.2. Hematite Nanoparticles

A tunable synthesis pathway to create hematite nanoparticles (NPs) has been outlined by Zhu et al.[19] 2 mmol iron chloride hexahydrate ($FeCl_3x6H_2O$), 40 mmol sodium acetate, and 1.0 g poly(vinylpyrrolidone) (PVP, avg. molecular weight = 40,000) were dissolved in 30 mL of deionized (DI) water and stirred at 40°C for 2 h. The mixture was then transferred to a Teflon-lined stainless-steel reactor vessel, and heated at 200°C for 18 h. After heating, the reactor was cooled to room temperature. Products were collected via centrifugation three times each with DI water and ethanol. Finally, powders were dried for 12 h at 70°C, under vacuum.

B.2.1.3. Nanoparticle Encapsulation: Fe_2O_3@MIL-125-NH_2(Ti)

After nanoparticle and MOF collection, the following synthesis procedure extended from *Nature* 2016, 539, 76-80 was performed to encapsulate iron oxide NPs on the outside of MIL-125-NH_2(Ti) crystals.[20] To achieved a ratio of 4mg MOF per mL solvent, 40mg of degassed MIL-125-NH_2(Ti) were added to 10mL of ethanol in Solution 1. Separately, 5.75mg of hematite NPs were dispersed in 6mL of ethanol in Solution 2. Both solutions 1 and 2were mixed briefly together. The solution was then kept at ambient conditions for 24 h, without agitation. Products were centrifuged twice in 15mL of ethanol for 10min each. Finally, composites were activated under vacuum at 110°C. The preparation and resulting composite are delineated in Figure B-2.

To enhance NP density and optimize distribution, the mixing process between Solutions 1 and 2 mentioned above were modified. Solution 1 was set under vigorous mixing using a magnetic stir bar. Then, Solution 2 was added carefully to Solution 1

dropwise. The addition process took roughly 30min. After additions were completed, mixture agitation continued for 3h at room temperature. Precipitate separation was performed the same as listed above.

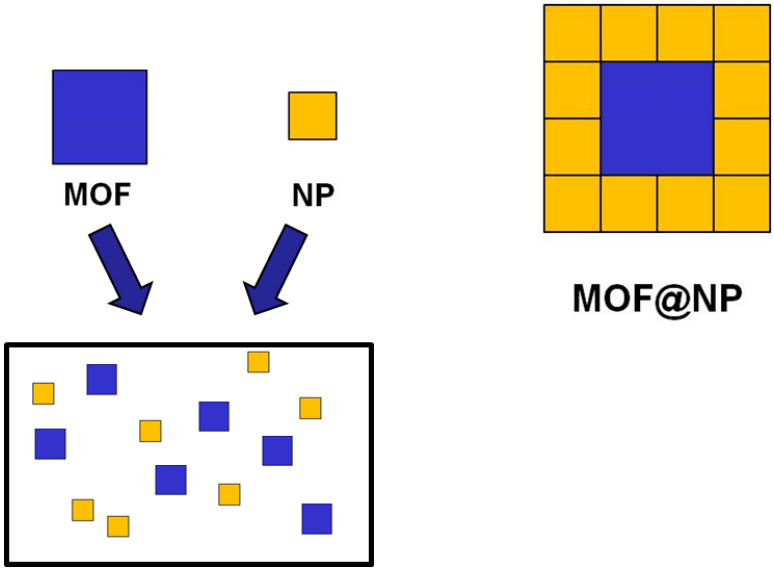

Figure B-2: Cartoon describing nanoparticles (NP) mixing with MOFs to create MOF@NP

B.2.1.4 Sandwich MOF: MIL-125-NH_2(Ti)@Fe_2O_3@MIL-125-NH_2(Ti)

MOF growth was attempted around iron oxide/MOF composites created in B.2.1.3. Nanoparticle Encapsulation: Fe_2O_3@MIL-125-NH_2(Ti), and is also based on Zhao et al.[20] Retrieved Fe_2O_3@MIL-125-NH_2(Ti) (roughly 40mg product) were dispersed in 6mL of DMF inside a 60mL glass scintillation vial. A separate MOF precursor solution was then also created by mixing 90mg of BDC-NH_2 to 7.5mL each of DMF and methanol. Finally, 75µL of titanium isopropoxide was micropipetted into the MOF precursor solution, and quickly stirred with a glass rod. Using a syringe, 1mL of the MOF precursor solution was added to the Fe_2O_3@MIL-125-NH_2(Ti) mixture. The vial was capped, and

heated isothermally at 120°C for 10h to onset MOF formation. Products were cooled to room temperature after reaction, and then centrifuged twice with 15mL of DMF and then ethanol. After separation, solids were degassed in a vacuum oven at 50°C. Figure B-3 schematically organizes the entire production methodology

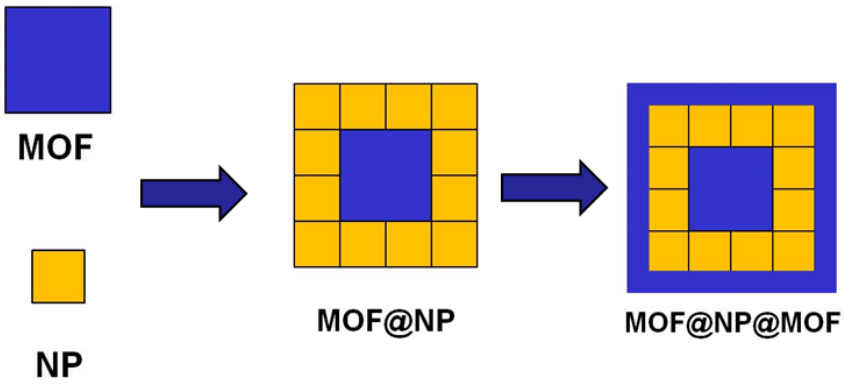

Figure B-3: Procedural flow chart of sandwich MOF formation

B.2.2. Characterization Methods

Please refer to Chapter 2 for details on PXRD, N_2 adsorption, and microscopy methods & equipment details

7.1.4.2 B.2.2.1 *XAS Measurements and Beamline H_2S Exposures*

XAS measurements on samples before and after H_2S exposure to ascertain chemical changes. Experiments were carried out at sector 12-BM in the Advanced Photon Source at Argonne National Laboratories. Below procedures are adapted from our submitted APS general user proposal 53482 in 2017.

Fe K-edge XAS measurements were collected for several powder samples before and after gas exposures. Hematite powder (purchased from a chemical supplier) and

laboratory prepared hematite nanoparticles were tested as a standard and *ex situ* sample (nanoparticles outside of the composite), respectively, for reference. Additionally, three batches of hematite/MOF composite samples were analyzed to allow for experimental repeatability. These samples were synthesized/purchased at Georgia Tech prior to beam time. Of course, XAS measurements of iron reference foil (from the synchrotron lab) was taken for data calibration. The following steps outline the experimental process, and a flowchart is provided to aid communication of the process in Figure B-4:

1. The sample was prepped in a sealed quartz tube (brought from Georgia Tech) using the "six-shooter" XAS sample holder. The tube was purged with inert, high purity argon, and heated to 200°C for 2h to remove guest adsorbates from the porous composite. After being allowed to cool, Fe K-edge (~7.112 keV) XAS measurements were be taken on "activated" samples. As such, materials were housed in the entire sealed tube assembly during prep and data acquisition to avoid changes from the surrounding atmosphere.
2. A 1000ppm H_2S/N_2 disposable bottle was used to expose samples to H_2S until H_2S is eluted on the tube outlet for at least 30min. The tube was then sealed and allowed to equilibrate for 1h prior to XAS measurements. The H_2S was purged with argon gas and heated to 200°C until H_2S was no longer detected in the effluent. After being allowed to cool, Fe K-edge XAS measurements were acquired on "exposed" samples. H_2S sensors were carried with the tube when moving it into the XAS chamber for personnel safety.

3. To study iron oxide regeneration in the powder samples, dry air was flowed through the tube for at least 1h at room temperature. Fe K-edge XAS measurements were then taken on the "regenerated" samples.

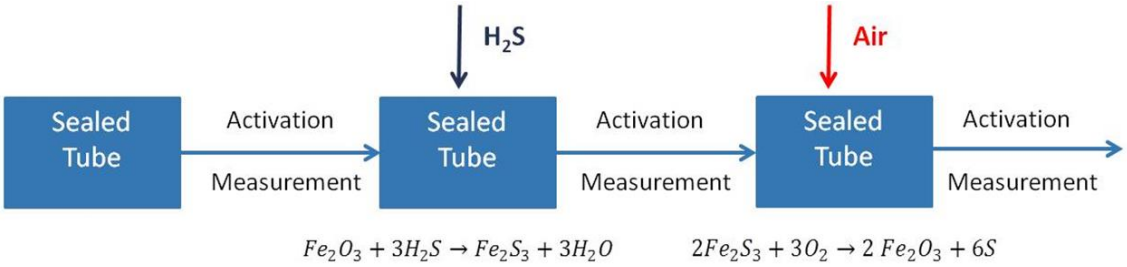

Figure B-4: Illustration of XAS experiment scheme

Two separate pellets of each sample were analysed for reproducibility. To ensure diffusion limitations or MIL-125-NH_2(Ti) uptake did not dictate whether or not iron oxide nanoparticles were exposed to H_2S, the entirety of the ~40L H_2S bottle was dosed onto samples of masses no greater than 5mg.

Samples were mixed with boron nitride binder in mass ratios and pellet thicknesses estimated using Hephaestus software and from the cross-sectional area of the six shooter hole (4-5mm diameter holes).[21] It was assumed samples were roughly 1wt% iron based on mass yields of MOF composites. Data acquisition parameters were performed using 0.3eV point spacings and 1s integration times in the XANES region, and 0.05 k-steps with 5s integration times in the EXAFS region—controlled using a macro at the beamline. Data analysis was performed using the Demeter software suite.[21]

B.3 Results

B.3.1. Composite Synthesis

TEM images of hematite nanoparticles, targeting 10nm diameters, are shown in Figure B-5. NPs appear to acquire a spherical-like shape and range from 1A-20nm in diameter. Figure B-6 evidences the tendency of NPs to aggregate. This is likely due to the PVP layer formed around synthesized nanoparticles, forming weak attraction to one-another.[19] Subsequently, this aggregation may hinder particle dispersion onto MOFs, discussed later.

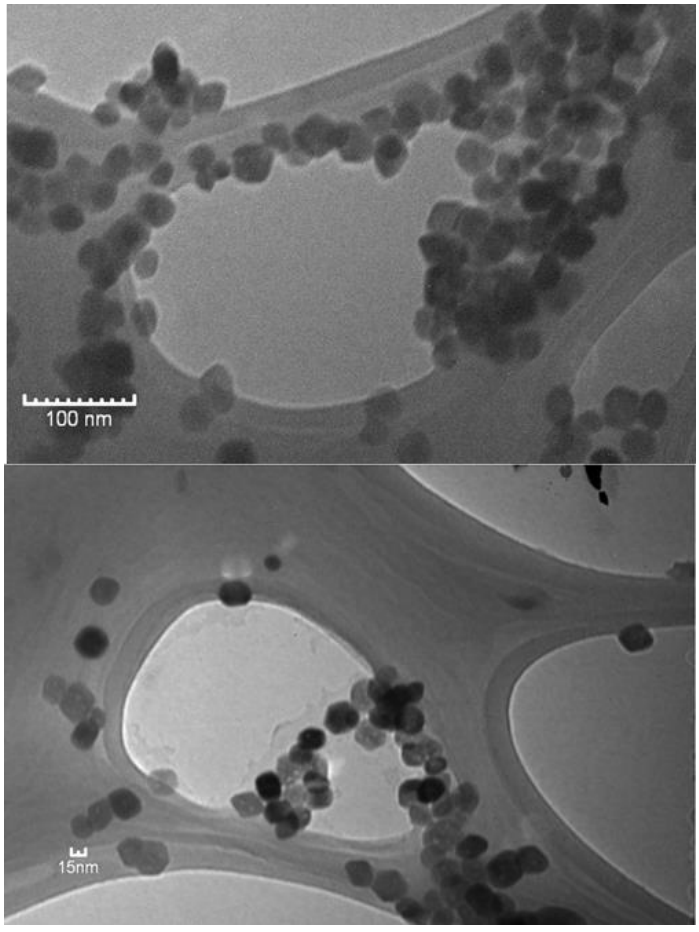

Figure B-5: TEM images of hematite nanoparticles

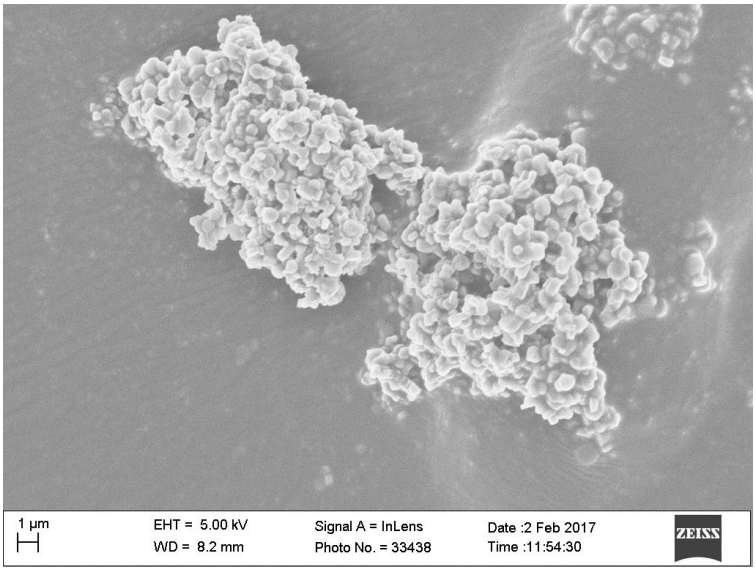

Figure B-6: SEM image of hematite NP aggregates

Particle distribution on the outside of MOF crystals was probed through electron microscopy. Figure B-7 evidences heterogeneous and non-uniform NP distribution around MOF crystals. Furthermore, MOF particles themselves appear to aggregate with one another, even through vigorous mixing in solution, which can block surface sites for nanoparticle adhesion. Hematite particles do appear to cluster around framework crystals however, showing the likely attraction of PVP surfactant to organic crystal surfaces. SEM observations in Figure B-8 echo maldistributed particles. In effort to improve dispersion, smaller additions of hematite particles were introduced dropwise to MOF particles, as described in Section B.2.1.3. Nanoparticle Encapsulation: Fe_2O_3@MIL-125-NH_2(Ti) Post-reaction TEM studies (Figure B-9) indicate both higher density and improved homogeneity of particle distribution on MIL-125-NH_2(Ti).

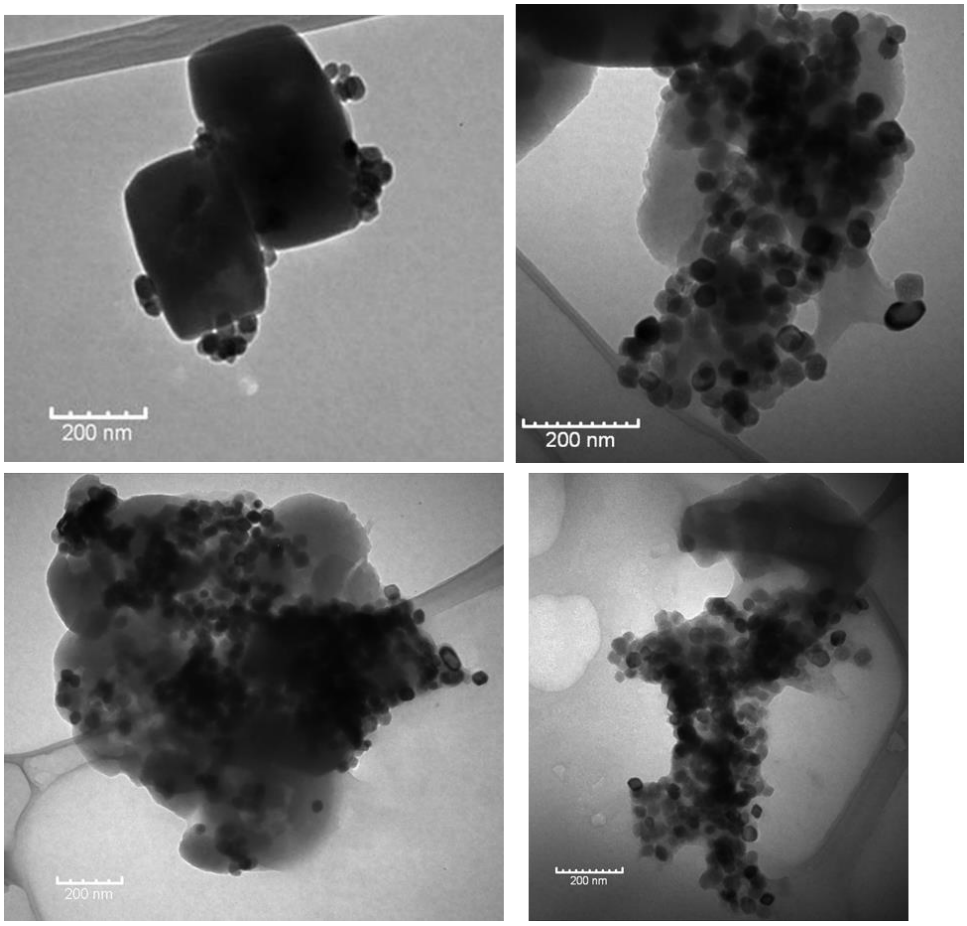

Figure B-7: TEM images of Fe_2O_3@MIL-125-NH_2(Ti)

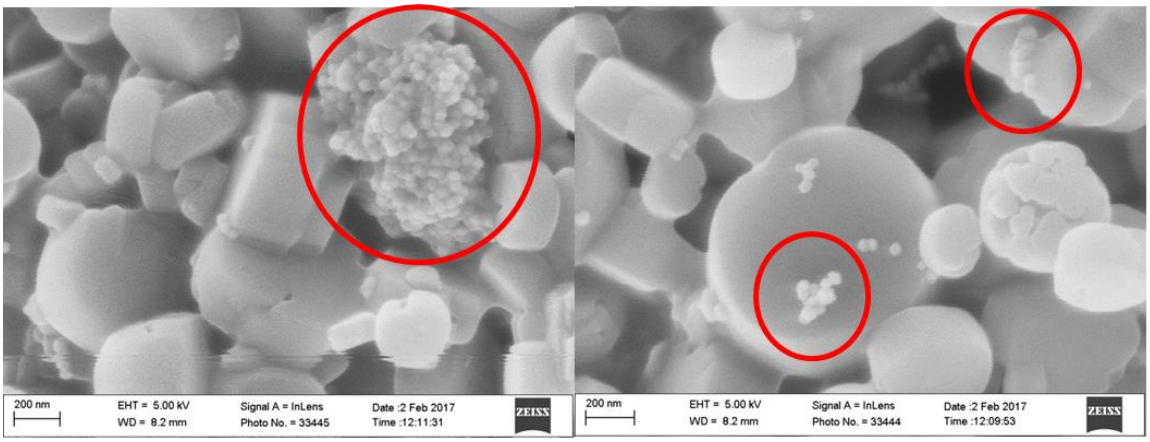

Figure B-8: SEM images of Fe_2O_3@MIL-125-NH_2(Ti) surfaces. Red circles highlight Fe_2O_3 NP locations

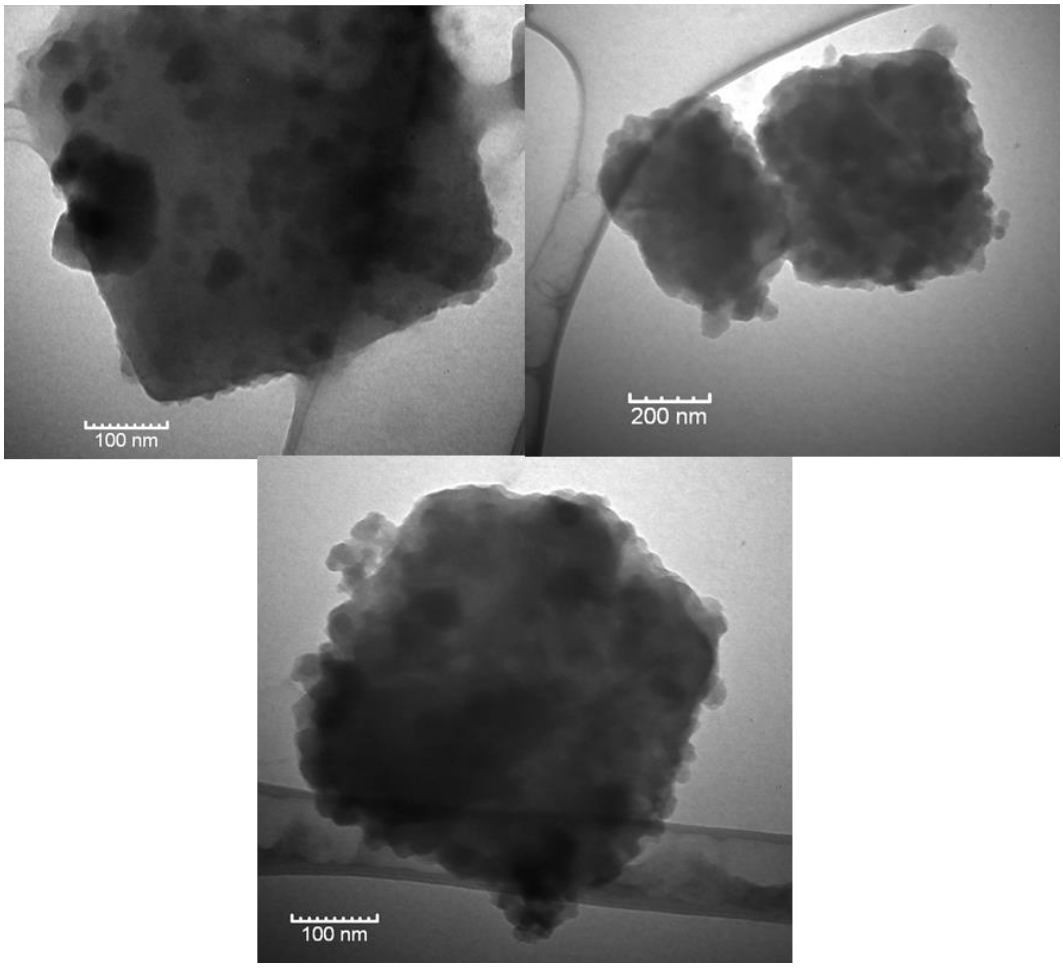

Figure B-9: Images of Fe_2O_3@MIL-125-NH_2(Ti) after improved NP mixing

The general procedure for "sandwich" MOF formation was adapted from prior work, although it has never been performed using the MIL-125-NH_2(Ti) system.[15,22] Post-reaction transmission images of MIL-125-NH_2(Ti)@Fe_2O_3@MIL-125-NH_2(Ti) in Figure B-10 show very poor retention of NPs along MOF surfaces. α-Fe_2O_3 NPs were likely displaced by reacting MOF ligands, although some NPs are still apparent.

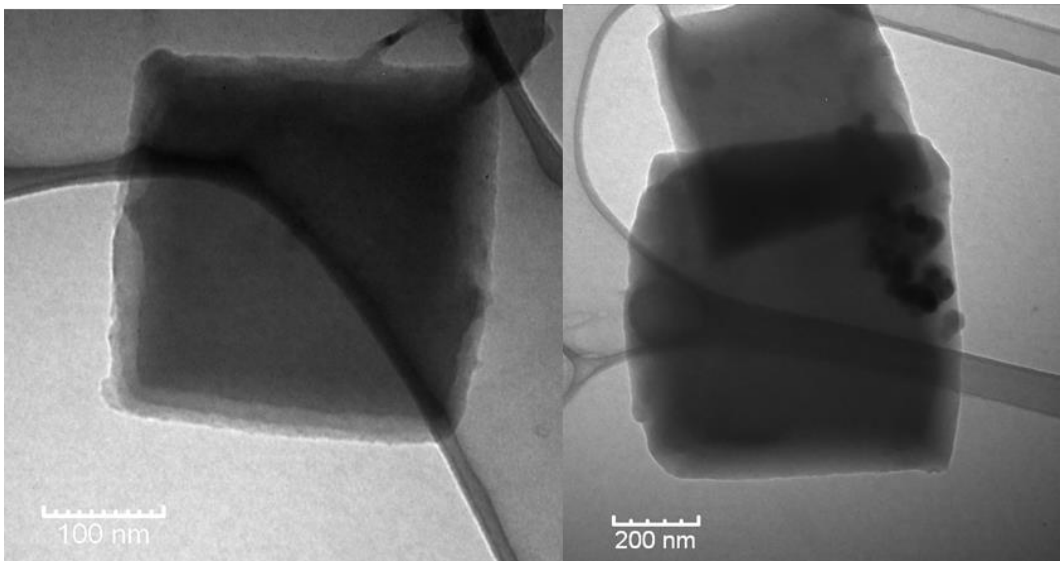

Figure B-10: TEM images of MIL-125-NH_2(Ti)@Fe_2O_3@MIL-125-NH_2(Ti)

MIL-125-NH_2(Ti)@Fe_2O_3@MIL-125-NH_2(Ti) and Fe_2O_3@MIL-125-NH_2(Ti) retain crystallinity through described reactions (Figure B-11a), indicating NP introduction does not distort the structure of the framework. This is possible in traditional encapsulation, since NPs reside within particle cavities, and distort the long-range order of host materials. Upon formation of Fe_2O_3@MIL-125-NH_2(Ti), Figure B-11b illustrates that mass normalized porosity drops for MIL-125-NH_2(Ti) materials due to the introduction of non-porous density. Fe_2O_3@MIL-125-NH_2(Ti) produced through the new mixing method has ~33% of the original BET surface area of MIL-125-NH_2(Ti)—drastically lower than the original Fe_2O_3@MIL-125-NH_2(Ti). This supports previously discussed visual observations on the introduction of more hematite species onto MOF particles.

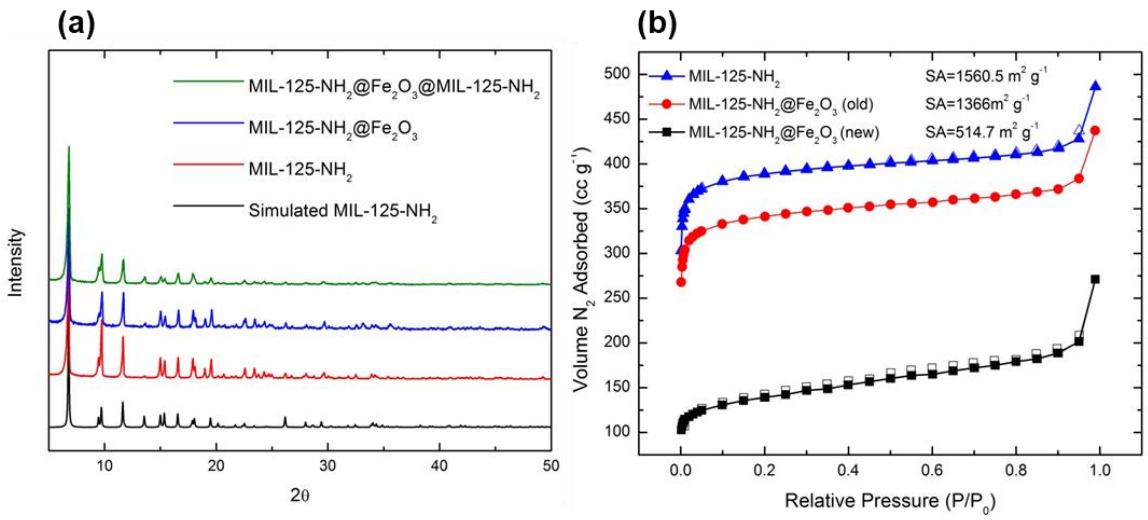

Figure B-11: Composite textural properties. (a) PXRD patterns of synthesized materials in comparison to simulated structure from Smalley et al.[23], (b) N_2 uptake curves at 77K for MIL-125-NH_2(Ti) materials.

XAS data was acquired for nanoparticle and MOF composite samples through H_2S exposure. Fe K-edge absorption edges and lineshapes in are consistent with iron(III) oxides.[4,24] Spectra for Fe_2O_3@MIL-125-NH_2(Ti) and MIL-125-NH_2(Ti)@Fe_2O_3@MIL-125-NH_2(Ti) in Figure B-12a & b do not evidence chemical changes in iron oxide species through H_2S exposure however. Interestingly, inspection of the Fe absorption edge of non-encapsulated hematite nanoparticle in Figure B-12c does appear to show a slight reduction of iron species after H_2S exposure. This would be expected from reaction, as iron oxide is reduced upon sulfidation. The small degree of change is likely caused by reactions only localized on NP surface sites, where unexposed Fe_2O_3 under the monolayer cannot undergo reaction. Iron oxide is re-oxidized after treatment in air, supporting the regenerability of hematite nanoparticles themselves, although it is likely elemental sulfur species are deposited on NP surfaces. Altogether, the data seem to indicate that integrating hematite NPs onto MIL-125-NH_2(Ti) supports seems to prevent reaction in some way. Because of

the large volume of H_2S exposed to studied samples, it is unlikely H_2S was just adsorbed elsewhere in the framework. Possibly neighboring MOF surfaces hindered access of H_2S to Fe_2O_3 surface sites.

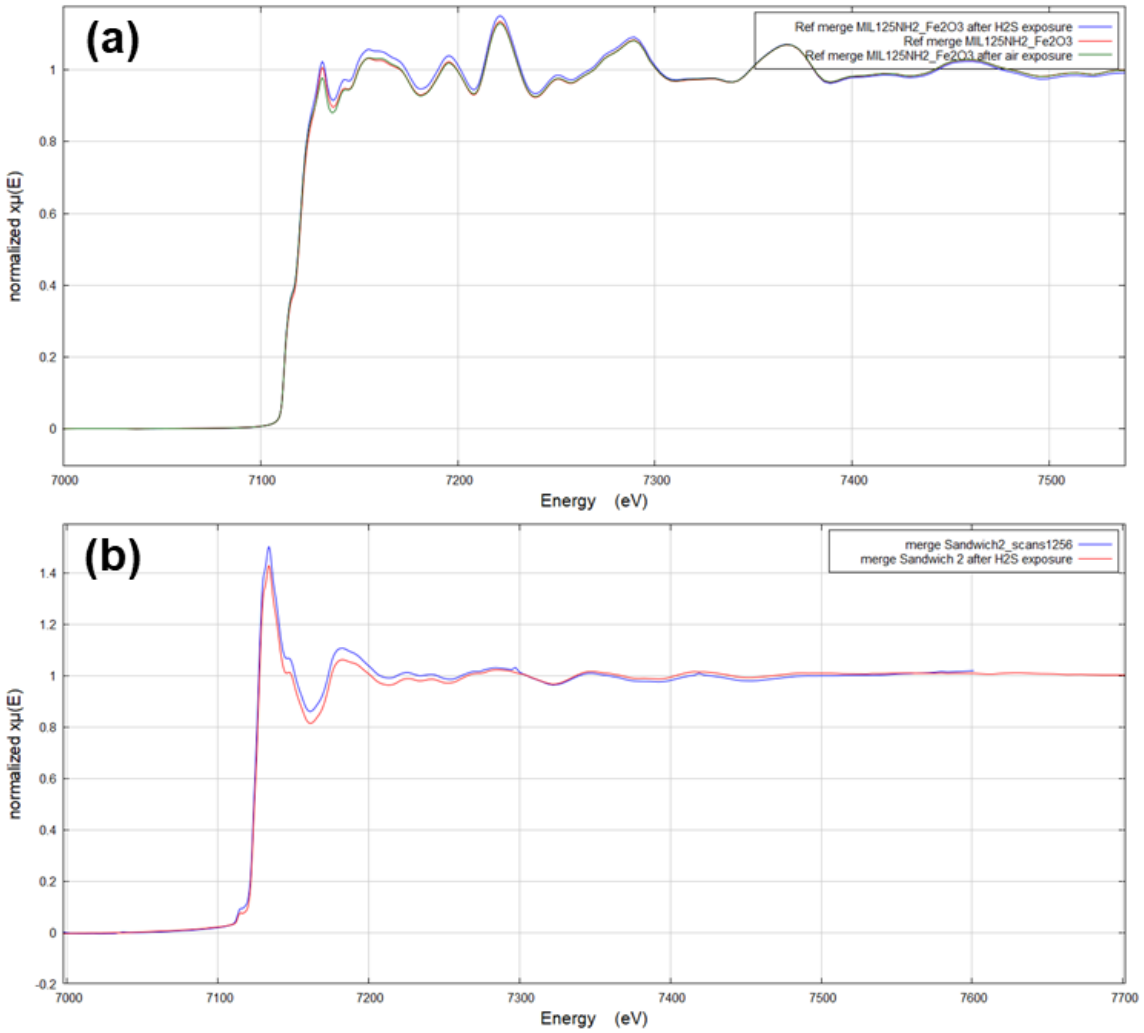
(a)
Ref merge MIL125NH2_Fe2O3 after H2S exposure
Ref merge MIL125NH2_Fe2O3
Ref merge MIL125NH2_Fe2O3 after air exposure
normalized xμ(E)
Energy (eV)
(b)
merge Sandwich2_scans1256
merge Sandwich 2 after H2S exposure
normalized xμ(E)
Energy (eV)

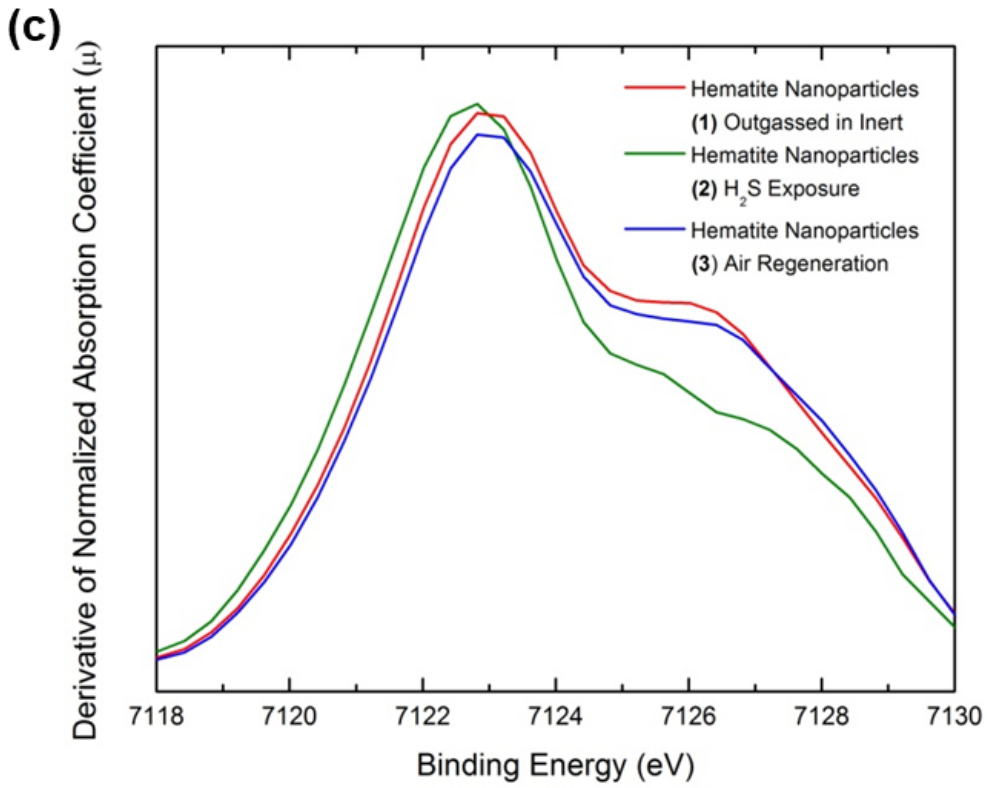
(c)
Hematite Nanoparticles
(1) Outgassed in Inert
Hematite Nanoparticles
(2) H2S Exposure
Hematite Nanoparticles
(3) Air Regeneration
Derivative of Normalized Absorption Coefficient (μ)
Binding Energy (eV)

Figure B-12: Fe K-edge XAS measurements for (a) Fe_2O_3@MIL-125-NH_2(Ti), (b) MIL-125-NH_2(Ti)@Fe_2O_3@MIL-125-NH_2(Ti), and (c) synthesized α- Fe_2O_3 NPs. Data in (c) shows the derivative of normalized μ on the absorption edge

B.4 Appendix B References

1. Abatzoglou, N. & Boivin, S. A review of biogas purification processes. *Biofuels, Bioprod. Biorefin.* **3**, 42–71 (2009).

2. Siefers, A. M. A Novel and Cost-Effective Hydrogen Sulfide Removal Technology Using Tire Derived Rubber Particles. *Iowa State University Digital Repository*. MS Thesis. (Iowa State University, 2010)

3. Bandosz, T. J. Towards understanding reactive adsorption of small molecule toxic gases on carbonaceous materials. *Catal. Today* **186**, 20–28 (2012)

4. Fauteux-Lefebvre, C., Abatzoglou, N., Braidy, N. & Hu, Y. Carbon Nanofilaments Functionalized with Iron Oxide Nanoparticles for in-Depth Hydrogen Sulfide Adsorption. *Ind. Eng. Chem. Res.* **54**, 9230–9237 (2015).

5. Parkinson, G. S. Iron Oxide Surfaces. *Surf. Sci. Rep.* **71**, 272–365 (2016).

6. Reshetenko, T. V., Khairulin, S. R., Ismagilov, Z. R. & Kuznetsov, V. V. Study of the reaction of high-temperature H2S decomposition on metal oxides (γ-Al_2O_3, α-Fe_2O_3, V_2O_5). *Int. J. Hydrogen Energy* **27**, 387–394 (2002).

7. Huang, G. *et al.* Synthesis and Characterization of γ-Fe_2O_3 for H_2S Removal at Low Temperature. *Ind. Eng. Chem. Res.* **54**, 8469–8478 (2015).

8. Ozekmekci, M., Salkic, G. & Fellah, M. F. Use of zeolites for the removal of H_2S: A mini-review. *Fuel Process. Technol.* **139**, 49–60 (2015).

9. Shi, M. *et al.* In situ oxidized magnetite membranes from 316L porous stainless steel via a two-stage sintering process for hexavalent chromium [Cr(VI)] removal from aqueous solutions. *Chem. Eng. J.* **265**, 84–92 (2015).

10. Qin, J.-X., Wang, Z.-M., Liu, X.-Q., Li, Y.-X. & Sun, L.-B. Low-temperature fabrication of Cu(i) sites in zeolites by using a vapor-induced reduction strategy. *J. Mater. Chem. A* **3**, 12247–12251 (2015).

11. Guo, Z. *et al.* Pt Nanoclusters Confined within Metal–Organic Framework Cavities for Chemoselective Cinnamaldehyde Hydrogenation. *ACS Catal.* **4**, 1340–1348 (2014).

12. Meilikhov, M. *et al.* Metals@MOFs - Loading MOFs with metal nanoparticles for hybrid functions. *Eur. J. Inorg. Chem.* 3701–3714 (2010)

13. Schroder, M. *Functional Metal-Organic Frameworks: Gas Storage, Separation and Catalysis*. (Springer, 2010)

14. Nasalevich, M. A. *et al.* Co@NH_2-MIL-125(Ti): cobaloxime-derived metal–organic framework-based composite for light-driven H2 production. *Energy Environ. Sci.* **8**, 364–375 (2015).

15. Lu, G. *et al.* Imparting functionality to a metal-organic framework material by controlled nanoparticle encapsulation. *Nat. Chem.* **4**, 310–316 (2012).

16. Puthiaraj, P. & Ahn, W.-S. Highly active palladium nanoparticles immobilized on NH_2-MIL-125 as efficient and recyclable catalysts for Suzuki-Miyaura cross coupling reaction. *Catal. Commun.* **65**, 91–95 (2015).

17. Tulig, K. & Walton, K. S. An alternative UiO-66 synthesis for HCl-sensitive nanoparticle encapsulation. *RSC Adv.* **4**, 51080–51083 (2014).

18. Hamon, L. *et al.* Comparative Study of Hydrogen Sulfide Adsorption in the MIL-53 (Al, Cr, Fe), MIL-47 (V), MIL-100 (Cr), and MIL-101 (Cr) Metal- Organic Frameworks at Room Temperature. *J. Am. Chem. Soc.* **131**, 8775–8777 (2009).

19. Zhu, M., Wang, Y., Meng, D., Qin, X. & Diao, G. Hydrothermal Synthesis of Hematite Nanoparticles and their Electrochemical Properties. *J. Phys. Chem. C* **116**, 16276–16285 (2012).

20. Zhao, M. *et al.* Metal–organic frameworks as selectivity regulators for hydrogenation reactions. *Nature* **539**, 76–80 (2016).

21. Ravel, B. About Demeter. (2006). Available at: https://bruceravel.github.io/demeter/. (Accessed: 24th March 2019)

22. Huo, F. A new breakthrough in selective catalysis: metal-organic framework nanocomposites with sandwich structure. *Sci. Bull.* **61**, 1726–1727 (2016).

23. Smalley, A. P., Reid, D. G., Tan, J. C. & Lloyd, G. O. Alternative synthetic methodology for amide formation in the post-synthetic modification of Ti-MIL125-NH_2. *CrystEngComm* **15**, 9368–9371 (2013).

24. Corrias, A., Ennas, G., Mountjoy, G. & Paschina, G. An X-ray absorption spectroscopy study of the FeK edge in nanosized maghemite and in Fe_2O_3-SiO_2 nanocomposites. *Phys. Chem. Chem. Phys.* **2**, 1045–1050 (2000)

APPENDIX C. SCRIPT FOR DETERMINING BREAKTHROUGH CAPACITIES

C.1 Calculating Breakthrough Capacities

A script written for MATLAB is provided below to assist adsorption capacity estimation from dynamic adsorption data. The script was used (although in sometimes adapted forms) to calculate breakthrough capacities for acid gas adsorbents reported in Chapter 4. It can also be modified to deduce desorption capacities, although this alteration is not included below. The reproduced code below utilizes data from (1) the target adsorbate and (2) a tracer gas to organize eluting concentration data as a function of time. Numerical integration through a built-in trapezoid rule function in MATLAB[1] and a series of unit conversions based on prior reports[2] is then utilized to calculate adsorption capacities at a specified time/adsorbate concentration.

The code is reported here with the intention to facilitate estimations of experimental adsorption data. Please note differences in experimental systems, test conditions (e.g. single component vs. multicomponent), or measurement outputs may warrant modification of the script. So future users are advised to understand the code before using it to deduce adsorption information.

C.1.1. MATLAB Script

```
%Dead Time and Breakthrough Capacity Calculator
%Acid Gas Breakthrough
%Jay Joshi
%Last Update: 01/15/2019
```

```
%This is a generic code to determine dead time, output a time vs conc
profile
%and determine dynamic saturation capacity. It
%requires a number of inputs, listed in chronological order:
    %volumetric flow rate (V)
    %time data (time, calibrated for dead time)
    %adsorbate eluted data (conc)
    %adsorbate identity
    %mass of adsorbent used (Mads)
%Uses trapezoid rule for numerical integration.

clear
clc
%-------------------------------------------------------------------------
----

%Dead Time Calculation
disp('Approximate Dead Time: Enter the TOTAL volumetric flow rate of
adsorbate mixture(mL/min)')
prompt='Flow Rate=';
V=input(prompt);
Vs=V/60;    %puts volumetric flow rate in mL/s
%Dead Volume is approximately 15.3 mL using He tests

%Capacity
%%First, calculate nitrogen tracer dead time

    %Define Inputs for tracer data
    disp('Enter in the time (s) range IN BRACKETS')
    prompt='time=';
    time=input(prompt);
    disp('Enter in the tracer concentration (%) range IN BRACKETS')
    prompt='tracer concentration (%)=';
    tracer=input(prompt);

    %Defining conversion factors for N2 tracer
    D_tracer=1.251/1000;  %g/mL
    MW_tracer=28;  %g/mol

    %Normalizing the N2 breakthrough data to 1
    inletconc_tracer=max(tracer)/100*1000*D_tracer/MW_tracer*1000;
%mmol/L of tracer at max concentration
    tracer_mmolL=tracer/100*1000*D_tracer/MW_tracer*1000;
    tracer_norm=tracer_mmolL/inletconc_tracer;  %Normalizes the
nitrogen tracer to a max value of 1

%Enter the concentration vs time data for the test gas

    %Define Inputs
    disp('Enter in the adsorbate concentration (%) range IN BRACKETS')
    prompt='adsorbate concentration (%)=';
    conc=input(prompt);  %conc is the vector for the gas concentrations
in percent (%)
```

```
    %Defining gas inputs and converting concentration. Adsorbent mass
input.
    disp('What is your adsorbate of interest?')
    disp('For H2S, Enter 1')
    disp('for CO2, Enter 2')
    disp('for SO2, Enter 3')
    prompt='component:';
    c=input(prompt);        %c represents the entered component. Allows
for: H2S, CO2, and SO2
     % (D) is gas density [g/cc]. (MW) is the molecular weight of the
adsorbate [g/mol]
        if c==1;
            D=0.001393;
            MW=34;
        elseif c==2
            D=0.001977;
            MW=44;
        elseif c==3
            D=0.00263;
            MW=64;
        else
            disp('Component not in library. Please include density and
molecular weight into script')
        end
    % If you are looking at a component not in the library, you can
also comment off the
    % 'if statement' and edit the parameters after uncommenting them.

    inletconc=max(conc)/100*1000*D/MW*1000;    %INPUT the concentration
of inlet gas (mmol/L)
    %inletconc=conc(end)/100*1000*D/MW*1000   %calculate inlet
concentration assuming the last value is the greatest

%Prompt's input of adsorbent mass in grams
disp('Enter in adsorbent mass, in grams')
prompt='Adsorbent Mass=';
Mads=input(prompt);

%Convert the adsorbate concentration data into several different units
conc_ppm=conc*10000; %provides concentration in ppm
conc_mmolL=conc/100*1000*D/MW*1000;    %provides concentration in
mmol/L
conc_norm=conc_mmolL/inletconc;      %provides normalized concentration
to 1
normtime=time/Mads/60;     %normalizes time over mass of adsorbent
(min/g)

%Calculate breakthrough capacity, and generate plots
    %Breakthrough capacity
    breakthrougharea=trapz(time,tracer_norm)-trapz(time,conc_norm);
%Calculating area difference between tracer and adsorbate.

%Uses trapezoid rule for curves normalized to one.
    breakthroughcapacity=breakthrougharea*inletconc*Vs/1000/Mads
%Calculate and output breakthrough capacity (mmol adsorbate/g
adsorbent)
```

```
    %Plotting
    clf;  %clears open figures. Comment this line out if you want to
plot multiple curves on top of each other
    plot((normtime),tracer_norm,'--') %plots tracer curve
    hold on;
    plot((normtime),conc_norm)   %plots normalized adsorbate curve
    xlabel('Normalized Time [min/g]')

    ylabel('Normalized Concentration (C/C0)')
```

C.2 Appendix C References

1. Trapezoidal numerical integration - MATLAB trapz. *MathWorks* (2019). Available at: https://www.mathworks.com/help/matlab/ref/trapz.html. (Accessed: 17th April 2019)

2. Grant Glover, T., Peterson, G. W., Schindler, B. J., Britt, D. K. & Yaghi, O. M. MOF-74 building unit has a direct impact on toxic gas adsorption. *Chem. Eng. Sci.* **66**, 163–170 (2011)